



**HAL**  
open science

# New processing routes by high-pressure torsion of different nature of magnesium based powders for improved hydrogen storage applications

Subrata Panda

► **To cite this version:**

Subrata Panda. New processing routes by high-pressure torsion of different nature of magnesium based powders for improved hydrogen storage applications. Materials Science [cond-mat.mtrl-sci]. Université de Lorraine, 2018. English. NNT : 2018LORR0337 . tel-02346615

**HAL Id: tel-02346615**

**<https://hal.univ-lorraine.fr/tel-02346615>**

Submitted on 22 Jun 2020

**HAL** is a multi-disciplinary open access archive for the deposit and dissemination of scientific research documents, whether they are published or not. The documents may come from teaching and research institutions in France or abroad, or from public or private research centers.

L'archive ouverte pluridisciplinaire **HAL**, est destinée au dépôt et à la diffusion de documents scientifiques de niveau recherche, publiés ou non, émanant des établissements d'enseignement et de recherche français ou étrangers, des laboratoires publics ou privés.



## AVERTISSEMENT

Ce document est le fruit d'un long travail approuvé par le jury de soutenance et mis à disposition de l'ensemble de la communauté universitaire élargie.

Il est soumis à la propriété intellectuelle de l'auteur. Ceci implique une obligation de citation et de référencement lors de l'utilisation de ce document.

D'autre part, toute contrefaçon, plagiat, reproduction illicite encourt une poursuite pénale.

Contact : [ddoc-theses-contact@univ-lorraine.fr](mailto:ddoc-theses-contact@univ-lorraine.fr)

## LIENS

Code de la Propriété Intellectuelle. articles L 122. 4

Code de la Propriété Intellectuelle. articles L 335.2- L 335.10

[http://www.cfcopies.com/V2/leg/leg\\_droi.php](http://www.cfcopies.com/V2/leg/leg_droi.php)

<http://www.culture.gouv.fr/culture/infos-pratiques/droits/protection.htm>

# THÈSE

Pour l'obtention du titre de :  
**DOCTEUR de L'UNIVERSITÉ DE LORRAINE**

Spécialité : Sciences des Matériaux

Présentée par :  
**SUBRATA PANDA**

---

**Nouveaux procédés d'élaborations par torsion sous forte pression de  
différentes natures de poudres de magnésium pour l'amélioration du  
stockage de l'hydrogène**

**New processing routes by high-pressure torsion of different nature of  
magnesium based powders for improved hydrogen storage applications**

---

Soutenu publiquement le 07/06/2018 à Metz Technopôle devant le jury composé de :

M. Jacques HUOT	Professeur à l'Université du Québec à Trois-Rivières, Canada	Rapporteur
M. Satyam SUWAS	Professeur à Indian Institute of Science, Bengaluru, India	Rapporteur
Mme Emilie GAUDRY	Professeur à l'Université de Lorraine, France	Examinatrice
Mme Julia IVANISENKO	Chargé de Recherche au INT, Karlsruhe Institute of Technology, Germany	Examinatrice
M. Kaveh EDALATI	Professeur à Kyushu University, Fukuoka, Japan	Examineur
M. Jianxin ZOU	Professeur à Shanghai Jiao Tong University, China	Invité
M. Laszlo S. TOTH	Professeur à l'Université de Lorraine, France	Co-directeur de thèse
M. Thierry GROSDIDIER	Professeur à l'Université de Lorraine, France	Directeur de thèse

*Laboratoire d'Excellence DAMAS, Laboratoire LEM3, Metz-Technopole, 57073  
Université de Lorraine – Pôle M4 : matière, matériaux, métallurgie, mécanique*

*Dedicated to my wife, Amiya Mishra for her enormous  
encouragements and supports*

## RÉSUMÉ DE LA THÈSE

---

Les techniques de déformation plastique sévère sont de plus en plus utilisées pour l'amélioration des propriétés de stockage de l'hydrogène au sein de différents hydrures métalliques. Cette étude porte principalement sur l'influence de déformations plastiques sévères réalisées par High Pressure Torsion (HPT ou torsion sous forte pression) sur différentes natures de poudres de magnésium pour la modification des propriétés d'absorption de l'hydrogène. Un nouveau procédé de métallurgie des poudres a été utilisé afin de produire une large gamme de combinaisons de matériaux. Il consiste en : (i) l'élaboration de poudres de magnésium ultrafines dites "propres" et (ii) la modification structurelles par HPT de la poudre précédemment formée. Pour comparaison, d'autres natures de poudres ont été obtenues soit par atomisation sous atmosphère gazeuse. Suite à une analyse permettant une meilleure compréhension du procédé HPT sur différents massifs de différentes structures cristallographiques (Al CFC vs. Mg HC), des échantillons massifs consolidés ont été fabriqués par HPT sur : (i) deux types de poudres de magnésium, (ii) une combinaison de poudres de Mg et de Fe et, (iii) une poudre composée de Mg dopée en graphène. Ces matériaux ont été soigneusement évalués pour leurs potentielles améliorations sur le stockage de l'hydrogène au sein de poudres de magnésium modifiées, comparés aux poudres initiales.

Parmi les poudres composites étudiées, la poudre de magnésium contenant du graphène a montrée d'excellentes propriétés d'absorption de l'hydrogène correspondant à des cinétiques d'activation plus rapides. Cette capacité de stockage supérieure a principalement été attribuée à des caractéristiques morphologiques uniques de ces particules de type "core-shell" pour lesquelles le magnésium à cœur est entouré par une couche protectrice mince formée par le graphène. L'utilisation de déformations plastiques sévères par HPT a fournis des différences notables, voire des tendances opposées, sur les propriétés d'absorption de l'hydrogène. Un avantage significatif du procédé HPT est de briser les couches d'oxyde MgO, imperméables au passage de l'hydrogène et de venir les disperser uniformément avec les additifs dans le Mg. Par l'introduction de défauts cristallins associés à un affinement microstructural, le procédé HPT a permis d'obtenir des améliorations significatives dès le premier cycle d'hydrogénation pour les poudres consolidées de Mg par rapport aux poudre initiales, tandis que des résultats inverses ont

été obtenus au sein de la poudre dopée au C et déformée par HPT. Un autre impact du procédé HPT a été de réduire l'hystérésis entre les plateaux de pression d'absorption et de résorption au cours des essais PCT (pressure-composition-temperature). De plus, il a été observé que le procédé HPT réduit de manière drastique la température de résorption pour toutes les combinaisons de poudres tandis que le taux de résorption de l'hydrogène a été légèrement diminué pour les produits consolidés. Toutefois, l'inconvénient majeur du procédé HPT, indépendamment de la nature des composés étudiés, est qu'il altère systématiquement la capacité de stockage maximum des poudres initiales.

## ABSTRACT OF THE THESIS

---

Severe plastic deformation (SPD) techniques are increasingly applied for improving the hydrogen storage properties of various kinds of metal hydrides. The present dissertation work mainly focuses on the effect of severe plastic deformation through high-pressure torsion (HPT) of different nature of magnesium based powders for modifying the hydrogen sorption properties. A new powder metallurgy route has been adopted in the present study to produce a wide variety of material combinations. This novel processing route consists of: (i) synthesis of a rather “clean” type of Mg based powder particles and (ii) structural modifications by HPT deformation of the as-synthesized powder precursors. Different nature of powders was obtained by either a gas-atomization process or an arc-plasma evaporation/condensation method. After improving our understanding of the HPT processing technique on bulk samples having different crystal structures (FCC Al vs. HCP Mg), consolidated bulk products with different chemistry were produced by HPT processing of: (i) two types of Mg powders, (ii) combination of Mg and Fe powders, and (iii) Mg/graphene based composite powder. These products were thoroughly assessed for microstructural evolutions as well as for potential improvements in hydrogen storage properties of Mg in comparison with the starting powder precursors.

Among the studied powder composites, the Mg/graphene based powder demonstrated excellent hydrogen sorption properties presenting faster activation kinetics. This superior storage property was mainly attributed to its unique morphological features consisting of a “core-shell” type powder morphology, in which the core of Mg powder particles was surrounded by a protective thin layer of graphene sheets. The severe plastic deformation through HPT has provided substantial differences, and even opposite trends, in the hydrogen sorption characteristics of Mg. A significant advantage of the HPT processing was to break the impervious MgO layer and to disperse them uniformly along with the catalytic additives within the Mg domains. Through the introduction of structural defects and microstructural refinement, the HPT processing has allowed significant improvements in the first hydrogenation kinetics for the consolidated Mg products compared to their initial powder precursors while it was reverse for the C-doped HPT products. Another significant impact of the HPT processing was to reduce the hysteresis between the absorption and desorption plateau pressures during the pressure-

composition-temperature (PCT) experiments. Moreover, it was revealed that the HPT processing has drastically reduced the hydrogen desorption temperatures for all powder combinations while the rate of dehydrogenation was slightly diminished for their consolidated products. Nevertheless, the major drawback of the HPT processing, irrespective of the nature of studied composites, was that it always impaired the maximum hydrogen storage capacity of the starting powder precursors.

# TABLE OF CONTENTS

---

<b>Introduction</b> .....	1
<b>Chapter 1: Bibliographic review and scope of thesis work</b> .....	9
Introduction .....	10
1.1 Hydrogen: a clean energy vector for future .....	11
1.2 Options for hydrogen storage .....	13
1.2.1 Solid-state storage of hydrogen .....	16
1.2.2 Lightweight metal hydrides .....	20
1.3 Modifications of hydrogen sorption properties .....	22
1.3.1 Mechanical effects of ball milling .....	23
1.3.2 Severe plastic deformation (SPD) techniques .....	26
1.3.3 Influence of additive/catalysts .....	35
1.4 Scope of thesis work .....	39
References .....	41
<b>Chapter 2: Experimental materials, methods and characterization techniques</b> .....	45
2.1 Selected materials .....	46
2.2 Processing routes .....	50
2.2.1 Arc-plasma method .....	50
2.2.2 High-pressure torsion (HPT) .....	51
2.2.3 Two-step HPT consolidation .....	53
2.3 Characterization techniques .....	54
2.3.1 X-ray tomography (XRT).....	54
2.3.2 X-ray diffraction (XRD) .....	55
2.3.3 Hardness testing .....	56
2.3.4 Scanning electron microscope (SEM) .....	57
2.3.5 Electron backscatter diffraction (EBSD) .....	57
2.3.6 SEM based transmission Kikuchi diffraction (SEM-TKD) .....	58

## Table of contents

---

2.3.7	Transmission electron microscope (TEM) .....	58
2.3.8	Sievert-type apparatus .....	59
2.3.9	Differential scanning calorimetry-thermogravimetry (DSC-TG) .....	60
2.3.10	Raman Spectroscopy .....	61
	References .....	62

### **Chapter 3: Understanding of high-pressure torsion (HPT) processing in case of bulk as well as powder materials for relatively thick-samples .....**

	Introduction .....	65
	<b>Part I: Effects of processing conditions on heterogeneities in strain, microstructure and hardness in two bulk materials: aluminum alloy and commercial purity magnesium .....</b>	<b>68</b>
3I.1	X-ray tomography .....	69
3I.1.1	Gradients in shear deformation .....	69
3I.1.2	Strain analysis .....	71
3I.2	EBSD characterizations .....	75
3I.2.1	Aluminum alloy .....	75
3I.2.2	Commercial purity Mg .....	79
3I.3	Evolutions of microhardness .....	81
3I.4	Discussion .....	84
	<b>Part II: HPT consolidation of two distinct Mg powders: Influences of nature of initial powder precursors on evolutions of microstructure, texture and strength .....</b>	<b>87</b>
3II.1	Structural characterizations .....	89
3II.1.1	X-ray diffraction (XRD) .....	89
3II.1.2	SEM observations .....	90
3II.2	EBSD and TKD characterizations .....	95
3II.2.1	Micro-HPT product obtained from atomized Mg .....	95
3II.2.2	Nano-HPT product obtained from condensed Mg .....	98
3II.3	Microhardness evolution .....	101
3II.4	Discussion .....	105
3II.4.1	Effects of severe plastic deformation through HPT .....	105

## *Table of contents*

---

3II.4.2 Significance of MgO oxides .....	108
Chapter's conclusions .....	111
References .....	113
<b>Chapter 4: Study of improvements in hydrogen storage properties of high-pressure torsion (HPT) consolidated magnesium products .....</b>	<b>115</b>
Introduction .....	116
4.1 First hydrogenation kinetics .....	119
4.2 Hydrogen sorption properties .....	121
4.2.1 Thermodynamics of absorption/desorption .....	121
4.2.2 Kinetics of hydrogen absorption .....	126
4.2.3 XRD of the hydrided products .....	129
4.3 Desorption performances .....	131
4.4 Microstructural modifications upon cycling .....	134
4.5 Discussion .....	137
4.5.1 Consequences of the processing route .....	137
4.5.2 Influences of the nature of initial powder precursors .....	139
4.5.3 Effects of the absorption/desorption cycling .....	141
Chapter's conclusions .....	142
References .....	144
<b>Chapter 5: Hydrogen storage properties of Mg-Fe based composites fabricated by high-pressure torsion consolidation of magnesium and iron powder precursors .....</b>	<b>145</b>
Introduction .....	146
5.1 Structural characterizations of the HPT composites .....	150
5.1.1 Consolidated microstructures .....	150
5.1.2 XRD analysis of the HPT composites .....	154
5.1.3 XRD analysis of the hydrided products .....	157
5.2 First hydrogenation kinetics .....	159
5.3 Hydrogen sorption properties .....	160

## *Table of contents*

---

5.3.1	Thermodynamics of absorption/desorption .....	160
5.3.2	Kinetics of hydrogen absorption .....	167
5.3.3	Hydrogen desorption by thermal decomposition .....	170
5.4	Discussion .....	175
5.4.1	Effects of the processing route .....	175
5.4.2	Nature of the initial powder precursors .....	177
5.4.3	Catalytic effects .....	179
	Chapter's conclusions .....	182
	References .....	184

## **Chapter 6: Hydrogen storage properties of as-synthesized and high-pressure torsion (HPT) consolidated magnesium-graphene based composites .....**

	Introduction .....	188
6.1	Structural characterizations .....	192
6.1.1	Morphology and microstructure .....	192
6.1.2	X-ray diffraction (XRD) analyses .....	195
6.1.3	Raman spectroscopic analysis .....	197
6.2	First hydrogenation characteristics .....	199
6.3	Hydrogen sorption properties .....	202
6.3.1	Thermodynamics of absorption/desorption .....	202
6.3.2	Kinetics of hydrogen absorption .....	205
6.3.3	Hydrogen desorption behaviors .....	207
6.4	Discussion .....	210
6.4.1	Peculiarity in powder formation and its consequences .....	210
6.4.2	Effects of severe plastic deformation through HPT .....	214
	Chapter's conclusions .....	217
	References .....	219

## *Table of contents*

---

### **Conclusions and perspectives**

Summary and conclusions .....	223
Perspectives .....	227

### **Appendix**

Calculation of hydrogen contents .....	229
Lists of figures .....	230
Lists of tables .....	235
Acknowledgements .....	237
Related papers published .....	239



## INTRODUCTION

---

In the advancement of socioeconomic developments, today's energy and transportation systems are primarily based on fossil fuel energy carriers such as coal, oil, natural gas etc. Due to the world's population growth as well as the progressive industrialization of the developing countries, the extended use of these carbon-based resources must lead to a significant counterpart between the future energy demand and the security of its supply. Concurrently, their high emissions of greenhouse gases, which keep rising day-by-day, need to be controlled in order to prevent the anthropogenic climate change. Hence, the sustainability of energy supply and the effects of global warming represent two major concerns about the future of world's economy which give rise to the challenge of finding a potential alternative.

Hydrogen economy is advancing significantly to replace the fossil fuel based energy systems primarily because hydrogen is emission-free at the point of final use, and thus avoids the transport-induced products of incomplete combustion ( $\text{CO}_x$ ,  $\text{NO}_x$ ,  $\text{SO}_x$  etc.) [I.1-I.3]. Hydrogen, especially in combination with fuel cells, is considered to be the most promising solution for the long-term transition to alternative automotive fuels for the 21<sup>st</sup> century. Portable applications of the hydrogen economy are primarily considered in three major fields: automotive, power sectors and industry markets. Hydrogen powered fuel cell vehicles are expected to be two to three times more fuel-efficient (50-60%) than the conventional gasoline fueled internal combustion engine vehicles (22%) [I.4,I.5].

Despite its unique advantages, hydrogen has not yet been widely exploited as a powerful alternative. Perhaps the most criticizing factor that limits its use is the difficulty involved in storing it conveniently and economically. Hydrogen can be stored by compression and/or liquefaction, but these options are not completely satisfactory in terms of cost and energy efficiency [I.6]. In addition, the storing of hydrogen in the form of gas or liquid also involves safety related issues. In this regard, metal hydrides are considered as excellent candidates for storing of hydrogen in the solid-state. Hydrides are chemical compounds formed when hydrogen reacts with certain metals, which offer a far higher bulk density than compressed gas or liquid hydrogen [I.7]. Using metal hydrides the storage becomes safe and efficient; owing to the relatively low pressure, reversibility and excellent energy efficiency.

In the last few decades, reversible reaction of hydrogen with metals, alloys or intermetallic compounds, namely rechargeable hydrides found its extreme importance in the field of energy sectors as the most promising solid-state hydrogen storage media for on-board applications while combining with fuel cells [I.7,I.8]. Among the solid-state storage media, the light metal alloys (group 1, 2 and 3 light metals) are more attractive in terms of their technical and economic advantages such as light-weight, low cost and high gravimetric capacity. Particularly Mg and Mg based alloys have been explored extensively due to both high gravimetric storage capacity (7.6 wt% for  $\text{MgH}_2$ ) and volumetric storage density ( $>120 \text{ kg H}_2 \text{ m}^{-3}$ ) [I.9]. Unfortunately, the M-H systems have a drawback of unfavorable thermodynamics and slow kinetics for hydrogen uptake and release. Indeed, thermodynamics dictate the relatively high sorption temperatures due to a high enthalpy of formation ( $-76 \text{ kJ/mol H}_2$  for  $\text{MgH}_2$ ) [I.10]. Reviews of recent investigations have shown that the kinetics of hydrogen sorption reaction can

be remarkably improved by reducing particle/grain size by means of mechanical milling or severe plastic deformation (SPD) techniques [I.11,I.12]. Furthermore, the incorporation of metallic/non-metallic elements or their oxides, some carbonaceous materials and halides as catalysts have demonstrated significant improvements in the absorption/desorption processes for many M-H systems [I.8].

The most versatile processing route for producing a wide variety of hydrogen storage materials is high energy ball-milling (HEBM) [I.13], developing nanocrystalline materials with numerous structural defects and potentially amorphous areas in the matrix phase which can basically accelerate the hydrogen diffusion processes. However, it is difficult to avoid agglomeration during milling of ductile materials, and impurities coming from the milling media and/or atmosphere are hard to control, and can significantly affect the functional properties of hydrogen storage materials [I.14]. For a large scale production, this is also an expensive approach in terms of specific energy and processing time. Moreover, extra care must be taken for handling very fine powder particles which can otherwise lead to severe environmental and health issues. In the recent years, processing routes involving severe plastic deformation (SPD) techniques such as equal channel angular pressing (ECAP), cold rolling (CR) and high-pressure torsion (HPT) etc. have been increasingly investigated to improve the hydrogen storage properties of various metal hydrides [I.15,I.16]. While, similar to the HEBM route, the SPD processing can also produce nanocrystalline/ultrafine-grained materials with numerous structural defects in the matrix phase [I.16], the SPD processing is less likely to introduce contamination within the heavily deformed materials.

In this context, the present dissertation work has followed two major goals. The first goal (mainly in **Chapter 3**) is to improve our understanding of high-pressure torsion (HPT) processing of relatively large Mg sample processed from bulk and powder materials through the evolution of their microstructure and texture, and mechanical properties (hardness). The second goal focuses on determining the effects of HPT on the improvements in hydrogen storage properties of Mg/MgO based composites sintered from atomized or condensed powders having different chemistry: based on Mg (**Chapter 4**), based on Mg-Fe (**Chapter 5**) and Mg-graphene (**Chapter 6**). In the following paragraphs, the primary objective of each chapter has been briefly described.

**Chapter 1** describes a short background of the current research by taking into account the related studies carried out in the recent past. At the beginning of this chapter, the advantages and disadvantages of lightweight metal hydrides for hydrogen storage applications are highlighted. Then, various kinds of processing routes involving mechanical milling and severe plastic deformation techniques are reviewed to characterize the fundamental merits and drawbacks of their applications. Furthermore, the effect of catalytic additives on the enhancement of hydriding/dehydriding properties is surveyed.

**Chapter 2** presents the experimental materials, methodology, and the different characterizing techniques employed in the present research.

**Chapter 3** is divided into two parts. In the first part, the evolutions of heterogeneity in strains and microstructures during the HPT processing of lightweight bulk metals (fcc-aluminum

compared to hcp-magnesium) are assessed by altering the die design and processing parameters. The effects of the crystallography (fcc vs. hcp) on the strain heterogeneity and the development of heterogeneous microstructures are also characterized for the improvements in mechanical properties. The second part of this chapter compares the powder consolidation behaviors of the two types of Mg powder precursors employing a new powder metallurgy route. This new approach consists of producing “clean” powder particles by a DC arc-plasma method followed by severe plastic deformation through HPT of the as-synthesized powder precursors. The consolidation of powder is carried out by a two-step (compaction + torsion) HPT procedure. The effect of the initial powder types on the evolution of strain heterogeneity and the associated development in microstructure, texture and microhardness is characterized by employing two kinds of powder precursors: condensed ultrafine Mg and atomized micro-sized Mg.

In **Chapter 4**, the two types of consolidated Mg products presented in **Chapter 3** are investigated for the improvements in hydrogen storage properties in comparison with that of its initial powder precursors. They are mainly characterized for activation kinetics, thermodynamics of absorption/desorption, and absorption kinetics using a Sievert-type apparatus. Desorption properties of the hydrided samples are analyzed by DSC-TG measurements. The effect of hydriding/dehydriding cycles on the modification of initial microstructures for the two types of powders and its HPT products is examined by scanning electron microscopy.

In **Chapter 5**, two types of Mg-Fe based composites - in the 9Mg-Fe and 2Mg-Fe stoichiometry - are processed by the two-step HPT process for characterizing the microstructural developments and the associated improvements in hydrogen storage properties of the

consolidated composites. The effects of nature of powder types (condensed or atomized) on the microstructural variations as well as the hydrogen storage characteristics are investigated by altering the composition of the composites.

**Chapter 6** focuses on the improvements in hydrogen storage properties of Mg-graphene based composite powder and its HPT-consolidated products. The Mg-graphene powder precursor synthesized by the arc-plasma method is consolidated into bulk HPT composite by the two-step HPT consolidation. The effect of graphene additives is thoroughly analyzed for the improvements in hydrogen storage properties of both the powder and its HPT composite while comparing with the carbon-free Mg.

Finally, the main conclusions drawn from **Chapter 3 to 6** are summarized and some perspectives based on the present research are highlighted at the end of the thesis.

## References

- [I.1] Barreto L, Makihira A, Riahi K. “The hydrogen economy in the 21st century: a sustainable development scenario.” *Int. J. Hydrogen Energy* 28 (2003) 267 – 84.
- [I.2] Crabtree GW, Dresselhaus MS, Buchanan MV. “The hydrogen economy.” *Phys. Today* 57 (2004) 39 – 44.
- [I.3] Jain IP. “Hydrogen the fuel for 21st century.” *Int. J. Hydrogen Energy* 34 (2009) 7368 – 78.
- [I.4] Amoo LM, Fagbenle RL. “An integrated impact assessment of hydrogen as a future energy carrier in Nigeria's transportation, energy and power sectors.” *Int. J. Hydrogen Energy* 39 (2014) 12409 – 33.
- [I.5] Hwang HT, Varma A. “Hydrogen storage for fuel cell vehicles.” *Curr. Opin. Chem. Eng.* 5 (2014) 42 – 8.
- [I.6] Momirlan M, Veziroglu TN. “The properties of hydrogen as fuel tomorrow in sustainable energy system for a cleaner planet.” *Int. J. Hydrogen Energy* 30 (2005) 795 – 802.
- [I.7] Schlapbach L, Züttel A. “Hydrogen-storage materials for mobile applications.” *Nature* 414 (2001) 353 – 8.
- [I.8] Sakintuna B, Lamari-Darkrim F, Hirscher M. “Metal hydride materials for solid hydrogen storage: a review.” *Int. J. Hydrogen Energy* 32 (2007) 1121 – 40.
- [I.9] Jain IP, Lal C, Jain A. “Hydrogen storage in Mg: a most promising material.” *Int. J. Hydrogen Energy* 35 (2010) 5133 – 44.
- [I.10] Principi G, Agresti F, Maddalena A, Russo SL. “The problem of solid state hydrogen storage.” *Energy* 34 (2009) 2087 – 91.
- [I.11] Huot J, Ravnsbæk DB, Zhang J, Cuevas F, Latroche M, Jensen TR. “Mechanochemical synthesis of hydrogen storage materials.” *Prog. Mater. Sci.* 58 (2013) 30 – 75.
- [I.12] Crivello JC, Dam B, Denys RV, Dornheim M, Grant DM, Huot J, et al. “Review of magnesium hydride-based materials: development and optimization.” *App. Phys. A* 122 (2016) 97.
- [I.13] Koch CC. “The synthesis and structure of nanocrystalline materials produced by mechanical attrition: a review.” *Nanostruct. Mater.* 2 (1993) 109-129.
- [I.14] Ares JR, Aguey-Zinsou KF, Klassen T, Bormann R. “Influence of impurities on the milling process of MgH<sub>2</sub>.” *J. Alloys Compd.* 434 (2007) 729-33.
- [I.15] Huot J, Skryabina NY, Fruchart D. “Application of severe plastic deformation techniques to magnesium for enhanced hydrogen sorption properties.” *Metals* 2 (2012) 329-43.
- [I.16] Zehetbauer M, Grössinger R, Krenn H, Krystian M, Pippan R, Rogl P, Waitz T, Würschum R. “Bulk nanostructured functional materials by severe plastic deformation.” *Adv. Eng. Mater.* 12 (2010) 692 – 700.



## CHAPTER 1: BIBLIOGRAPHIC REVIEW AND SCOPE OF THESIS WORK

---

Introduction .....	10
1.1 Hydrogen: a clean energy vector for future .....	11
1.2 Options for hydrogen storage .....	13
1.2.1 Solid-state storage of hydrogen .....	16
1.2.2 Lightweight metal hydrides .....	20
1.3 Modifications of hydrogen sorption properties .....	22
1.3.1 Mechanical effects of ball milling .....	23
1.3.2 Severe plastic deformation (SPD) techniques .....	26
1.3.3 Influence of additives/catalysts .....	35
1.4 Scope of thesis work .....	39
References .....	41

## **Introduction**

This chapter mainly deals with a comprehensive background of the present dissertation by taking into account the different aspects of studies conducted in the recent pasts. Beginning of this chapter presents the importance of hydrogen economy in the future of world's energy systems and its perspectives. The most critical issue in the hydrogen based energy systems is the effective storing of hydrogen in a safer and convenient way, and its transportation. This aspect is discussed by comparing the merits and drawbacks of the available storing systems. Furthermore, different solid-state hydrogen storage materials are reviewed in terms of their characteristic features in the different energy fields, such as in automotive industries, and power sectors and space research. In addition, the processing routes applying for the enhancement of hydrogen sorption properties of various kinds of M-H systems are reviewed to identify the economically viable paths for further research in these fields. Furthermore, the catalytic effects of various metallic/non-metallic elements or their oxides, carbon-based materials and other additives on the improvement of hydrogen absorption/desorption kinetics, the stability of metal hydrides upon cycling, and the reduction of desorption temperatures are highlighted. Finally, a comprehensive conclusion is drawn based on the literature review and the potential areas of further research in this field are pointed out for the present dissertation work.

## **1.1 Hydrogen: a future energy vector**

Jules Verne (*L’Ile mystérieuse*, 1874), sometimes also called the “Father of Science Fiction” wrote that “Yes, my friends, I believe that water will one day be used as fuel, that hydrogen and oxygen, which make it, used separately or simultaneously, will provide a source of inexhaustible heat and light and with an intensity the coal could never reach” [1.1]. Today’s world is now realizing how important was this prophecy in terms of both global warming and security of energy supply. Although hydrogen was used in many countries for street lighting as well as domestic energy supply (like cooking, heating, lighting), the breakthrough in fuel cell technology in the late 1990s is the main reason behind the revival of interest in hydrogen economy. In fuel cells, electricity and water are usually produced from hydrogen and oxygen in an electrochemical reaction which also releases some heat. In contrast to conventional electricity generation, which takes place in a three-stage conversion processes (chemical energy – thermal energy – mechanical energy – electricity), in a fuel-cell, chemical energy is directly converted into electrical energy. Therefore, the fuel cells can make the most of their high conversion efficiencies (> 60%) compared to the internal combustion engine [1.2]. Hence, the combination of both hydrogen and fuel-cells opens a new challenge to the world’s economy regarded as key energy solutions for the 21<sup>st</sup> century.

Hydrogen is the most abundant element in the universe, which is frequently found in large quantities in water, hydrocarbons etc. Since hydrogen is generated from water and returning to water when oxidized as an environment friendly fuel, it has been widely considered as the clean fuel of the future generation. Being a secondary energy carrier that can be produced from any primary energy sources and/or from the renewable energies (hydro, wind, solar,

biomass, geothermal), hydrogen offers a long term potentiality of sustainable hydrogen economy. Hydrogen can also be produced from natural gas, coal, hydrocarbons, and even municipal waste as well as by water splitting. Hydrogen can then be utilized in high efficiency power-generation systems including fuel-cells for both vehicular transportation and distributed electricity generation [I.4]. Hydrogen can also be used as storage medium for electricity generated from intermittent renewable resources such as solar, wind, wave and tidal power. However, the transition from a carbon-based energy system to a hydrogen-based economy involves significant scientific, technological and socioeconomic strategies for the implementation of hydrogen and fuel-cells as the clean energy technologies of the future world [I.5].

Presently, there are three major technological obstacles that must be overcome to achieve a viable hydrogen-based economy. First, the cost of efficient and sustainable hydrogen production, and its delivery must be significantly reduced. Second, appropriate hydrogen storage systems for both vehicular and stationary applications must be developed. Third, the cost of fuel-cells and the associated storage systems must be reduced. Currently, hydrogen is produced in large quantities by “reforming” process from hydrocarbons by applying heat and by splitting water through various processes including electrolysis, photo-electrolysis, high-temperature decomposition and photo-biological water splitting [1.3]. A recent US Department of Energy (DOE) report suggests that solar is most likely to be the only source of energy capable of producing enough hydrogen. The present options for transporting hydrogen include compressed gas in tube cylinders, liquid hydrogen tanks and a few examples of local networks of hydrogen pipelines [1.4]. All these options contribute significantly to the cost of hydrogen for end users

and, in some cases, decentralized local hydrogen production using methane reforming or electrolysis of water will be economically feasible. While the production of hydrogen and its distribution has been recently gained significant advancements using a variety of new technologies, the storing of hydrogen in a convenient and efficient way remain unrealistic in terms of materials developments, infrastructures and new technologies.

## **1.2 Options for hydrogen storage**

Storing of hydrogen is regarded as one of the most critical issues in the hydrogen based economy, in fact, without effective storage systems, a hydrogen economy will be difficult to achieve. One of the crucial technological barriers to the widespread use of hydrogen is the lack of a safe, low-weight and low-cost hydrogen storage media with a high energy density [I.7]. Hydrogen gas is difficult to store because of its low density. At atmospheric pressure and room temperature, it takes a volume of 11 m<sup>3</sup> to store 1 kg of hydrogen. Hydrogen contains more energy on a weight-to-weight basis than any other substance. Unfortunately, since it is the lightest chemical element, it also has a very low energy density per unit volume (see Table 1.1).

To overcome these challenges the fuel cell technologies office (FCTO) is following two strategic pathways, directing both near-term and long-term possibilities [1.5]. The near-term pathway focuses on compressed gas storage, using advanced pressure vessels made of fiber reinforced composites that are capable of reaching about 700 bar pressure, with a major emphasis on system cost reduction. The long-term pathway aims on both (i) cold and cryo-compressed hydrogen storage, where increased hydrogen density and insulated pressure vessels

may allow for DOE targets to be met, and (ii) materials-based hydrogen storage technologies, including sorbents, chemical hydrogen storage materials, and metal hydrides, with improved properties having potential to meet DOE hydrogen storage proposals.

**Table 1.1** – Gravimetric and volumetric energy content of different kinds of fuels (container weight and volume are excluded), after Ref. [1.3].

<b>Fuels</b>	<b>Specific energy (kWh/kg)</b>	<b>Energy density (kWh/dm<sup>3</sup>)</b>
Liquid hydrogen	33.3	2.37
Hydrogen (200 bar)	33.3	0.53
Liquid natural gas	13.9	5.6
Natural gas (200 bar)	13.9	2.3
Petrol	12.8	9.5
Diesel	12.6	10.6
Coal	8.2	7.6
LiBH <sub>4</sub>	6.16	4.0
Methanol	5.5	4.4
Wood	4.2	3.0
Electricity (Li-ion battery)	0.55	1.69

In recent years, the storing of hydrogen is mainly focused upon high-pressure (up to 700 bar) gas cylinders or cryogenically cooled (liquefied) fluid hydrogen. While the novel high-pressure tanks made of carbon-fiber-reinforced composite materials are promising for regular use up to 600 bar, they need a special inert inner coating to prevent the high-pressure hydrogen reacting with the polymer. They also impose a considerable safety risk: the compression itself is the most dangerous and complicated part. On the other hand, liquefaction of hydrogen is believed to be more attractive from the point of view of increasing the mass per container volume. As the critical temperature of hydrogen is  $-241\text{ }^{\circ}\text{C}$  (above this temperature hydrogen is gaseous), liquid hydrogen containers are open systems to prevent strong overpressure. Therefore, heat transfer through the container leads directly to the loss of hydrogen. Other adverse effect of these storage systems (gas or liquid) is a significant energy penalty: up to 20% of the energy content of hydrogen is required to compress the gas and up to 40% to liquefy it [1.3]. The usage of high-pressure and cryogenic storage confronts the public perception and acceptability associated with the use of pressurized gas and liquid hydrogen containment. The physical limits for the storage density of compressed and liquid hydrogen have more or less been reached, while there is still potential in the development of solid-state hydrogen storage materials, such as systems involving metal hydrides. Several classes of solid-state storage materials demonstrate higher energy density than that of liquid hydrogen (for example,  $\text{LiBH}_4$ , see Table 1.1).

### **1.3.1 Solid-state storage of hydrogen**

Chemically or physically combined storage of hydrogen in metallic/non-metallic materials has potential advantages over the gas and liquid storage methods. Many metals and alloys are capable of reversibly absorbing large amounts of hydrogen, and thus, lead to the formation of solid-state storage materials under moderate temperature and pressure that gives them the important safety advantage over the gas and liquid storage options.

Metal hydrides are composed of metal atoms that constitute a host lattice and hydrogen atoms. The simple metal hydrides are formed by gas-solid interactions, and usually the reaction of hydrogen gas with a metal surface can be expressed by a simplified one-dimensional potential curve [1.6], see Figure 1.1(a). In the first step, the attractive van der Waals forces are responsible for the interaction of the hydrogen molecules approaching the metal surface leading to physisorption of hydrogen. The hydrogen has to overcome an activation barrier for dissociation and formation of the M-H bond. The height of the activation barrier depends on the surface elements involved. The activated hydrogen atoms are then chemisorbed by sharing their electron with the metal atoms at the surface. In the next step, the chemisorbed hydrogen atom can jump in the subsurface layer and finally diffuse on the interstitial sites through the host metal lattice, see Figure 1.1(a).

The thermodynamic aspects of hydride formation from gaseous hydrogen are described by pressure-composition isotherms (see Figure 1.1(b)). Metal and hydrogen usually form two different kinds of hydrides;  $\alpha$ -phase at which only some hydrogen is in solid-solution in the metal matrix and  $\beta$ -phase at which hydride is fully formed. When solid-solution and hydride

phases coexist, there is a plateau in the isotherms, the length of which determines the amount of hydrogen stored. The two-phase region ends in a critical point,  $T_c$ , above which the transition of  $\alpha$ - to  $\beta$ -phase is continuous. The equilibrium pressure,  $P_{eq}$ , is related to the changes in enthalpy,  $\Delta H$  and entropy,  $\Delta S$  respectively, as a function of temperature by the van't Hoff equation:

$$\ln\left(\frac{P_{eq}}{P_{eq}^\circ}\right) = \frac{\Delta H}{R} \cdot \frac{1}{T} - \frac{\Delta S}{R}$$

The enthalpy term characterizes the stability of the metal-hydrogen bond, and is especially important to the heat management required for practical engineering devices. The entropy term mostly signifies to the change from molecular hydrogen gas to dissolved atomic hydrogen during hydrogen absorption process and is more or less constant for all hydrides.

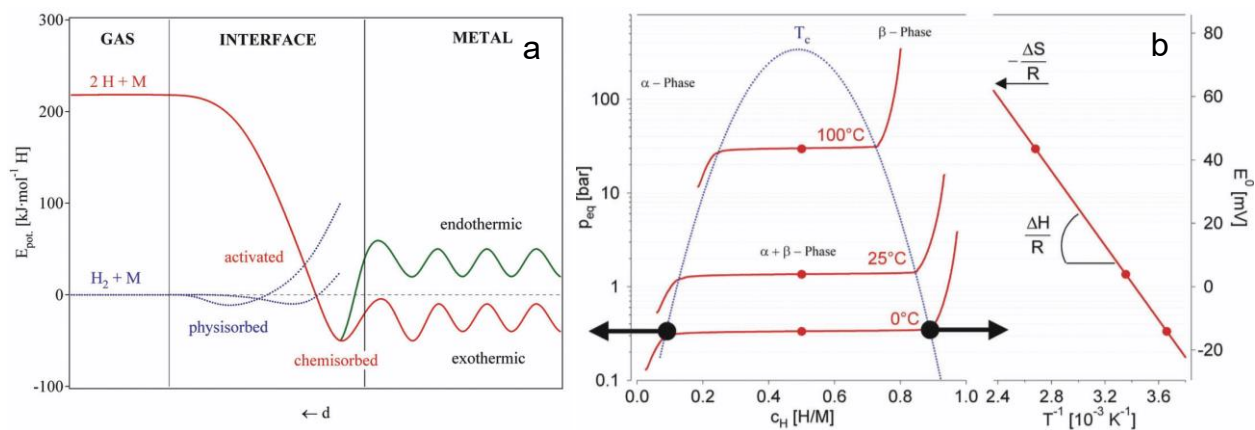


**Figure 1.1** – (a) One-dimensional potential energy curve for the reaction of hydrogen gas with a metal, and (b) pressure-composition isotherms for hydrogen absorption in a typical metal system, after Ref. [1.7].

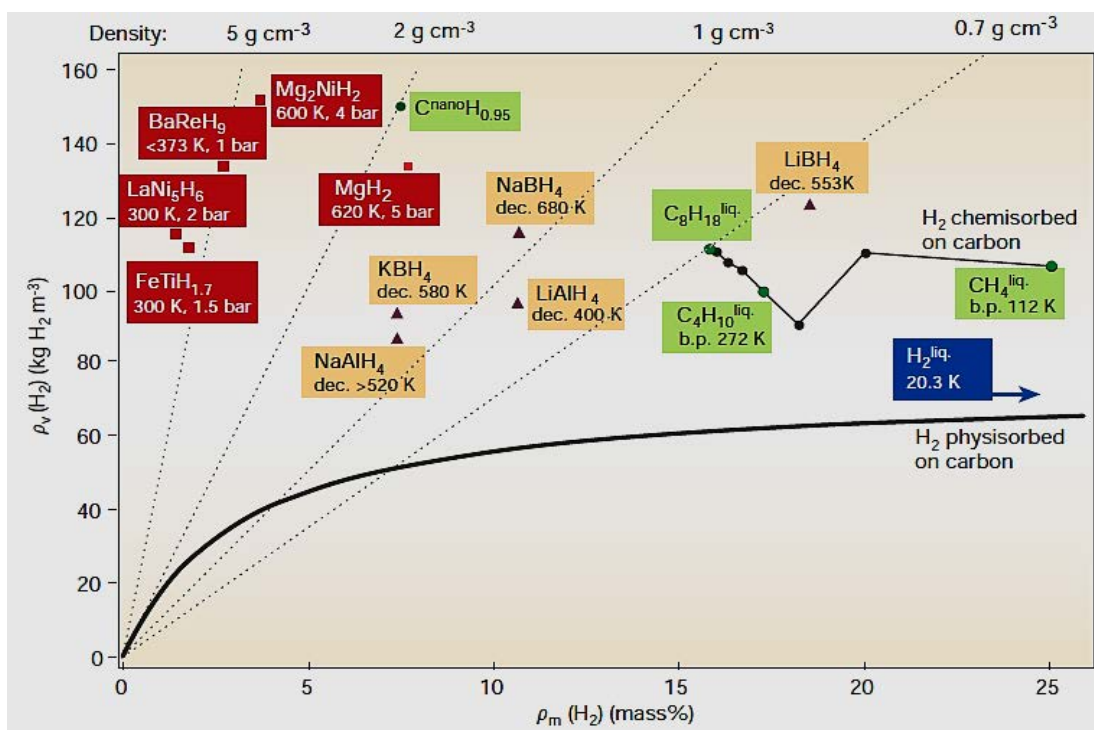


**Figure 1.2** – Hydrogen storage capacity (per mass and volume) of metal hydrides, carbon nanotubes, petrol and other hydrocarbons, after Ref. [1.7].

Hydrogen storage in metallic materials depends on different parameters and consists of several mechanistic steps. Metals differ in the ability to dissociate hydrogen, this ability being dependent on surface structure, morphology and purity [1.7]. Metal hydrides have higher storage density (6.5 H atoms/cm<sup>3</sup> for MgH<sub>2</sub>) than hydrogen gas (0.99 H atoms/cm<sup>3</sup>) or even liquid hydrogen (4.2 H atoms/cm<sup>3</sup>) [1.8]. As can also be noticed from Figure 1.2, the metal based hydrides exhibit excellent volumetric storage density compared to other storage systems, while they show poor gravimetric storage capacity except some light metal complex hydrides such as LiBH<sub>4</sub>, NaBH<sub>4</sub>, LiAlH<sub>4</sub> etc. Hence, it clearly indicates that metal hydride storage is a safe, volume-efficient storage method for on-board vehicular applications. A great deal of effort has

been made on new hydrogen-storage systems including metal hydrides or complex hydrides, intermetallic compounds, carbonaceous materials, metal-organic frameworks etc.

Physisorption of hydrogen due to Van der Waals interactions of gas molecules onto the solid surface has been the subject of intensive research for a long time. The initial research on hydrogen storage in carbon materials was dominated by announcements of high storage capacities in carbon nanostructures [1.8,1.9]. Materials with a large specific surface area like activated or nanostructured carbon and carbon nanotubes or nanofibers are possible substrates for physisorption. Also, the big advantages of physisorption are the low operating pressure, the relatively low cost of the materials involved, and the simple design of the storage system. In view of today's knowledge although they have good reversibility properties, several rigorous studies point out that the gravimetric and volumetric hydrogen density on carbon are rather so small that they cannot store the amount of hydrogen required for automotive applications [1.10].

Research on intermetallic compounds, another class of storage materials, was already attempted more than 40 years ago. The knowledge of hydrogen absorption by  $\text{LaNi}_5$  [1.11] and  $\text{FeTi}$  [1.12] opened new possibilities for industrial developments. The different families of intermetallic compounds classified on the basis of their crystal structures, such as  $\text{AB}_2$  type (Laves phase),  $\text{AB}_5$  type phases and Ti-based body centered cubic, BCC alloys are well known as hydrogen-storage materials [1.13]. Alloys derived from  $\text{LaNi}_5$  show some very promising properties, including fast and reversible sorption with small hysteresis, plateau pressure of a few bars at room temperature and good cycling life. For practical applications at ambient temperature and pressure, low energy density per unit weight of these compounds is an important critical

disadvantage. For instance, the hydrogen capacity of the most popular LaNi<sub>5</sub>-based alloys operating at moderate temperature does not exceed 1.4 wt%. Therefore, the intermetallic compounds do not satisfy the requirements for on-board storage because of their low storage capacities up to 2 wt% and along with high costs.

### **1.3.2 Lightweight metal hydrides**

Lightweight metal (Li, Be, Na, Mg, B and Al) based hydrides have a much higher storage capacity by weight, and are therefore preferred for automotive applications. They are especially interesting due to their light weight and the number of hydrogen atoms per metal atom, which is in many cases at the order of  $H/M = 2$ . Sodium, lithium and beryllium are the only elements lighter than magnesium that can form solid-state compounds with hydrogen known as complex hydrides. The hydrogen content reaches the value of 18 wt% for LiBH<sub>4</sub> [1.14,1.15]. Use of complex hydrides for hydrogen storage is challenging because of both kinetic and thermodynamic limitations. Although the storage capacities of complex hydrides are theoretically high, there is a big difference between the theoretical and the practical attainable hydrogen capacities. The complex hydrides released hydrogen by the step reactions unlike the metallic hydrides. Repeated hydrogenation cycles need to be applied for the potential applications to ensure the reversibility of these materials. Moreover, the slow kinetics problem is a significant obstacle for practical on-board applications [1.7].

Among the lightweight metal hydrides, Mg-based materials for on-board hydrogen storage applications appeal significant research interests mainly due to its high gravimetric and volumetric hydrogen storage capacity, low cost and abundant on the earth's crust, and its hydrides are reversible and recyclable [1.16,1.17]. However, the main obstacles of Mg-based materials for practical applications are the high temperature of hydrogen desorption, slow

absorption/desorption kinetics and a high reactivity towards air and oxygen. High thermodynamic stability of  $\text{MgH}_2$  results in a relatively high desorption enthalpy, which corresponds to an unfavorable desorption temperature of above  $300\text{ }^\circ\text{C}$  at 1 bar [1.18].

Nevertheless, the Mg-based materials are potential candidates for the following applications:

- 1) On-board hydrogen storage,
- 2) Heat-storage and
- 3) Stationary and portable energy storage.

Most of the research in Mg based hydrogen storage materials so far aims at on-board storage. According to the targets from DOE, for this kind of applications, it requires a gravimetric storage capacity of at least 4.5 wt% (i.e. 1.5 kWh/kg system) for the year 2020 [1.5]. Although  $\text{MgH}_2$  can store 7.6 wt% H, when considering the additional weight for necessary components including tank body and heat transfer additives besides the hydrogen storage materials in the system (some amount of catalysts and other elements are necessary to enhance the kinetics, and also to reduce the thermodynamic stability by alloy formation), important issues (rather slow kinetics and high operating temperatures) remain for Mg based materials to be applied for on-board applications based on current technology and the capacity requirement.

The Mg– $\text{MgH}_2$  system can also be used for thermal storage due to its favorable thermodynamic properties. This kind of thermal storage systems can be connected to the high temperature concentrating solar power plants [1.19]. By this technology, solar power may continuously generate electricity at night or in cloudy days. It was estimated that the Mg– $\text{MgH}_2$  system has a heat storage density 25 times higher than the current nitrate salt mixture, which

indicate a promising application of the Mg-MgH<sub>2</sub> system for heat storage in solar power plants. Mcphy Energy Company in France recently developed stationary hydrogen storage system based on Mg-based materials [1.1].

With the development of solid oxide fuel cell (SOFC) which may work at high temperatures (600–1000 °C), the Mg–MgH<sub>2</sub> system can be used as portable and stationary energy storage by connecting with SOFC. Other kinds of metal hydrides known as ternary metal hydrides, Mg-M-H systems which can be obtained when magnesium reacts with transition metal elements (M = Ni, Co, Fe, Cu etc.) in presence of hydrogen, have excellent thermochemical heat storage properties at high temperature applications [1.20].

### **1.3 Modifications of hydrogen sorption properties**

The solid-state hydrogen storage materials possess the highest potential to be used together with fuel cell technology for the generation of electric power in a clean, inexpensive, safe and efficient manner. However, one of the drawbacks for this system is its rather sluggish kinetics in the charging/discharging processes, and, at least for practical applications, strategies have to be developed to solve this problem. The hydrogen sorption kinetics of the lightweight metal hydrides is mainly influenced by

- particle size/surface area,
- crystallite size/large fraction of grain boundaries,
- additives/catalysts.

Nanostructured materials are proved to present enhanced hydrogen absorption/desorption kinetics compared with micrometer scale ones due to larger surface area, more nucleation sites for hydrogen reactions, and shorter distance for hydrogen diffusion in the metals or hydrides. Furthermore, thermodynamic properties of the Mg based system dictate the high operating temperature which is too high for practical on-board applications [1.18]. So far, one of the effective techniques to diminish the thermodynamic stability of  $MgH_2$  is alloy formation of Mg with other metal elements. However, the enthalpy of desorption does not always decrease during alloy formation compared to  $MgH_2$ . The different approaches for improving the kinetics and thermodynamics of hydrogen absorption/desorption processes in the M-H systems are briefly discussed in the following sub-sections.

### **1.3.1 Mechanical effects of ball milling**

The effects of mechanical deformation by high-energy ball milling (HEBM) on the hydrogen storage behavior of metal hydrides have been intensively studied in the last decades [1.11]. This is a well-known processing route to prepare materials in nanometer scale and non-equilibrium state. The main effects of HEBM are increased surface area, formation of micro/nanostructures and creation of defects on the surface and also in the interior of the material. The induced lattice defects may aid the diffusion of hydrogen in materials by providing many sites with low activation energy of diffusion. The imposed micro-strain assists diffusion by reducing the pressure hysteresis of hydrogen absorption and desorption. In addition, processing by HEBM can also significantly reduce both powder and grain (crystallite) size, break the oxide layer on magnesium powder and provide fresh surfaces, as well as dispersing additives through the

composite materials, and thus, good interfacial contact with the light metal hydrides and a fine dispersion of the additives can be achieved.

Huot et al. [1.21] investigated the structural differences between milled and unmilled  $\text{MgH}_2$ . The specific surface area is increased by milling about 10-fold. Faster hydrogen desorption kinetics and reduction in activation energy observed for the milled  $\text{MgH}_2$  compared to the unmilled one were contributed to the defects introduced during ball milling, the small particle size, and by the increased specific surface area basically enhanced the nucleation site density and reduced the diffusion lengths. Zaluska et al. [1.16] claimed that the crystallite size is one of the important factors determining the hydrogen sorption kinetics of light metal hydrides, in particular in case of  $\text{MgH}_2$ . The fast and the slow kinetic regimes can be related to the sorption behaviour of the grain boundary area and the interior of the crystallites. The results indicate that for large particle sizes the crucial crystallite size for  $\text{MgH}_2$ , above which the sorption kinetics decreases substantially, is in the range between 80–200 nm, most likely around 100 nm. On the other hand, in spite of the similar crystallite sizes after milling (5-20 nm) and after long term cycling ( $\sim 80$  nm), the sorption kinetics of the two milled  $\text{MgH}_2$  samples are quite different:  $\text{MgH}_2$  with an average particle size of 500 nm shows faster absorption and much faster desorption compared to the sample milled for 20 h with a particle size of about 5  $\mu\text{m}$  [1.17].

In another approach, a hydrogen-absorbing material can be hydrogenated during ball milling. It was shown that ball milling under hydrogen atmosphere which is known as reactive ball milling (RBM) is a convenient way for the formation of metal hydrides which causes simultaneous hydrogen uptake and mechanical deformation resulting from ball milling. Huot et

al. [1.22] produced  $\text{MgH}_2$  under hydrogen atmosphere by ball milling. This method improved the hydride formation kinetics. Hanada et al. [1.23] investigated the structural effects on hydrogen storage properties of mechanically milled  $\text{MgH}_2$  under protective hydrogen atmosphere. They reported that both amount of desorbed hydrogen and desorption temperature initially decrease with milling time, and finally after 80 h of milling they reach to a saturation of 6.5 wt% and 330 °C, respectively. The results obtained indicate that the reduction of crystallite size as well as the introduction of lattice strain in  $\text{MgH}_2$  during milling gives rise to the decrease in hydrogen storage capacity and also its desorption temperature.

However, considering a mass production by HEBM demonstrates several disadvantages [I.11,I.14]: (i) its upscaling is very expensive, (ii) it consumes much time and energy; (iii) it needs extensive precautions for minimizing the environmental and health risks, and especially for minimizing contamination by oxygen and other materials involved in the process. In this context, the severe plastic deformation based techniques such as equal channel angular pressing, high-pressure torsion, cold forging and cold rolling have been explored to process/synthesize Mg based alloys resulting in materials with interesting hydrogen storage properties [I.16].

### **1.3.2 Severe plastic deformation (SPD) techniques**

Severe plastic deformation (SPD) is a general term used to describe a group of techniques that produce large strains in the material which in turn result in a high defect density and nanocrystalline structure. The SPD techniques could replace and/or complement HEBM for the synthesis and preparation of metal hydrides. The advantages of SPD over the ball milling are that usually SPD can be easier to scale up to industrial level, the impurity level is lower, and it has fewer safety concerns [1.24]. Moreover, due to the comparably short processing time and relatively simple setup, including those for continuous SPD processing, the production costs can be dramatically reduced.

The use of SPD techniques in the processing of metal hydrides is relatively new, and in this field of research is rapidly increasing. Processing by SPD produces multiple defects in the crystalline lattice such as vacancies and dislocations and this has a positive effect on the diffusion kinetics. For example, defects could act as nucleation site for a chemical reaction (such as hydrogenation) while grain boundaries could act as fast diffusion pathways. Therefore, these techniques are particularly attractive in the synthesis and preparation of metal hydrides. Recently, the most popular SPD techniques for the processing of Mg-based metal hydrides include equal channel angular pressing (ECAP), cold rolling (CR) and high-pressure torsion (HPT). These techniques and their related results are shortly discussed in the following paragraphs.

#### **1.3.2.1 Equal channel angular pressing (ECAP)**

In equal channel angular pressing (ECAP) technique, severe plastic deformations are introduced into a material by forcing a sample (billet) with a piston through a die consisting of two channels of equal cross-section, which intersect at an angle ( $\Phi$ ) between  $90^\circ$  and  $120^\circ$  [1.25], see Figure

1.3. The outer arc of curvature where the two channels intersect is labeled  $\Psi$ . Since the billet assumes the form of the cross-section of the die, it can be repeatedly processed to increase the micro-strains and reduce the crystallite size in the material. ECAP is quite efficient in processing metals and alloys producing porosity-free materials with average crystallite sizes between 2  $\mu\text{m}$  and 100 nm in substantial quantities with lower concentration of impurities and at a lower cost than ball-milling [1.26]. Through the grain refinement process, the proportion of high-angle grain boundary increases due to dislocations recovery. While ECAP has emerged as well-known procedure for the fabrication of ultrafine-grained metals and alloys with enhanced mechanical and functional properties, it is the recent years that have been investigating the effects of ECAP processing on H-sorption properties of Mg-based hydrogen storage materials.

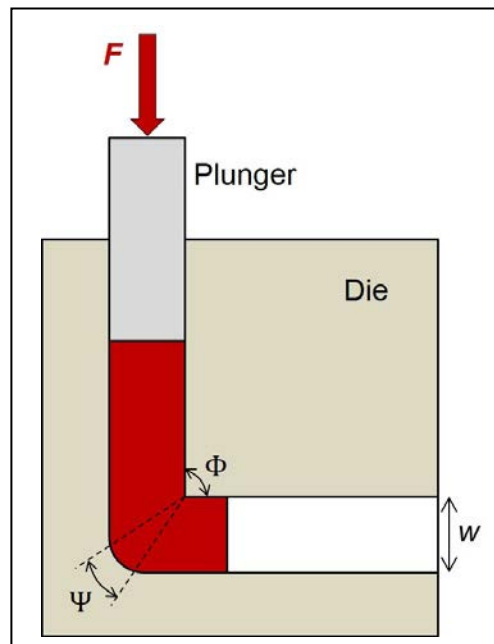


**Figure 1.3** – Schematic illustration of an equal channel angular pressing (ECAP) technique, after Ref. [1.25].

In a pioneering work, Skripnyuk et al. [1.24] have reported that the hydrogenation properties of an ECAP-processed commercial Mg alloy, ZK60, are similar to or even better than those of a ball-milled one. The alloys were processed by HEBM, ECAP, and a combination of ECAP and HEBM. The ECAP processing was made through route A (no billet rotation between passes) with eight passes at 250-300 °C and one additional pass at room temperature. They found that after ECAP/HEBM treatment the hysteresis in the PCT isotherms completely disappears (see Figure 1.4). However, the most important effect of this processing was on the hydrogen desorption kinetics.

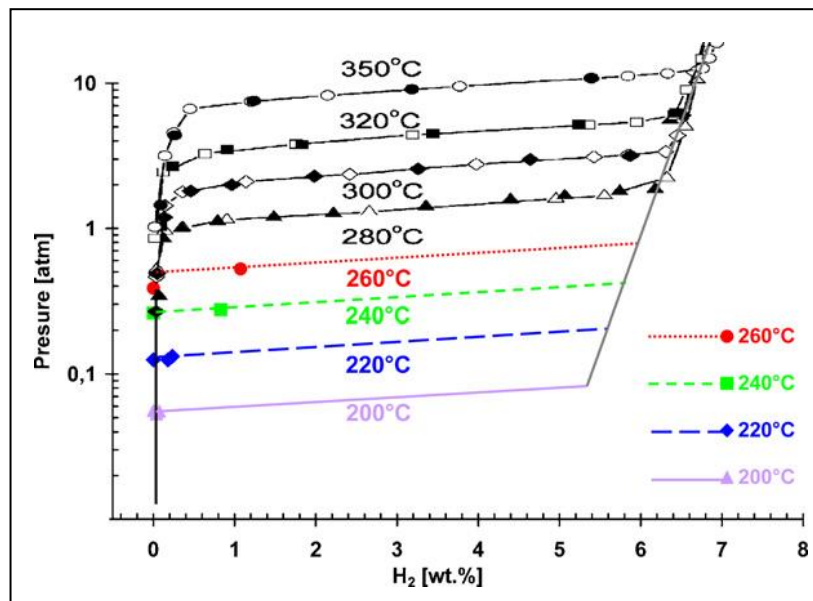


**Figure 1.4** – Pressure–composition–temperature (PCT) isotherms of the ZK60 system. Black lines and points determined on ECAP and/or HEBM processed ZK60 represent the findings of Skripnyuk et al. [1.24]. Colored data for ZK60-4x measured at 200 – 260 °C, after Ref. [1.27]. Open and filled symbols indicate hydrogen absorption and desorption, respectively.

Recently, Krystian et al. [1.27] performed ECAP on the same alloy and were able to decrease the grain size down to 250 nm, the smallest value ever achieved by this technique. The lowest temperature at which the ECAP processed ZK60 could be charged and discharged, the so-called onset temperature, was 200 °C (see colored lines in Figure 1.4). However, at temperatures below 280 °C the desorption process becomes very sluggish and cannot meet requirements for any practical applications. In contrast, the hydrogen storage capacity was measured to be 6.6 wt% and rapid hydrogen desorption kinetics of less than 5 min at 350 °C was recorded. The long term durability of the material was proven in a cyclic absorption/desorption test up to 1000 cycles and no deterioration in storage capacity or in kinetics was observed which is exceptional for nanomaterials for hydrogen storage.

Løken et al. [1.28] used ECAP and HEBM to process the ternary eutectic Mg–Mg<sub>2</sub>Ni–MmMg<sub>12</sub> (72 wt% Mg - 20 wt% Ni-8 wt% Mm, Mm = mischmetal). Eight ECAP passes at 400 °C (route B<sub>C</sub>) gave an improvement in the hydrogen absorption and desorption rates. However, HEBM gave an even larger improvement and reduced the absorption and desorption times to one third of those of the as-cast alloy. In a recent investigation involving ECAP processing of commercial magnesium AZ31 extruded alloy, a preferential (0001) texture fibre was found in the longitudinal section of the AZ31 alloy [1.29]. They have observed an influence of this texture on the capacity and kinetics of hydrogen sorption properties.

### **1.3.2.2 Cold rolling (CR)**

In cold rolling (CR) process, a sheet of metal is introduced between rollers where it is compressed and squeezed. The amount of strain introduced by CR determines the hardness and other properties of the finished product. The metal is usually subjected to high compressive stresses as a result of the friction between the rolls and the metal surface. Usually, rolling is classified according to the processing temperature as compared with the metal recrystallization temperature:

- 1) Hot Rolling (HR) is when the process is carried out at a temperature exceeding the recrystallization temperature of the rolled material, and
- 2) Cold Rolling (CR) is when rolling temperature is below recrystallization temperature.

Since cold rolling is operating at below the recrystallization temperature of the metal, it has been extensively applied for synthesis and preparation of nanocrystalline materials for hydrogen storage. Because of the limited number of slip planes in Mg-based systems, work hardening occurs rapidly after only a few rolling passes. Thus, upon rolling a Mg foil will quickly break up in small pieces and made further rolling more and more difficult. Nevertheless, for hydrogen storage applications mechanical integrity is not so important for the materials. In fact, after a few hydrogenations many metal hydrides turn into powder because of the important decrepitation due to the significant volume change during de-/hydrogenation. Consequently, cold rolling of magnesium and magnesium alloys have been actively investigated.

Ueda et al. [1.30] were the first to attempt to synthesize a metal hydride ( $Mg_2Ni$ ) using cold rolling of raw elements followed by a heat treatment. For stoichiometry  $2Mg+Ni$ , single phase  $Mg_2Ni$  was obtained, and the sample could be completely hydrogenated to  $Mg_2NiH_4$ . The

formation of  $Mg_2Ni$  was explained by interdiffusion between Mg and Ni during the heat treatment. In the case of Mg–Pd system, Dufour and Huot studied the effect of adding 2.5 at% of Pd to Mg by cold rolling and by ball milling [1.31]. Palladium is evenly distributed in both samples but the particle size is almost one order of magnitude bigger in the laminated compound compared to the ball-milled one. However, as shown in Figure 1.5, the first hydrogenation (activation) of laminated sample is much faster and shows a much shorter activation time compared to a ball-milled sample. Moreover, when the cold rolled sample was subjected to five cycles of hydrogen absorption/desorption, and stored in air for one month the activation was still faster than the ball-milled sample. This shows that cold rolled samples have much better resistance to air contamination. This is probably due to the much smaller specific surface area of a cold rolled material compared to its ball-milled counterpart.

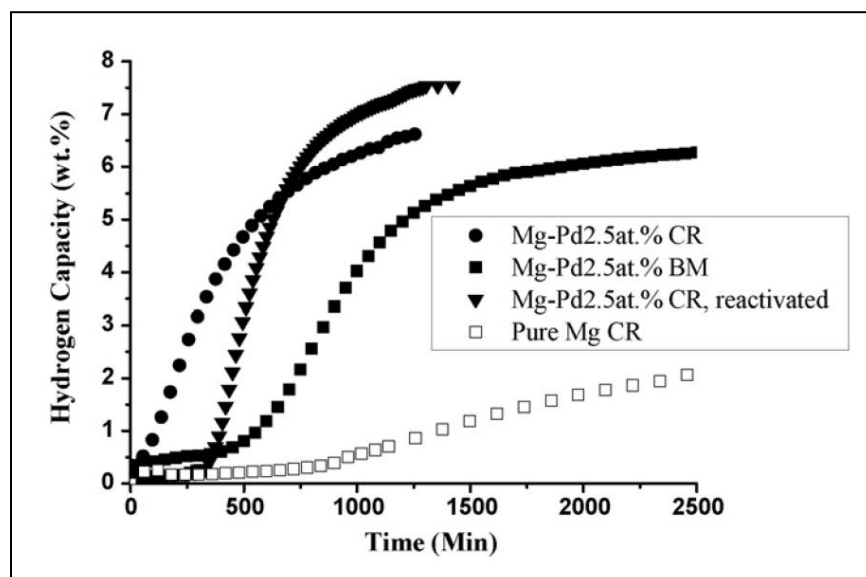


**Figure 1.5** – Activation curves of cold rolled Mg–Pd 2.5 at%, ball milled Mg–Pd 2.5 at%, and cold rolled pure magnesium. Activation temperature 350 °C, hydrogen pressure 1.3 MPa. CR = cold rolled, BM = ball-milled, after Ref. [1.31].

Recently, very attractive results have been reported for the use of CR in commercial MgH<sub>2</sub> which led to refined microstructure and a strong texture, and presented fast absorption/desorption kinetics [1.32,1.33]. A close similarity between the kinetic properties of cold rolled MgH<sub>2</sub> and ball milled MgH<sub>2</sub> has been observed. However, CR processing has several advantages over HEBM techniques, i.e. drastic reduction of processing time, lower cost and less consumption of energy. In addition, cold rolled MgH<sub>2</sub> shows a better resistance to air contamination with materials processed by ball milling. More recently, it was reported that CR processing was also successful in incorporating different types of additives in MgH<sub>2</sub> resulting in enhanced absorption/desorption kinetics [1.34,1.35]. Experiments combining ECAP, cold rolling (CR) and HEBM to process commercial extruded AZ31 alloy showed the deformability of the alloy during ECAP processing was suitable for temperatures above 150 °C. However, a (0001) texture, suggested to be favorable for the absorption of hydrogen, was obtained only with a combination of ECAP and subsequent cold rolling [1.36].

### **1.3.2.3 High-pressure torsion (HPT)**

Compared to other SPD techniques, high-pressure torsion (HPT) is a relatively simple and quick processing technique, and also easy to apply on powder materials. It is also very efficient to produce small grain size and large fraction of high-angle grain boundaries. Among the HPT processing routes available, the more versatile one is under processing through quasi-constraint conditions [1.37]. The principle of a quasi-constraint HPT facility is schematically illustrated in Figure 1.6. The sample, generally in the form of a thin disk, is located between two anvils within a cavity. A hydrostatic pressure is applied and plastic torsional straining is achieved by rotation of the lower anvil or both. The diameter of the cylindrical cavities and the initial diameter of the

HPT sample are identical. However, the sum of both depths of the cavities is somewhat smaller than the initial height of the HPT sample. This implies that during loading a small amount of the material will flow laterally in the ring shaped region between the two anvils. The friction in this region confines the free flow of the material out of the HPT tool and leads to a back pressure and induces a defined hydrostatic pressure within the processing zone. More details of this technique can be found in Ref. [1.37].

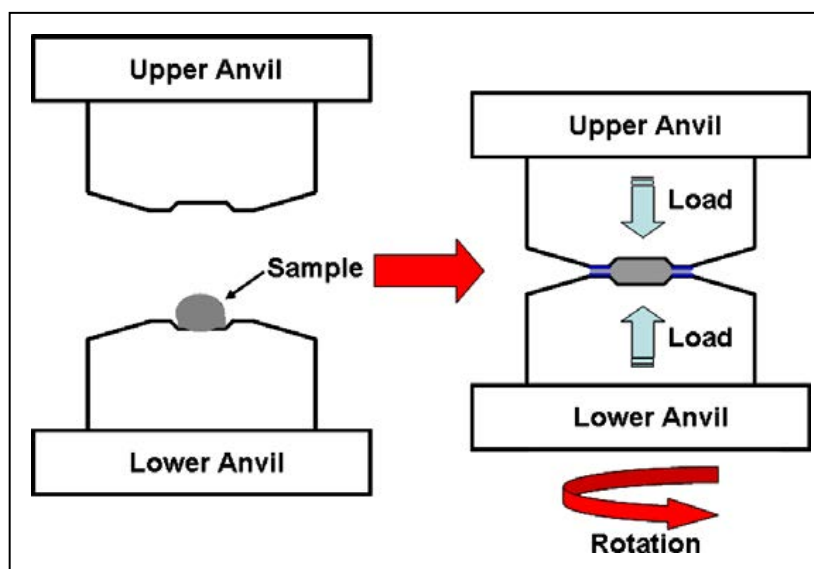


**Figure 1.6** – Schematic illustrations of a quasi-constrained HPT facility, after Ref. [1.38].

Application of HPT to hydrogen storage materials is relatively new. One of such study was performed by Kusadome et al. [1.38] on  $\text{MgNi}_2$  alloy, which does not usually absorb hydrogen. The crystallite size of  $\text{MgNi}_2$  phase changed from more than 100 nm before HPT processing to about 20 nm after 10 HPT revolutions. Moreover, the HPT processing introduced a

substantial strain into the material, and MgNi<sub>2</sub> became a weak hydrogen absorber (0.1 wt%) with hydrogen accumulating in grain boundaries of the alloy. These results provide a very clear demonstration that hydrogen is preferentially stored in the MgNi<sub>2</sub> after processing by HPT with greater storage occurring after larger numbers of revolutions at least up to 5 revolutions.

A certain similarity between HPT and ball milling can be made based on the recent work by Leiva et al. [1.39], who detected the formation of a metastable phase  $\gamma$ -MgH<sub>2</sub> and a substantial reduction of crystallite sizes from 30 to 20 nm while using HPT to consolidate the metal hydride powder. Previously, the formation of  $\gamma$ -MgH<sub>2</sub> upon mechanical processing was reported for and chiefly associated with the HEBM [1.40]. It was also suggested from HPT on pure Mg that the refinement of grain size (i.e. amounts of grain boundary) played a more effective role than the amount of dislocations for improving H-storage properties [1.41]. Bulk Mg nanostructured materials were produced by HPT and other SPD techniques, and the results pointed out that the combination of grain refinement associated with multiple texture components, but still strong (0002) texture component can be relevant in improving H-sorption properties [1.42]. A new method – applying HPT on arc plasma evaporated ultrafine-grained powder – has been recently introduced to produce bulk Mg-MgO based nanocomposite for H storage [1.43,1.44]. The improved H-sorption properties of these bulk composites were mainly attributed to the refinement of the Mg matrix, and the uniform dispersion of fine MgO particles developed during the intense shear training by HPT and their catalytic activities.

Although processing through severe plastic deformation (SPD) techniques has been recently used to enhance hydrogen storage properties of materials, the level of understanding the

impact of SPD routes on the hydrogen storage properties of metal hydrides is still relatively small. Only a limited number of attempts have been made and just a few research groups are investigating the use of SPD for the preparation of metal hydrides. However, first results are encouraging and show similarities with mechanical milling in the effectiveness of obtaining a nanocrystalline structure. Also, it was already showed that these techniques are good candidates for improvement of sorption kinetics and cost reduction for the industrial scale. More work is still required to have a better fundamental and practical understanding of the effect of these techniques on the synthesis of metal hydrides.

### **1.3.3 Influence of additives/catalysts**

Catalysis is one of the critical factors in the improvement of hydrogen sorption kinetics in metal hydride systems that enable fast and effective dissociation of hydrogen molecules. The effective catalysts, even added in small amounts may enhance the formation of hydride in reasonable extent [1.45]. There has been intensive research about finding a proper catalyst to enhance the hydriding properties. It was reported that the rate of absorption is usually controlled by the following factors: the rate of hydrogen dissociation at the surface, the capability of atomic hydrogen to penetrate from the surface which is typically covered by an impervious oxide layer into the metal-matrix, the rate of hydrogen diffusion into the bulk metal and through the hydride already formed.

Palladium is a good catalyst for hydrogen dissociation reaction. The hydriding properties are enhanced by catalysis through nanoparticles of Pd located on magnesium surface [1.45]. The reactivity of palladium after exposure to oxygen is recovered during exposure to hydrogen because of the easy decomposition of palladium oxide. Zaluski et al. [1.46] have reported on the

presence of Pd as a catalyst in nanocrystalline  $Mg_2Ni$ ,  $LaNi_5$  and  $FeTi$  systems, enhance the absorption rates even at lower temperatures and maintain less sensitivity to air exposures. However, high cost of palladium is the main disadvantage for industrial applications.

Hydrogen molecules have a strong affinity for nickel and readily dissociate and adsorb onto surface-layer of nickel clusters [1.47]. Through the addition of 1 at% of nickel to magnesium, Holtz and Imam [1.48] achieved a 50% increase in hydrogen capacity, a decrease in the temperature for the onset of hydrogenation from 275 to 175 °C, and a lowering of the dehydrogenation onset temperature from 350 to 275 °C. In addition to Pd and Ni, Ge can be used for the catalysis of hydrogenation kinetics [1.49]. The presence of Ge decreases the hydride decomposition temperature in a range from 50 to 150 °C, depending on the catalyst amount. But the catalytic effect of Ge disappears after few cycles of de-/hydrogenation. Vanadium also acts as a catalyst for the dissociation of hydrogen molecules. It was reported using V as a catalyst that hydrogen capacity can be increased up to 5.8 wt% while the thermodynamic parameters of  $MgH_2$  were not altered [1.50].

The poor kinetics of  $MgH_2$  is greatly improved by addition of different oxide catalysts that enhance hydriding properties at relatively low temperature, such as  $V_2O_5$  and  $Cr_2O_3$  [1.51]. The presence of oxide particles may accelerate the formation of many defects in the Mg powder. Defects provide hydrogen an easy path to Mg matrix. It was also proposed that  $Cr_2O_3$  yields fast hydrogen absorption, whereas  $V_2O_5$  and  $Fe_3O_4$  cause the most rapid desorption of hydrogen. The addition of  $TiO_2$  also resulted in a markedly improved hydrogenation performance of Mg, rapid kinetics, low working temperature and excellent oxidation resistance [1.52]. By mechanical

grinding, Barkhordarian et al. [1.53] investigated the catalytic effect of transition metal oxides in Mg–MgH<sub>2</sub> system for hydrogen sorption reactions. It was found that among their tested oxides, Nb<sub>2</sub>O<sub>5</sub> shows the best catalytic properties to improve the sorption kinetics. They believed that metals with multiple valences could show better catalytic efficiency due to electronic exchange reactions with hydrogen.

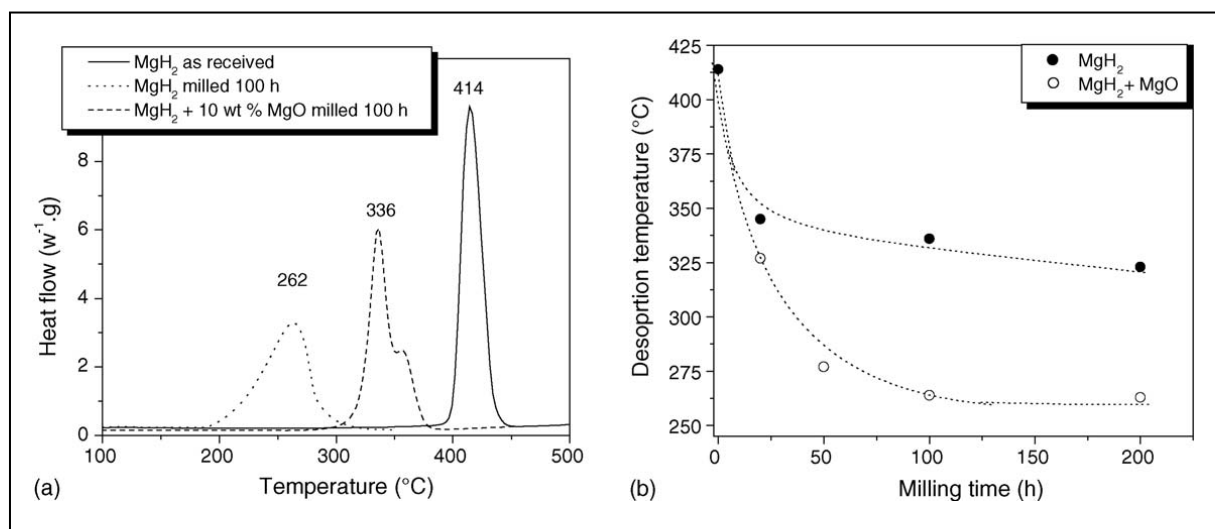


**Figure 1.7** – (a) DSC curves of the starting material (MgH<sub>2</sub> as-received) and milled with or without MgO for 100 h, and (b) evolution of MgH<sub>2</sub> decomposition temperature measured by DSC with the milling time, after Ref. [1.54].

The catalytic effects of native magnesium oxide (MgO) have also been intensively studied by many authors [1.54-1.56]. Mechanical milling with MgO allows decrease of MgH<sub>2</sub> particle size until strong particles agglomeration prevents further decrease. The addition of MgO to the grinding medium, which has good lubricant and dispersing properties, allows further

decrease of  $\text{MgH}_2$  particles size by reducing agglomeration and cold welding. The sorption kinetics obtained is comparable to the fastest reported in the literature, for  $\text{MgH}_2$  milled with a catalyst transition metal or metal oxide (see Figure 1.7). The role of  $\text{MgO}$  is rationalized in a concept of “Process Control Agent”. The improved hydrogen storage thermodynamic and kinetic properties were attributed to the structural refinement in  $\text{Mg}$  and the positive catalytic effect from the dispersed nanometric  $\text{MgO}$  induced under the HPT treatment of originally condensed and passivated ultrafine  $\text{Mg}$  particles [1.43,1.44]. The influence of oxygen contamination on hydride formation in  $\text{Pd}$  covered thin films of  $\text{Mg}$  has been studied [1.55]. The oxygen enhances the formation of  $\text{MgH}_2$  in the film by creating new pathways of  $\text{MgO}$  for hydrogen transport through the film.

Apart from metallic catalysts, some non-metallic elements have also been studied as additives to improve the hydrogen storage properties of  $\text{Mg}$ . For example, carbon-based materials have recently been noted to facilitate the activation process of  $\text{Mg}$  and improve the absorption/desorption kinetics of  $\text{Mg}$ -based materials [1.57-1.63]. It was reported that milling of a small amount of graphite is sufficient to drastically improve the activation characteristics of several hydrogen storage materials including  $\text{Mg}$ ,  $\text{Ti}$ ,  $\text{V}$ ,  $\text{Mg}_2\text{Ni}$  and  $\text{FeTi}$  [1.58]. Shang and Guo [1.59] investigated the effect of graphitic carbon on hydrogen sorption properties of mechanically milled  $\text{MgH}_2$ . The results clearly showed that graphite has little influence on desorption temperature and kinetics of  $\text{MgH}_2$ , but leads to rapid hydrogen uptake in the re-hydrogenated sample. These were attributed to the interaction between crystalline graphite and the disassociation of hydrogen molecules at the  $\text{MgH}_2$  or  $\text{Mg}$  surface. Graphite coating on the powder particles could also inhibit the formation of a new oxide layer on the  $\text{Mg}$  powder surfaces [1.63].

## **1.4 Scope of thesis work**

It should be appreciated from the current literature reviews that there have been significant amounts of research conducted on the improvements in hydrogen storage properties of a wide variety of metal hydrides. These studies can be categorized into three main directions, namely suitable storage media, processing of materials, and appropriate catalytic additions. While the materials systems are important in terms of desirable hydrogen storage capacity for onboard applications, the processing routes as well as the certain catalysts can significantly enhance the hydrogenation/dehydrogenation kinetics, and also bring down the thermodynamics stability in some metal hydride systems.

Considering several disadvantages encountered by the high energy ball-milling (contamination, stickiness, health issues etc.), in the present works a new powder metallurgy route is proposed for investigating the improvements in hydrogen sorption properties of Mg based materials. This new approach mainly consists of producing “clean” powder particles by an arc-plasma evaporation/condensation plus severe plastic deformation through HPT of the as-synthesized powder precursors [1.43]. It has been widely regarded that HPT processing is an effective route for powder consolidation due to its unique working principle: simple shear deformation of individual particles by introducing extremely large amounts of shear strain under high hydrostatic pressures. Moreover, this new processing route has potentially several advantages. Compared to HEBM, it is less likely to introduce contamination within the heavily deformed material. Also, in comparison with the other SPD processing routes, it is easier to apply on powder materials and simpler to control the chemistry of powder mixtures.

Furthermore, effect of catalytic additives is also tested by incorporating them either before the arc-plasma condensation or before the HPT consolidation process [1.44].

Finally, the objectives of the present research can be summarized as follows.

1. To analyze the origin of heterogeneities in strains and microstructures during HPT processing of relatively thick-sample with different crystal structures.
2. To study the effects of nature of the starting powder types on the consolidation behaviors of Mg powders by HPT, in terms of microstructure, texture and microhardness.
3. To assess the influences of structural heterogeneities introduced by HPT on the improvements in hydrogen sorption properties of the consolidated products in comparison with that of its initial powder precursors.
4. To understand the effects of severe plastic deformation processing route on the modifications of hydrogen storage properties in presence of catalytic elements.

## References

- [1.1] [www.mcphy.com](http://www.mcphy.com)
- [1.2] Winter CJ. "Into the hydrogen energy economy – milestones." *Int. J. Hydrogen Energy* 30 (2005) 681-85.
- [1.3] Edwards PP, Kuznetsov VL, David WI, Brandon NP. "Hydrogen and fuel cells: towards a sustainable energy future." *Energy Policy* 36 (2008) 4356-62.
- [1.4] Edwards PP, Kuznetsov VL, David WI. "Hydrogen energy." *Phil. Trans. Royal Soc. London A: Math., Phys. and Eng. Sci.* 365 (2007) 1043-56.
- [1.5] <https://energy.gov/eere/fuelcells/hydrogen-storage>.
- [1.6] David E. "An overview of advanced materials for hydrogen storage." *J. Mater. Process. Technol.* 162 (2005) 169-77.
- [1.7] Weast RC, Astle MJ, Beyer WH. "Redox Potential: CRC handbook of chemistry and physics." 64th Edition (1984), Boca Raton, Florida: CRC Press.
- [1.8] Nijkamp MG, Raaymakers JEMJ, Van Dillen AJ, De Jong KP. "Hydrogen storage using physisorption—materials demands." *Appl. Phys. A* 72 (2001) 619-23.
- [1.9] Züttel A, Sudan P, Maun P, Kiyobayashi T, Emmenegger C, Schlapbach L. "Hydrogen storage in carbon nanostructures." *Int. J. Hydrogen Energy* 27 (2002) 203-12.
- [1.10] Darkrim FL, Malbrunot P, Tartaglia GP. "Review of hydrogen storage by adsorption in carbon nanotubes." *Int. J. Hydrogen Energy* 27 (2002) 193-02.
- [1.11] Van Vucht JH, Kuijpers F, Bruning HC. "Reversible room-temperature absorption of large quantities of hydrogen by intermetallic compounds." *Philips Res. Rep.* 25 (1970) 133-40.
- [1.12] Reilly JJ, Wiswall RH. "Formation and properties of iron titanium hydride." *Inorg. Chem.* 13 (1974) 218-22.
- [1.13] Dantzer P. "Properties of intermetallic compounds suitable for hydrogen storage applications." *Mater. Sci. Eng. A* 329 (2002) 313-20.
- [1.14] Züttel A, Wenger P, Rentsch S, Sudan P, Maun P, Emmenegger C. "LiBH<sub>4</sub> a new hydrogen storage material." *J. Power Sources* 118 (2003) 1-7.
- [1.15] Jain IP, Jain P, Jain A. "Novel hydrogen storage materials: a review of lightweight complex hydrides." *J. Alloys Compd.* 503 (2010) 303-39.
- [1.16] Zaluska A, Zaluski L, Ström-Olsen JO. "Nanocrystalline magnesium for hydrogen storage." *J. Alloys Compd.* 288 (1999) 217-25.
- [1.17] Dornheim M, Doppiu S, Barkhordarian G, Boesenberg U, Klassen T, Gutfleisch O, Bormann R. "Hydrogen storage in magnesium-based hydrides and hydride composites." *Scr. Mater.* 56 (2007) 841-6.

- [1.18] Bogdanović B, Bohmhammel K, Christ B, Reiser A, Schlichte K, Vehlen R, Wolf U. “Thermodynamic investigation of the magnesium–hydrogen system.” *J. Alloys Compd.* 282 (1999) 84-92.
- [1.19] Corgnale C, Hardy B, Motyka T, Zidan R. “Metal hydride based thermal energy storage system requirements for high performance concentrating solar power plants.” *Int. J. Hydrogen Energy* 41 (2016) 20217-30.
- [1.20] Reiser A, Bogdanovic B, Schlichte K. “The application of Mg-based metal-hydrides as heat energy storage systems.” *Int. J. Hydrogen Energy* 25 (2000) 425-30.
- [1.21] Huot J, Liang G, Boily S, Neste AV, Schulz R. “Structural study and hydrogen sorption kinetics of ball-milled magnesium hydride.” *J. Alloys Compd.* 293 (1999) 495-500.
- [1.22] Huot J, Akiba E, Takada T. “Mechanical alloying of Mg–Ni compounds under hydrogen and inert atmosphere.” *J. Alloys Compd.* 231 (1995) 815-9.
- [1.23] Hanada N, Ichikawa T, Orimo SI, Fujii H. “Correlation between hydrogen storage properties and structural characteristics in mechanically milled magnesium hydride MgH<sub>2</sub>.” *J. Alloys Compd.* 366 (2004) 269-73.
- [1.24] Skripnyuk VM, Rabkin E, Estrin Y, Lapovok R. “The effect of ball milling and equal channel angular pressing on the hydrogen absorption/desorption properties of Mg-4.95 wt% Zn-0.71 wt% Zr (ZK60) alloy.” *Acta Mater.* 52 (2004) 405-14.
- [1.25] Valiev R, Langdon TG. “Principles of equal-channel angular pressing as a processing tool for grain refinement.” *Prog. Mater. Sci.* 51 (2006) 881-981.
- [1.26] Langdon TG. “The characteristic of grain refinement in materials processed by severe plastic deformation.” *Rev. Adv. Mater. Sci.* 13(2006) 6-14.
- [1.27] Krystian M, Zehetbauer MJ, Kropik H, Mingler B, Krexner G. “Hydrogen storage properties of bulk nanostructured ZK60 Mg alloy processed by equal channel angular pressing.” *J. Alloys Compd.* 509 (2011) S449-S455.
- [1.28] Løken S, Solberg JK, Maehlen JP, Denys RV, Lototsky MV, Tarasov BP, Yartys VA. “Nanostructured Mg–Mn–Ni hydrogen storage alloy: Structure-properties relationship.” *J. Alloys Compd.* 446 (2007) 114-20.
- [1.29] Jorge AM, Prokofiev E, Lima GF, Rauch E, Veron M, Botta WJ, Kawasaki M, Langdon TG. “An investigation of hydrogen storage in a magnesium-based alloy processed by equal-channel angular pressing.” *Int. J. Hydrogen Energy* 38 (2013) 8306-12.
- [1.30] Ueda TT, Tsukahara M, Kamiya Y, Kikuchi S. “Preparation and hydrogen storage properties of Mg–Ni–Mg<sub>2</sub>Ni laminate composites.” *J. Alloys Compd.* 386 (2004) 253-7.
- [1.31] Dufour J, Huot J. “Rapid activation, enhanced hydrogen sorption kinetics and air resistance in laminated Mg–Pd 2.5 at.%.” *J. Alloys Compd.* 439 (2007) L5-L7.
- [1.32] J Liang, J Huot. “A new approach to the processing of metal hydrides.” *J. Alloys Compd.* 509 (2011) L18-22.

- [1.33] Leiva DR, Floriano R, Huot J, Jorge AM, Bolfarini C, Kiminami CS et al. "Nanostructured MgH<sub>2</sub> prepared by cold rolling and cold forging." *J. Alloys Compd.* 509 (2011) S444-8.
- [1.34] Bellemare J, Huot J. "Hydrogen storage properties of cold rolled magnesium hydrides with oxides." *J. Alloys Compd.* 512 (2012) 33-8.
- [1.35] Vincent SD, Lang J, Huot J. "Addition of catalysts to magnesium hydride by means of cold rolling." *J. Alloys Compd.* 512 (2012):290-5.
- [1.36] Leiva DR, Fruchart D, Bacia M, Girard G, Skryabina N, Villela ACS et al. "Mg alloy for hydrogen storage processed by SPD." *Int. J. Mater. Res.* 100 (2009) 1739-46.
- [1.37] Zhilyaev AP, Langdon TG. "Using high-pressure torsion for metal processing: Fundamentals and applications." *Prog. Mater. Sci.* 53 (2008) 893-979.
- [1.38] Kusadome Y, Ikeda K, Nakamori Y, Orimo S, Horita Z. "Hydrogen storage capability of MgNi<sub>2</sub> processed by high pressure torsion." *Scr. Mater.* 57 (2007) 751-3.
- [1.39] Leiva DR, Jorge AM, Ishikawa TT, Huot J, Fruchart D et al. "Nanoscale Grain Refinement and H-Sorption Properties of MgH<sub>2</sub> Processed by High-Pressure Torsion and Other Mechanical Routes." *Adv. Eng. Mater.* 12 (2010) 786-92.
- [1.40] Huot J, Swainson I, Schulz R. "Phase transformation in magnesium hydride induced by ball milling." *Ann. Chim. Sci. Mat.* 31 (2006) 135-44.
- [1.41] Edalati K, Yamamoto A, Horita Z, Ishihara T. "High-pressure torsion of pure magnesium: evolution of mechanical properties, microstructures and hydrogen storage capacity with equivalent strain." *Scr. Mater.* 64 (2011) 880-3.
- [1.42] Botta WJ, Jorge Jr AM, Veron M, Rauch EF, Ferrie E, Yavari AR, Huot J, Leiva DR. "H-sorption properties and structural evolution of Mg processed by severe plastic deformation." *J. Alloys Compd.* 580 (2013) S187-91.
- [1.43] Zou JX, Perez-Brokate CF, Arruffat R, Bolle B, Fundenberger JJ, Zeng XQ, Grosdidier T, Ding WJ. "Nanostructured bulk Mg+MgO composite synthesized through arc plasma evaporation and high pressure torsion for H-storage application." *Mater. Sci. Eng. B* 183 (2014) 1-5.
- [1.44] Grosdidier T, Fundenberger JJ, Zou JX, Pan YC, Zeng XQ. "Nanostructured Mg based hydrogen storage bulk materials prepared by high pressure torsion consolidation of arc plasma evaporated ultrafine powders." *Int. J. Hydrogen Energy* 40 (2015) 16985-91.
- [1.45] Zaluski L, Zaluska A, Ström-Olsen JO. "Nanocrystalline metal hydrides." *J. Alloy Compd.* 253 (1997) 70-9.
- [1.46] Zaluski L, Zaluska A, Tessier P, Ström-Olsen JO, Schulz R. "Catalytic effect of Pd on hydrogen absorption in mechanically alloyed Mg<sub>2</sub>Ni, LaNi<sub>5</sub> and FeTi." *J. Alloys Compd.* 217 (1995) 295-300.
- [1.47] Baer R, Zeiri Y, Kosloff R. "Hydrogen transport in nickel (111)." *Phys. Rev. B* 55 (1997) 952-74.

- [1.48] Holtz RL, Imam MA. "Hydrogen storage characteristics of ball-milled magnesium–nickel and magnesium–iron alloys." *J. Mater. Sci.* 34 (1999) 2655-63.
- [1.49] Gemari FC, Castra FJ, Urretavizcaya G, Meyer G. "Catalytic effect of Ge on hydrogen desorption from MgH<sub>2</sub>." *J. Alloys Compd.* 334 (2002) 277-84.
- [1.50] Liang G, Huot J, Boily S, Neste AV, Schulz R. "Hydrogen storage properties of the mechanically milled MgH<sub>2</sub>–V nanocomposite." *J. Alloy Compd.* 291 (1999) 295-99.
- [1.51] Oelerich W, Klassen T, Bormann T. "Metal oxides as catalysts for improved hydrogen sorption in nanocrystalline Mg-based materials." *J. Alloys Compd.* 315 (2001) 237-42.
- [1.52] Wang P, Wang AM, Zhang HF, Ding BZ, Hu ZQ. "Hydrogenation characteristics of Mg-TiO<sub>2</sub> (rutile) composite." *J. Alloys Compd.* 313 (2000) 218-23.
- [1.53] Barkhordarian G, Klassen T, Bormann R. "First hydrogen sorption kinetics of nanocrystalline Mg using Nb<sub>2</sub>O<sub>5</sub> catalyst." *Scr. Mater.* 49 (2003) 213-17.
- [1.54] Ageuy-Zinsou KF, Fernandez JA, Klassen T, Bormann R. "Using MgO to improve the (de) hydriding properties of magnesium." *Mater. Res. Bull.* 41 (2006) 1118-26.
- [1.55] Ingason AS, Olafsson S. "Influence of MgO nano-crystals on the thermodynamics, hydrogen uptake and kinetics in Mg films." *Thin solid films* 515 (2006) 708-11.
- [1.56] Ageuy-Zinsou KF, Nicolaisen T, Fernandez JA, Klassen T, Bormann R. "Effect of nanosized oxides on MgH<sub>2</sub> (de)hydriding kinetics." *J. Alloys Compd.* 434 (2007) 738-42.
- [1.57] Imamura H, Sakasai N, Fujinaga T. "Characterization and hydriding properties of Mg-graphite composites prepared by mechanical grinding as new hydrogen storage materials." *J. Alloys Compd.* 253 (1997) 34-7.
- [1.58] Bouaricha S, Dodelet JP, Guay D, Huot J, Schulz R. "Activation characteristics of graphite modified hydrogen absorbing materials." *J. Alloys Compd.* 325 (2001) 245-51.
- [1.59] Shang CX, Guo ZX. "Effect of carbon on hydrogen desorption and absorption of mechanically milled MgH<sub>2</sub>." *J. Power Sources* 129 (2004) 73-80.
- [1.60] Yao X, Wu CZ, Wang H, Cheng HM, Lu GQ. "Effects of carbon nanotubes and metal catalysts on hydrogen storage in magnesium nanocomposites." *J. Nanosci. Nanotech.* 6 (2006) 494-8.
- [1.61] Huang ZG, Guo ZP, Calka A, Wexler D, Liu HK. "Effects of carbon black, graphite and carbon nanotube additives on hydrogen storage properties of magnesium." *J. Alloys Compd.* 427 (2007) 94-100.
- [1.62] Wu C, Cheng HM. "Effects of carbon on hydrogen storage performances of hydrides." *J. Mater. Chem.* 20 (2010) 5390-400.
- [1.63] Adelhelm P, De Jongh PE. "The impact of carbon materials on the hydrogen storage properties of light metal hydrides." *J. Mater. Chem.* 21 (2011) 2417-27.

## CHAPTER 2: EXPERIMENTAL MATERIALS, METHODS AND CHARACTERIZATION TECHNIQUES

---

2.1 Selected materials .....	46
2.2 Processing routes .....	50
2.2.1 Arc-plasma method .....	50
2.2.2 High-pressure torsion (HPT) .....	51
2.2.3 Two-step HPT consolidation .....	53
2.3 Characterization techniques .....	54
2.3.1 X-ray tomography (XRT) .....	54
2.3.2 X-ray diffraction (XRD) .....	55
2.3.3 Hardness testing .....	56
2.3.4 Scanning electron microscope (SEM) .....	57
2.3.5 Electron backscatter diffraction (EBSD) .....	57
2.3.6 SEM based transmission Kikuchi diffraction (SEM-TKD) .....	58
2.3.7 Transmission electron microscope (TEM) .....	58
2.3.8 Sievert-type apparatus .....	59
2.3.9 Differential scanning calorimetry-thermogravimetry (DSC-TG) .....	60
2.3.10 Raman Spectroscopy .....	61
References .....	62

## **2.1 Selected materials**

Since the sole purpose of the present research was to improve the hydrogen storage properties of lightweight metal systems while processed by severe plastic deformation through high-pressure torsion (HPT), the primary materials employed in the present study are based on magnesium metals. A wide variety of materials combinations employed in this study is described as follows.

In **Chapter 3**, the first part of the chapter deals with HPT deformation of two kinds of bulk lightweight metals - a face centered cubic aluminum alloy (A5086) and a commercial purity magnesium (~ 99.8%) of hexagonal closed-packed symmetry - to characterize the effect of the crystallographic nature on deformation heterogeneities in case of the relatively thick-HPT samples. In the second part of **Chapter 3**, HPT consolidation behaviors of two types of magnesium powders - micro-sized powder particles and ultrafine powder particles - are reported for relatively thick-samples. While the micro-sized Mg powder particles with a particle size distribution in the range of 5 - 70  $\mu\text{m}$  were produced from commercial purity magnesium (~ 99.8%) by using an inert-gas atomization process by SFM SA (Switzerland), the ultrafine powder particles were synthesized by a DC arc-plasma evaporation/condensation method to obtain particle sizes in the range of 50 - 800 nm. Figure 2.1(a) depicts a scanning electron microscope (SEM) image illustrating the morphological aspects of the micro-sized powder particles. The atomization process has led to fairly rounded particles having a particle size distribution centered at around 15  $\mu\text{m}$ . The grain-structures in the atomized powder can be clearly apparent at higher magnification of a particular particle as shown in the inset of Figure 2.1(a) indicating an average grain size of about 5  $\mu\text{m}$ .

Figure 2.1(b) gives representative SEM and transmission electron microscope (TEM) images illustrating the morphological characteristics of the ultrafine powder particles. It was estimated from several SEM and TEM images that the particle size distribution was essentially in the sub-micrometer range with an average particle size below 300 nm, and that each powder particle generally corresponds to a single crystal [2.1-2.3]. The hexagonal shape of some finer powder particles as visible in the TEM image is due to the hexagonal structure of the Mg phase.

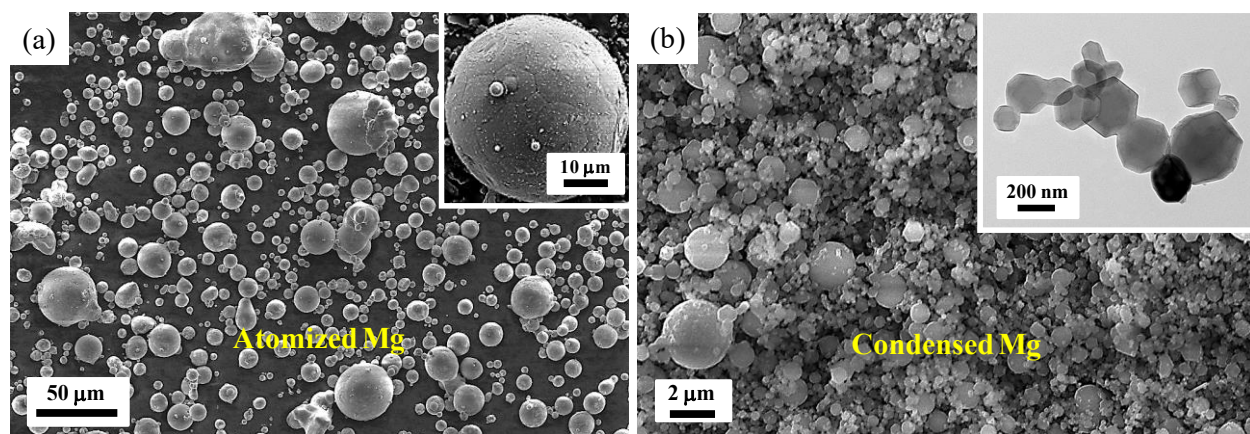


**Figure 2.1** – Morphological aspects of the Mg powder precursors for (a) the atomized micro-sized powder and (b) the condensed ultrafine powder particles.

**Chapter 4** presents the improvements in hydrogen storage properties of the two types of HPT-consolidated products fabricated in **Chapter 3** in comparison with their starting powder precursors.

**Chapter 5** reports the HPT consolidation of Mg/Fe based powder mixtures in the two stoichiometric ratios (i.e. 9Mg-Fe and 2Mg-Fe). Two types of raw materials - micrometer range powder particles and ultrafine powder particles in both Mg and Fe phases – are used to study the effect of initial powder precursors on the microstructural developments as well as the hydrogen storage properties of the Mg-Fe composites. While the micro-sized Fe powder particles were obtained by water atomization process (Höganäs, Sweden), the ultrafine Fe powder particles were synthesized by the DC arc-plasma method. Figure 2.2 compares the morphological aspects between the two kinds of Fe powders. It can be readily noted that the atomized Fe powder has a more irregular shape and a wide range of particle size distribution (i.e. 5 to 150  $\mu\text{m}$ ), whereas the condensed powder particles are in spherical shape with particle size distribution in the sub-micrometer range (i.e. 50 to 600 nm).

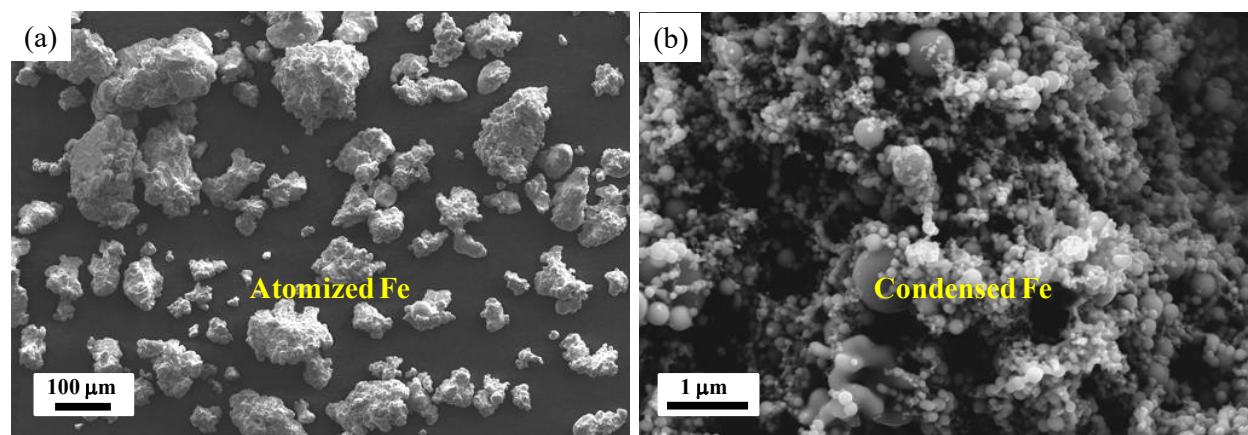


**Figure 2.2** – Morphological aspects of the Fe powder precursors in the case of (a) atomized micro-sized powder and (b) condensed ultrafine-grained powder particles.

**Chapter 6** addresses the improvements in hydrogen storage properties of Mg in the presence of graphene additives for as-synthesized powder and its HPT-consolidated product. The Mg/graphene powder composite was synthesized by the DC arc-plasma evaporation of a mixture of Mg powder and 3 wt% graphene monolayer (GM) precursors while bulk product was produced by the HPT consolidation of the as-synthesized powder. The Mg powder precursor was a commercial purity Mg (~99.9%) with a mean particle size of 100  $\mu\text{m}$ . The GM powder (~99.8%, XFNANO, China), synthesized by a chemical method, consists of short range stacks of graphene sheets with 0.8-1.2 nm thickness in the form of fine powder particles with 0.5 to 2  $\mu\text{m}$  diameter. Figure 2.3 illustrates the morphological evolution of the Mg-graphene composite powder through SEM and TEM images. They clearly demonstrate that the Mg-3GM powder particles had a wide range of particle size distribution starting from 50 nm to 800 nm, which is similar like C-free Mg powder.

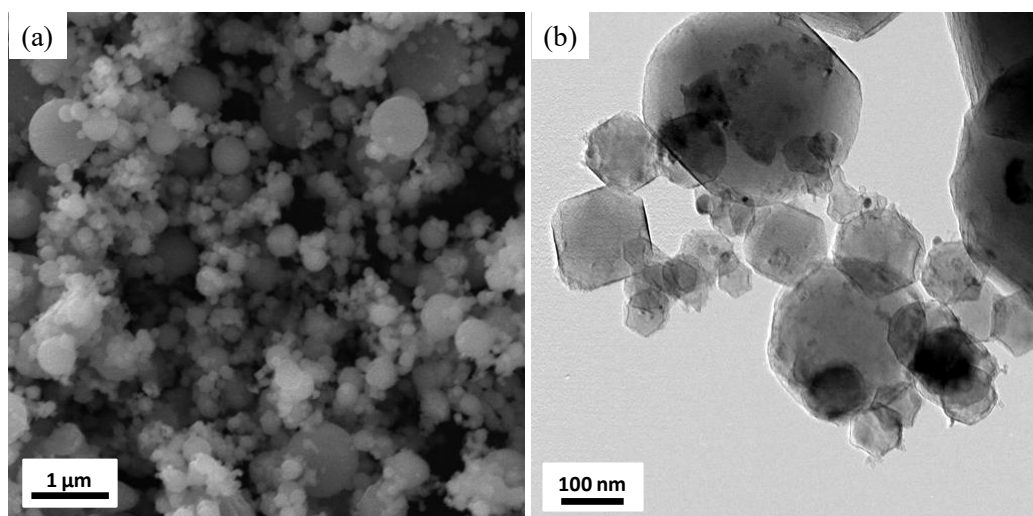


**Figure 2.3** – (a) SEM and (b) TEM images illustrating the morphological features of the Mg/graphene based composite powder obtained by the DC arc-plasma method.

## 2.2 Processing routes

### 2.2.1 Arc-plasma method

A wide variety of ultrafine powder particles with different chemistry was synthesized by a DC arc-plasma evaporation/condensation method (in collaboration with NERC-LAF, China). A schematic setup of this process is illustrated in Figure 2.4 [2.4]. It mainly consists of two important parts: reaction chamber and collecting chamber. The material to be converted into nanometric powder particles is used as anode targets evaporated by the arc discharge. The evaporation rate is usually controlled by increase/decrease of the partial pressure of hydrogen or argon gas (normally a mixture of Ar and H<sub>2</sub> is admitted to the chamber).

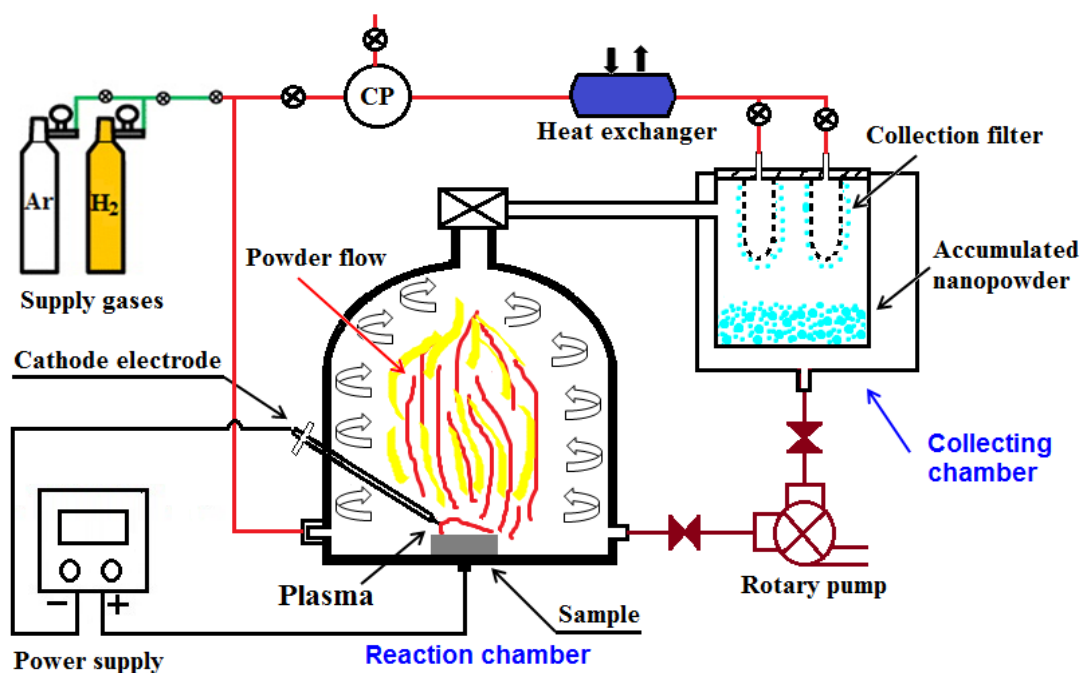


Figure 2.4 – Schematic illustrations of a DC arc-plasma processing route applied in the present study for producing different nature of ultrafine powder particles, inspired from Ref. [2.4].

In the present study, the target materials were processed from their corresponding powder precursors by compression under a uniaxial load of 25 MPa to form 10 mm diameter cylinders with a height of 7 mm. They were mounted as the anode material into the reaction chamber. The chamber was filled with a mixture of 0.70 atm Ar and 0.10 atm H<sub>2</sub> after it was evacuated to  $5 \times 10^{-2}$  Pa. The DC current was set at 140 A during the arc evaporation process to obtain a wide range of powder particles. In order to prevent these fine particles from burning in open atmosphere, the condensed powder particles were passivated in a mixture of 50 kPa Ar + 10 kPa normal air for 2 h before opening the collecting chamber. The powder precursors were then transferred to a glove box for further processing.

### **2.2.2 High-pressure torsion (HPT)**

The bulk samples were processed by a severe plastic deformation (SPD) processing route using high-pressure torsion (HPT) to interpret the deformation characteristics of relatively thick-samples. Among the three types of HPT processing conditions, a more versatile one - quasi-constrained HPT facility [1.37] where the materials lateral flow is partially restricted - was employed in the present study. A photograph of the HPT facility and its associated experimental setup available at the laboratory LEM3 are given in Figure 2.5. The left-side of figure shows a hydraulic press along with the experimental set up at the higher magnification. A sketch of the upper and lower anvils is provided at the right-side of the figure. The geometry of both anvil dies used in the present study is given as: depth of the depression - 1.2 mm, the angle of the lateral wall - 15° and lower diameter of the depression - 20 mm.

The bulk thick-samples with 20 mm in diameter and 3 mm in thickness were processed by the single-step HPT facility. The disk-shape samples were first put in the depression of the lower anvil followed by bringing down the upper anvil to compress the sample up to the intended hydrostatic pressures. Immediately after reaching to the applied pressure ( $\sim 1.2$  GPa), the motor was run to rotate the lower anvil at a constant angular speed of 0.125 rpm in the direction as shown in Figure 2.5. During the HPT processing, a significant amount of strains was imposed to the materials by rotating the lower anvil up to  $180^\circ$  and  $270^\circ$ . The above experiments were conducted at room temperature and under quasi-constrained conditions.

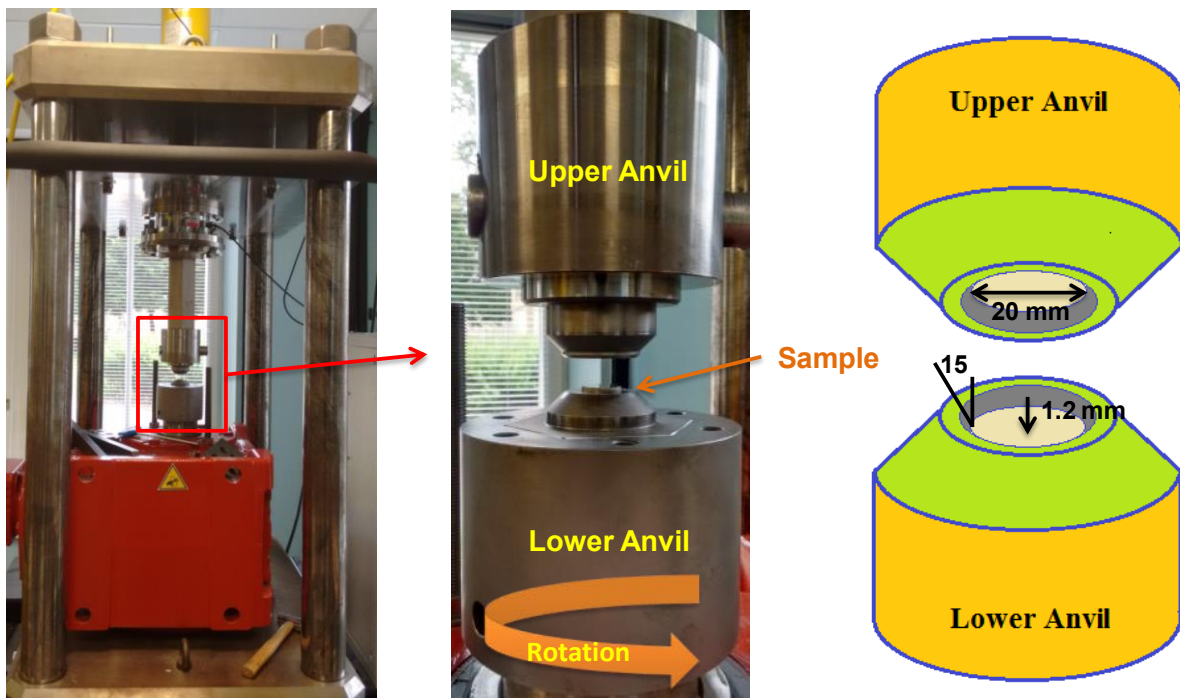


**Figure 2.5** – High-pressure torsion (HPT) facility and its associated experimental setup employed for the present dissertation work. This facility is available at the laboratory LEM3, Metz, France.

### 2.2.3 Two-step HPT consolidation

The powder samples were consolidated into bulk products by using a two-step HPT processing route as illustrated in Figure 2.6. In step - 1, the powder was first compacted by uniaxial compression under a hydrostatic pressure of 1.5 GPa holding for 10 min into an intermediate body in a form of disk with 20 mm diameter and 3 mm thickness. In step - 2, the intermediate disks were subsequently deformed by torsional straining using the quasi-constrained HPT facility (see in Figure 2.5) under a hydrostatic pressure of 1.2 GPa. Different amounts of strains were introduced into the disks by varying the torsional straining up to different levels of revolutions.

Both HPT treatments were carried out at room temperature. After the HPT processing, all the HPT-processed samples (obtained from the bulk or the powder materials) were preserved at - 80 °C in order to avoid any kind of restoration processes associated with the low homologous temperature materials (i.e. Al, Mg etc.) [2.5].

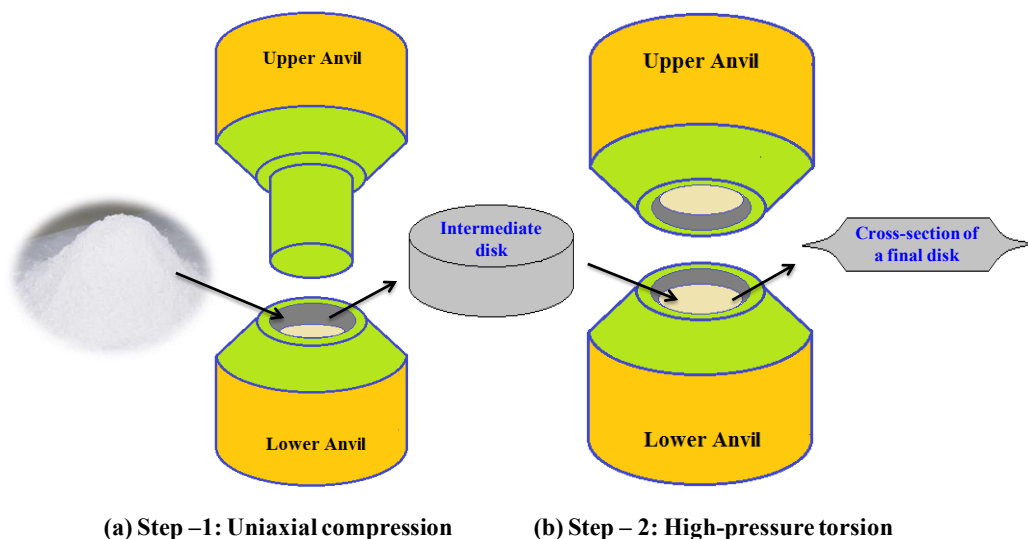


**Figure 2.6** – (a) Uniaxial compression of the initial powders into an intermediate disk, and (b) HPT processing of the precompact green body into consolidated bulk products.

## 2.3 Characterization techniques

### 2.3.1 X-ray tomography (XRT)

The deformation behaviors of the bulk HPT samples (Al alloy and commercial purity Mg) were characterized by using an X-ray tomography (XRT) imaging technique (EasyTom, equipped with RX Solutions X-Act software). To witness the deformation heterogeneities for the thick-HPT samples (~ 3 mm), a 1 mm diameter pin made of solder alloy (tin + lead) was inserted through the thickness of the disks at a radial distance of ~7.5 mm. The initial sketch of a disk-shape sample along with the insert is shown in Figure 2.7.

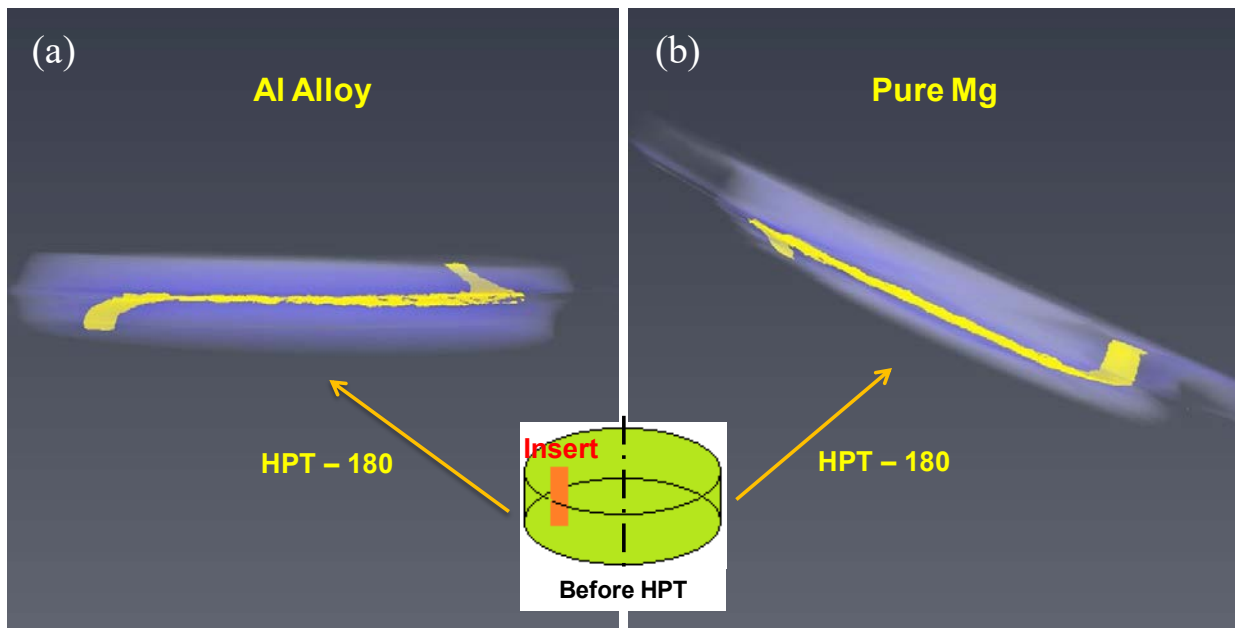


**Figure 2.7** – Reconstructed 3D images of the HPT deformed disks for (a) Al alloy and (b) pure Mg, obtained from the XRT data using the Avizo<sup>®</sup> 3D software.

After HPT processing, the disks were examined under the XRT imaging conditions to obtain a series of projection images recorded on a high-resolution 2D detector system while the sample was rotated around a fixed axis [2.6]. Due to the absorption contrast between the insert material (solder alloy) and the light metal matrix, the shape of the deformed insert across the sample volume can be reconstructed by using the Avizo<sup>®</sup> 3D software [2.7]. Some reconstructed 3D images are presented in Figure 2.7 for the HPT deformed samples in two different crystallographic structures: an fcc Al alloy and a hcp commercial purity Mg.

### **2.3.2 X-ray diffraction (XRD)**

Structural phases and phase compositions of the powder samples before and after the HPT treatments as well as the hydrogenated samples were characterized by X-ray diffraction (XRD) using a X-ray diffraction apparatus (D/max 2550VL/PCX) equipped with a monochromatic Cu-K<sub>α</sub> ( $\lambda = 0.1542$  nm) radiation source operated at 40 kV and 30 mA. The XRD data was recorded under the following conditions: range - 20 to 80°, step size - 0.02° 2 $\theta$ , scan speed - 10°/min.

The powder samples were carefully protected from open atmosphere to reduce the contamination as much as possible, while the bulk samples were loaded directly to the diffraction apparatus right after polishing. The designated surfaces of the HPT-disks were first mechanically ground to flatten the surface followed by cloth polishing with oil-based diamond paste to a mirror-like finishing. JADE software (MDI JADE 7 Materials Data XRD Pattern Processing, Identification, and Quantification [2.8]) and the Reference Intensity Ratio (RIR) method [2.9] were employed to determine the structural phases as well as the phase compositions in some of the assessed samples.

### 2.3.3 Hardness testing

The Vickers microhardness was measured for some of the bulk HPT samples by using a Micro Hardness tester (Leitz/Durimet, diamond pyramid) available at the laboratory LEM3. A dwell time of 15 s with loads of in the range of 25 to 100 g depending of the materials properties was imposed during the hardness measurements.

For microhardness measurements, the samples were first cut diagonally and the cross-sections were cold mounted in a resin, ground mechanically with abrasive papers, and further polished on cloth with diamond paste to a mirror-like finishing. The developments of hardness were examined on several cross-sectional planes across the disk-thickness. In order to obtain the radial evolution of the microhardness, measurements were also conducted at  $0.1R$ ,  $0.25R$ ,  $0.5R$ ,  $0.75R$  and  $0.9R$  radial positions across the through-thickness of the HPT-disks. A schematic diagram of one-half of a cross-sectional plane utilized for hardness measurements is described in Figure 2.8.

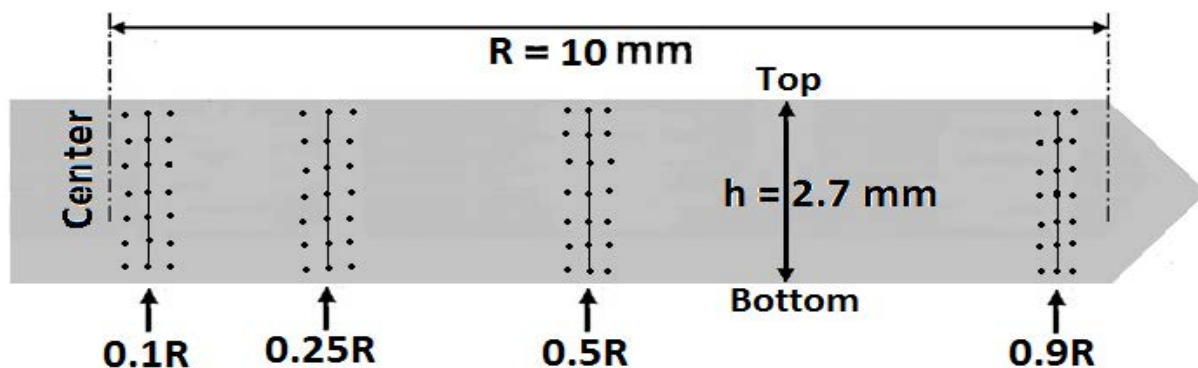


**Figure 2.8** – A cross-sectional plane of one-half of an HPT-disk showing the positions selected for the Vickers microhardness measurements.

#### **2.3.4 Scanning electron microscope (SEM)**

The morphological aspects of the initial powder precursors, and the microstructural developments in the bulk HPT products were materialized by using a field emission gun scanning electron microscope (SEM – Zeiss Supra40).

The powder materials were stuck to the surface of sample holder using Ag paste before the SEM observations. The intended surfaces of the bulk and consolidated samples were first mechanically ground using abrasive papers to flatten the surfaces followed by cloth polishing up to 0.5  $\mu\text{m}$  with oil-based diamond paste. The usage of water was avoided as much as possible during the polishing stages due to the hygroscopic nature of Mg materials. Finally, the thin surface oxide layers if any formed during polishing stages were removed by ion etching using GATAN PECS II (Model 685) operated at 4 keV with a milling angle of 5°.

#### **2.3.5 Electron backscatter diffraction (EBSD)**

Inverse Pole Figure (IPF) maps depicting grain orientations for the as-received as well as the HPT deformed samples was developed by electron backscatter diffraction (EBSD) technique attached to a field emission gun scanning electron microscope (SEM – Zeiss Supra40).

For this measurement, an identical sample preparation method was used as followed for the SEM studies. The EBSD measurements were conducted at the different acquisition conditions depending on the sample preparation, the microstructural features and the indexing success rate. A fraction of zero solutions less than 25% recorded during the EBSD measurements is reported in the present study. The evolutions of texture in a local area (i.e. microscopic) were materialized by utilizing the EBSD based patterns. The EBSD maps were obtained by employing the HKL

Channel 5, and the Atom software [2.10], while the microtexture based on the EBSD measurements was determined by using the JTEX software [2.11].

### **2.3.6 SEM based transmission Kikuchi diffraction (SEM-TKD)**

Due to the resolution limitations in the normal EBSD techniques for characterizing the highly deformed samples and the fine-grained materials, SEM-based transmission Kikuchi diffraction (SEM-TKD) using an on-axis detector attached to a conventional EBSD facility was employed for some of the nanostructured materials. The details of this TKD facility and its acquisition techniques may be found in a recent publication [2.12].

For this measurement, a very small size sample was cut from the HPT-disks, and then mechanically ground followed by cloth polishing using oil-based diamond paste to avoid the surface oxidation as much as possible. Finally, a thin-foil out of the polished surface was prepared using a focused ion beam (FIB) facility available in the laboratory LEM3.

### **2.3.7 Transmission electron microscope (TEM)**

The morphology and microstructure of the arc-plasma condensed powder particles in different compositions were observed by using a JEM 2100F transmission electron microscopy (TEM) operated at 200 kV. The phase characterizations were also performed in TEM using selected area electron diffraction (SEAD). The method used for indexation of SAED pattern can be found in Ref. [2.13]. The powder samples were first ultrasonically dispersed into high purity ethanol solution (to avoid oxide formation) and then a drop of suspended particles was taken on a completely dried Cu grid for TEM analysis.

### 2.3.8 Sievert-type apparatus

Hydrogen-storage properties of different kinds of Mg based material systems in the powder states as well as in the HPT-consolidated forms were investigated by using a Sievert-type volumetric apparatus (Type PCT-2, National Engineering Research Center of Light Alloy Net Forming, China). A schematic diagram of the working principle for a Sievert-type apparatus employed in the present study is given in Figure 2.9.

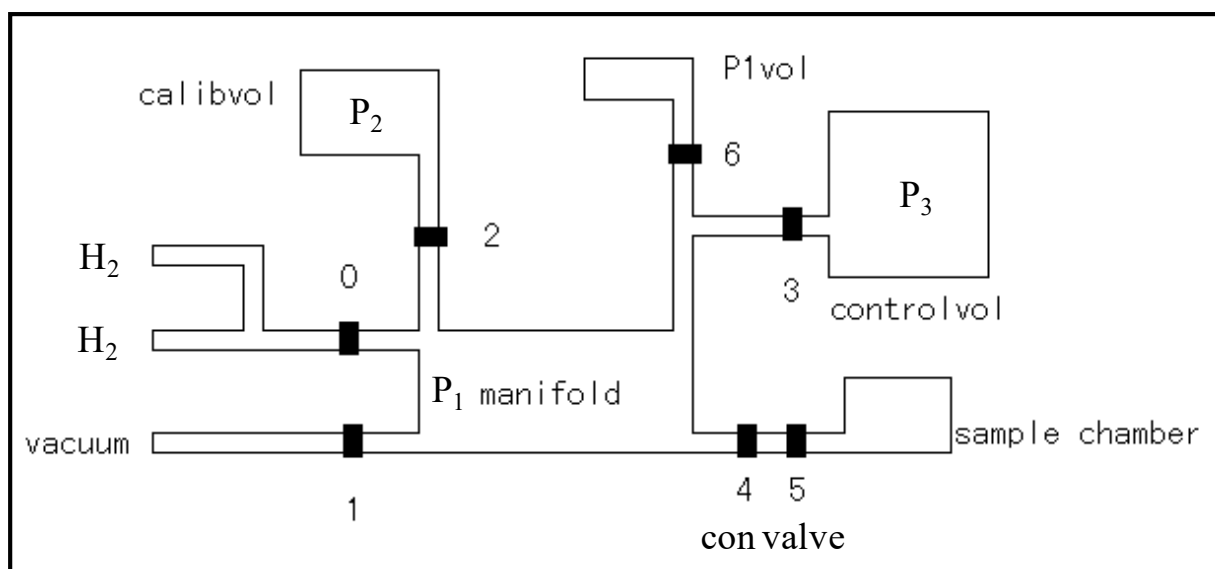


**Figure 2.9** – A schematic diagram of the working principle for a Sievert-type volumetric apparatus [2.14] employed in the present research.

In all the cases, prior to the hydrogen sorption measurements the HPT-consolidated products were broken into powder particle by a ceramic mortar to fit into the testing vessel. For all the experiments, the samples were first activated at 400 °C for 8 or 10 h under a hydrogen

pressure of 3.5 MPa and then desorbed at the same temperature under vacuum until complete dehydrogenation. These one-cycled samples were referred to as activated samples wherever applicable.

Thermodynamic properties of hydrogen absorption/desorption processes were obtained by measuring pressure-composition-temperature (PCT) isotherms of the activated samples at different temperatures, and followed by dynamic hydrogen absorption kinetics at different operating temperatures. Finally, the cycled samples after the PCT and the kinetic study were hydrogenated through dynamic hydrogen absorption at 400 °C for 6 h under a hydrogen pressure of 3.5 MPa to obtain fully hydrided products for the following characterization.

- i) X-ray diffraction (XRD) analysis to identify the structural phases and compositions.
- ii) Differential scanning calorimetry-thermogravimetry (DSC-TG) analysis to study the desorption properties of the hydrided samples and
- iii) Scanning electron microscope (SEM) for the microstructural developments upon the hydrogen absorption/desorption cycling.

### **2.3.9 Differential scanning calorimetry-thermogravimetry (DSC-TG)**

The hydrogen desorption properties of all the hydrided samples were characterized by simultaneous differential scanning calorimetry-thermogravimetry (DSC-TG, Netzsch STA449F3 Jupiter<sup>®</sup>) measurements under 0.1 MPa of purified argon with 60 ml min<sup>-1</sup> as sweep gas and 40 ml min<sup>-1</sup> as protection gas. The heating rate was set at 3, 5 and 10 °C/min, with the temperature rising from 25 °C to 500 °C.

The characteristic onset and peak temperatures for desorption were determined from the DSC profile analyses whereas the desorption kinetics (i.e. wt% H/min) and the hydrogen

discharge quantity were subtracted from the TG curves. In order to assess the desorption kinetics, the Kissinger method [2.15] based on DSC analysis and the related peak temperature depending on heating rate was employed to determine the apparent activation energy for desorption.

### **2.3.11 Raman Spectroscopy**

Carbon based materials were characterized by Raman Spectroscopy [2.16]. The Raman measurements were carried out on a Raman apparatus (LabRAM HR Evolution - HORIBA) using the 532 nm line of an Ar ion laser focused to 2 mm<sup>2</sup>. The laser power was 500 mW and the spectral resolution of the apparatus was 5 cm<sup>-1</sup>. The spectra were recorded in the range of 80 - 3000 cm<sup>-1</sup>.

## References

- [2.1] Cui Z, Zhang Z, Hao C, Dong L, Meng Z, Yu L. "Structures and properties of nanoparticles prepared by hydrogen arc plasma method." *Thin solid films* 318 (1998) 76-82.
- [2.2] Shao H, Wang Y, Xu H, Li X. "Hydrogen storage properties of magnesium ultrafine particles prepared by hydrogen plasma-metal reaction." *Mater. Sci. Eng. B* 110 (2004) 221-6.
- [2.3] Shao H, Liu T, Wang Y, Xu H, Li X. "Preparation of Mg-based hydrogen storage materials from metal nanoparticles." *J. Alloys Compd.* 465 (2008) 527-33.
- [2.4] Uda M, Okuyama H, Suzuki TS, Sakka Y. "Hydrogen generation from water using Mg nanopowder produced by arc plasma method." *Sci. Tech. Adv. Mater.* 13 (2012) p. 025009.
- [2.5] Edalati K, Horita Z. "Significance of homologous temperature in softening behavior and grain size of pure metals processed by high-pressure torsion." *Mater. Sci. Eng. A* 528 (2011) 7514-23.
- [2.6] Baruchel J, Buffiere JY, Maire E. "X-ray tomography in material science." Hermes, Paris, 2000.
- [2.7] Avizo for Materials Science, <<https://www.fei.com/software/>>.
- [2.8] MDI JADE 7 Materials Data XRD Pattern Processing, Identification, and Quantification, <<http://www.materialsdata.com/>>.
- [2.9] Snyder RL. "The use of reference intensity ratios in X-ray quantitative analysis." *Powder Diff.* 7 (1992) 186-93.
- [2.10] Beausir B, Fundenberger JJ, Université de Lorraine - Metz, 2015, "ATOM – Analysis Tools for Orientation Maps." <<http://atom-software.eu/>>.
- [2.11] Fundenberger JJ, Beausir B, Université de Lorraine - Metz, 2015, "JTEX - Software for Texture Analysis." <<http://jtex-software.eu/>>.
- [2.12] Fundenberger JJ, Bouzy E, Goran D, Guyon J, Yuan H, Morawiec A. "Orientation mapping by transmission-SEM with an on-axis detector." *Ultramicroscopy* 161 (2016) 17-22.
- [2.13] Williams DB, Carter CB, Veysiere P. *Transmission electron microscopy: a textbook for materials science.* New York: Springer; 1998.
- [2.14] Checchetto R, Trettel G, Miotello A. "Sievert-type apparatus for the study of hydrogen storage in solids." *Meas. Sci. Technol.* 15 (2003) 127.
- [2.15] Kissinger HE. "Reaction kinetics in differential thermal analysis." *Anal. Chem.* 29 (1957) 1702-6.
- [2.16] Socrates G. "Infrared and Raman characteristic group frequencies: tables and charts." John Wiley & Sons; 2001.

# CHAPTER 3: UNDERSTANDING OF HIGH-PRESSURE TORSION (HPT) PROCESSING IN CASE OF BULK AS WELL AS POWDER MATERIALS FOR RELATIVELY THICK-SAMPLES

---

Introduction .....	65
<b>Part I:</b> Effects of processing conditions on heterogeneities in strain, microstructure and hardness in two bulk materials: aluminum alloy and commercial purity magnesium .....	68
3I.1 X-ray tomography (XRT) .....	69
3I.1.1 Gradient in shear deformation .....	69
3I.1.2 Strain analysis .....	71
3I.2 EBSD characterizations .....	75
3I.2.1 Aluminum alloy .....	75
3I.2.2 Commercial purity Mg .....	79
3I.3 Evolutions of microhardness .....	81
3I.4 Discussion .....	84

**Part II: HPT consolidation of two distinct Mg powders: Influences of nature of initial powder precursors on evolutions of microstructure, texture and strength** ..... 87

3II.1 Structural characterizations ..... 89

    3II.1.1 X-ray diffraction (XRD) ..... 89

    3II.1.2 SEM observations ..... 90

3II.2 EBSD and TKD characterizations ..... 95

    3II.2.1 Micro-HPT product obtained from atomized Mg ..... 95

    3II.2.2 Nano-HPT product obtained from condensed Mg ..... 98

3II.3 Microhardness evolution ..... 101

3II.4 Discussion ..... 105

    3II.4.1 Effects of severe plastic deformation through HPT ..... 105

    3II.4.2 Significance of MgO oxides ..... 108

Chapter's conclusions ..... 111

References ..... 113

## **Introduction**

Severe plastic deformation (SPD) techniques are well known for their effective potential to fabricate ultrafine-grained/nanocrystalline bulk materials with enhanced mechanical and functional properties for a large variety of metal systems. Among the existing techniques, equal-channel angular pressing (ECAP) [1.25] and high pressure torsion (HPT) [1.37] are the most attractive because they can incorporate very high strains without a significant change in the overall dimensions of the samples. Because of higher imparted equivalent strain, HPT processing outperforms ECAP to achieve nanostructured materials and produces higher fractions of high-angle grain boundaries [1.41]. Moreover, because of full confinement, “difficult-to-work” materials, for example, hcp metals show some additional plasticity without cracking if high hydrostatic pressure applied during torsional straining. Although the feasibility of the HPT processing is, in the vast majority of cases, restricted to fabrication of thin samples with thickness of around 0.8 mm [1.41,3.1-3.4], some recent studies have revealed that there have been significant structural heterogeneities across the disk-thickness when relatively thick samples are subjected to HPT [3.5-3.8]. In particular, Sakai et al. [3.5] have observed that one turn of revolution of a cylindrical sample of Al-Mg-Sc alloy with a diameter of 10 mm and a thickness of about 8 mm have induced a strong localization of shear deformation in the middle-plane around the periphery of the cylinder which resulted in evolution of higher microhardness and refinement of microstructures with grain size of  $\sim 200$  nm. Hohenwarter et al. [3.6] have observed the variation in microhardness across the thickness of Armco iron samples for different thickness to diameter (T/D) ratios under a hydrostatic pressure of 2.8 GPa up to 10 rotations. They claimed that a fairly homogeneous microstructure can be generated if the geometric ratio is carefully considered along with the material-dependent saturation strain.

Magnesium based alloys are generally produced by casting processes, which generate coarse and segregated microstructures; they are limiting the mechanical strength [3.9]. Also, the significant grain growth and residual porosities at high-temperature post-treatments - involving liquid phase - may adversely alter the materials properties. In contrast, the powder metallurgy (PM) process represents an effective way for mechanical improvement through the reduction in segregation scale, improvement in densification and microstructural refinement [3.10]. One of the major drawbacks for the PM process in Mg is the lack of ductility inherited from the presence of oxides at the surface of the powder particles which are difficult to remove during “conventional” sintering. Therefore, an additional plastic deformation step is generally required [3.11]. Among the plastic deformation processes, solid-state sintering through SPD techniques are the most desirable, offering real alternatives to the conventional press/sinter routes. Indeed, the particle-particle interactions during severe plastic deformation are mainly governed by shearing rather than diffusion to achieve required bonding, and thus can be carried out at much lower temperatures [3.12].

In this context, the present chapter deals with two important goals. In the first part, HPT processing was conducted on two bulk metals having fundamentally different crystallographic structures: a face centered cubic (fcc) Al alloy (A5086) and a commercial purity Mg of hexagonal closed-packed (hcp) symmetry. The HPT processing parameters were selected as such that it can bring some potential inhomogeneities within the HPT-samples for these two types of light materials. They were further analyzed for the improvements in mechanical properties.

The second part of this chapter involves on the HPT consolidation of two types of Mg powders: atomized micro-sized powder produced by inert-gas atomization, and condensed ultrafine powder synthesized by arc-plasma evaporation/condensation method. The morphology and microstructure of the powder particles were given in the section 2.1, **Chapter 2**. Since the initial powder particles are very different, it can be expected from the present study that the nature of the initial powder precursors influences the powder consolidation, and the associated developments in microstructure and mechanical properties in the two types of consolidated products. At the end, it will be possible to distinguish the various factors that may affect the deformation heterogeneities in the bulk as well as in the powder materials when subjected to HPT.

## **Part I: Effects of processing conditions on heterogeneities in strain, microstructure and hardness in bulk materials: aluminum alloy and commercial purity magnesium**

In this study, the HPT processing was carried out at room temperature under quasi-constrained conditions [1.37] using an HPT facility available at LEM3-Labex DAMAS. The disks with higher thickness than the regular HPT thin-disks were processed using a fairly sharp inclined lateral wall following the geometrical parameters of the anvil die described in [3.7]. Some disks were preserved after the compression stage for comparative studies. It was also estimated that the thickness of the disks after compression has been reduced by on average of 3.3% and 5.3% for Al alloy and Mg, respectively. Following HPT processing, X-ray tomography (XRT) was used to examine the quantitative deformation in 3D view with the help of an insert (solder alloy) by the difference in absorption contrast of the insert and the light metal matrix. Also, a set of characterization techniques coupling global (macroscopic) and local (microscopic) investigations such as SEM, EBSD were used to examine the inhomogeneities in strain gradients, and their consequences in evolutions of microstructure and hardness. The development of material strength was characterized by Vickers hardness measurements. The details of each characterization technique can be found in the section 2.3, **Chapter 2**.

### **3I.1 X-ray tomography (XRT)**

The deformation heterogeneities in the two different crystallographic structures upon severe plastic deformation through HPT process were mainly characterized by the XRT measurements. The XRT data was analyzed by using the Avizo<sup>®</sup> 3D software [2.6]. Figures 3.1 and 3.2 summarize the major findings obtained by the XRT measurements when using a solder pin to materialize the shear deformation and quantitatively estimate the local strain distributions for the two materials and the two HPT rotations.

#### **3I.1.1 Gradients in shear deformation**

A plan and side view of a HPT-disk processed at 180° rotation reconstructed from XRT data is shown in Figure 3.1(a). It is readily apparent from the plan and side views that the solder pin inserted into the HPT-disks before the HPT processing deforms significantly through its middle portion as compared to the top and bottom parts. A typical measurement of the pin-width at the middle section shows two times more materials spreading than that observed at the top and bottom parts suggesting a heterogeneous deformation across the thickness-height.

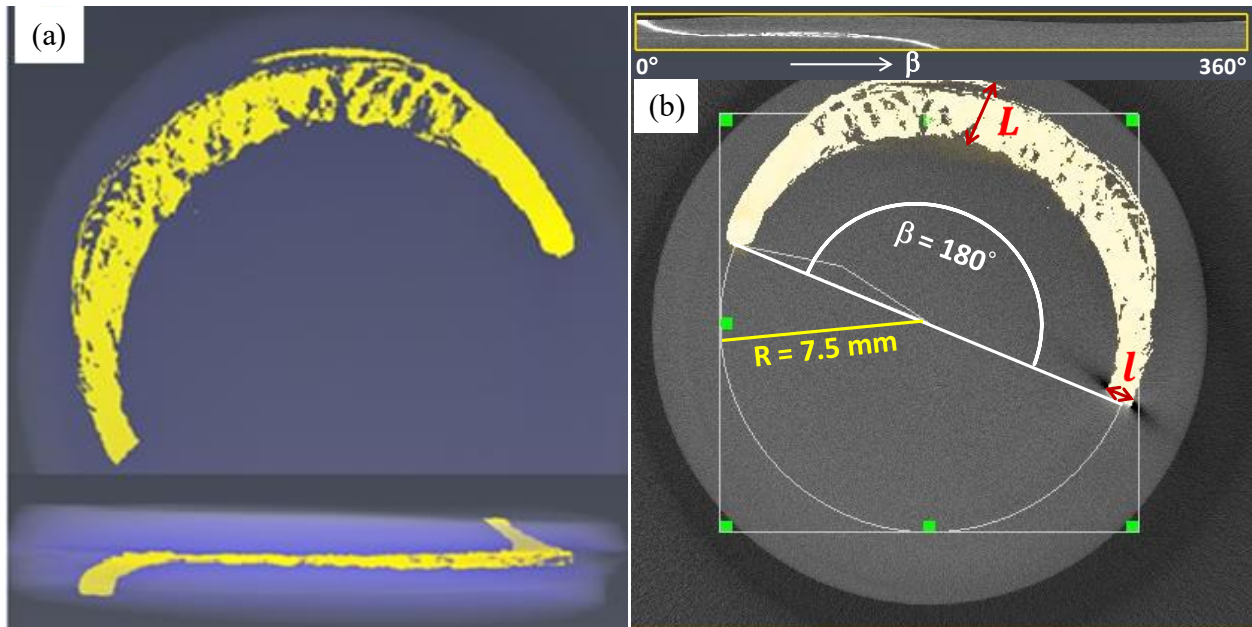


**Figure 3.1** – (a) Plan and side view of a 3D image of a HPT-processed disk delineating the trace of the pin after  $180^\circ$  rotation and (b) longitudinal (top) and cross-sectional 2D images obtained from the XRT analyses.

The longitudinal and cross-sectional 2D images developed by Avizo<sup>®</sup> 3D software are presented in Figure 3.1(b) for the same HPT-disk as shown in Figure 3.1(a). As can be asserted from the cross-sectional image,  $\beta$  depicts the tracing angle of the inserted pin. It is worthy to note from the Figure 3.1(b) that the tracing angle ( $\beta$ ) is related to the imposed torsional rotations, indicating no slippage occurred during the HPT processing. However, it is apparent that the shear deformation is severely localized in the middle planes, thus, presenting a deformation gradient between the top and bottom surfaces which is clearly depicted in the longitudinal image (top image of Figure 3.1(b)). During the torsion stage significant material loss happened through the formation of protrusions that were squeezed between the two anvils. As the material outflow could happen only in the middle section of the disk, significant deformation took place within the disk in its radial direction. This is why in the cross-sectional tomography image; the thickness of the insert is varying as a function of its position.

### **3I.1.2 Strain analysis**

The evolutions of shear strains across the thickness-height were evaluated by analyzing a small material volume as demonstrated in Figure 3.2(c). As can be seen from the figure, at a radial distance of 7.5 mm ( $= R$ ) and along the thickness of 2.7 mm ( $= h$ ) this material volume was selected for calculation of localized shear strains. It is possible to calculate the local shear strain  $\gamma(z)$  from the inclination of the deformed insert as a function of the axial position,  $z$ . From the schematic of a small material volume, one can write:

$$\tan(\alpha) = \gamma(z) \dots\dots\dots (1)$$

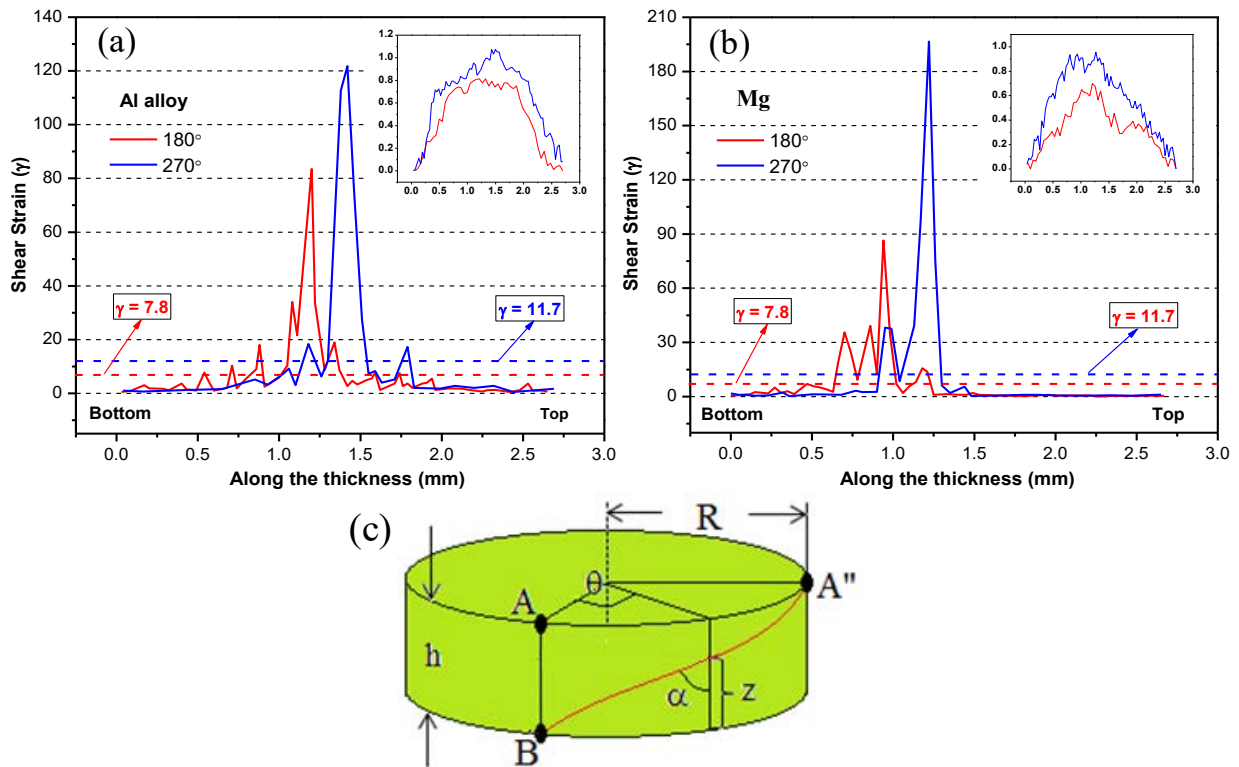


**Figure 3.2** – The distribution of strains across the through-thickness in (a) Al alloy and (b) Mg for 180° and 270° rotations. The distribution of the radial strains is also provided in the insets of (a) and (b), respectively. Figure 3.2(c) delineates a schematic diagram of a processed HPT-disk for the calculation of shear strain localization.

The distributions of the shear strain across the thickness-height are plotted in Figures 3.2(a-b) for both materials processed through 180° and 270° rotations. The horizontal dotted lines show the theoretical strains (7.8 and 11.7 for 180° and 270° rotations, respectively) for a homogenous distribution at the edge of the disk. It is apparent from the figures that there is a strong localization of the shear strain in the middle sections of the disks. Thus, a heterogeneous strain distribution is developed across the through-thickness in both materials. It can be seen from the shape of the curves that, for given processing conditions, the localization is always more intense in the Mg sample than in the Al alloy, and it is also restricted to narrower regions within the thickness of the samples. The maximum strain localization is obtained in the 270° Mg and is more than 16 times the average theoretical average strain.

The radial strain component can be calculated from the local radial diameter of the deformed insert. As can be noticed from the cross-sectional image of Figure 3.1(b), on the top and bottom planes of the disk, the pin diameter is  $l$ , while it is larger at any other position,  $L$ . The logarithmic radial strain is then obtained as:

$$\varepsilon = \ln(L/l) \dots\dots\dots (2)$$

The strain distributions in the radial direction are demonstrated in the insets of Figure 3.2(a) and 3.2(b) for the Al alloy and Mg, respectively. They show a maximum value up to about 1.0 in the middle section of the Al alloy disk.

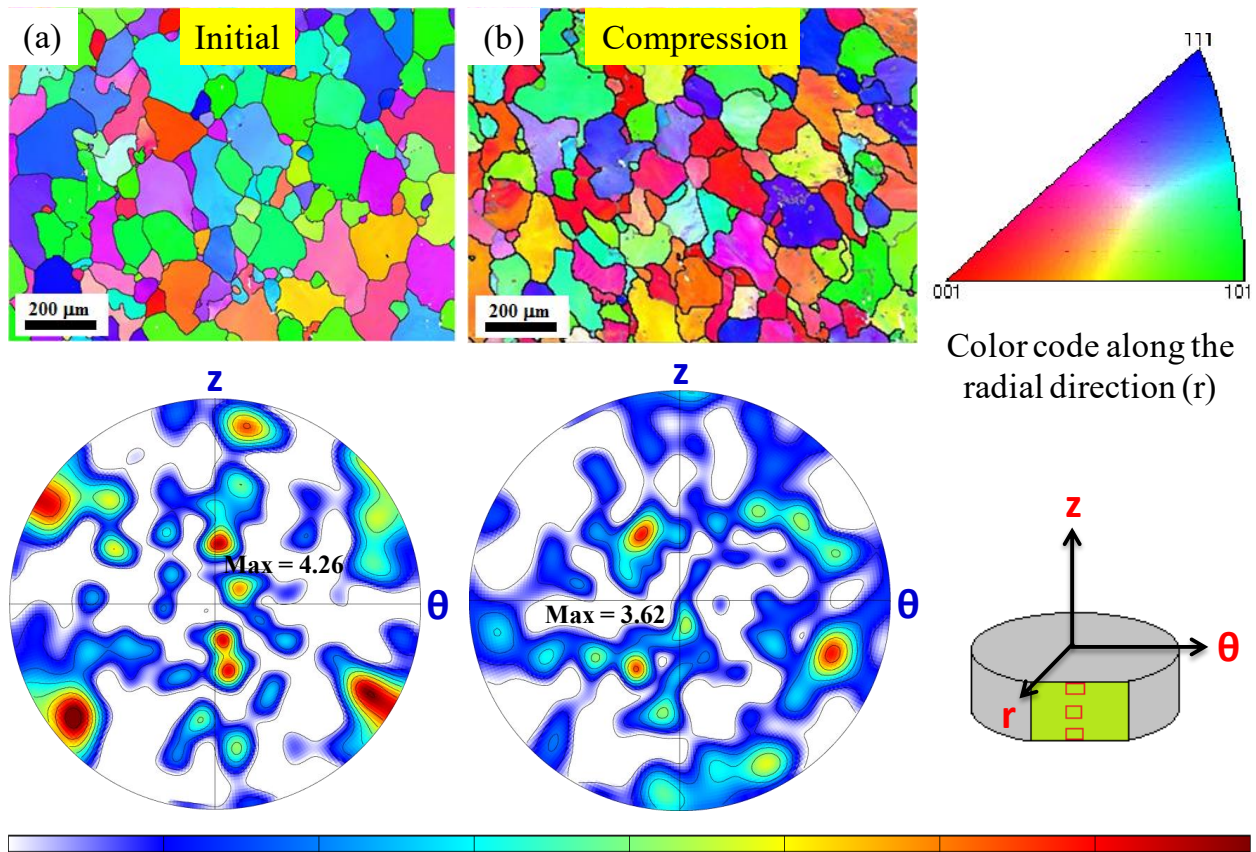


**Figure 3.3** – EBSD orientation maps and the corresponding (111) pole figures for the (a) initial specimen and (b) after simple uniaxial compression by 3.3% in the Al alloy.

## **3I.2 EBSD characterizations**

### **3I.2.1 Aluminum alloy**

The orientation maps and the corresponding pole figures are presented in Figures 3.3 and 3.4. The initial Al alloy displays an equiaxed microstructure with an average grain size of 130  $\mu\text{m}$  (Figure 3.3(a)) and a fairly weak texture. After 3.3% compression (Figure 3.3(b)) the texture is still weak and the grain interiors show orientation gradients due to the imposed plastic strain.

The microstructure changes significantly after HPT processing through 270° (see Figure 3.4). It is worthy to mention here the differences in the scale bars in these orientation maps. At all four examined positions of the disk, a refined microstructure can be seen. The refinement is less developed in the center region of the disk where the shear strain is the smallest (Figure 3.4(a)). At the outer region the grain refinement is extensive; the smallest grain size is obtained in the middle plane of the sample, in agreement with the largest shear strain at this location (Figure 3.4(c)). Here the average grain size is only 275 nm and the grains are elongated along the shear direction.

3 (Part I): Chapter Effects of processing conditions on heterogeneities in strain, microstructure and hardness in bulk materials: aluminum alloy and commercial purity magnesium

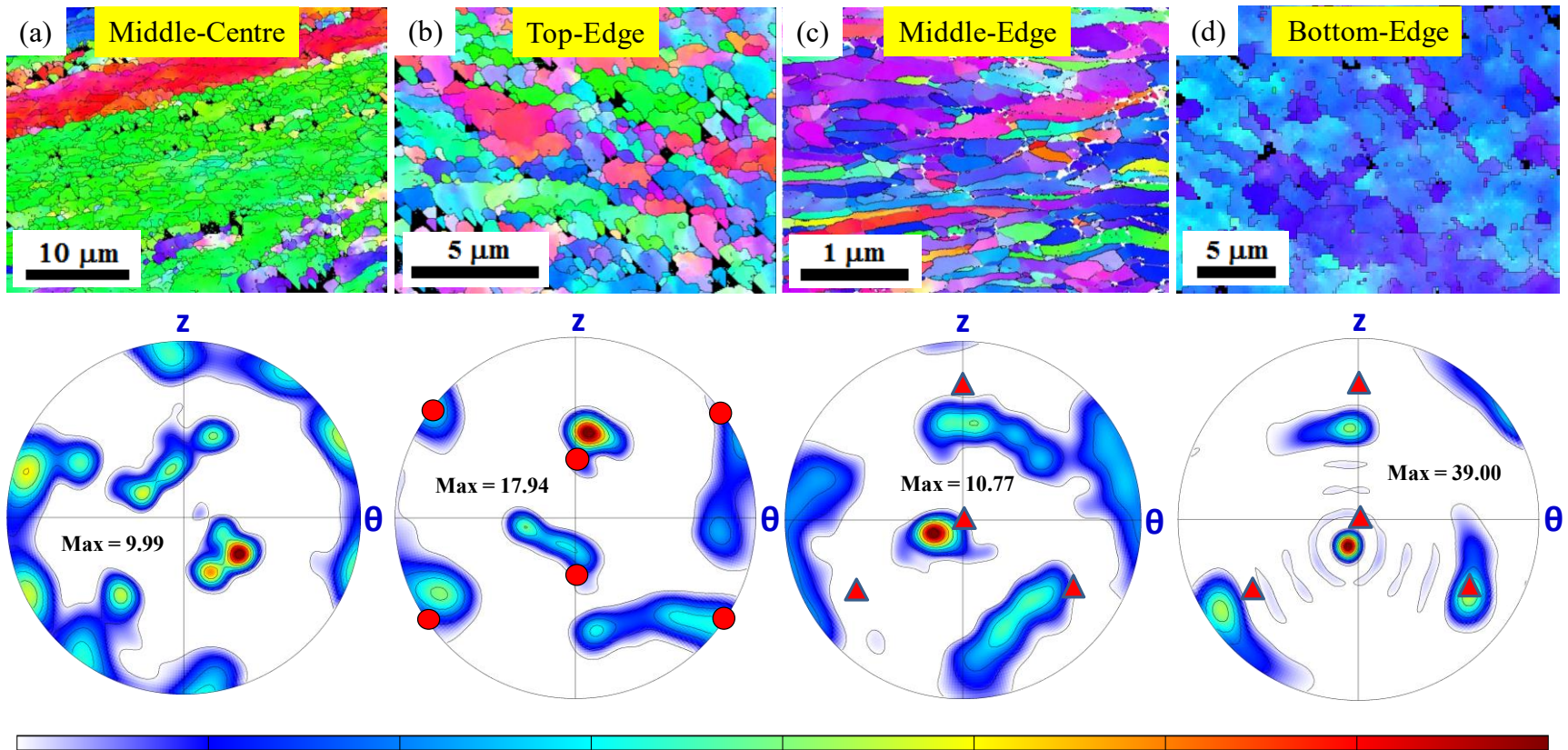


**Figure 3.4** – EBSD orientation maps of HPT-processed (270°) Al alloy and the corresponding (111) pole figures obtained (a) at the centre of the disk on its middle plane, and at the edge of the disk on its (d) top, (e) middle and (f) bottom sections. The location of the C (red circles) and B (red triangles) ideal orientations of fcc simple shear textures are also shown. Note the differences in scale bars.

The corresponding textures depicted in the (111) pole figures do not show typical shear textures for the simple reason that the number of observed grain orientations are not sufficient to reach the satisfactory statistics that is necessary to obtain representative textures. Most of the orientations are concentrated around a small number of texture components which are not necessarily in ideal positions. This is due to the small area size studied in EBSD where the refined microstructure is originating probably from just a few initial grains. Nevertheless, distinct features can be seen in the pole figures in the top and middle positions as shown in Figure 3.4(b) and 3.4(c), respectively. In case of the top plane, nearly an ideal C component seems to be developed while in the middle position, an orientation near the B ideal component of shear textures can be seen with large orientation spread around the radial direction of the sample; the direction of the orientation spreading is the same as the applied rigid body rotation of simple shear. At the bottom, the grain orientations are also near to the B component, and show a similar spreading approximately around the rigid body rotation axis. These ideal orientations are defined by: B:(11 $\bar{2}$ )[1 $\bar{1}$ 0], C:(100)[0 $\bar{1}$ 1] and are characteristic components of the shear textures in aluminum [3.13].

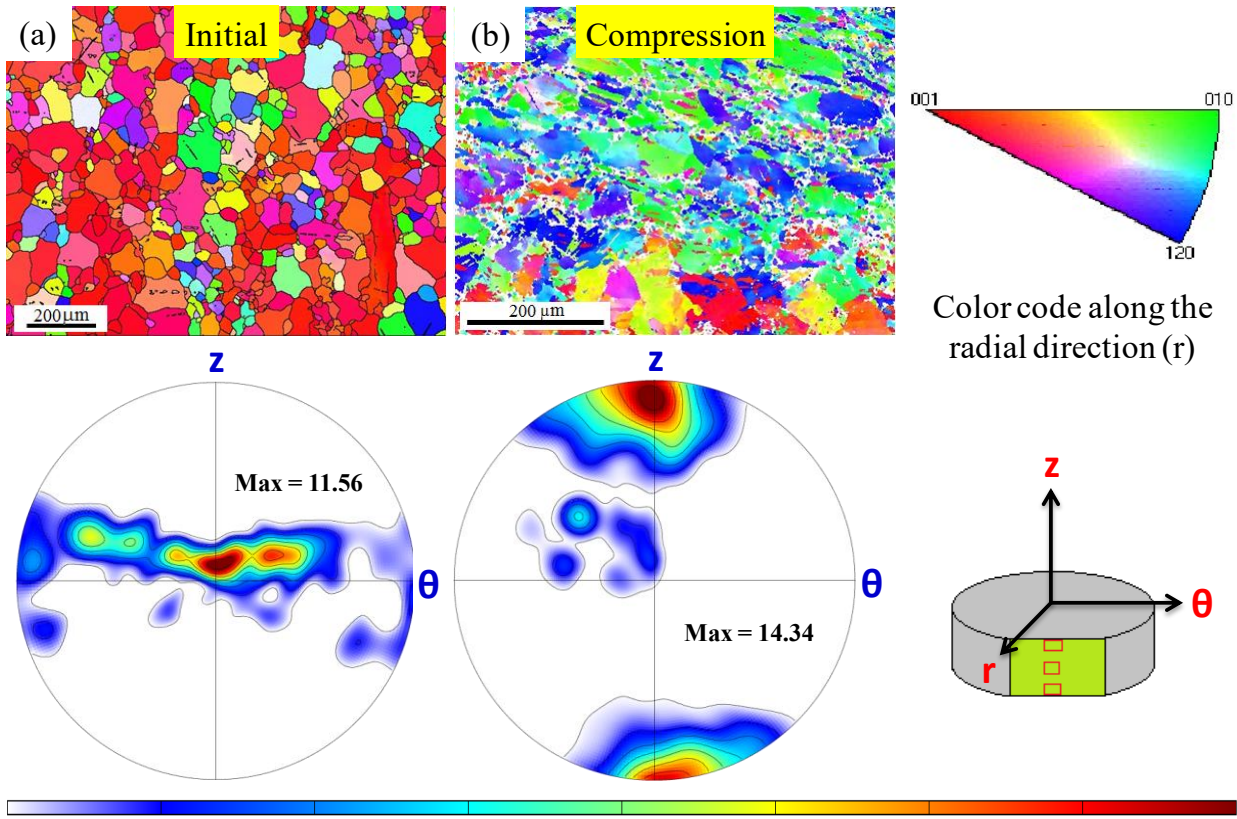


**Figure 3.5** – EBSD orientation images and the corresponding (0002) pole figures for the (a) initial specimen and (b) after simple uniaxial compression by 5.3% in the commercial purity Mg.

### **3I.2.2 Commercial purity Mg**

The EBSD micrographs and the localized microtexture are displayed in Figures 3.5 and 3.6 for the different experimental conditions. Figure 3.5(a) depicts an equiaxed microstructure of the initial extruded Mg with an average grain size of 65  $\mu\text{m}$  and its microtexture can be characterized by a basal fiber texture with  $c$ -axis perpendicular to the extrusion direction (ED), where  $z$  direction and ED are parallel. As can be seen in Figure 3.5(b), a completely twinned microstructure is developed upon 5.3% uniaxial compression. The texture seems to be rotated by  $90^\circ$  which is the result of massive twinning. Indeed, in compression of Mg, the most frequent twinning system is extension twin which rotates the original grain orientations by  $86^\circ$ .

During subsequent twisting of the disk under a hydrostatic pressure of 1.2 GPa, a heterogeneous microstructure developed (Figure 3.6). Please note again the differences in size of the microstructures and the related scale bars. At the center of the disk processed by HPT, Figure 3.6(a) displays similar kinds of features than after compression, in particular a heavily twinned microstructure. Figures 3.6(b-d) depict the orientation maps obtained at the outer edge of the disk at the top, middle and bottom sections, respectively. Here, the  $270^\circ$  HPT rotation has generated significant differences in the local microstructural aspects. While there is limited evidence of further grain refinement in the top external position (Figure 3.6(b)), some more significant fragmentation took place at the bottom, Figure 3.6(d). The most refined microstructure is displayed in the middle external part (Figure 3.6(c)) where about 2  $\mu\text{m}$  equiaxed grains are present.

3 (Part I): Chapter Effects of processing conditions on heterogeneities in strain, microstructure and hardness in bulk materials: aluminum alloy and commercial purity magnesium

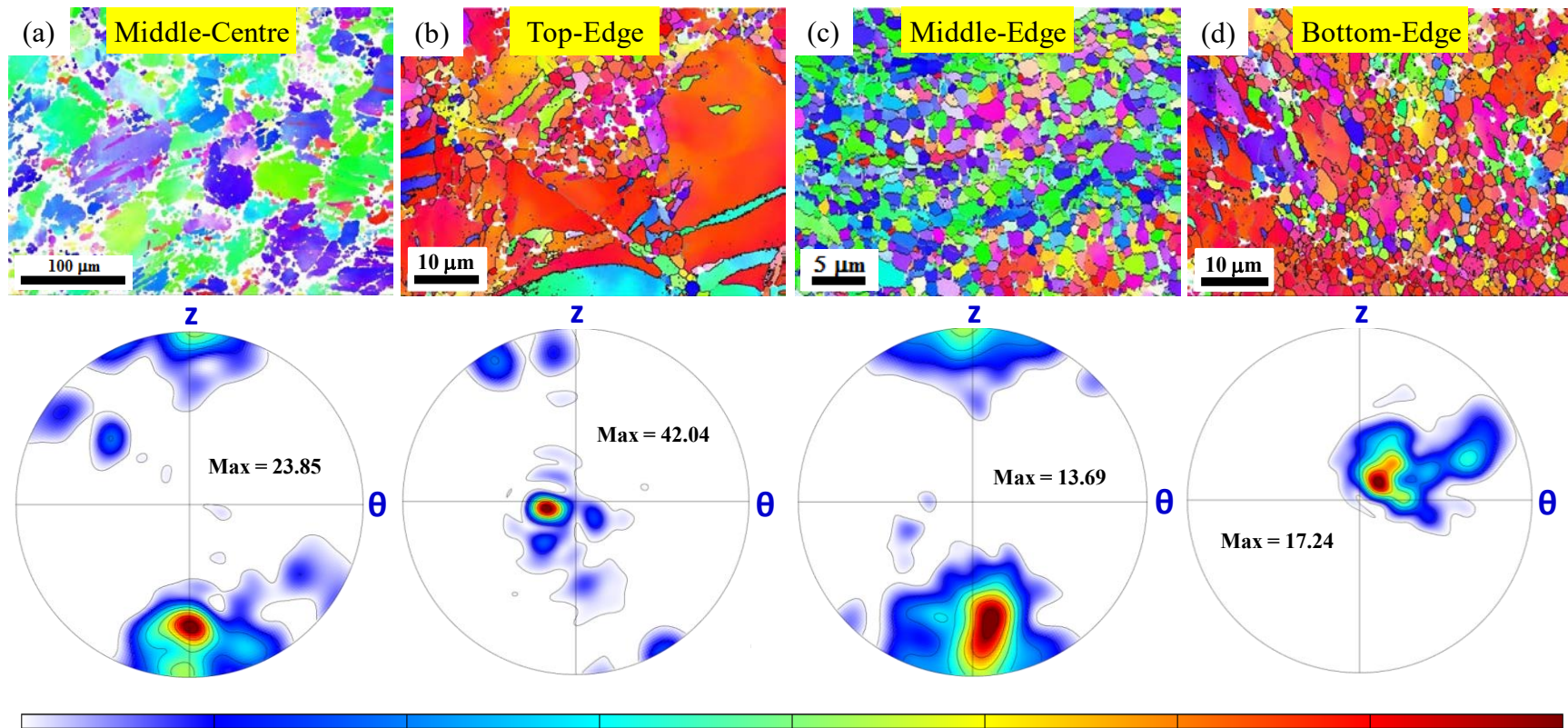


**Figure 3.6** – EBSD orientation maps of the HPT-processed ( $270^\circ$ ) commercial purity Mg and the corresponding (0002) pole figures obtained (a) at the centre of the disk on its middle plane, and at the edge of the disk on its (b) top, (c) middle, and (d) bottom sections. Note the differences in scale bars.

While the number of analyzed grains was not sufficient to evaluate the textures at the top and bottom positions, there are enough grains in the middle position to consider the corresponding pole figure statistically acceptable. At that position the texture is a *B* fiber which is a characteristic stable texture under simple shear of Mg [3.14]. The high indexing rate in the EBSD map suggests that a limited amount of dislocations was stored in these fine grains. Thus, from the aspect of the microstructure and the local texture analysis, it is very clear that the microstructure at the middle-edge of the Mg disk has undergone a dynamic recrystallization process during the large shear deformation imparted during the HPT processing.

### **3I.3 Evolutions of microhardness**

Vickers microhardness measurements were conducted across the through-thickness as well as along the radial direction of the HPT-disk where the positions selected for measurements can be found from Figure 3.7(e). The average values of microhardness after HPT for the top, middle and bottom planes of the disks are displayed at four radial positions in Figure 3.7(a) and 3.7(c) for the Al alloy and Mg, respectively. For comparison, the hardness values of the initial sample (dashed lines) and after the compression stage (see Figures 3.7(a, c)) are also shown. It is clearly visible that, even after the initial compression stage, the hardness values increases from the center to the periphery of the compressed disk. This is consistent with other results from the literature which showed both from modeling and experimental approaches that the central regions are less deformed than the outer ones in the compressed state which results in different dislocation densities [3.15].

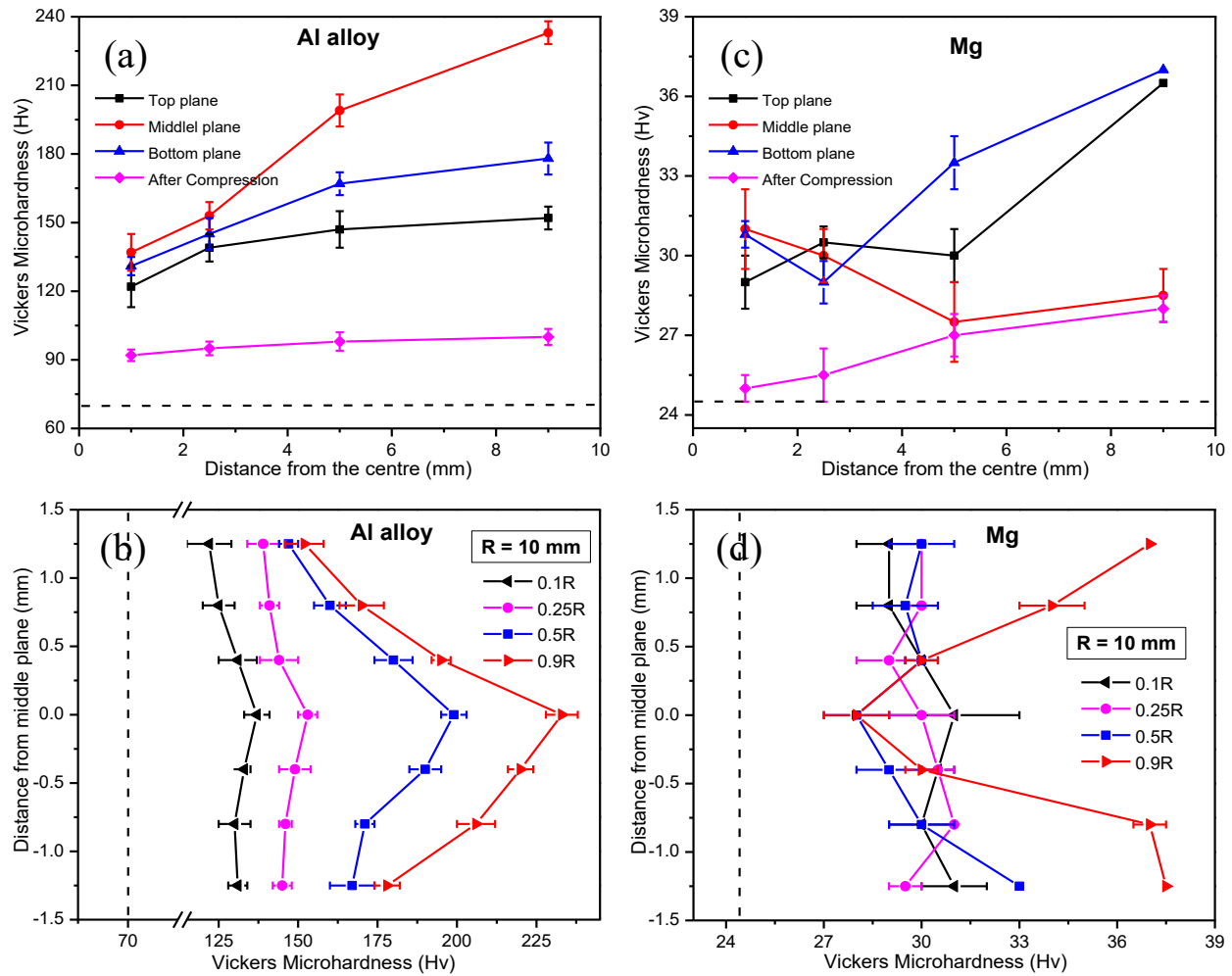


**Figure 3.7** – Distributions of Vickers microhardness in the radial direction (a, c) on the top, middle and bottom planes; and in the axial direction (b, d) across the disk-thickness in Al alloy (a-b) and Mg (c-d).

From the results obtained here, it is worthy to note that the magnitude of this radial hardness gradient after compression is much more important for the hcp Mg than for the fcc Al alloy. After HPT by 270° rotation, it is apparent from the figures that the microhardness generally monotonically increases from the centre to the edge of the disks on the top and bottom planes. Exception is the middle plane of Mg, where it decreases from the centre to the edge of the disk. The distributions of the microhardness in the axial direction are also depicted in Figures 3.7(b, d). There are two characteristic features in these figures: (i) the variations in microhardness across the through-thickness are more prominent at the outer edge of the disk in both materials, and (ii) in the middle plane the microhardness is higher in the outer region, except for Mg, where it is smaller with respect to the top and bottom planes. The present results for the Al alloy are consistent with the results obtained for long cylindrical samples as reported by Sakai et al. [3.5].

### **3I.4 Discussion**

As it is well known that the hardness and microstructure inhomogeneities are strongly influenced by the processing parameters and geometries [3.6,3.7] but tend to decrease when increasing the number of HPT turns [3.16]. The formation of a dead metal zone during HPT processing is the primary experimental factor that affects the strain inhomogeneity along the thickness direction. This undeforming zone within the HPT disk is mostly determined by: (i) the angle of the inclined lateral wall and (ii) the depression depth of the HPT anvil. We recall that the present comparative analysis for strain heterogeneity was carried out under "critical" processing conditions: for fairly thick samples in an anvil having a low angle of lateral walls ( $15^\circ$ ) and a fractional number of turns ( $180^\circ$  and  $270^\circ$ ).

Two major components of the strain state could be obtained quantitatively from the local shape change of the pin which was detected by X-ray tomography measurements; the shear strain and the radial tensile strain (see Figure 3.2). Both of these components showed a gradient with high values in the middle section of the disk. The variations in the radial strain component can be clearly related to the material outflow which was taking place in the middle section of the disk. Such a material flow necessarily creates a radial tensile strain in the disk. It seems plausible that this radial strain localization favors the localization of the shear strain as well. Huge shear strains were measured in the middle section, many times more than the expected homogeneous strain. For similar processing conditions, these shear strains were always more important for the hcp Mg material; reaching even 16 times the expected strain for the  $270^\circ$  rotation condition. The evolution of hardness after the initial stage of compression also indicates the formation of stronger heterogeneities in the hcp Mg sample. To this respect, it is interesting to mention that, in

an attempt to process the commercial GW103 and AZ91 Mg alloys at room temperature under the same "critical" experimental conditions, the strain concentration at the center of the samples was such that the top and bottom parts of the disk were hardly deformed while intense shearing occurred at the mid-thickness, creating flow localization and cracking along the radial plane. These results clearly demonstrate the easiest development of strain inhomogeneities in hcp Mg (and in particular its alloys), and are consistent with previous results reported in [3.4].

The consequence of the strong strain localizations was visible in the evolution of the microstructures (Figures 3.4 and 3.6) while the material strength was monitored by Vickers hardness measurements (Figure 3.7). In both materials, grain refinement took place due to the imposed severe plastic deformation but the two materials have responded differently at the highest level of strain. For the Al alloy, grain refinement took place and hardening increased rather monotonically with the local strain. In the middle section, the grain refinement process reached the steady state due to the extreme large strains. In the outer section, grain sizes as low as 275 nm were reached in the Al alloy. The occurrence of steady state at very large shear strains is a well-known mechanism during plastic deformation by the SPD processing [1.41,3.2,3.17] where the grain size, crystallographic texture and the flow stress remains constant. When evaluating the relative influence of pressure and torsional strain on processing by high-pressure torsion an Al-6061 alloy, Xu et al. [3.16] found an increase in hardness due to an increase in the applied pressure (from 1.25 GPa to 4 GPa) while, in contrast, the final hardness at the periphery of the discs appeared to be almost independent of the applied pressure. Similarly, when studying an Al-5483 alloy processed by HPT over 5 turns, Bazarnik et al. [3.18] found that the microstructure and hardness were influenced by the applied pressure to a minor extend.

Comparatively, for Mg, it has been found that the flow stress did not increase monotonically with strain and the micro hardness dropped in the middle section of the disk. This behavior can be attributed to the localized extremely high shear strain in the middle plane which has induced dynamic recrystallization (DRX). The signature of the DRX in the microstructure is the presence of equiaxed grains (see Figure 3.6(c)) and the absence of elongation in that part of the disc despite the large shear strain. Edalati et al. [1.41] also reported the presence of equiaxed grains and a softening in pure Mg after HPT processing through more than 1 revolution. This softening at the large shear strains is a well-known phenomenon in pure Zn, Al and Mg metals [1.41,2.5], which is followed by a steady-state condition.

While the lowering of microhardness in the middle plane of the Mg disk can be ascribed to the DRX witnessed by the presence of a rather equiaxed microstructure, it is interesting to note that, for the Al alloy, an elongation of the grains is clearly visible (Figure 3.4(c)) but with a much less ratio than what would be expected from the large shear value. We believe that this reduction in the shape elongation is due to combined effects of grain fragmentation and elongation by strain. The new grain fragments are nearly spherical when they are formed and elongate to a limited extent due to further deformation until they become fragmented, too. The grain refinement by fragmentation at extreme large strains itself is a DRX process [3.19]. The speed of this process is certainly higher in Mg, which can explain the nearly spherical grain shape in the middle section of the Mg disk. In contrast, in the Al alloy, the fragmented grains can elongate substantially during further shear. This difference is due to the metallurgical state of the Al alloy which contains precipitates.

## **Part II: HPT consolidation of two distinct Mg powders: Influences of nature of initial powder precursors on the evolutions of microstructure, texture and strength**

Two kinds of Mg powder precursors - atomized micro-sized Mg powder and condensed ultrafine Mg powder - were separately consolidated by the two-step HPT facility at room temperature. The details of this two-step HPT procedure were presented in the section 2.2.3, **Chapter 2**. The powder was first compressed into an intermediate disk with 20 mm in diameter and 3 mm in thickness by uniaxial compression under a pressure of 1.5 GPa and a holding time of 10 min. Subsequent torsional straining was conducted by HPT on the pre-compacted disks under a pressure of 1.2 GPa. The final step was conducted under quasi-constrained conditions where the materials lateral flow is partially restricted [1.37]. The torsional straining was imposed by rotating the lower anvil at 0.125 rpm for up to 2 revolutions. A total maximum shear strain ( $\gamma$ ) of about 42 was estimated at the periphery of a disk for the 2 turns HPT samples. In the subsequent sections, these consolidated products are designated as micro-HPT and nano-HPT products according to their original powder precursors: the atomized micro-sized powder and the condensed ultrafine powder, respectively. The HPT-products were analyzed by a combination of several characterization techniques such as XRD, SEM, FIB, EBSD, and SEM-TKD. The development of material strength was characterized by Vickers hardness measurements. The details of each characterization technique can be found in the section 2.3, **Chapter 2**.

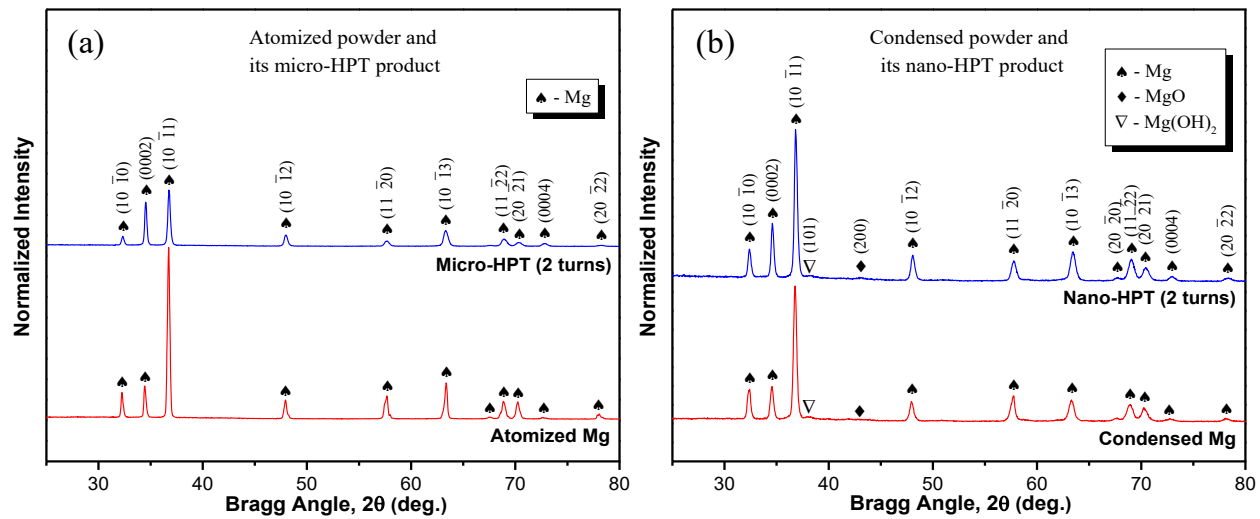


**Figure 3.8** – Normalized X-ray diffraction (XRD) patterns recorded on the initial powder precursors and their HPT-products: (a) atomized Mg powder and its micro-HPT product, and (b) condensed Mg powder and its nano-HPT product.

**Table 3.1** - Phase compositions and crystallographic parameters for the two types of consolidated products determined from the XRD profile refinement.

Samples	Mg (wt%)	MgO (wt%)	Mg(OH) <sub>2</sub> (wt%)	Lattice constants (nm)	Intensity ratio ( $I_{0002}/I_{1010}$ )
Atomized Mg	100	-	-	$a = b = 0.3208 \pm 2e4$ $c = 0.5209 \pm 3e4$	$1.24 \pm 0.15$
2 turns micro-HPT	100	-	-	$a = b = 0.3200 \pm 3e4$ $c = 0.5192 \pm 2e4$	$4.11 \pm 0.17$
Condensed Mg	93	5	2	$a = b = 0.3207 \pm 3e4$ $c = 0.5206 \pm 3e4$	$1.08 \pm 0.16$
2 turns nano-HPT	92	5	3	$a = b = 0.3194 \pm 2e4$ $c = 0.5185 \pm 4e4$	$1.73 \pm 0.19$

## **3II.1 Structural characterizations**

### **3II.1.1 X-ray diffraction (XRD)**

Figure 3.8 compares the XRD patterns of the initial powder precursors to their HPT-consolidated products. The phase compositions and crystallographic parameters were determined from the XRD profile refinement by using the JADE software [2.8] and the Reference Intensity Ratio (RIR) method [2.9], and the results are given in Table 3.1. Besides the major contribution from hexagonal Mg in all XRD profiles, a minor peak of MgO is also detected for the condensed powder and its nano-HPT product, Figure 3.8(b). The amount of oxides in the condensed powder and its nano-HPT product was estimated to be 5 wt% (Table 3.1). In addition, a trace amount of Mg(OH)<sub>2</sub> was also identified through its (101) reflection in the condensed powder and its nano-HPT product. This phase along with MgO oxide might have formed during the controlled passivation process conducted in the mixture of Ar + normal air. In contrast, the atomized powder and its micro-HPT product did not show such kinds of additional peaks (see Figure 3.8(a)), which may be due to the lower surface area available for such "contamination".

The lattice parameters of the Mg phase determined for the initial powders and their HPT-products are provided in Table 3.1. The results reveal that the lattice constants of the Mg phase in the condensed powder were:  $a = b = 0.3207$  nm and  $c = 0.5206$  nm, while the parameters for its nano-HPT product were  $a = b = 0.3194$  nm and  $c = 0.5185$  nm. Considering the associated errors, the differences in the lattice parameters indicate that there might have been some lattice distortions in the Mg crystal structure during the intense shear straining by HPT, which could have been further increased due to the presence of the hard MgO particle interfaces in the nano-HPT product. However, these changes in the lattice parameters seem to be less pronounced in the

case of micro-HPT product obtained from the less contaminated atomized powder (atomized Mg:  $a = b = 0.3208$  nm and  $c = 0.5209$  nm and its micro-HPT product:  $a = b = 0.3200$  nm and  $c = 0.5192$  nm). Furthermore, it is interesting to notice from Table 3.1 that the HPT consolidation of the powder precursors led to significant differences in their peak intensities. For example, there are considerable differences in the peak intensity ratio of (0002) to ( $10\bar{1}0$ ) planes before and after HPT processing. This ratio increased significantly after HPT processing of the micro-sized powder while the increment is not significant for the nano-HPT counterpart. The discrepancy in the peak ratios imply the development of different kinds of textures after shear straining through HPT when different types of powders are used.

### **3II.1.2 SEM observations**

Keeping in mind that the products sintered by HPT consolidation for relatively large thicknesses, such as used in the present study, can be characterized by significant microstructural heterogeneities within their thickness-height [3.8], the SEM study was conducted at the periphery and across the disk-thickness. Typical SEM micrographs obtained under backscattered electron (BSE) imaging conditions are displayed in Figure 3.9. These images essentially compare the developments of microstructure at the periphery and within the thickness-height for the micro-HPT product, Figures 3.9(a-c) and for the nano-HPT product, Figures 3.9(d-f).

In the micro-HPT product consolidated from the atomized powder particles, the microstructure at the middle-section of the HPT-disk displays a recrystallized equiaxed grain-structure, Figure 3.9(b). This observation is consistent with the results obtained in the previous section for such a thick-sample in the bulk materials, where shear strain was extremely localized in the middle-thickness [3.20]. This localization of the shear strain induced dynamic recovery/recrystallization processes, and thus resulted in an average grain size of about 0.5 to 1  $\mu\text{m}$ . In contrast, the top and bottom parts of the micro-HPT disk exhibited fairly heterogeneous microstructures with some deformation-unaffected local domains (Figures 3.9(a, c)). This is clearly visible, for example, by the presence of inter-particle oxide layers (as shown by the arrows) that witness the presence of poorly deformed atomized powder particles. Some grains are rather ill-defined in these regions, while others are well visible within the original particle boundaries, suggesting a wide range of grain size distributions (i.e.  $\sim 0.5 \mu\text{m}$  to  $1.5 \mu\text{m}$ ). Since the presence of the MgO phase was not detected by the XRD measurements for the atomized powder (Figure 3.8(a)), it is possible that the oxide content was so small that it did not give rise to any XRD signal under the applied experimental conditions.

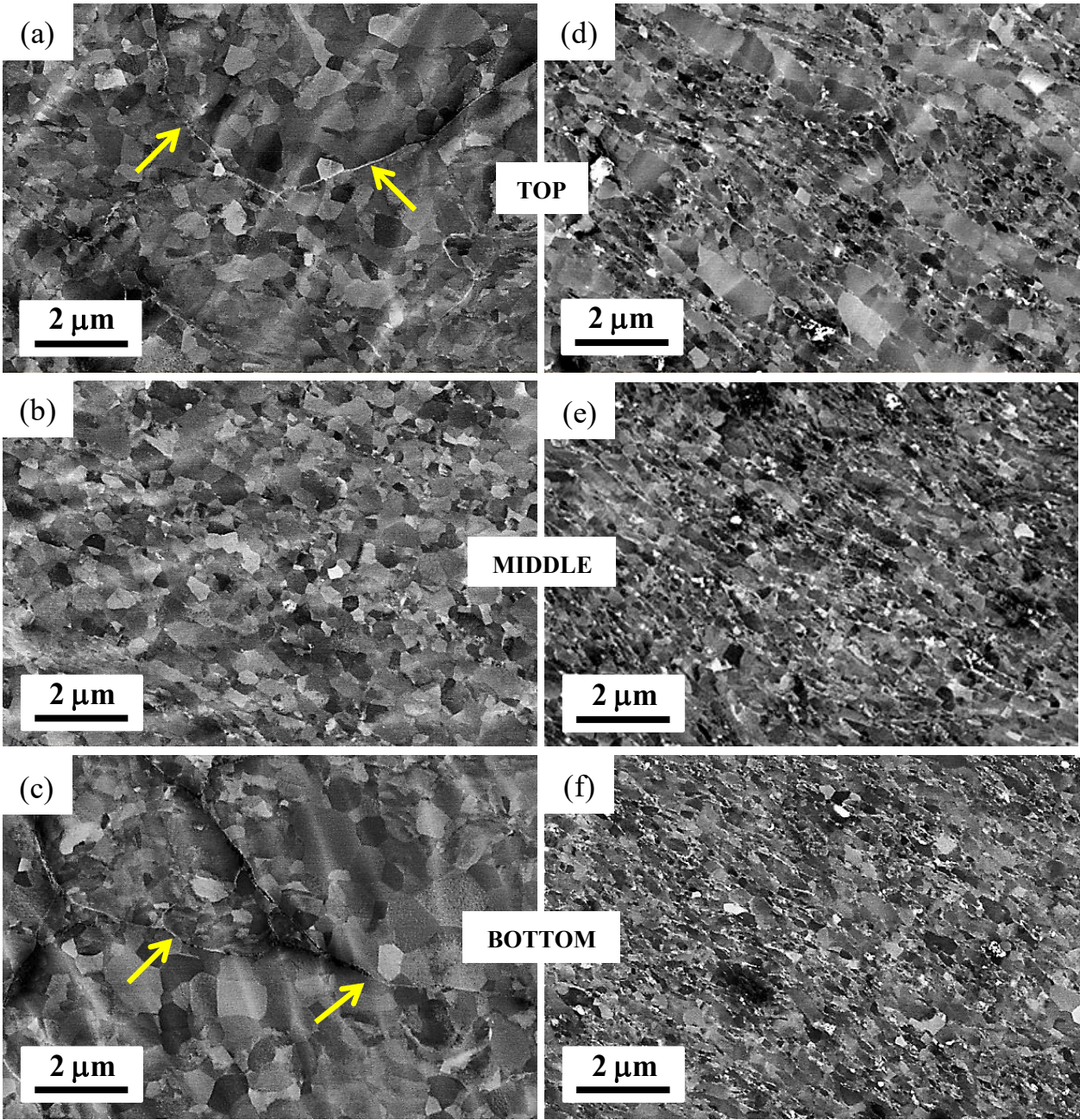


**Figure 3.9** – SEM backscattered electron micrographs acquired at the outer-edge and across the through-thickness of the 2 turns HPT-disks for (a-c) micro-HPT product and (d-f) nano-HPT product.

In the case of the nano-HPT product, it is readily apparent from the right-side images that the whole sample was rather homogeneously deformed towards the formation of slightly elongated domains across the disk-thickness, Figures 3.9(d-f). However, the microstructure at the bottom part seems to be more fragmented than the other parts of the sample, so a gradient-microstructure developed across the thickness-height. Since the ultrafine powder particles were coated with a thin layer of MgO oxides, it is thereby reasonable to anticipate that these oxide layers were extremely sheared and/or sometimes fragmented into fine particles (appeared as white spots under BSE imaging conditions). Also, it is interesting to notice that some of these oxide layers were aligned with the grain boundaries that were essentially inclined at about 45°. Figure 3.10 gives a FIB micrograph obtained from the middle-section of the nano-HPT disk sample prepared for TKD measurements. The microstructural features in the FIB image were well consistent with the SEM observations. It is interesting to note that this micrograph clearly shows some residual porosity (as shown by the arrows) even after 2 turns of the ultrafine powder particles. It may imply that the densification of the nano-HPT product was not completely achieved.

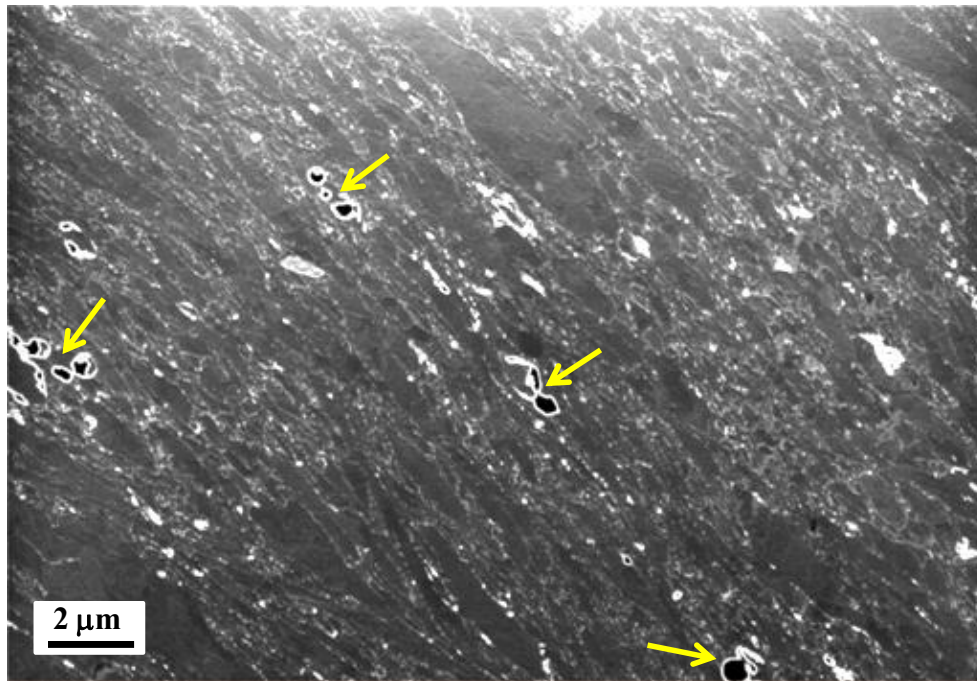


**Figure 3.10** – In-situ FIB micrograph of the nano-HPT product recorded during the foil preparation for TKD measurements. Arrows indicate the vacancies left after the 2 turns HPT consolidation of condensed Mg powder.

## **3II.2 EBSD and TKD characterizations**

In order to gain some insights into the HPT consolidation deformation behavior of the Mg powder particles, some additional samples were processed at lower level of shear strains (i.e.  $N = 1/2$  and  $3/4$ ) for both powder systems under identical experimental conditions. Grain orientation mapping for the deformed samples was carefully acquired by using a normal EBSD technique for the micro-HPT product, while a SEM-based TKD technique was utilized for the nano-HPT product due to their nanostructural features. The local EBSD and TKD measurements were carried out at the periphery and on the middle-thickness of the HPT-disks, and the corresponding results are described in the following subsections for the two types of consolidated products.

### **3II.2.1 Micro-HPT product obtained from atomized Mg**

The EBSD orientation maps accompanied with grains misorientation distribution and microtexture for the micro-HPT product deformed up to  $1/2$ ,  $3/4$  and 2 turns are given in Figure 3.11. A schematic diagram of an HPT-disk showing the location and the acquisition direction of the EBSD measurements for all samples is provided in the inset of Figure 3.11(b). The color code in the inset of Figure 3.11(e) refers to the crystallographic directions parallel to the normal direction of the sample surface. Furthermore, it should be noted that low-angle grain boundaries (LAGBs,  $> 3-15^\circ$ ) and high-angle grain boundaries (HAGBs,  $> 15^\circ$ ) were denoted by white and black lines, respectively, in all EBSD maps.

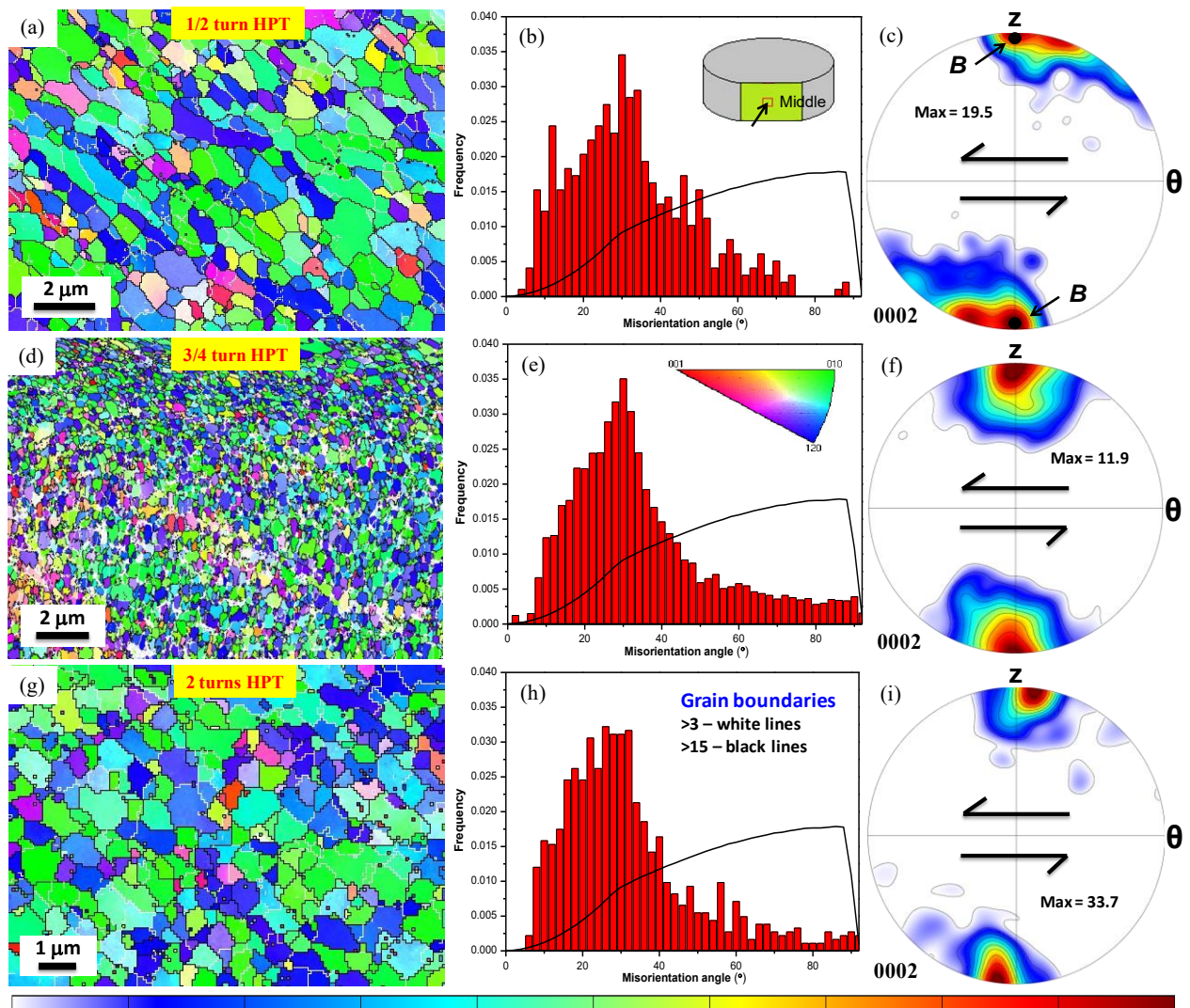


**Figure 3.11** – EBSD orientation images accompanied with grain boundary misorientations and associated microtexture in (0002) pole figure for the 1/2 turn (a-c), 3/4 turn (d-f) and 2 turns (g-i) micro-HPT product, acquired at the outer edge and middle-section of the HPT-disks (see the inset of Figure 3.11(b)). The Mackenzie distribution of misorientation angles (uncorrelated) is plotted by solid black line. Note the differences in scale bar.

The HPT consolidation of atomized powder only up to 1/2 turn has led to the formation of recovered/recrystallized microstructures (Figure 3.11(a)). The grains were elongated at an inclination angle of about 45° from the direction of imposed shear. Figure 3.11(b) gives the grain misorientation angle distribution. A high frequency of medium-angle boundaries can be noticed in the early stages of HPT processing, which is pronounced at around 30°, and can be attributed to the development of a basal fibre texture in Mg materials [3.21]. Moreover, it appears that the LAGBs are basically limited within the elongated grain domains indicating a close orientation relationship between the neighboring grains, which can be further appreciated from the color gradients within the original grain boundaries. This clearly suggests that at this stage of deformation the grain-structure was only partially recovered from its highly deformed state due to dynamic recovery/recrystallization processes, well-known for deformation of materials at low homologous temperatures, such as pure Zn, Al and Mg metal systems [1.41,2.5,3.20].

Figure 3.11(c) presents the evolution of microtexture in (0002) pole figure after 1/2 turn. It is readily apparent that there is a strong *B* fibre, which is the main ideal fibre of hexagonal simple shear textures [3.14]. It has been observed previously that upon free-end torsion [3.14], or in HPT processing [3.3] of pure Mg, the *c*-axis - initially aligned with the shear plane - basically rotates by 90° to become parallel with the torsion axis. In the present study the *c*-axes of the grains in the powder sample are initially randomly oriented and similarly become significantly aligned with the shear plane normal due to the large shear strain (of about 10 for 1/2 revolution).

Further torsional straining by 3/4 and 2 turns led to recrystallized microstructures accompanied with equiaxed grain-structures, Figures 3.11(d, g). The elongated shape of the

grain-domains after 1/2 HPT turn was transformed into equiaxed grain-structures in the 3/4 turn HPT-product, while the well-defined equiaxed grain-structures in the 2 HPT turns product were inclined at 45° from the shear plane, Figure 3.11(g). These microstructural features are suggesting that the generation of equiaxed microstructures - particularly at the middle-portion - can be associated with the occurrence of complete dynamic recrystallization [3.20]. The average grain size for these microstructures was in the range of 0.5 to 1 μm for 3/4 turn HPT product and 1 to 1.5 μm for 2 HPT turns product. The frequency distribution of grain misorientation shown in Figures 3.11(e, h) for the 3/4 and 2 turns infers that most of the grain boundaries were concentrated at around 30°, which also supports the occurrence of a dynamic recovery/recrystallization process. In the case of the 2 HPT turns product, the shear texture component appears tilted from its ideal position. The sense of this tilt is opposite to the direction of the applied shear direction by about 5° (Figure 3.11(i)).

### **3II.2.2 Nano-HPT product obtained from condensed Mg**

The microstructure of the HPT-compacted nanopowder was examined by transmission Kikuchi diffraction (TKD) because of the much smaller grain size. The TKD technique used in our laboratory is unique in the sense that it is applied in a direct on-axis configuration permitting rapid measurement [2.12]. At the same time, the maximum size of the examined surface is limited; much smaller than in EBSD. For this reason, the statistical data (disorientation distribution, crystallographic texture) are less representative compared to the EBSD results shown in Figure 3.11 for the micro-products. Nevertheless, important morphological features and in-grain disorientations can be characterized by these TKD measurements.

The evolution of grain orientations and the corresponding microtexture for the nano-HPT product deformed up to 1/2, 3/4 and 2 turns are given in Figure 3.12. At the early stages of deformation (i.e. after 1/2 turn), the TKD orientation map in Figure 3.12(a) reveals a rather heterogeneous grain-structure consisting of a wide range of grain/particle size distribution. The larger particles seem to be inclined at around 45° to the shear direction while the smaller ones did not respond much to the applied shear strains (i.e.  $\gamma = 10$  for 1/2 revolution). As mentioned earlier, since the surfaces of ultrafine Mg particles have been originally coated with a thin layer of MgO oxides, these oxide layers were not indexed in the TKD measurements and appeared as non-indexed zones along the particle boundaries. The frequency distribution of grain misorientation shown in Figure 3.12(b) clearly indicates a mixed type of grain boundaries for this microstructure. As expected from the microstructural heterogeneities, the texture in this sample was not developed as expected from the applied strain (see Figure 3.12(c)). The c-axes should be positioned at the top and bottom parts of the pole figure in Figure 3.12(c), which is visible, however, large population of grains were very far from these positions.

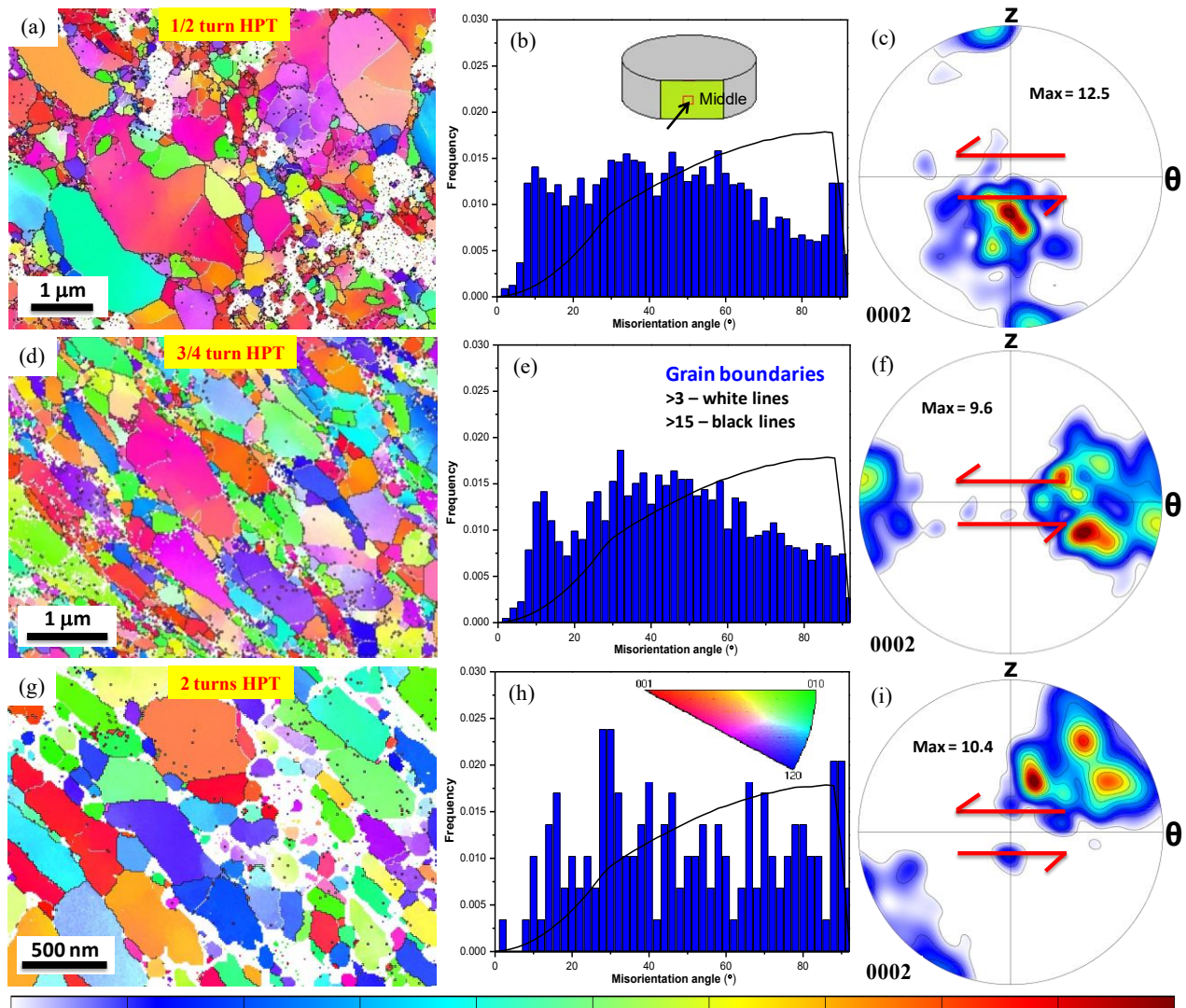


**Figure 3.12** – TKD-based EBSD orientation maps accompanied with grain boundary misorientations and associated microtexture in (0002) pole figure for the 1/2 turn (a-c), 3/4 turn (d-f) and 2 turns (g-i) nano-HPT product, obtained at the outer edge and middle-section of the HPT-disks (see the inset of Figure 3.12(b)). Note the differences in scale bar.

For the subsequent deformation through 3/4 and 2 turns, a rather homogeneously deformed microstructure was developed in the HPT-products, Figures 3.12(d, g). In both cases, the grains/particles were significantly elongated with an inclination angle of about 45° from the applied shear. It is readily apparent that some parts of the microstructure seem extremely fragmented to grain sizes less than 100 nm, while the courser grain-structures were probably generated from initially larger powder particles. Also, the grain/particle boundaries, which were essentially consisted of oxide layers, were not index during the TKD measurements. Since the given TKD map for the 2-turns HPT sample contained a limited number of grains, Figure 3.12(i) was constructed from several small TKD maps in order to obtain statistically representative texture using the Jtex software [2.11].

### **3II.3 Microhardness evolution**

The mechanical strengths of the 2 turns HPT products were characterized by Vickers microhardness across the radial as well as the axial directions; the results are shown in Figure 3.13. Since it was revealed that for relatively thick HPT specimens the evolution of microhardness can vary significantly across the through-thickness [3.20], it was carefully examined on several cross-sectional planes across the thickness-height. For comparison, the hardness values recorded for the HPT bulk Mg [1.41,3.20,3.22] are also given in Figure 3.13.

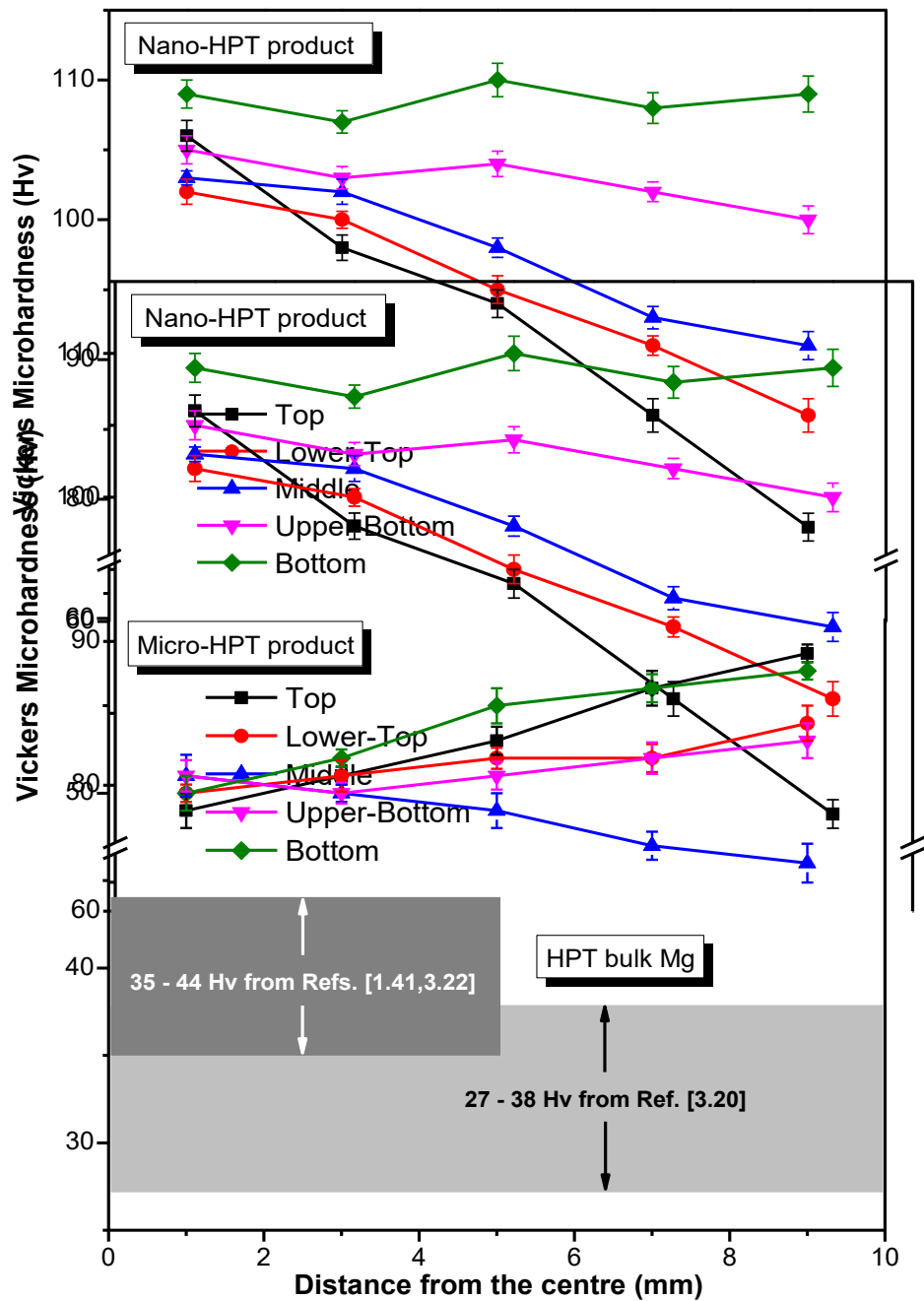


Figure 3.13 – Variations of Vickers microhardness (Hv) along the radial direction as well as across the disk-thickness for the 2 turns micro-HPT product and nano-HPT product. The hardness values reported for bulk HPT Mg [1.41,3.20,3.22] are also given in the same graph.

Because of the presence of finer grains and oxide particles, the hardness of the nano-HPT product is always twice higher than that of the micro-HPT product. It is readily apparent from Figure 3.13 for the micro-HPT product that there was a radical fall in the microhardness in the middle-section displaying the lowest value at the outer-edge of the HPT-disk, whereas the hardness values in the radial direction monotonically increased at locations nearer to the top and bottom surfaces. This can be expected from the microstructural evolutions in the middle-section of the micro-HPT disk (see Figure 3.9(b)), in which a recrystallized microstructure developed during the intense shear straining by HPT. Comparatively, there is an increase in hardness values towards the outer-edge for the bottom and top locations. This is due to the fact that while the strain increases towards the periphery of the disk, it does not reach sufficient amount (contrary to what happens at the middle section) to trigger dynamic recrystallization. Such increase in hardness for the HPT-processed sample with increasing strain followed by a hardness drop due to recrystallization was also reported for pure bulk Mg in Refs. [1.41,3.20,3.22]. Finally, having an intermediate behavior, the hardness values at the disk-center - that are associated with comparatively lower strains - were almost the same across the disk-thickness.

It is also interesting to note that the hardness values in the micro-HPT product obtained from atomized powder precursor are always higher than the ones reported on HPT pure Mg for which the precursor was a bulk sample [1.41,3.20,3.22]. This must be due to the presence of a small fraction of oxide always present at the periphery of the Mg powder particles that provided with some hardening and pinned the grain boundaries to reach finer grain size after deformation. Recently, Mondet et al. [3.10] have reported that a significant improvement in hardness was achieved due the grain size refinement in the spark plasma sintered AZ91 Mg alloy. Consistently,

as far as the mechanical contribution of the grain size is concerned, the nano-HPT product associated with much finer grain size exhibited excellent hardening behavior followed by the micro-HPT one in comparison with the results obtained for the HPT bulk Mg samples [1.41,3.20,3.22].

In the case of nano-HPT products (see Figure 3.13), the microhardness evolution demonstrates a completely different hardening response than that of its micro-counterpart. Because of the small powder particle size and the presence of oxides, the hardness values were always higher at the disk-center, with an average value of more than 105 Hv for all cross-sectional planes. While the bottom surface exhibited consistently higher hardness values across the radial direction, the other cross-sectional planes showed a monotonic drop in the microhardness values from the disk-centre to the periphery. These features are in fact consistent with the microstructural development examined by SEM, where the bottom part revealed a more significant grain refinement than the other parts (see Figures 3.9(d-f)). It is also clearly evident that at the outer-edge of the HPT-disk, the hardness values continuously decreased from the bottom to the top surface.

## **3II.4 Discussion**

It was revealed from the HPT consolidation of two distinct Mg powders that the nature of the initial powder precursors had significant impacts on the powder consolidation behavior. The evolutions of the microstructures, the texture and the microhardness for the two HPT-consolidated products were significantly dissimilar in nature. In the following subsections, the characteristic differences between the two types of HPT-products will be enlightened on the basis of two important aspects associated with the present study: the effect of severe plastic deformation through HPT on the behavior of the powder consolidation, and the distinct physicochemical nature of the initial powder precursors.

### **3II.4.1 Effects of severe plastic deformation through HPT**

During HPT processing, huge amount of strain can be introduced into the material assisted by the large applied hydrostatic pressures which prevent crack formation. In a consequence, better uniformity, a homogeneous distribution of the second phase particles (if present), and more grain-size refinement in the matrix phase [3.2,3.17] can be achieved. However, HPT consolidation of the starting powder particles are mainly governed by particle-particle shearing, rather than diffusion, under very high hydrostatic pressures which may lead to the required bonding between the powder particles, even at low processing temperatures.

The effectiveness of the powder consolidation was assessed by measuring the relative density of the bulk HPT-products using the Archimedes principle; the results are given in Table 3.2. A relative density of about 92% and 96% was achieved for the micro-HPT and nano-HPT product, respectively, after cold consolidation of 2 turns under a hydrostatic pressure of 1.2 GPa,

at room temperature. The densification of the HPT-products is fairly consistent with the results reported for other kinds of metallic powders consolidated by HPT [3.8,3.12,3.23,3.24]. The relatively higher bulk density obtained for the nano-HPT product is possibly due to the contribution from MgO oxides owing to higher density than pure Mg. However, this value is less than the theoretical one when considering 5 wt% MgO content in the initial condensed powder (see Table 3.1). In contrast, the lower bulk density for the micro-HPT product can be associated with the relatively poor consolidation at the top and bottom parts of the HPT-disks as witnessed from the SEM study (see Figures 3.9(a-c)). Thus, it can be anticipated that a broader range of particle size distribution (i.e. 50 to 800 nm), and the presence of MgO oxide particles in the condensed powder, could have assisted to achieve higher densification in the nano-HPT product as compared to its micro-counterpart.

**Table 3.2** – Relative density of the HPT products consolidated from the atomized Mg and condensed Mg powder particles.

HPT-samples	Calculated density ( $d_c$ , g cm <sup>-3</sup> )	Theoretical density ( $d_t$ , g cm <sup>-3</sup> )	Relative density ( $d_c/d_t$ , %)
2 turns micro-HPT	1.596	1.738	91.8 ± 0.5
2 turns nano-HPT	1.715	1.784 (5 wt% MgO)	96.1 ± 0.8

It has been a great concern for long time that processing of Mg based materials through powder metallurgy routes confronts significant difficulties due to their high reactivity towards open atmosphere forming an impervious native oxide layer around the powder particles. While these oxides are initially considered obstacles for direct contact between the particles [3.10], the massive shear straining through severe plastic deformation techniques can fragment these oxide layers and creates freshly new surfaces, enhancing in this way the direct bonding between the metallic phases to obtain metal-matrix composites [3.12,3.24]. It was revealed from the present study that the initial ultrafine particles underwent severe plastic deformation and became elongated towards the applied shear direction while the oxide layer fractured into small particles. These oxide particles were uniformly distributed through the Mg matrix and simultaneously the grain size was refined. The nanometric oxide particles particularly aligned along the grain boundaries generated a significant Zener pinning effect towards the evolution of elongated and nanostructured grain domains across the sample volume (see Figures 3.9(d-f)). Comparatively, the HPT consolidation of the atomized powder particles produced equiaxed recrystallized microstructures in the middle-section. At the same time, the top and bottom parts of the HPT-disks were relatively less deformed, even after 2 HPT turns (see Figures 3.9(a-c)). The generation of equiaxed microstructures, particularly at the middle-portion, can be associated with the occurrence of complete recrystallization processes plausibly due to the localization of shear strain in the middle-section of the HPT-disks while for a relatively thick HPT specimen [3.20].

### **3II.4.2 Significance of MgO oxides**

It was observed that the amount of MgO oxides is significantly higher for the ultrafine Mg powder precursor due to its large surface area fraction. Also, as a secondary phase, it influenced significantly the development of the microstructure, including the final attainable grain size. Consistently with the lattice distortion of Mg phase determined by the XRD analysis of the nano-HPT products, it can thus be speculated that the MgO nanoparticles, particularly located at the grain boundaries of the elongated Mg domains, may impose severe obstacles towards the deformation of Mg matrix. Simultaneously, they generated a significant Zener pinning for the migration of grain boundaries affecting the grain size evolution within the fine elongated domains having an average grain width of about 200 to 300 nm. While a saturation grain size of  $\sim 2.5 \mu\text{m}$  was obtained for the HPT deformed bulk Mg [1.41,3.20], the HPT consolidation of Mg powder led to a significant grain size refinement which was estimated to be 0.2 to  $1 \mu\text{m}$  depending on the initial powder precursors. The refinement in grain size for the consolidated products can be associated with the pinning effect of oxide particles on the grain boundary migrations, thus, suppressing the recovery and recrystallization processes during the concurrent deformation. Thereby, a substantially finer microstructure developed for the Mg/MgO based nano-HPT products compared to its micro-counterpart.

Furthermore, the presence of MgO oxides severely impacted the texture evolution in the two types of HPT-products. A strong shear texture was developed for the micro-HPT product at large shear strains. It clearly implies that the HPT consolidation of the atomized powder particles was mainly governed by the simple shear deformation of the powder particles under a very high hydrostatic pressure [3.8,3.12,3.24]. However, it was noticed, that the location of the *B* fibre was

somewhat deviating from its ideal position with increasing shear strain; it was tilted against the shear sense (see Figure 3.11(i)). This is consistent with the findings of Bonarski et al. [3.3] who reported that upon HPT deformation of pure bulk Mg, the *c*-fibre axis deviates from its ideal position and this angular deviation increases - while the texture strength decreases - by increasing the hydrostatic pressure. According to Skrotzki et al. [3.25], the occurrence of dynamic recrystallization processes at relatively large shear-strains might prevent the rotation of the *c*-axes from reaching the ideal position. In addition, the appearance of a large fraction of LAGBs along with the elongated microstructural features after 2 turns suggests that due to the continuous shear deformation in HPT processing the grain fragmentation and the associated texture evolution can be attributed to a repetitive deformation/recrystallization phenomenon and even a steady state regime can be reached [1.41,3.19].

In contrast to the micro-HPT product, the texture evolution in the Mg/MgO nanocomposites was more complicated probably due to the influence of MgO oxide layers that surrounded the Mg core. It was observed from sequential torsional straining of the condensed powder particles that the presence of MgO oxide particles somewhat hindered the evolution of ideal shear texture in the nano-HPT composites, although a significant densification was achieved through the particle fragmentation followed by adequate bonding between the metallic phases after 2 HPT turns deformation. In spite of the high HPT rotation, the texture showed many orientations out of ideal positions. This must imply that many nano-particles did not deform plastically; they were probably only rotating under the applied shear.

The evolution of the microhardness across the sample volume demonstrated distinct hardening mechanisms in the two types of HPT-products. The nano-HPT product exhibited significantly higher microhardness; almost twice higher than the micro-HPT products (nano-HPT: 108 Hv and micro-HPT: 55 Hv). This discrepancy in the development of microhardness can be attributed to their distinct microstructural features. The enhanced strengthening for the nano-HPT composite can be correlated to the presence of extremely small dispersed secondary oxide particles that also pin the grain boundary during deformation and leads to thin elongated Mg domains. Comparatively, the deformation induced stored energy in the micro-HPT product were annihilated by the recrystallization processes, and thus, developed an equiaxed recrystallized grain-structure promoting softening. This softening behavior at large shear strains is a common feature for pure magnesium and other metal systems due to their low homologous temperatures facilitating the grain boundary migrations through diffusion processes [2.5].

## **Chapter's conclusions**

Severe plastic deformation through HPT was conducted on bulk as well as powder materials to study the deformation heterogeneities for relatively thick samples. In the first part, two bulk materials - an Al alloy with fcc crystal structure and a commercial purity hcp Mg - were investigated to characterize the strain heterogeneities and their effects on local texture/microstructure development and the associated hardness. Accordingly, the “critical” HPT processing conditions - an anvil having a low angle of lateral walls ( $15^\circ$ ) and a fractional number of turns ( $180^\circ$  and  $270^\circ$ ) - were selected to induce strain gradients within the sample volume.

In the second part, two types of HPT-products were produced by HPT consolidation of two distinct Mg powder precursors at the identical experimental conditions as applied for the above mentioned bulk materials. The effect of strain heterogeneities on the evolution of the microstructure, the texture and the mechanical strength in the resultant bulk HPT products was materialized via XRD, SEM, FIB, EBSD, and Vickers microhardness analyses. The main conclusions from these two studies can be summarized as follows.

- 1) The local shape change of the witness solder pin after HPT processing of the bulk samples clearly revealed two major components at the local shear strain: shear strain directly imparted by the torsion as well as a radial tensile strain component due to the materials outflow.
- 2) For given experimental conditions, both the hardness analysis (after the initial stage of compression) and the strain analysis (after HPT deformation) revealed higher strain localization and strain inhomogeneities in the hcp materials (despite the activation of twinning) than in the fcc materials.
- 3) Plastic deformation was highly localized in the middle plane at the outer edge of the disks for the bulk as well as the atomized micro-sized powder while it was rather homogeneously

- distributed throughout the sample volume for the nano-HPT composites obtained from the condensed ultrafine powder.
- 4) The HPT processing of bulk Mg and atomized Mg powder showed similar response in the evolution of the microstructure, in particular through the thickness direction at the periphery of the disk, where the interplay between significant strain hardening and possible dynamic recrystallization could occur.
  - 5) There has been significant grain size refinement for the HPT-consolidated products (0.5  $\mu\text{m}$  for the micro-HPT and 200 - 300 nm for nano-HPT product) in comparison with the bulk HPT Mg ( $\sim 2.5 \mu\text{m}$ ). This was most probably associated with the presence of uniformly dispersed nanometric oxide particles in the HPT-consolidated products, imposed significant Zener pinning to the migrating grain boundaries and restricted the grain size evolution within the fine elongated domains, particularly for the nano-HPT composite.
  - 6) The physicochemical nature of the initial powder precursors had significant influences on texture evolutions in the two types of HPT-products. Due to the shear localization at the middle-section and subsequent dynamic recrystallization in the bulk Mg as well as in the atomized Mg powder, a strong basal texture was developed whereas the presence of MgO oxides hindered the evolution of ideal shear texture in the nano-HPT composites.
  - 7) As a consequence, the nanometric Mg/MgO composites exhibited twice higher microhardness than that of its micro-counterpart, and even higher than the bulk HPT Mg. While the softening due to dynamic recrystallization was responsible for their lower hardness, the uniform dispersion of oxide nanoparticles in the elongated Mg domains produced sufficient dislocation pinning, and thus, imposed significant dispersion strengthening by the Orowan mechanism.

## References

- [3.1] Edalati K, Horita Z. “A review on high-pressure torsion (HPT) from 1935 to 1988.” *Mater. Sci. Eng. A* 652 (2016) 325-52.
- [3.2] Xu C, Horita Z, Langdon TG. “The evolution of homogeneity in processing by high-pressure torsion.” *Acta Mater.* 55 (2007) 203-12.
- [3.3] Bonarski BJ, Schafner E, Mingler B, Skrotzki W, Mikulowski B, Zehetbauer MJ. “Texture evolution of Mg during high-pressure torsion.” *J. Mater. Sci.* 43 (2008) 7513-8.
- [3.4] Al-Zubaydi A, Figueiredo RB, Huang Y, Langdon TG. “Structural and hardness inhomogeneities in Mg-Al-Zn alloys processed by high-pressure torsion.” *J. Mater. Sci.* 48 (2013) 4661-70.
- [3.5] Sakai G, Nakamura K, Horita Z, Langdon TG. “Developing high-pressure torsion for use with bulk samples.” *Mater. Sci. Eng. A* 406 (2005) 268-73.
- [3.6] Hohenwarter A, Bachmaier A, Gludovatz B, Scheriau S, Pippan R. “Technical parameters affecting grain refinement by high pressure torsion.” *Int. J. Mater. Res.* 100 (2009) 1653-61.
- [3.7] Lee DJ, Kim HS. “Finite element analysis for the geometry effect on strain inhomogeneity during high-pressure torsion.” *J. Mater. Sci.* 49 (2014) 6620-8.
- [3.8] Zhao YJ, Massion R, Grosdidier T, Toth LS. “Gradient structure in high pressure torsion compacted iron powder.” *Adv. Eng. Mater.* 17 (2015) 1748-53.
- [3.9] Avedesian MM, Baker H. “ASM speciality handbook: magnesium and magnesium alloys.” *International ASM* (1999) 78-84.
- [3.10] Mondet M, Barraud E, Lemonnier S, Guyon J, Allain N, Grosdidier T. “Microstructure and mechanical properties of AZ91 magnesium alloy developed by Spark Plasma Sintering.” *Acta Mater.* 119 (2016) 55-67.
- [3.11] Straffellini G, Dione Da Costa L, Menapace C, Zanella C, Torralba JM. “Properties of AZ91 alloy produced by spark plasma sintering and extrusion.” *Powder Metall.* 56 (2013) 405-10.
- [3.12] Xia K. “Consolidation of particles by severe plastic deformation: mechanism and applications in processing bulk ultrafine and nanostructured alloys and composites.” *Adv. Eng. Mater.* 12 (2010) 724-9.
- [3.13] Toth LS, Neale KW, Jonas JJ. “Stress response and persistence characteristics of the ideal orientations of shear textures.” *Acta Mater.* 37 (1989) 2197-10.
- [3.14] Beausir B, Toth LS, Neale KW. “Ideal orientations and persistence characteristics of hexagonal close packed crystals in simple shear.” *Acta Mater.* 55 (2007) 2695-05.
- [3.15] Lee DJ, Yoon EY, Ahn DH, Park BH, Park HW, Park LJ, Estrin Y, Kim HS. “Dislocation density-based finite element analysis of large strain deformation behavior of copper under high-pressure torsion.” *Acta Mater.* 76 (2014) 281-93.

- [3.16] Xu C, Horita Z, Langdon TG. "Evaluating the influence of pressure and torsional strain on processing by high-pressure torsion." *J. Mater. Sci.* 43 (2008) 7286-92.
- [3.17] Pippin R, Scheriau S, Taylor A, Hafok M, Hohenwarter A, Bachmaier A. "Saturation of fragmentation during severe plastic deformation." *Annu. Rev. Mater. Res.* 40 (2010) 319-43.
- [3.18] Bazarnik P, Romelczyk B, Huang Y, Lewandowska M, Langdon TG. "Effect of applied pressure on microstructure development and homogeneity in an aluminium alloy processed by high-pressure torsion." *J. Alloys Compd.* 688 (2016) 736-45.
- [3.19] Toth LS, Gu CF, Beausir B, Fundenberger JJ, Hoffman M. "Geometrically necessary dislocations favor the Taylor uniform deformation mode in ultra-fine-grained polycrystals." *Acta Mater.* 117 (2016) 35-42.
- [3.20] Panda S, Toth LS, Fundenberger JJ, Perroud O, Guyon J, Zou JX, Grosdidier T. "Analysis of heterogeneities in strain and microstructure in aluminum alloy and magnesium processed by high-pressure torsion." *Mater. Charact.* 123 (2017) 159-65.
- [3.21] Del Valle JA, Perez-Prado MT, Ruano OA. "Deformation mechanisms responsible for the high ductility in a Mg AZ31 alloy analyzed by electron backscattered diffraction." *Metall. Mater. Trans. A* 36 (2005) 1427 – 38.
- [3.22] Joshi M, Fukuta Y, Gao S, Park N, Terada D, Tsuji N. "Fabrication of fine recrystallized grains and their mechanical property in HPT processed pure magnesium." *IOP Conf. Ser.: Mater. Sci. Eng.* 63 (2014) p. 012074.
- [3.23] Edalati K, Horita Z, Fujiwara H, Ameyama K. "Cold consolidation of ball-milled titanium powders using high-pressure torsion." *Metall. Mater. Trans. A* 41 (2010) 3308-17.
- [3.24] Bachmaier A, Pippin R. "Generation of metallic nanocomposites by severe plastic deformation." *Int. Mater. Rev.* 58 (2013) 41-62.
- [3.25] Skrotzki W, Scheerbaum N, Oertel CG, Brokmeier HG, Suwas S, Toth LS. "Recrystallization of high-purity aluminium during equal channel angular pressing." *Acta Mater.* 55 (2007) 2211-18.

## CHAPTER 4: STUDY OF IMPROVEMENTS IN HYDROGEN STORAGE PROPERTIES OF HIGH-PRESSURE TORSION (HPT) CONSOLIDATED MAGNESIUM PRODUCTS

---

Introduction .....	116
4.1 First hydrogenation kinetics .....	119
4.2 Hydrogen sorption properties .....	121
4.2.1 Thermodynamics of absorption/desorption .....	121
4.2.2 Kinetics of hydrogen absorption .....	126
4.2.3 XRD of the hydrided products .....	129
4.3 Desorption performances .....	131
4.4 Microstructural modifications upon cycling .....	134
4.5 Discussion .....	137
4.5.1 Consequences of the processing route .....	137
4.5.2 Influences of the nature of initial powder precursors .....	139
4.5.3 Effects of the absorption/desorption cycling .....	141
Chapter's conclusions .....	142
References .....	144

## **Introduction**

A considerable amount of research has been devoted to develop an advanced hydrogen storage media, particularly for vehicular applications. As a promising hydrogen carrier, magnesium has been considered as an excellent candidate for H-storage mainly due to its light weight, abundance on the earth's crust and high gravimetric and volumetric storage capacity [1.8]. However, the main obstacles of Mg based materials for potential industrial applications include its rather sluggish kinetics in the charging/discharging processes, and stable thermodynamic properties dictating the high operation temperature which is too high for practical on-board applications [1.18].

Significant improvements in the hydrogen sorption kinetics of Mg/MgH<sub>2</sub> systems have been achieved by the use of high energy ball-milling (HEBM) [1.8,4.1], which were primarily considered to be the effect of nanometric crystallite/grain size, introduction of lattice defects and increase of reactive surface area. The catalytic action of transition metals or oxides was also considered to be beneficial. In particular, Barkhordarian et al. [4.1] showed that milling of MgH<sub>2</sub> with 1 mol% of different oxides such as TiO<sub>2</sub>, V<sub>2</sub>O<sub>5</sub> or Nb<sub>2</sub>O<sub>5</sub> leads to an improvement in magnesium H-sorption kinetics. Aguey-Zinsou et al. [2.56] considered that the major effect of the M<sub>x</sub>O<sub>y</sub> oxides was related to the refinement of the size of MgH<sub>2</sub> particles during milling. Although the milling route results in considerable improvements in hydrogen sorption properties, it suffers from two major drawbacks. Firstly, it is difficult to avoid agglomeration during milling of Mg or Mg alloys [4.2]. Secondly, impurities coming from the milling tools and gas adsorption are hard to control and can affect significantly the hydrogen sorption properties [1.14].

To avoid these drawbacks, severe plastic deformation (SPD) techniques have recently been employed to produce wide range of Mg based hydrogen storage materials [1.15]. It was suggested from high-pressure torsion (HPT) of pure bulk Mg that the refinement in grain size (i.e. increase in amount of grain boundaries) played an effective role than the amount of dislocations for modifying the hydrogen storage properties [1.41]. Although the compaction of powders under high pressure plus torsional straining has already been initiated in the 90's [4.3], the SPD-assisted powder consolidation for improving hydrogen storage performances has received comparatively little attention [1.32,1.38,4.4]. Kusadome et al. [1.38] investigated the effect of HPT on hydrogenation of  $MgNi_2$  powders, and they reported that this intermetallic (normally accepted as non-absorber) can absorb 0.1 mass% H after HPT. They also claimed that hydrogen was mainly confined at the grain boundaries rather than at the tetragonal sites of the host lattice. A noticeable improvement in the hydrogen uptake capacity of  $Mg_{70}Ni_{30}$  alloy was recently observed by Revesz et al. [4.4] when the ball-milled powders were subjected to HPT deformation. Liang and Hout [1.32] found that the application of cold rolling on  $MgH_2$  powders could be an efficient processing route to produce nanocrystalline structure for improving hydrogen sorption properties. A new processing method - applying HPT on arc-plasma evaporated ultrafine-grained powder - has been recently introduced to produce bulk Mg-MgO based nanocomposites for hydrogen storage applications [1.43,1.44]. The enhanced hydrogen sorption properties of these bulk composites were mainly attributed to the refinement of the Mg matrix and the dispersion of fine MgO particles formed during intense shearing by HPT.

Motivated by the potential improvements in hydrogen sorption properties of Mg based materials processed by powder consolidation route; this chapter has been designed for a thorough study on hydrogen storage properties of two types of consolidated Mg products - micro-HPT product from atomized micro-sized powder and nano-HPT product from condensed ultrafine powder - as described in the Part II of **Chapter 3**. Prior to hydrogen storage measurements, the bulk HPT-products were broken using a ceramic mortar to micrometer range powder particles to fit into the testing vessel. The ground samples were first activated by dynamic hydrogen absorption at 400 °C for 8 h under a hydrogen pressure of 3.5 MPa followed by dehydrogenation at the same temperature under vacuum until complete desorption. These one-cycled samples will be referred to as activated products in the subsequent text. They were further employed for measuring the pressure-composition-temperature (PCT) isotherms and the subsequent absorption profiles at different testing temperatures. It should be noted here that the hydrided products after each cycle were completely desorbed at 400 °C under vacuum.

Finally, the recycled samples were fully hydrogenated through dynamic hydrogen absorption at 400 °C for 6 h under a hydrogen pressure of 3.5 MPa. Desorption properties of the fully hydrided samples were investigated by DSC-TG analyses at a heating rate of 3, 5 and 10 °C/min with the temperature rising from 25 to 500 °C. The initial powder particles were also examined under the identical experimental conditions for a comparative study. Since the morphology and microstructures of the initial powder particles and their HPT-consolidated products were already discussed in the previous chapters, they will be mainly investigated for the improvements in hydrogen sorption properties in the following sections.

## 4.1 First hydrogenation kinetics

Figure 4.1 compares the first hydrogen absorption kinetics measured at 400 °C under a hydrogen pressure of 3.5 MPa for all the samples. It should be noted that because of their more sluggish behavior, 10 h were used instead of 8 h for the runs carried out on the atomized and its micro-HPT products to try to reach a more steady state plateau. It is readily apparent from the comparison between the two powders that, while the atomized powder could reach almost the theoretical value of 7.6 wt% H for pure Mg, the condensed powder showed comparatively a reduced H uptake capacity with a plateau located at about ~ 7.2 wt% H.

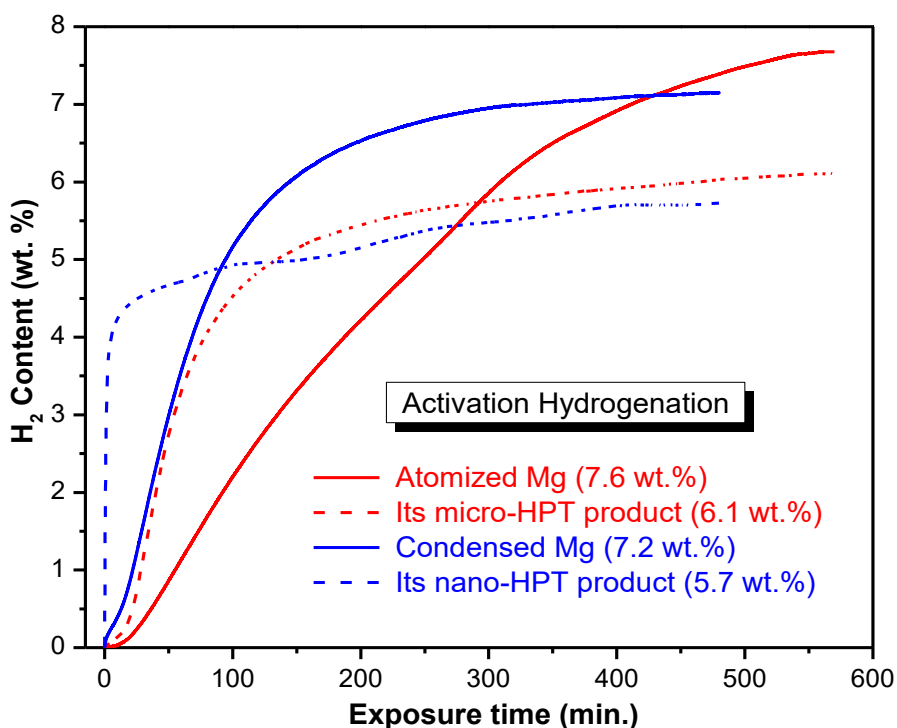


**Figure 4.1** – First hydrogenation (i.e. activation kinetics) recorded for all the studied samples at 400 °C under a hydrogen pressure of 3.5 MPa; maximum H-storage quantities under steady-state conditions are given in the parenthesis.

It is also clear from Figure 4.1 that the kinetics of hydrogen storage is much faster for the condensed ultrafine powder than for the atomized micro-sized one. The increase in surface area due to the reduced scale of the condensed powder and the presence of the MgO phase formed during their passivation process that acts as a catalyst, can explain the fastest kinetics. In return, as a fraction of these condensed powder particles had reacted with oxygen, less Mg was available to react with hydrogen; which explains a lower hydrogen storage capacity of the condensed and passivated powder. Furthermore, it can be readily seen that the atomized powder exhibited an incubation stage at the beginning of M-H interactions as compared to its counterpart. It is suggested that at the beginning of M-H interactions a large number of nuclei were formed in the ultrafine condensed powder than that for the atomized powder, which clearly substantiates its faster absorption kinetics.

Comparing now in Figure 4.1 the behavior of the powders with their HPT consolidated products, it is obvious that the effect of the HPT process is, in both cases, to increase the storage kinetics while reducing the storage capacity. For example, the capacity of the atomized powder after 10 h of storage is reduced from about 7.6 % down to 6.1 % after HPT processing. The structural defects (vacancies, dislocations) as well as the reduction in grain size induced by the severe plastic deformation are likely to create diffusion path and increase the reactivity of the material surface, thus improving the storage kinetics. Comparatively, the reduction of the storage capacity is a little more surprising. As will be shown by the XRD analysis of the hydrogenated samples (see Figure 4.5), this lower capacity is due to the fact that some of the magnesium did not participate in the hydrogenation reactions.

In addition, it may be considered, on this first cycle, that the fully consolidated and sintered HPT samples produced in the present study did not allow hydrogen to fully penetrate into the interior of the bulk HPT products. Alternatively, it is possible that, while the increased amount of structural defects and grain boundaries that act as faster diffusion path, some of these crystallographic perturbations may alter the amount of hydrogen that can be stored in the magnesium lattice. Further analysis, both theoretical and experimental, should be carried out to elucidate the effect of the nature and quantity of structural defects induced by severe plastic deformation on the storage ability.

## **4.2 Hydrogen sorption properties**

### **4.2.1 Thermodynamics of absorption/desorption**

Pressure-composition-temperature (PCT) isotherms of the initial powders and their HPT-products were recorded on the one-cycled activated products at the temperature ranges of 325 – 400 °C depending on the respective samples. The corresponding PCT diagrams and the associated van't Hoff plots are given in Figure 4.2 and 4.3, respectively. The characteristics data of the PCT diagrams and the thermodynamic properties (enthalpy and entropy) obtained from the van't Hoff plots are listed in Table 4.1 and 4.2, respectively.

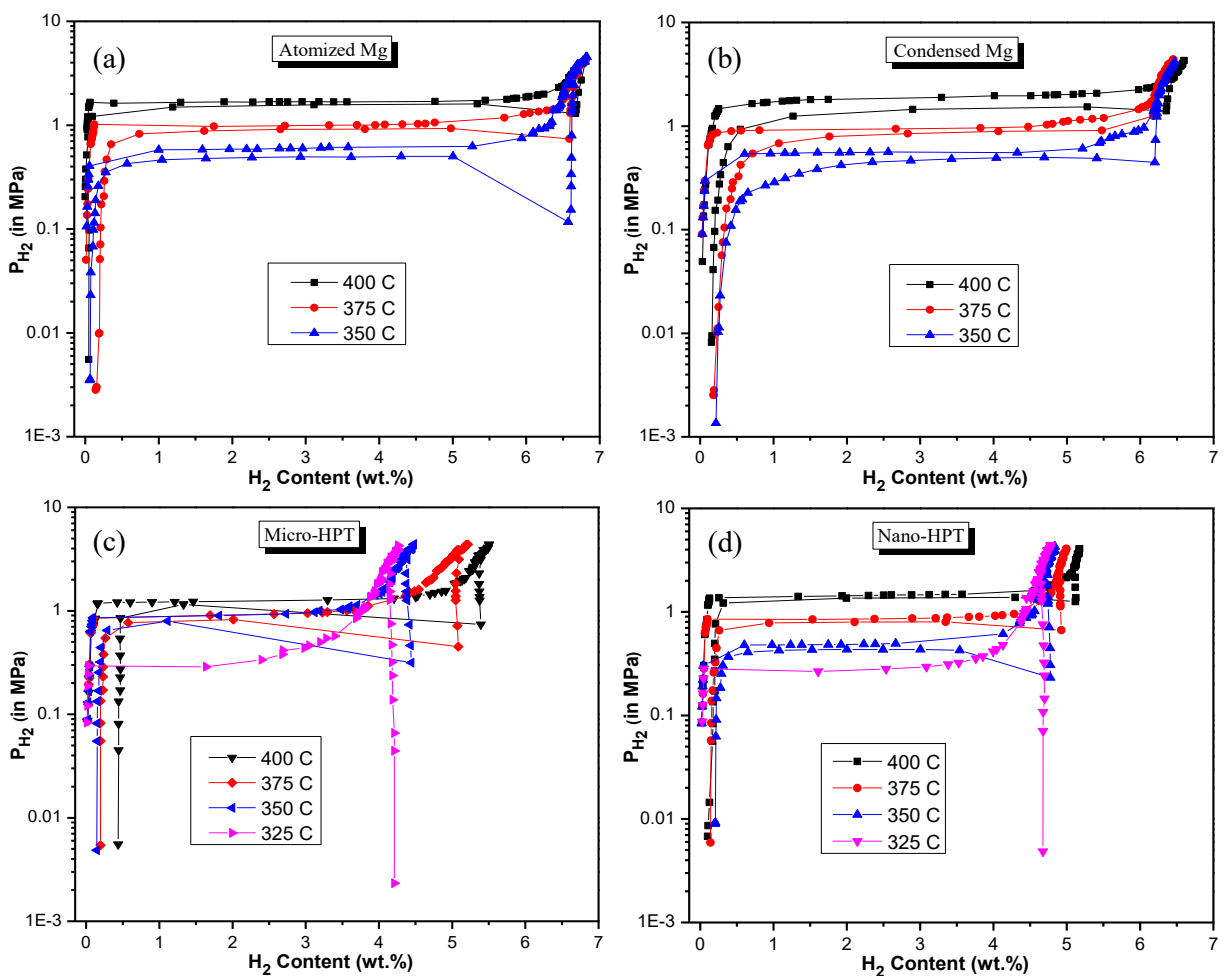


**Figure 4.2** – Pressure-composition-temperature (PCT) isotherms recorded on the one-cycled activated products at different temperatures for (a, b) the initial powder particles, and (c, d) their HPT-consolidated products.

In these cycles, as seen from the PCT diagrams and the data at 400 °C from Table 4.1, the maximum hydrogen uptake capacity for the atomized powder and its micro-HPT product were determined to be 6.8 and 5.5 wt% H, respectively, higher than the storage capacity of the condensed powder and its nano-HPT product, 6.6 and 5.2 wt% H, respectively. However, these capacities are comparatively lower than those obtained during the first hydrogenation given in Figure 4.1. This fact is most probably related to the different measurement conditions: the PCT

experiments were carried out at near equilibrium conditions where the pressure is adjusted by the thermodynamics, while the activation process was conducted under a fixed pressure of 3.5 MPa. The higher hydrogen pressure during the dynamic hydrogenation represents an external driving force and leads to higher H-storage quantities. In addition, as can be noted from Table 4.1, the hydrogen uptake quantities for the HPT-products progressively decrease with the lowering of testing temperatures while it is less pronounced for the loose powder particles. This fact is partly associated with the atom diffusion mechanisms that are hindered by the lowering of operation temperatures [1.18], and also could be attributed to the incomplete hydrogenation for the bulk consolidated samples due to their sintered microstructures (see Figure 3.9, **Chapter 3**).

Consistently with the fact that the equilibrium pressure depends on temperature [1.18], the equilibrium pressure of absorption/desorption processes decreases radically when the operating temperature is lowered (Table 4.1). However, it is interesting to note that there is a significant improvement on pressure hysteresis for the nano-HPT product as compared to its powder counterpart at any operating temperatures. For the micro-HPT product, while the absorption plateau pressure is clearly readable from its PCT diagrams, the desorption isotherms recorded only few points before complete dehydrogenation did not show defined plateau pressures (Figure 4.2(c)). This peculiar characteristic of the micro-HPT product suggests a faster desorption kinetics only after a certain depression associated with the high dissociation energy-barrier. Furthermore, it has to be noted from the PCT diagrams that the appearance of humps in some of the desorption curves is associated with the fact that a stable thermodynamic equilibrium was not reached for these samples at the given experimental conditions. This artifact is more pronounced for the HPT products due to their slower desorption kinetics which is possibly related to their bulk nature and sintered microstructures.

**Table 4.1** – The characteristics data of the PCT diagrams for both initial powder precursors and their HPT products.

Samples	Temperature (°C)	H content (wt%)	P <sub>abs</sub> (MPa)	P <sub>des</sub> (MPa)	Pressure hysteresis (MPa)
Atomized Mg	400	6.81	1.679	1.570	0.109
	375	6.81	0.996	0.909	0.087
	350	6.83	0.606	0.494	0.112
Micro-HPT	400	5.50	1.247	1.154	0.093
	375	5.21	0.928	0.826	0.102
	350	4.47	0.915	0.795	0.120
	325	4.26	0.287	-	-
Condensed Mg	400	6.59	1.886	1.446	0.440
	375	6.45	0.941	0.844	0.097
	350	6.47	0.561	0.492	0.069
Nano-HPT	400	5.20	1.440	1.371	0.069
	375	4.99	0.855	0.799	0.056
	350	4.84	0.483	0.434	0.049
	325	4.78	0.266	-	-

**Table 4.2** – The thermodynamic properties obtained from the van't Hoff plots for both initial powders and their HPT products.

Properties	Atomized Mg	Micro-HPT	Condensed Mg	Nano-HPT
$\Delta H_{\text{abs}}$ (kJ/mol)	$-72.4 \pm 2.9$	$-77.5 \pm 0.9$	$-84.4 \pm 0.9$	$-75.4 \pm 0.4$
$\Delta H_{\text{des}}$ (kJ/mol)	$80.5 \pm 0.7$	$74.7 \pm 1.4$	$78.9 \pm 2.1$	$80.2 \pm 1.0$
$\Delta S_{\text{abs}}$ (J/mol. K)	$-130.5 \pm 4.1$	$-120.5 \pm 1.5$	$-149.6 \pm 1.4$	$-114.7 \pm 0.7$
$\Delta S_{\text{des}}$ (J/mol. K)	$142.5 \pm 1.2$	$134.7 \pm 2.2$	$139.6 \pm 3.3$	$140.5 \pm 1.6$

The thermodynamics of hydrogen uptake/release for the Mg/MgH<sub>2</sub> system were assessed by determining enthalpy and entropy changes using the van't Hoff plot ( $\ln P$  vs.  $1000/T$ ) as shown in Figure 4.3, and the corresponding enthalpy and entropy values are given in Table 4.2. It is apparent that while the HPT processing of the ultrafine condensed powder has led to decrease (increase) in the absolute values of absorption (desorption) enthalpy, the HPT consolidation of the atomized powder exhibits an opposite trend on the alteration of sorption enthalpy. Although there has been significant reduction in the absorption entropy for the HPT products, it should be noted that all samples have an almost constant value of desorption entropy. These thermodynamic modifications upon HPT processing could be related to the differences in the microstructure developments between the two types of HPT products (Figure 3.9, **Chapter 3**). Although it was noticed that the SPD processing can modify thermodynamic properties of the initial powder precursors in some extent, these effects are indeed insignificant compared to the chemical destabilization processes that forms intermediate states by introducing a new element or compound [4.5].

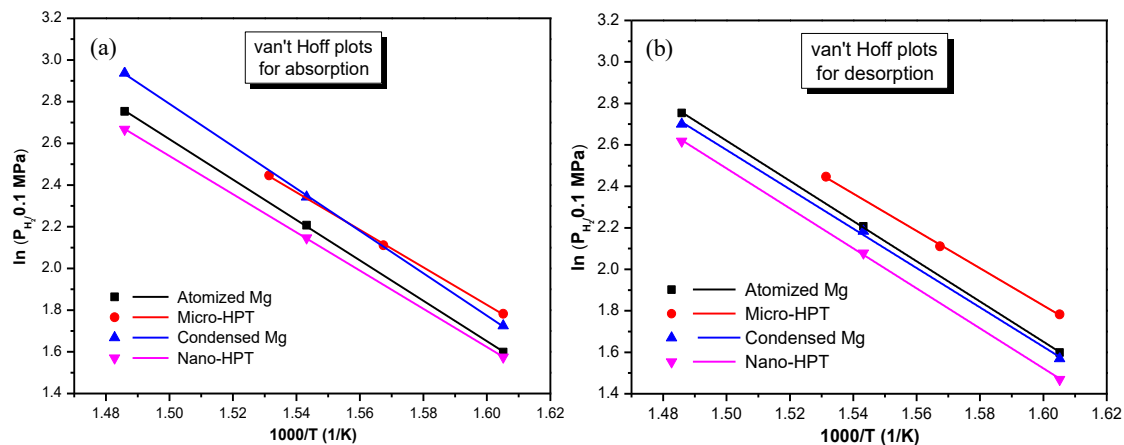


**Figure 4.3** – The van't Hoff plots for (a) absorption and (b) desorption obtained from the PCT isotherms for determining the hydrogen absorption/desorption enthalpy and entropy.

### 4.2.2 Kinetics of hydrogen absorption

The dynamic hydrogen absorption profiles recorded at 300 °C, 350 °C and 400 °C are presented in Figure 4.4 for all the studied samples. These results were obtained from the samples those were already used for the thermodynamic measurements. The details of absorption kinetic behaviors at different temperatures and times (1, 60 and 180 min) are provided in Table 4.3 for a comparative study.

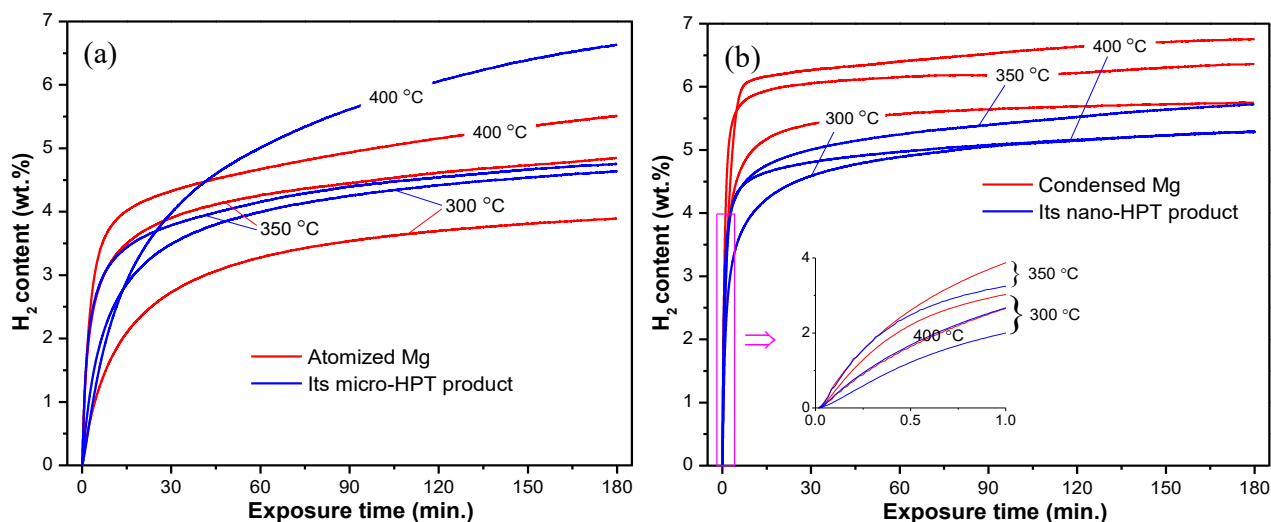


**Figure 4.4** – Dynamic hydrogen absorption profiles recorded at 300 °C, 350 °C and 400 °C under a constant hydrogen pressure of 3.5 MPa for (a) the atomized powder and its micro-HPT product and (b) the condensed powder and its nano-HPT product. The inset of Figure 4.4(b) shows the absorption kinetics obtained for 1 min exposure.

**Table 4.3** - Details of absorption kinetics behaviors for all the studied samples subtracted from their absorption curves given in Figure 4.4.

Samples	H uptake (wt%) at 300 °C			H uptake (wt%) at 350 °C			H uptake (wt%) at 400 °C			Absorption activation energy (kJ/mol)
	1 min	60 min	180 min	1 min	60 min	180 min	1 min	60 min	180 min	
Atomized Mg	0.3	3.3	3.9	1.3	4.3	4.9	1.2	4.7	5.5	112.0 ± 3.0
Micro-HPT	0.5	4.0	4.6	1.3	4.2	4.8	0.2	5.0	6.6	70.0 ± 1.0
Condensed Mg	3.0	5.6	5.7	3.9	6.2	6.4	2.7	6.4	6.7	87.0 ± 2.0
Nano-HPT	2.0	4.9	5.3	3.3	5.3	5.7	2.7	5.0	5.3	43.0 ± 2.0

Figure 4.4(a) presents variations in kinetics behaviors of the atomized powder and its HPT-product with increase in the operating temperatures. This can be clearly noticed from Table 4.3. At 300 °C, the micro-HPT product exhibit relatively faster kinetics and higher hydrogen storage capacity than their initial atomized powder, while they show almost similar kinetics and storage capacities at 350 °C. However, at 400 °C, there has been a changeover in the kinetics curves at around 45 min of exposure: while the powder sample trends to saturate its storage capacity, the micro-HPT product picks up a faster kinetics along with higher hydrogen storage capacity. Comparatively, it was reversed for the condensed powder and its nano-HPT product (see Figure 4.4(b) and Table 4.3), where the condensed powder presents faster kinetics and higher storage capacity than that of its nano-HPT product. Furthermore, if we compare the final hydrogenation kinetics at 400 °C (see Table 4.3) with that of the activation kinetics (see Figure

4.1), the atomized powder exhibits faster kinetics than that of its micro-HPT product, which is basically a reverse phenomenon than what was observed during the activation process. At the same time, both the condensed powder and its nano-HPT composite displayed almost similar hydrogenation kinetics.

The kinetic curves displayed in Figure 4.4 were fitted using the Johnson–Mehl–Avrami–Kolmogorov (JMAK) model [4.6] to calculate the activation energy for absorption. Although other models such as the contracting volume and the surface controlled models were also tested, due its most popularity and versatility the JMAK has been used in this study. It basically describes a process of nucleation and growth using the relation  $\ln [-\ln (1 - \alpha)] = n \ln k + n \ln t$ , where  $\alpha$  is the fraction of Mg transformed into MgH<sub>2</sub> at time  $t$ ,  $k$  is an effective kinetic parameter, and  $n$  is the Avrami exponent or the order of the reaction, which provides information about the dimensionality of the transformation. The initial part of the absorption curves was used to linearly fit with the JMAK equation and from the  $\ln [-\ln (1 - \alpha)]$  vs.  $\ln t$  plot, the effective kinetic parameter ( $k$ ) was calculated. Based on the experimental data obtained at different temperatures, the Arrhenius equation was employed to determine the average apparent activation energies; the results are given in Table 4.3. It is obvious that the HPT processing of powder precursors has led to the reduction in apparent activation energies for the HPT-consolidated products. This is probably associated with the microstructural modifications of the powder precursors due to the severe plastic deformation through HPT. It is also possible that the improvements in thermal conductivity of the consolidated products may further enhance the electron transfer phenomena associated with the hydrogenation reaction. However, the activation energy value for the nano-HPT product is significantly lower ( $E_a = 43.0 \pm 2.0$  kJ/mol H<sub>2</sub>) than that of the micro-HPT one

possibly due to its rather homogeneous nanometric features and catalytic effects of the uniformly dispersed fine MgO particles.

### **4.2.3 XRD of the hydrided products**

Following the PCT and kinetic measurements, a final hydrogenation of these recycled samples was carried out at 400 °C for 6 h under a hydrogen pressure of 3.5 MPa. One part of these hydrided samples was used for the XRD characterizations (this section) while other parts were employed for the characterization of desorption properties (next section).

The XRD patterns of the hydrogenated samples are shown in Figure 4.5. It is clearly visible from these patterns that most of the hcp-Mg phase has transformed into  $\beta$ -MgH<sub>2</sub> at the final hydrogenation. However, the presence of hcp-Mg and some MgO peaks are also visible in all the XRD patterns. The peaks originating from the non-reacting hcp-Mg clearly indicate an incomplete hydrogenation even at 400 °C and for a fairly longer duration. The MgO oxides in the hydrogenated atomized powder and its micro-HPT product, which were not detected previously (see section 3II.1.1, **Chapter 3**), could be contaminated during handling of the hydrogenated products out of the glove box before the XRD measurements. The amounts of hydrogen stored in these hydrided samples determined from the final hydrogenation curves are given in Table 4.4. It is readily noted that the steady-state hydrogen content of all the assessed samples varies significantly, and is independent of their initial absorption kinetics at the same temperature (see Table 4.3). For example, if one compares the hydrogen uptake quantities at the activation stage (see Figure 4.1) with the results provided in Table 4.4, it is very clear that the hydrogen storage capacity has been reduced upon hydriding/dehydriding cycling for the atomized powder (i.e. 7.6 vs. 6.2 wt%) while it has enhanced for its micro-HPT product (i.e. 6.1 vs. 6.6 wt%).

Comparatively, there was a fairly negligible loss in the hydrogen contents for both condensed powder and its nano-HPT product upon cycling operations.

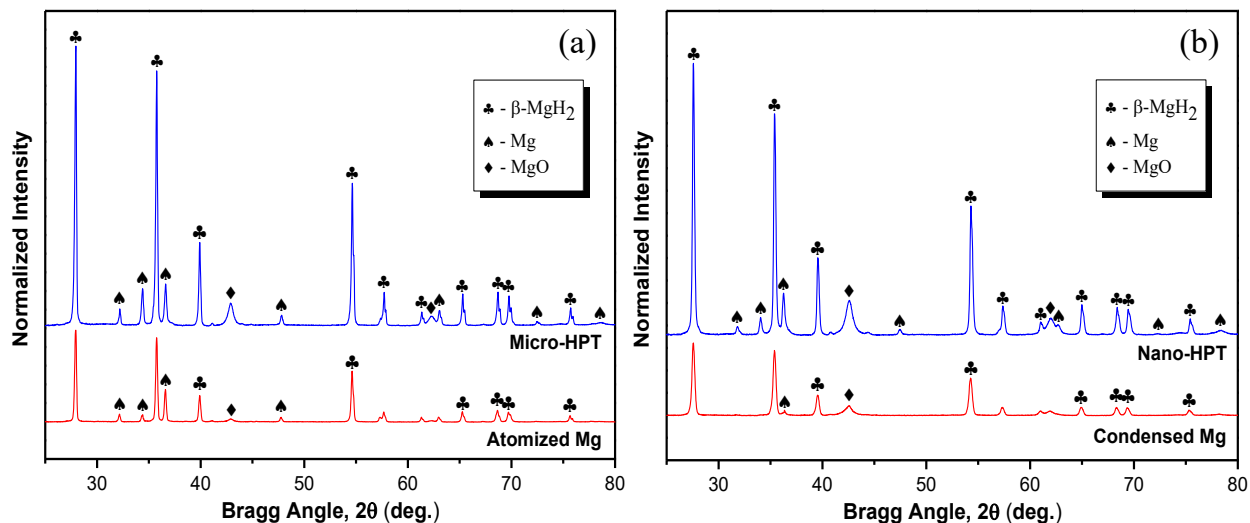


**Figure 4.5** – X-ray diffraction (XRD) patterns recorded from the hydrided samples for (a) the atomized powder and its micro-HPT product and (b) the condensed powder and its nano-HPT product.

The quantitative phase composition of the hydrided samples was determined from the XRD analyses using the Reference Intensity Ratio (RIR) method [2.9]; the results are summarized in Table 4.4. As can be noted, the approximate values of the  $MgH_2$  formed in each sample are well consistent with the results representing the hydrogen contents obtained from the absorption profiles. It is obvious that the extent of hydrogenation reaction was lower in the atomized powder containing significant amounts of non-reacting Mg. Among the assessed samples, the ultrafine condensed powder containing negligible amounts of non-reacting Mg was almost completely transformed into the  $MgH_2$  phase.

**Table 4.4** – The steady-state hydrogen uptake capacity and the phase composition of the hydrogenated samples.

Samples	H uptake (wt%)	MgH <sub>2</sub> (wt%)	Mg (wt%)	MgO (wt%)
Atomized Mg	6.2	79.8 ± 1.5	18.0 ± 1.2	2.2 ± 0.5
Micro-HPT	6.6	86.3 ± 1.0	7.9 ± 2.0	5.8 ± 1.1
Condensed Mg	7.0	88.1 ± 1.7	3.1 ± 0.5	8.8 ± 1.4
Nano-HPT	5.5	83.2 ± 0.5	8.4 ± 1.0	8.4 ± 0.9

### 4.3 Desorption performances

The hydrogen desorption behaviors of the final hydrogenated samples were investigated by simultaneous differential scanning calorimetry–thermogravimetry (DSC-TG) measurements, and the corresponding DSC-TG curves for a heating rate of 10 °C/min are presented in Figure 4.6. The characteristic desorption properties subtracted from the DSC-TG analyses are given in Table 4.5. The amount of desorbed H was determined from the TG curves.

It is apparent from Figure 4.6(a) that the DSC curve of the atomized powder is substantially sharper than that of its micro-HPT product, whereas the latter possesses much lower desorption temperatures. Upon SPD processing of the atomized powder, the onset temperature of desorption and the corresponding peak maximum values are reduced to 403.0 °C and 421.0 °C with respect to their initial values of 427.9 °C and 445.0 °C, respectively. However, the atomized

powder exhibited a faster desorption kinetics than that of its HPT product (2.88 vs. 1.92 wt%/min, see Table 4.5). As noticed from Figure 4.6(b), although both samples show approximately similar peak maxima, the nano-HPT product start to desorb hydrogen at relatively lower temperature range compared to its powder precursor. In addition, as can be noted from Table 4.5 both samples exhibited a similar desorption kinetics under the identical experimental conditions.

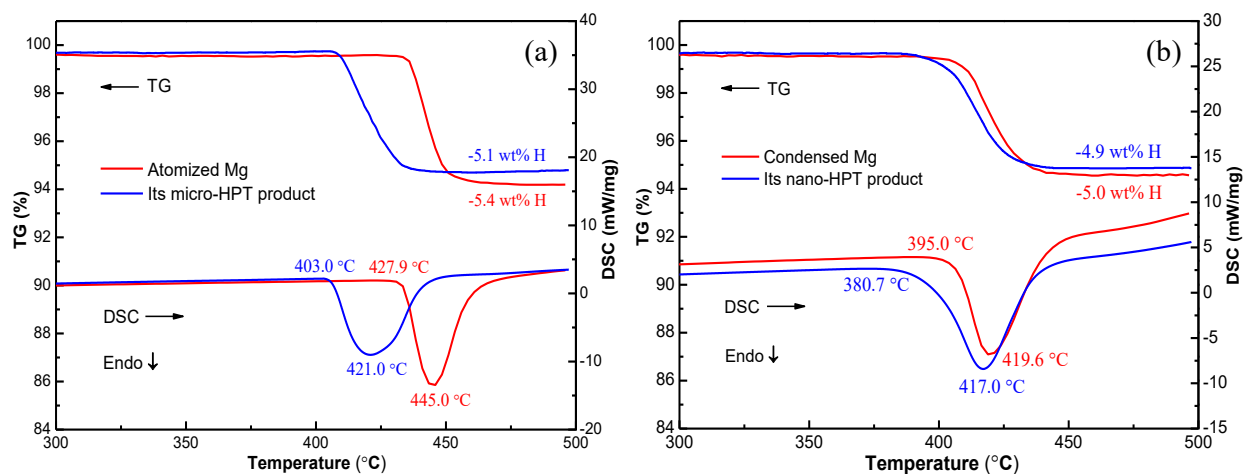


**Figure 4.6** – DSC and TG profiles obtained at a heating rate of 10 °C/min from the hydrided samples for (a) the atomized Mg powder and its micro-HPT product and (b) the condensed Mg powder and its nano-HPT product.

**Table 4.5** - The desorption properties of all the hydrided samples subtracted from the DSC-TG curves.

Samples	Onset of desorption (°C)	Peak temperature (°C)	Desorption kinetics (wt%/min)	H released (wt%)	Desorption activation energy (kJ/mol)
Atomized Mg	427.9	445.0	2.88	5.4	212.0 ± 5.0
Micro-HPT	403.0	421.0	1.92	5.1	170.0 ± 5.0
Condensed Mg	395.0	419.6	1.99	5.0	173.0 ± 7.0
Nano-HPT	380.7	417.0	1.77	4.9	209.0 ± 6.0

In terms of the released hydrogen determined from the calorimetry analysis, it is clear from Table 4.5 that the atomized powder and its micro-HPT product discharge more hydrogen than the condensed powder and its nano-HPT product. It is also readily apparent that the initial powder precursors can desorb relatively more hydrogen than their respective bulk HPT-products. However, these recovered hydrogen quantities are somewhat lower than the hydrogen uptake quantities recorded after the final hydrogenation (see Table 4.4). This difference can possibly be related to the presence of the non-reacting Mg and MgO oxides detected from the XRD analysis of the hydrided samples (see Figure 4.5).

In order to characterize the desorption kinetics, apparent activation energy for desorption was determined on the basis of DSC analysis using the Kissinger method [2.15]. The activation energies for all studied samples are listed in Table 4.5. The HPT processing of the atomized powder precursor led to the reduction in dissociation energy barrier related to the breaking up of

the M-H bonds compared to the powder sample, resulting in relatively lower activation energy for the micro-HPT product. On the contrary, the lower activation energy for the condensed powder can be associated with the fact that the individual powder particles in the loose powder can be able to discharge hydrogen in a faster way than that from the consolidated volume, which has a large fraction of grain boundaries.

#### 4.4 Microstructural modifications upon cycling

In order to visualize the morphological as well as the structural modifications upon absorption/desorption cycles, the final hydrogenated samples were characterized by a scanning electron microscope (SEM-Zeiss Supra40). The effects of the treatments can be clearly visible in the SEM images as shown in Figures 4.7 and 4.8.

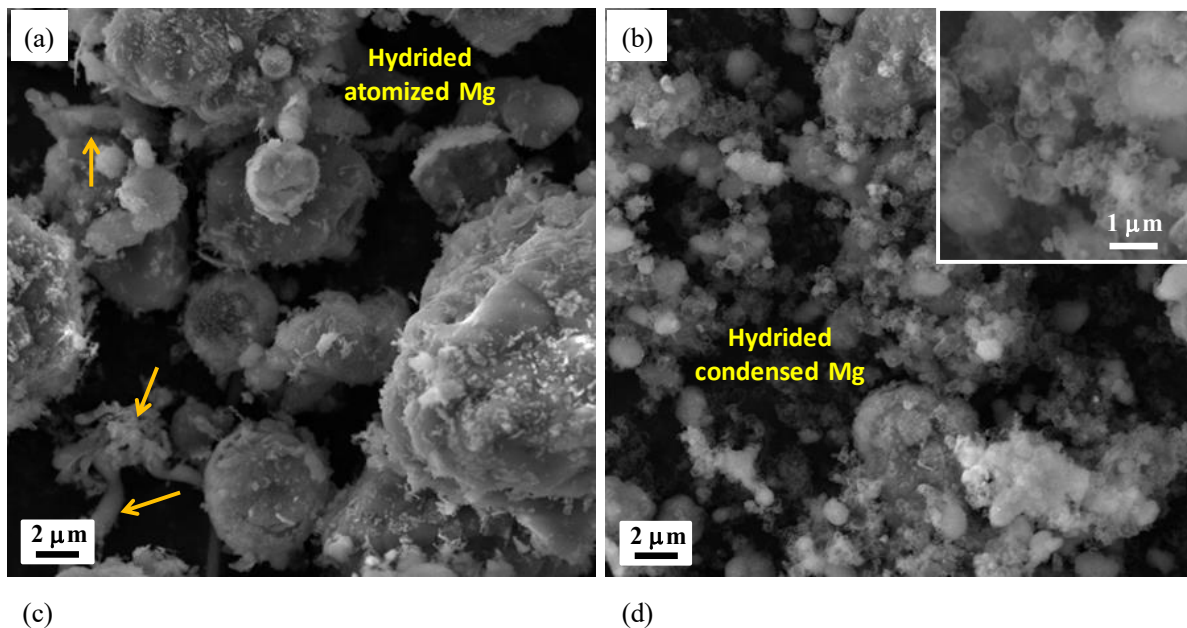


**Figure 4.7** – SEM micrographs illustrating the morphological modifications upon absorption/desorption cycling for (a) the atomized powder and (b) the condensed powder.

For the hydrided atomized powder, an advanced stage of sintering process between powder particles can be identified from Figure 4.7(a), which basically creates particle agglomeration. The particle agglomeration upon cycling was also observed in other studies [4.7-4.9]. It is interesting to notice some worm-like structures that appeared upon cycling in this sample as indicated by arrows. In contrast, the hydrided condensed powder particles were less affected upon cycling and retained their original particle morphology (see Figure 4.7(b)). This fact could be related to the presence of the oxide layers coated the condensed powder particles during the passivation after condensation that prevented particle coarsening. The transparency of the nanoparticles as shown in the inset is clearly due to the complete hydride formation of the nanocrystalline single crystals in this condensed powder.

In case of the hydrided HPT-products (see Figure 4.8), significant amounts of microcracks were generated within the interior of the bulk materials (shown by arrows), probably due to the repetitive volume expansions during the absorption/desorption operations. It should be noted that these crack propagations were more pronounced for the micro-HPT product than that of its nano-counterpart. As far as the microstructure is concerned, while there has been limited grain growth for both the HPT-products, the microstructure of the nano-HPT product is seemed to be somewhat altered from its as-processed elongated microstructural features. However, there are some areas where the nano-HPT product retained its original elongated features (see Figure 4.8(b), delimited by lines) while leading to some extent of grain growth.

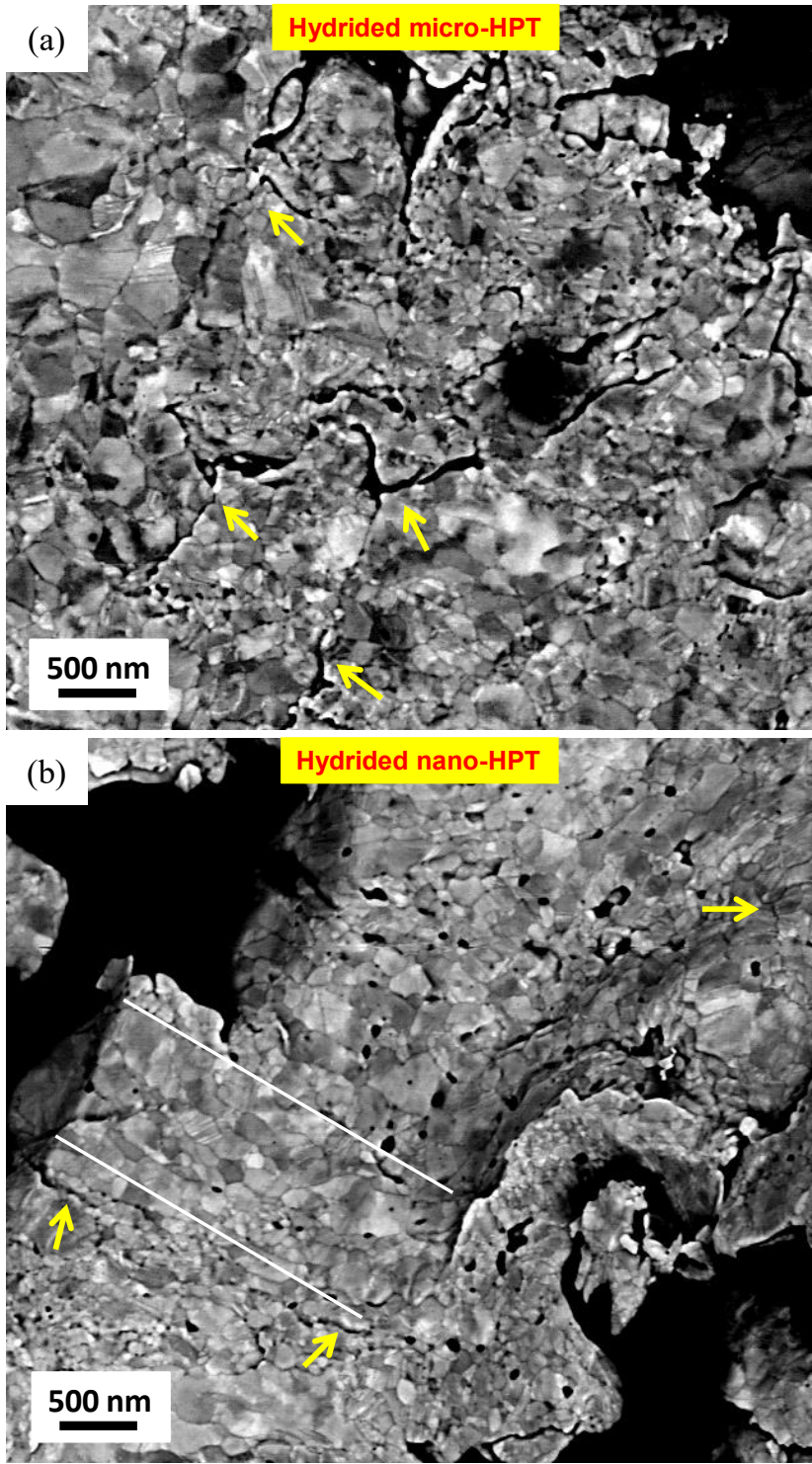


**Figure 4.8** – Representative backscattered electron (BSE) micrographs of the hydrided HPT-products showing the microstructural evolutions upon absorption/desorption cycling.

## **4.5 Discussion**

The current investigation revealed that, despite a substantial amount of severe plastic deformation imparted by the HPT processing to the two types of Mg powders, the exact nature of the starting powder precursors had a pronounced effect on the hydrogen sorption properties while comparing with their powder counterparts. In addition, it was also noted that the hydriding/dehydriding cycling has substantially altered the microstructural features of the two types of powder precursors and their HPT-consolidated products. These aspects are recalled and discussed hereafter in the following sub-sections.

### **4.5.1 Consequences of the processing route**

The effect of the HPT processing has been analyzed by activating the HPT-products at 400 °C under a hydrogen pressure of 3.5 MPa in comparison with their initial powder precursors (Figure 4.1). Subsequently, they were employed for absorption/desorption thermodynamics and kinetics measurements conducted at different temperatures (Figures 4.2 and 4.4). The thermodynamics, kinetics and hydrogen desorption properties were compared between the loose powder particles and their HPT-consolidated products (Tables 4.1-4.5).

For both types of powder precursors, through the introduction of structural defects, the effect of the HPT processing was to enhance substantially the kinetics of hydrogen sorption while reducing the storage capacity. The effect of severe plastic deformation processing routes on hydrogen sorption properties has been reported by many authors, particularly for the first hydrogenation kinetics [1.32,1.39,1.41,1.42,1.15,4.10]. The enhancement in activation kinetics was mainly attributed to the structural defects such as dislocations, twin boundaries, and

microcracks, and sometimes due the developments of crystallographic texture. It was pointed out in **Chapter 3** that a rather homogeneous and nanometric grain structured was developed for the nano-HPT product than that of its micro-counterpart, and the former was also associated with several structural defects such as micro-cracks/porosities, large fraction of high angle grain boundaries etc. Hence, the nano-composites performed better hydrogenation kinetics than the micro-HPT product. While the enhancement of hydrogenation kinetics can be associated with such structural defects, the earlier saturation in the hydrogen storage capacities for the HPT-products could be attributed to the incomplete hydrogenation of the rather bulk consolidated products restricting further hydrogen diffusion into the interior of the bulk materials. The presence of un-reacted Mg phase in the XRD patterns of the hydrided products (see Figure 4.5) is clearly due to the consequence of the incomplete hydrogenation for the HPT-products.

Furthermore, another advantage of the HPT processing is that it reduces the hysteresis between the absorption and desorption plateau pressures and improves the enthalpy and entropy of hydride formation (see Table 4.2). For both the HPT-products, the effects of HPT processing have provided significant reduction in the apparent activation energy for absorption (see Table 4.3) compared to their powder precursors. Another important aspect of the HPT processing was to improve the desorption properties of metal hydrides. The HPT consolidation of the atomized powder has substantially reduced the desorption temperatures for the micro-HPT product while concurrently diminishing the desorption kinetics (see Table 4.5). Similarly, the nano-HPT composite exhibited a much lower onset temperature than that of its powder precursor while their peak maxima were within the same temperature ranges. The improvement in desorption properties upon SPD processing have also been reported by other group of researchers

[4.11,4.12], which was mainly attributed to the microstructural modifications and the structural defects induced due to the severe plastic deformation routes.

#### **4.5.2 Influences of the nature of initial powder precursors**

The overall absorption kinetics was faster for the condensed powder and its Mg-MgO nano-composites in comparison with that of the atomized powder and its micro-HPT product. The enhanced hydrogenation of the condensed powder was most probably associated with its nanocrystalline morphology accompanied with large surface areas, shorter diffusion paths, and the potential catalytic effects of MgO oxides. While the presence of an MgO layer is often regarded as an obstacle for hydrogen sorption – since it prevents the hydrogen atoms from entering into the Mg substrate [1.14] - it is claimed that a faster hydrogen uptake rate can be achieved due to the presence of oxides that can basically serve as nucleation sites for hydride growth. In addition, it has also been reported in Refs. [1.54,1.56] that if MgH<sub>2</sub> is well intermixed with MgO, an improved hydrogen sorption kinetics is obtained due to the reduced particle size of MgH<sub>2</sub> and some catalytic effects of MgO particles on absorption kinetics. In terms of storage, the only disadvantage with MgO was that it has impaired the storage capacity in the condensed powder and its nano-HPT composites in comparison with the atomized powder and its micro-HPT product having less contaminated by oxides.

In terms of desorption, the atomized powder exhibited a relatively faster desorption kinetics than that of the condensed powder particles (2.88 vs. 1.99 wt%/min), which could be related to its higher peak temperature for the atomized powder. Indeed, the condensed powder precursor revealed much lower desorption temperatures (395.0 and 419.6 °C vs. 427.9 and 445.0

°C), possibly due to the ultrafine-grained particle sizes and the catalytic activities of the oxide phase. In the case of consolidated products, the effect of the HPT consolidation was, for both precursors, to reduce the onset of desorption and the peak temperatures. This is particularly true for the atomized powder precursor (Table 4.5). It was further revealed that after some incubation, the micro-HPT product showed a faster desorption rate (1.92 wt%/min) accompanied with much lower activation energy ( $E_a = 170.0 \pm 5.0$  kJ/mol H<sub>2</sub>) than its nano-counterpart (1.77 wt%/min and  $209.0 \pm 6.0$  kJ/mol H<sub>2</sub>).

Furthermore, it was also observed that upon thermal decomposition of the hydrided products the atomized powder and its micro-HPT product recovered more hydrogen in comparison with their nanometric counterparts (Table 4.5). The EBSD analyses revealed that the nano-HPT composite contained a much higher fraction of high angle grain boundaries (HAGBs) than its micro-HPT counterpart (see Figures 3.11 and 3.12, **Chapter 3**). It is believed that these HAGBS can act as potential trapping sites for hydrogen, and thereby, can hinder or prolong the dehydrogenation reaction of metal hydrides. This interpretation corroborates the findings of Edalati et al. [4.13] on Ti-V-Cr alloys. Indeed, in a comparative study of the hydrogen sorption behavior of the bulk SPD by HPT and surface SPD by SMAT, the authors found that the HPT material containing highly misoriented ultrafine grains could not release the hydrogen that was rapidly trapped on charging [4.13]. While the lowering in hydrogen discharge quantities for the condensed powder and its nano-HPT product can be attributed to the large fraction of grain boundaries, the associated nano-sized oxide particles uniformly distributed throughout the Mg matrix might have accelerated the earlier decomposition of metal hydrides due to its catalytic

activities. This, however, suggests that some trapping sites at the Mg/MgO interfaces were less effective than the true Mg/Mg boundaries in this type of consolidated products.

### **4.5.3 Effects of the absorption/desorption cycling**

While the reduction in the hydrogen storage capacity for the atomized powder (i.e. from 7.6 to 6.2 wt% H) can be readily attributed to its microstructural modifications upon cycling (see Figure 4.7), at the same time the generation of numerous microcracks within the initial microstructure of the micro-HPT product might have enhanced its hydrogen uptake capability (6.1 to 6.6 wt% H after cycling). On the contrary, the presence of MgO oxide phase in the condensed powder particles as well as its nano-HPT composites could have limited the microstructural modifications upon cycling (see Figures 4.7 and 4.8). For the condensed powder particles, a thin layer of MgO oxide formed during the passivation process has significantly prevented the alteration of particle morphology compared to the atomized powder precursor containing fewer oxides. Similarly, the initial nanostructural features in the nano-HPT product have been retained most probably due to the Zener pinning effects of the oxide particles on the migrating grain boundaries. Due to this effect, the condensed powder and its consolidated products did not show deterioration in their hydrogen storage capacities even after the repetitive absorption/desorption cycles. Thus, it can be assumed that the HPT-processed samples could have better mechanical stability than their powder counterparts when exposed to repetitive thermal treatments at very high operating temperatures.

## **Chapter's conclusions**

A comparative study on hydrogen storage performances of two types of HPT consolidated magnesium products and their initial powder precursors was conducted using a Sievert type apparatus. The modifications in hydrogen sorption properties were assessed by examining the activation kinetics as well as the thermodynamics of absorption/desorption cycles and the kinetics of hydrogen absorption. Desorption properties of the final metal hydrides were investigated by calorimetry analysis. The effects of hydriding/dehydriding cycling on the alteration of microstructures was evaluated by SEM study of the final hydrided products. The main findings from the present study can be summarized as follows.

- 1) For both types of powder precursors - the atomized micro-sized powder and the condensed ultrafine powder, - through the introduction of structural defects and microstructural refinement, the HPT processing has provided with significant improvements in the hydrogenation kinetics for the HPT-products compared to their initial powder precursors.
- 2) A significant advantage of the HPT processing was to reduce the hysteresis between the absorption and desorption plateau pressures during the PCT experiments.
- 3) The nano-HPT composites characterized by elongated nanometric Mg domains - which were essentially pinned by the fine MgO oxide particles - showed faster absorption kinetics with respect to the micro-HPT materials and presented much lower apparent activation energy ( $E_a = 43.0 \pm 2.0$  kJ/mol H<sub>2</sub>). This could be attributed to its nanometric microstructure and the catalytic effect of the uniformly dispersed MgO oxide particles. In contrast, its initial powder precursors had the advantage of having slightly higher hydrogen storage capacity.

- 4) While the HPT processing of the condensed powder led to the reduction in hydrogen storage capacity of the nano-HPT composites, it showed significant improvements in the storage capacity of the micro-HPT product obtained from the atomized powder.
- 5) The micro-HPT product obtained from the atomized powder precursors presented a significant decrease in the desorption temperatures compared to the loose powder while diminishing the desorption kinetics. Furthermore, despite the fact that the nano-HPT product revealed a slightly lower onset of desorption, they exhibited slower desorption kinetics and higher activation energy than the micro-HPT product.
- 6) The types of grain boundaries in the consolidated products play an important role on the desorption properties of metal hydrides. The large fraction of HAGBs and Mg/MgO interfaces in the nano-HPT composite significantly affect its desorption kinetics and hydrogen release capacity in comparison with the micro-HPT product having less contaminated by oxides and associated with large fraction of low angle GBs.
- 7) The HPT-consolidated products were less affected by the absorption/desorption heat treatments than their initial powder precursors. Particularly, the original particle morphology of the atomized powder was significantly modified upon cycling and consequently it revealed a lower hydrogen storage capacity than that of its micro-HPT product (6.2 vs. 6.6 wt% H).

## References

- [4.1] Barkhordarian G, Klassen T, Bormann R. “Fast hydrogen sorption kinetics of nanocrystalline Mg using Nb<sub>2</sub>O<sub>5</sub> as catalyst.” *Scr. Mater.* 49 (2003) 213-17.
- [4.2] Cakmak G, Ozturk T. “ECAP processing and mechanical milling of Mg and Mg–Ti powders: a comparative study.” *J. Mater. Sci.* 46 (2011) 5559-67.
- [4.3] Korznikov AV, Safarov IM, Laptionok DV, Valiev RZ. “Structure and properties of superfine-grained iron compacted out of ultradisperse powder.” *Acta Mater.* 39 (1991) 3193-97.
- [4.4] Revesz A, Kánya Z, Verebelyi T, Szabo PJ, Zhilyaev AP, Spassov T. “The effect of high-pressure torsion on the microstructure and hydrogen absorption kinetics of ball-milled Mg<sub>70</sub>Ni<sub>30</sub>.” *J. Alloys Compd.* 504 (2010) 83-8.
- [4.5] Vajo JJ, Mertens F, Ahn CC, Bowman RC, Fultz B. “Altering hydrogen storage properties by hydride destabilization through alloy formation: LiH and MgH<sub>2</sub> destabilized with Si.” *J. Phys. Chem. B* 108 (2004) 13977-83.
- [4.6] Mintz MH, Zeiri Y. “Hydriding kinetics of powders.” *J. Alloys Compd.* 216 (1995) 159-75.
- [4.7] Gattia DM, Montone A, Pasquini L. “Microstructure and morphology changes in MgH<sub>2</sub>/expanded natural graphite pellets upon hydrogen cycling.” *Int. J. Hydrogen Energy* 38 (2013) 1918-24.
- [4.8] Nachev S, De Rango P, Fruchart D, Skryabina N, Marty P. “Correlation between microstructural and mechanical behavior of nanostructured MgH<sub>2</sub> upon hydrogen cycling.” *J. Alloys Compd.* 645 (2015) S434-7.
- [4.9] Gattia DM, Montone A, Di Sarcina I, Nacucchi M, De Pascalis F, Re M, Pesce E, Antisari MV. “On the degradation mechanisms of Mg hydride pellets for hydrogen storage in tanks.” *Int. J. Hydrogen Energy* 41 (2016) 9834-40.
- [4.10] Edalati K, Akiba E, Horita Z. “High-pressure torsion for new hydrogen storage materials.” *Sci. Tech. Adv. Mater.* 19 (2018) 185-93.
- [4.11] Skryabina N, Medvedeva N, Gabov A, Fruchart D, Nachev S, de Rango P. “Impact of Severe Plastic Deformation on the stability of MgH<sub>2</sub>.” *J. Alloys Compd.* 645 (2015) S14-7.
- [4.12] Leiva DR, Chanchetti LF, Floriano R, Ishikawa TT, Botta WJ. “Exploring several different routes to produce Mg-based nanomaterials for Hydrogen storage.” *IOP Conf. Ser.: Mater. Sci. Eng.* 63 (2014) p. 012115.
- [4.13] Edalati K, Novelli M, Itano S, Li HW, Akiba E, Horita Z, Grosdidier T. “Effect of gradient-structure versus uniform nanostructure on hydrogen storage of Ti-V-Cr alloys: Investigation using ultrasonic SMAT and HPT processes.” *J. Alloys Compd.* 737 (2018) 337-46.

# CHAPTER 5: HYDROGEN STORAGE PROPERTIES OF Mg-Fe BASED COMPOSITES FABRICATED BY HIGH-PRESSURE TORSION CONSOLIDATION OF MAGNESIUM AND IRON POWDER PRECURSORS

---

Introduction .....	146
5.1 Structural characterizations of the HPT composites .....	150
5.1.1 Consolidated microstructures .....	150
5.1.2 XRD analysis of the HPT composites .....	154
5.1.3 XRD analysis of the hydrided products .....	157
5.2 First hydrogenation kinetics .....	159
5.3 Hydrogen sorption properties .....	160
5.3.1 Thermodynamics of absorption/desorption .....	160
5.3.2 Kinetics of hydrogen absorption .....	167
5.3.3 Hydrogen desorption by thermal decomposition .....	170
5.4 Discussion .....	175
5.4.1 Effects of the processing route .....	175
5.4.2 Nature of the initial powder precursors .....	177
5.4.3 Catalytic effects .....	179
Chapter's conclusions .....	182
References .....	184

## **Introduction**

Magnesium based materials are attractive candidates for storing of hydrogen and/or using as thermochemical energy reservoirs [1.19,1.20,5.1], partly due to its ability to form simple hydrides ( $\text{MgH}_2$ ), and ternary complex hydrides when combines with transition metal elements (Fe, Co, Ni). Among the complex hydrides, the  $\text{Mg}_2\text{FeH}_6$  stands out primarily due to its highest known volumetric storage density ( $150 \text{ kg H}_2 \text{ m}^{-3}$ ) and lower hydrogen dissociation pressure at elevated temperatures [5.2]. In addition, it is formed by low cost metallic elements, while its hydrogenation reaction is reversible and has very high cyclic stability [5.1]. Zhou et al. [5.3] claimed that  $\text{Mg}_2\text{FeH}_6$  can reduce the structural stability of  $\text{MgH}_2$ , which, in turn, improves the dehydrogenation properties. However, as Mg and Fe do not form any intermetallics under equilibrium conditions [5.4], the synthesis of this complex hydride is not trivial.

Different processing routes have been employed to synthesize the  $\text{Mg}_2\text{FeH}_6$  compound. A more versatile processing route - reactive ball milling at room temperature under hydrogen atmosphere which involves one-step synthesis of metal hydrides - was recently employed by Asselli et al. [5.5,5.6] to prepare the  $\text{Mg}_2\text{FeH}_6$  hydride from a stoichiometric mixture of 2Mg-Fe. They reported that the hydrogen uptake capacity increased from 3.2 to 5.2% when changed the proportions to 3Mg-Fe, due to the nearly complete consumption of the metallic elements, and also the presence of  $\text{MgH}_2$  phase. However, the processing by ball milling can suffer from several drawbacks. Firstly, impurities coming from the milling tools and gas adsorption are hard to control and can affect significantly the H-sorption properties [I.14]. Also, even if effective at laboratory scale, the high energy ball-milling (HEBM) in terms of power and time as well as

potential safety concerns of handling the metal hydrides pose problem of scaling up towards industrial levels. Therefore, low cost and easily accessible techniques that could replace the HEBM should be investigated.

The application of SPD techniques has provided with significant improvements in hydrogen activation processes of metallic materials [1.31,5.7-5.9], and the SPD processed materials are found to be good for air-resistant and thermal stability [5.9]. However, one of the drawbacks of these SPD techniques when applied on bulk samples - compared to HEBM for example, where different nature of powders can be mixed - is that the chemistry of the sample before processing is fixed, so that it becomes difficult to introduce small fractions of catalysts. Lima et al. [5.10] have first attempted to synthesize Mg-Fe based bulk metal hydrides by hydrogenation of samples processed by high-pressure torsion (HPT) of a powder mixture of 2Mg-Fe. They reported a thermodynamic destabilization of the hydrides due to the high density of dislocations in HPT-processed samples, that led to the reduction in hydrogen desorption temperatures. In other studies, Lima and co-workers [5.11,5.12] investigated the extruded Mg-Fe alloy for hydrogen sorption improvements with or without presence of carbon additives. They claimed that the addition of carbon mainly accelerated the formation of porosities, which in turn, enhanced the desorption kinetics of the  $Mg_2FeH_6$  and  $MgH_2$  hydride mixtures [5.12].

Motivated by a limited number of studies focusing on severe plastic deformation applied on powder samples to produce Mg-Fe based composites for hydrogen storage applications [5.10-5.12], and also following the approach initiated in **Chapter 3** (the effect of the nature of the initial powder precursors), in the present study Mg-Fe based composites in two atomic

stoichiometries (i.e. 9Mg-Fe and 2Mg-Fe) have been processed by a two-step HPT consolidation. The details of this two-step HPT procedure can be referred to the section 2.2.3, **Chapter 2**. Thus, two types of powder precursors - atomized micro-sized powder and condensed ultrafine powder - in both Mg and Fe phases were employed to study the effect of nature of the initial powder precursors on hydrogen sorption properties of the Mg-Fe composites.

Accordingly, five types of composites in the two stoichiometric ratios (i.e. 9Mg-Fe and 2Mg-Fe) were processed using a variety of powder combinations. The labeling, compositional details and the processing conditions of these five composites are given in Table 5.1. For the sake of simplicity in the reading of this chapter, the micro-sized atomized powder is referred with an “m” while the ultrafine condensed one is labeled with an “n”. The composites are thus abbreviated based on the nature of their precursor powder materials and the corresponding at% of Fe phase. For example, in the mMg-10nFe composite, mMg stands for micro-sized Mg and 10nFe refers to 10 at% of nano-sized Fe particles. As can be seen from Table 5.1, three composites namely, mMg-10mFe, mMg-10nFe and nMg-10nFe were designed for the 9Mg-Fe composition (10 at% Fe), while mMg-33mFe and nMg-33nFe composites were processed for the 2Mg-Fe stoichiometry (33 at% Fe). A short-time mixing was carried out for all the composites in a reciprocating vessel (without steel/ceramic balls) for 30 min at a vibrational frequency of 20 Hz to ensure a uniform distribution of the ingredient materials before the HPT treatments.

Hydrogen sorption properties of the HPT composites were characterized by using a conventional Sievert type pressure-composition-temperature (PCT) volumetric apparatus. Prior to hydrogen storage measurements, the bulk HPT composites were broken by a ceramic mortar to micrometer range powder particles to fit into the testing vessel. The ground samples were first

activated by dynamic hydrogen absorption at 400 °C for 8 h under a hydrogen pressure of 3.5 MPa followed by hydrogen desorption at the same temperature under vacuum until complete dehydrogenation. These one-cycled samples will be referred to as activated products in the subsequent text. The subsequent thermodynamic and kinetic measurements were performed following the identical procedure as the one described in **Chapter 4**. The structural evolutions before and after hydrogenation treatments were characterized by the XRD and SEM analyses.

**Table 5.1** – The compositional details of the HPT-consolidated composites, and their processing conditions applied in the present study.

Stoichiometric ratios	Name of the HPT composite	Powder precursors	HPT consolidation <sup>ξ</sup>	
			Pre-compaction	HPT
9Mg-Fe (10 at% of Fe)	mMg-10mFe	micro-sized Mg and micro-sized Fe	At room temperature, $P = 1.5$ GPa, $t = 10$ min	At room temperature, $P = 1.2$ GPa, $\omega = 0.125$ rpm, $N = 2$ turns
	mMg-10nFe	micro-sized Mg and nano-sized Fe		
	nMg-10nFe	nano-sized Mg and nano-sized Fe		
2Mg-Fe (33 at% of Fe)	mMg-33mFe	micro-sized Mg and micro-sized Fe		
	nMg-33nFe	nano-sized Mg and nano-sized Fe		

<sup>ξ</sup> $t$  = holding time,  $P$  = compressive pressure,  $\omega$  = rotational speed,  $N$  = number of turns

## **5.1 Structural characterizations of the HPT composites**

### **5.1.1 Consolidated microstructures**

Secondary electron (SE) and some backscattered electron (BSE) micrographs of the HPT-processed composites in the 9Mg-Fe and 2Mg-Fe stoichiometry are given in Figure 5.1 and 5.2, respectively. In both types of grades, the brighter areas correspond to either Fe-rich domains or oxides while the dark areas are related to microcracks or porosities (delimited by yellow contours in Figure 5.1). Due to the micro-sized powder precursors in the mMg-10mFe composite, Figure 5.1(a) presents a lower magnification SE image demonstrating the deformation characteristics of the Fe particles together with Mg matrix while Figure 5.1(b) describes the detailed features of their interactions at higher magnification.

It has been shown in earlier studies related to HPT processing of bulk thick-samples that the shear deformation can be significantly localized in the middle-section of the HPT-disks when processed under quasi-constrained conditions [3.20]. Examples of shear localization are clearly visible in Figures 5.1(b, c). The shear localization is often accompanied by some cracking along the shear direction (see arrows in Figures 5.1(b, c)). This heterogeneous nature in shear deformation and associated strain localizations was also noticed for bulk Mg [3.20], and AZ31 or AZ91 Mg alloys [3.3,5.13] processed by HPT. They are mainly attributed to the inherent brittleness of Mg or its alloys as a consequence of the failure to fulfill von Mises criterion of five independent slip systems [5.14], when processing at room temperature. In the lower part of Figure 5.1(b), the material flow essentially followed these shear domains while the upper part seems to be oriented towards the applied shear direction at an angle of  $\sim 45^\circ$ . The bright Fe domains are typically aligned along these directions. Furthermore, it can be observed that the

massive shear straining by HPT has led to the formation of a dynamically recrystallized microstructure with an average grain size of about 500 nm. The occurrence of dynamic recrystallization was also reported in the **Chapter 3** while investigating the HPT consolidation of atomized Mg powder particles without Fe additives. As can be noticed from Figure 5.1(a), the Mg and Fe domains are rather well intermixed but some large domains of mFe particles were also prevailed.

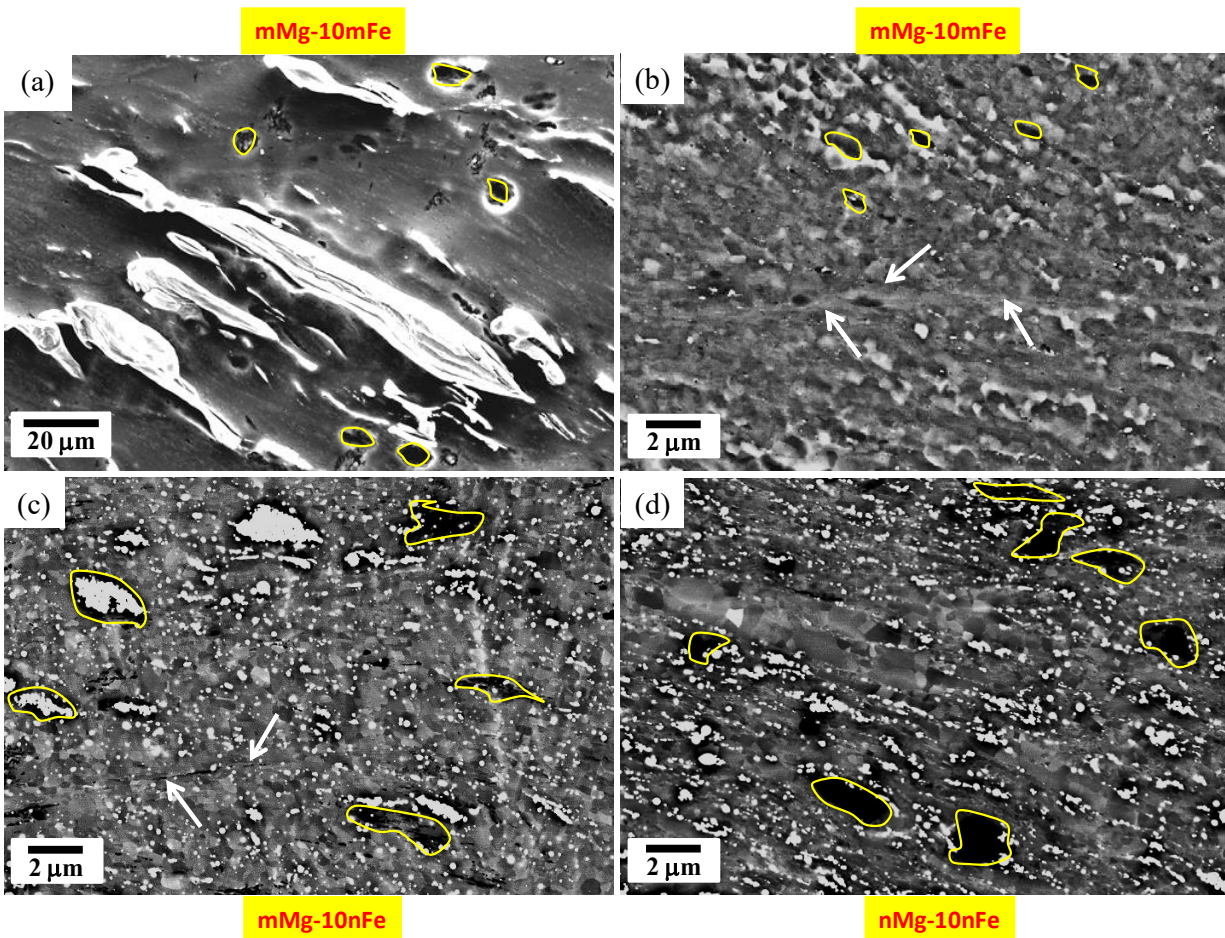


**Figure 5.1** – (a) SE and (b-d) BSE micrographs acquired on the middle-thickness of the HPT-disks for the (a, b) mMg-10mFe, (c) mMg-10nFe and (d) nMg-10nFe composites for the 9Mg-Fe stoichiometry.

As noticed from Figure 5.1(c), the mMg-10nFe composite displays some clustering of the nFe particles that were squeezed between the mMg particles. Apart from these clustering of aggregated particles, a rather random distribution of the nFe particles is also observed. Due to the limited oxide content in the atomized powder, dynamic recrystallization of the mMg matrix phase took place. However, due to the uniform distribution of nFe particles, the Mg grain size in this composite is slightly lower than in the mMg-10mFe sample (Figure 5.1(b)). As previously mentioned, microcracks are also visible in this composite spreading towards the applied shear-stresses. Since the clustered Fe nanoparticles are very hard and difficult to deform upon shear straining, they are likely to act as hard interfaces from which the microcracks originate. The extreme localization of shear strains at the middle-section of the HPT-disks might have led to the formation of shear bands followed by microcracks as indicated by arrows.

In the case of nMg-10nFe composite (Figure 5.1(d)), the microstructure consists of elongated fine Mg grain domains, separated by nFe particles and/or oxides aligned essentially along the microscopic shear direction. These oxide particles originally present due to the passivation of the ultrafine Mg powder and the hard nFe particles have generated significant Zener pinning on the grain boundaries that has restricted the grain evolution towards elongated domains having an average thickness of about 200 to 300 nm. It should be noted that the shear deformation by HPT has generated significant amounts of microcracks or porosities in this sample. The fact that they are numerous in this composite than in the two previous ones is obviously due to the fact that the nMg powder particles surrounded by a fine oxide layer are more difficult to deform and trend to agglomerate than the mMg particles present in the other two composites.

For the 2Mg-Fe stoichiometry, the corresponding SE and BSE images of the two composites are shown in Figure 5.2. Consistently, while the mMg-33mFe composite shows a substantial deformation of the mFe particles along with Mg matrix (Figures 5.2(a-b)), the clustering of nFe particles is a common feature in the nMg-33nFe composite, Figures 5.2(c-d). Furthermore, due to the higher amounts of Fe particles, these composites might have generated significantly higher amounts of microcracks across the thickness-height as well as through the middle-section of the HPT-disks.

Due to the fewer oxide content in the mMg powder, it can be safely anticipated that most of the white domains in the BSE image of the mMg-33mFe composite is due to the Fe phase only (Figures 5.2(a-b)). Thus, it is noticed that the Fe domains have a bi-modal particle size distribution. Severely fragmented very fine domains in the range of 200 to 300 nm are clearly visible while other domains with relatively larger sizes were elongated along the shear direction (Figure 5.2(b)). Although the Fe particles are heavily deformed along with the Mg matrix, the intermixing between the two phases remains limited and that the strain accommodation was done by the initiation and propagation of microcracks particularly in the Mg matrix but also in the Fe domains leading to their fragmentation. Although the microstructure of the nMg-33nFe composite consists of some clustering of nFe particles, there has been significant intermixing between the ingredient nanoparticles. Again, the orientation of the Fe clusters clearly reveals the shearing direction during the HPT processing.

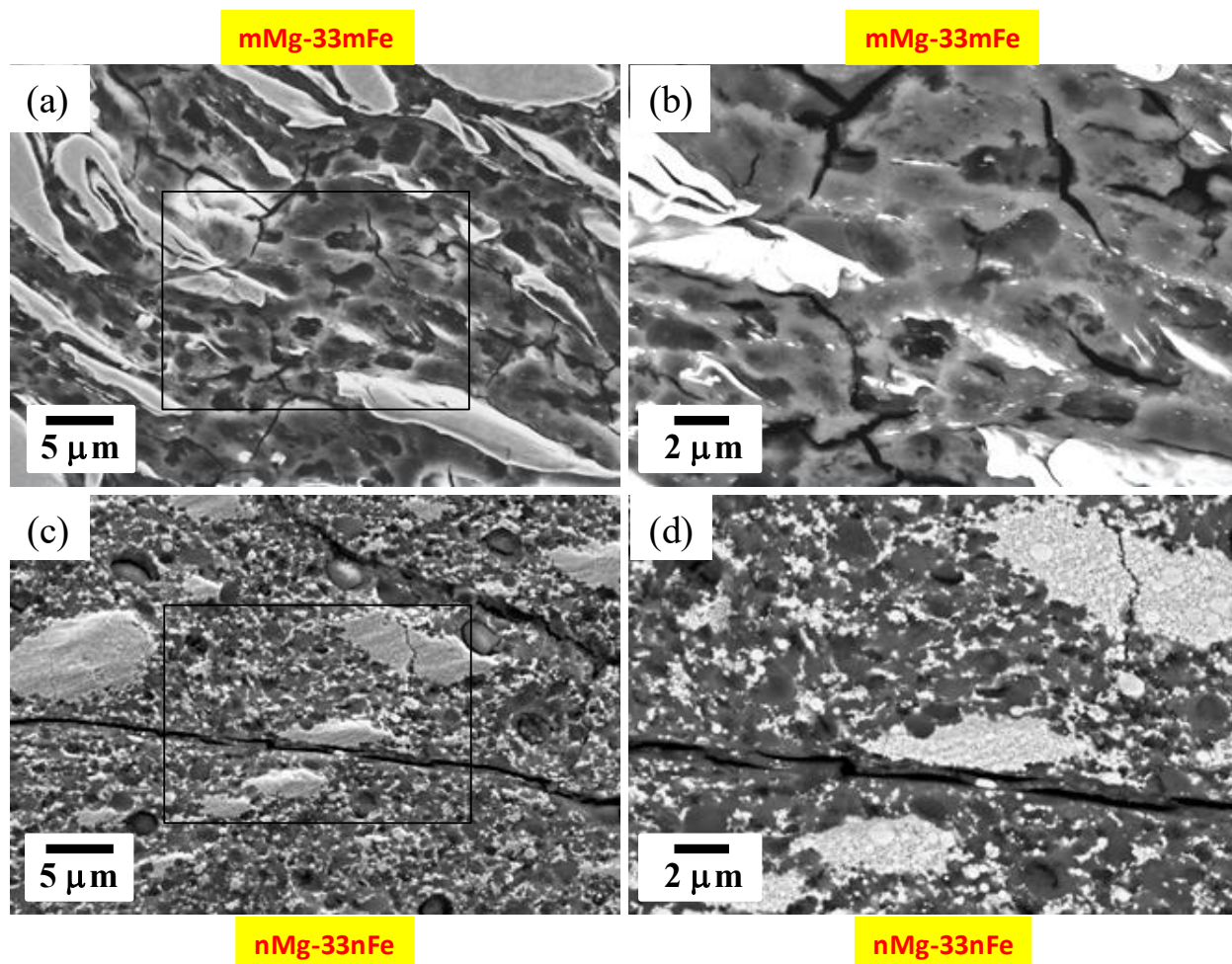


**Figure 5.2** – SE (left) and BSE (right) micrographs obtained from the middle-thickness of the HPT-disks for the (a, b) mMg-33mMg and (c, d) nMg-33nFe composites in the 2Mg-Fe grade.

### 5.1.2 XRD analysis of the HPT composites

The traces of XRD patterns recorded for the HPT-processed composites as well as the final hydrided composites are shown in Figure 5.3 and 5.4, respectively. The main contributor in the XRD patterns of Figure 5.3 is the hcp-Mg phase together with, depending on the stoichiometry, more or less significant amounts of the  $\alpha$ -Fe phase. In addition, a very little amount of MgO is also detected for all the composites. Since the oxide phase was not detected in the initial micro-

sized Mg powder (referred to **Chapter 3**), the powder could have been contaminated during the mixing prior to HPT processing.

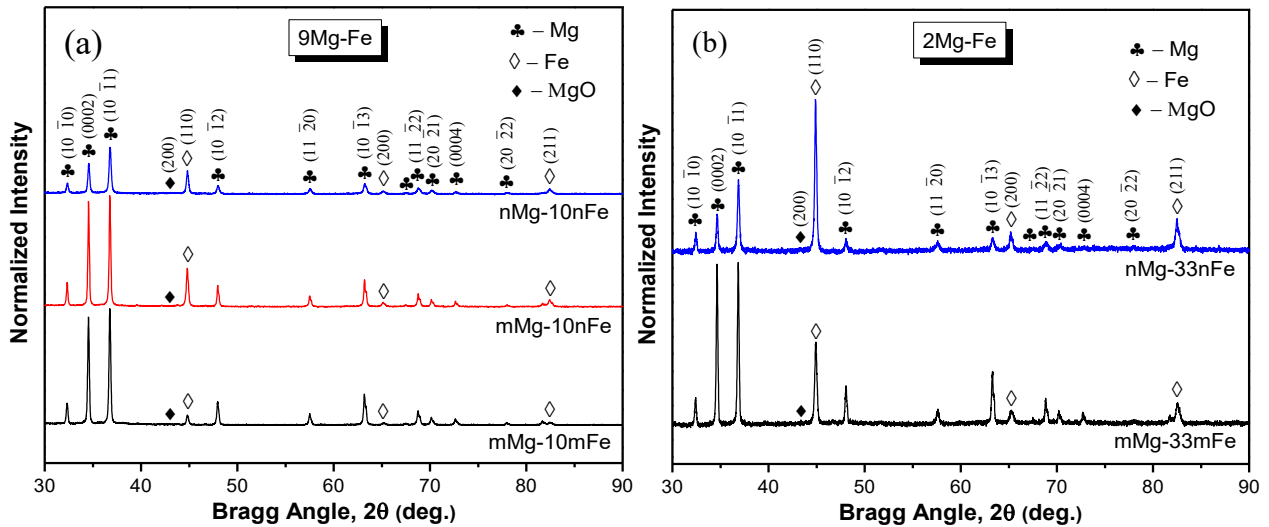


**Figure 5.3** – Normalized X-ray diffraction patterns obtained from the HPT-processed composites for the (a) 9Mg-Fe and (b) 2Mg-Fe stoichiometric ratios.

It is interesting to note that there have been significant differences in the peak intensities for the hcp-Mg phase. Indeed, for both stoichiometry, either the 9Mg-Fe or the 2Mg-Fe, the relative peak intensity for the mMg containing composites shows a different trends than that for the nMg containing composites. In order to interpret these differences, the intensity ratio of the (0002) and (10 $\bar{1}$ 0) planes (i.e.  $I_{0002}/I_{10\bar{1}0}$ ) for all the composites was determined from their corresponding peak maximum and the results are listed in Table 5.2. It is proved that the  $I_{0002}/I_{10\bar{1}0}$  values are considerably higher for the mMg based composites while it has been weak in the nMg containing composites. For the loose mMg and nMg powder, the  $I_{0002}/I_{10\bar{1}0}$  was estimated

to be 1.24 and 1.08, respectively (Table 3.1, **Chapter 3**). Also, the theoretical  $I_{0002}/I_{10\bar{1}0}$  ratio for a loose Mg powder (ICDD-JCPDS card No. 35-0821) can be obtained being 1.44. This clearly indicates that very different kinds of texture have been developed in the SPD composites consolidated from atomized and condensed Mg powders. This fact could be associated with the differences in plastic deformation behaviors of the magnesium matrix coming from the distinct nature of powder precursors. As the XRD measurements were conducted on the plane perpendicular to the torsion axis (i.e. on the disk surface), it is suggested that a basal texture has been developed for the mMg based composites. The current results are well consistent with the findings for the micro-HPT and the nano-HPT product obtained from the atomized mMg and condensed nMg powders, respectively (Table 3.1, **Chapter 3**).

**Table 5.2** – The crystallographic data obtained by XRD profile fit analysis for the HPT-processed composites.

Crystallographic data	mMg-10mFe	mMg-10nFe	nMg-10nFe	mMg-33mFe	nMg-33nFe
$I_{0002}/I_{10\bar{1}0}$ (for Mg)	$4.41 \pm 0.18$	$3.60 \pm 0.11$	$2.27 \pm 0.15$	$6.32 \pm 0.12$	$1.98 \pm 0.16$
Lattice constants of Mg (nm)	a = b = 0.3203 c = 0.5202	a = b = 0.3202 c = 0.5199	a = b = 0.3203 c = 0.5197	a = b = 0.3200 c = 0.5196	a = b = 0.3201 c = 0.5179

Based on the XRD profile fit analysis, the lattice constants of Mg in the Mg-Fe based composites can be calculated, and the values are provided in Table 5.2. The current lattice constants are compared with the values obtained for the HPT bare Mg products. For example, the lattice parameters of the Mg phase for the HPT-consolidated bare Mg products are:  $a = b = 0.3207$  nm and  $c = 0.5207$  nm (for micro-HPT), and  $a = b = 0.3212$  nm and  $c = 0.5215$  nm (for nano-HPT) as described in **Chapter 3**, while the parameters are  $a = b = 0.3203$  nm and  $c = 0.5202$  nm for the corresponding mMg-10mFe composite (after 10 at% mFe addition to mMg) and  $a = b = 0.3203$  nm and  $c = 0.5197$  nm for the nMg-10nFe composite (after 10 at% nFe addition to nMg). Thus, for both types of Mg powder precursors, the lattice constants did not change much after the Fe additions suggesting that there was no atomic diffusion of Fe phase into the Mg crystal. However, a little contraction along the  $c$ -axis with increasing amounts of mFe can be noticed from Table 5.2, while this is more pronounced for the nFe based composites. Since the nFe particles act as hard interfaces and also impose severe constraints to the shear deformation of Mg matrix, they may introduce some crystallographic perturbations into the Mg lattice.

### **5.1.3 XRD analysis of the hydrided products**

The resulting XRD patterns of the 9Mg-Fe based composites (Figure 5.4(a)) mainly consist of  $\beta$ -MgH<sub>2</sub> as the primary phase contributor accompanied with some Mg<sub>2</sub>FeH<sub>6</sub> phase. For the 2Mg-Fe stoichiometry (Figure 5.4(b)), the mMg-33mFe and nMg-33nFe composites consist of a mixture of Mg<sub>2</sub>FeH<sub>6</sub> and  $\beta$ -MgH<sub>2</sub> phases. In addition, MgO and some non-reacted hcp-Mg and  $\alpha$ -Fe phases with varying proportions are also detected for all studied composites.

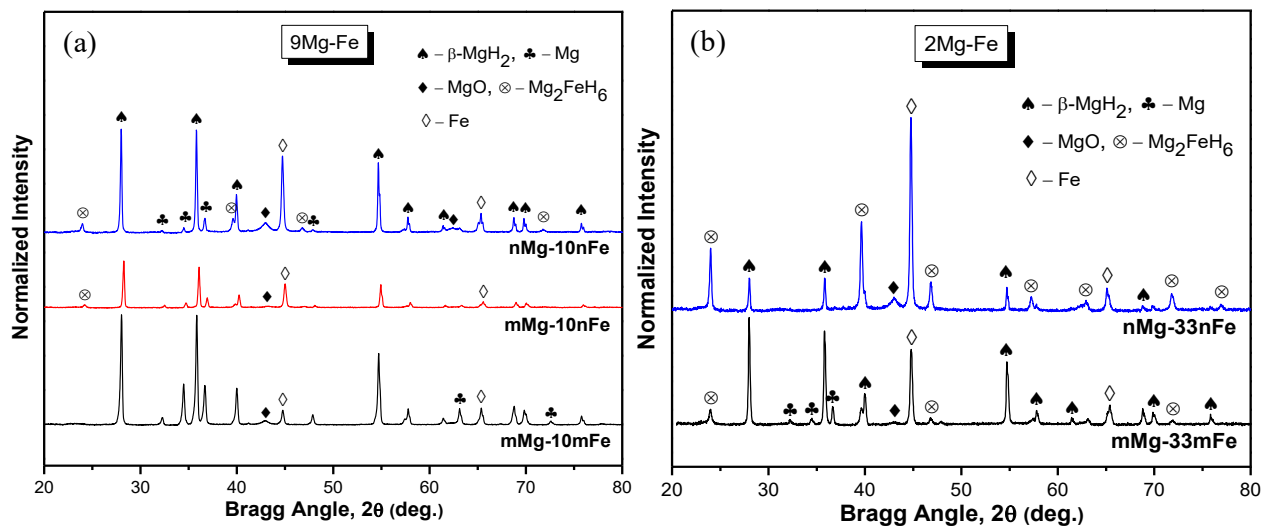


**Figure 5.4** – Normalized X-ray diffraction patterns recorded on the final hydrided composites for the (a) 9Mg-Fe and (b) 2Mg-Fe stoichiometry.

The differences in phase compositions in the respective hydrided products can be speculated from the variations in XRD peak intensities for both stoichiometric composites. It is to be noted that the formation of binary hydride (i.e.  $\text{MgH}_2$ ) varies significantly within the studied composites possibly due to the differences in the powder precursors and the associated microstructural developments. As expected from the stoichiometric compositions, the formation of ternary metal hydride (i.e.  $\text{Mg}_2\text{FeH}_6$ ) increases with increasing amount of Fe additions. It is interesting to note that while the  $\beta\text{-MgH}_2$  phase is the primary component for the mMg-33mFe composite, the nMg-33nFe composite mainly consists of  $\text{Mg}_2\text{FeH}_6$  phase. Furthermore, due to the differences in the initial powder precursors employed in this study, the amount of un-reacted Mg and Fe, also MgO vary significantly in the final hydrided products.

## 5.2 First hydrogenation kinetics

Figure 5.5 gives the first hydrogenation curves obtained by dynamic hydrogen absorption of the assessed composites at 400 °C for 8 h under a hydrogen pressure of 3.5 MPa. In terms of the overall hydrogenation rate of the 9Mg-Fe composites (Figure 5.5(a)), it is obvious that the mMg-10nFe composite reveals faster kinetics followed by the atomized and then the condensed powder based composites although they started with almost similar absorption rate. The nMg-10nFe composite presents an earlier saturation of the hydrogen uptake capacity leading a value of 3.7 wt%, which is followed by the mMg-10nFe and then the mMg-10mFe composites with respective storage quantity of 4.7 and 5.4 wt% H. However, these storage capacities are considerably lower than the theoretical value for the 9Mg-Fe stoichiometry (i.e. 6.8 wt%), most probably due to the incomplete hydrogenation of the consolidated composites.

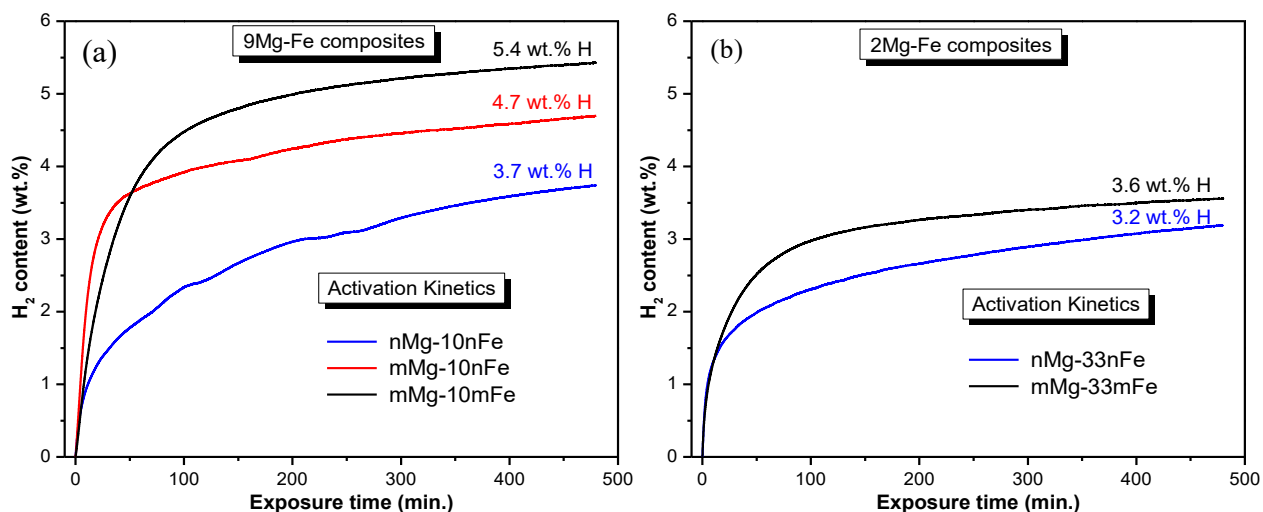


**Figure 5.5** – First hydrogenation kinetics curves obtained at 400 °C for 8 h under a hydrogen pressure of 3.5 MPa for the (a) 9Mg-Fe and (b) 2Mg-Fe composites.

For the 2Mg-Fe composites (Figure 5.5(b)), a similar kind of absorption kinetics is observed. Although they started with an identical hydrogenation rate, due to the drop in the absorption kinetics for the condensed powder based composite it ends up with a lower hydrogen storage capacity than that of its micro-counterpart (3.2 vs. 3.6 wt%). Again, the storage capacity is lower than the theoretical value for the 2Mg-Fe composition (i.e. 5.4 wt%). However, it should be noted that similar to the micro-HPT Mg product (see Figure 4.1, **Chapter 4**), the composites obtained from the atomized powder precursors presented higher storage capacities during the first hydrogenation of the as-processed composites. Also, the Fe additives significantly improved the first activation kinetics of the micro-HPT Mg product passing through an incubation stage (see Figure 4.1, **Chapter 4**). Within the same stoichiometric compositions and the identical experimental conditions, the variation in the kinetics and the storage capacities among the composites could be associated with the nature of powder precursors in both Mg and Fe phases.

## **5.3 Hydrogen sorption properties**

### **5.4.32 Thermodynamics of absorption/desorption**

Thermodynamics behaviors of the 9Mg-Fe based composites were investigated by measuring the pressure-composition-temperature (PCT) isotherms of the one-cycled activated samples in the temperature range of 300 - 400 °C, and the corresponding PCT diagrams are presented in Figure 5.6. The thermodynamic properties of these three composites are compared in Tables 5.3 with that of the HPT-consolidated Mg products obtained from the atomized and condensed powder precursors without Fe additives (referred to **Chapter 4**).

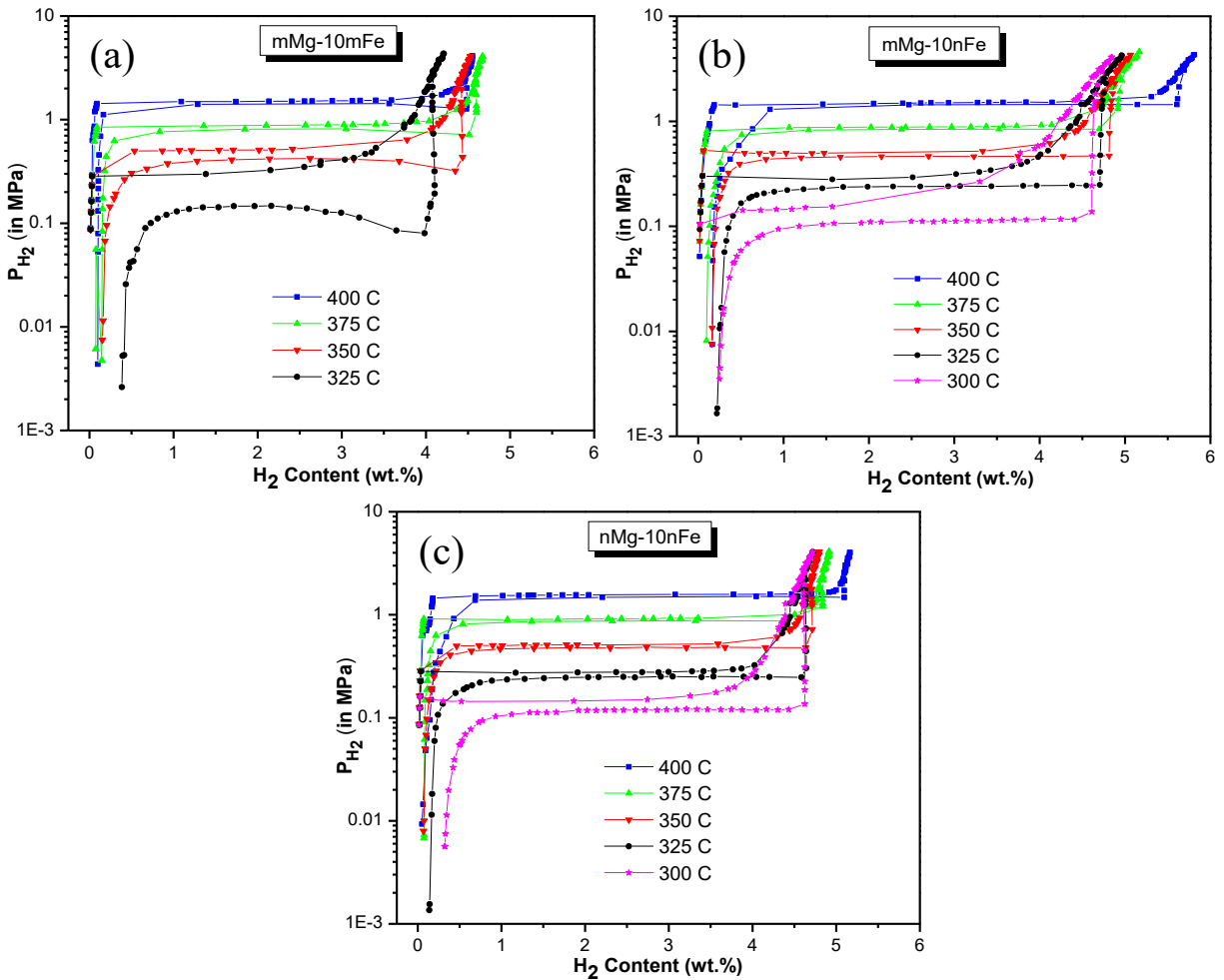


**Figure 5.6** – Pressure-composition-temperature (PCT) isotherms obtained at different temperatures from the one-cycled activated composites: (a) mMg-10mFe, (b) mMg-10nFe and (c) nMg-10nFe for the 9Mg-Fe stoichiometry.

The variations in hydrogen storage quantity with temperature during the PCT experiments for the 9Mg-Fe composites are compared with that of the Fe-free HPT-consolidated Mg products as reported in **Chapter 4**, and the corresponding results are presented in Figure 5.7. It is obvious that the hydrogen uptake quantities for all the samples smoothly increase with increasing the operating temperatures. The relatively higher hydrogen uptake quantities observed for the mMg-

10nFe and nMg-10nFe composites could be associated with the formation of ternary metal hydrides as detected by the XRD analyses (Figure 5.4(a)). Moreover, it is interesting to note from Figure 5.7 that the addition of 10 at% nFe to the atomized mMg powder (i.e. mMg-10nFe) led to the significant improvement in the hydrogen storage capacity (see circle and rhombic symbols), at the same time there has not been much modification in the storage capacity for the nMg containing composites (see up and down triangles).

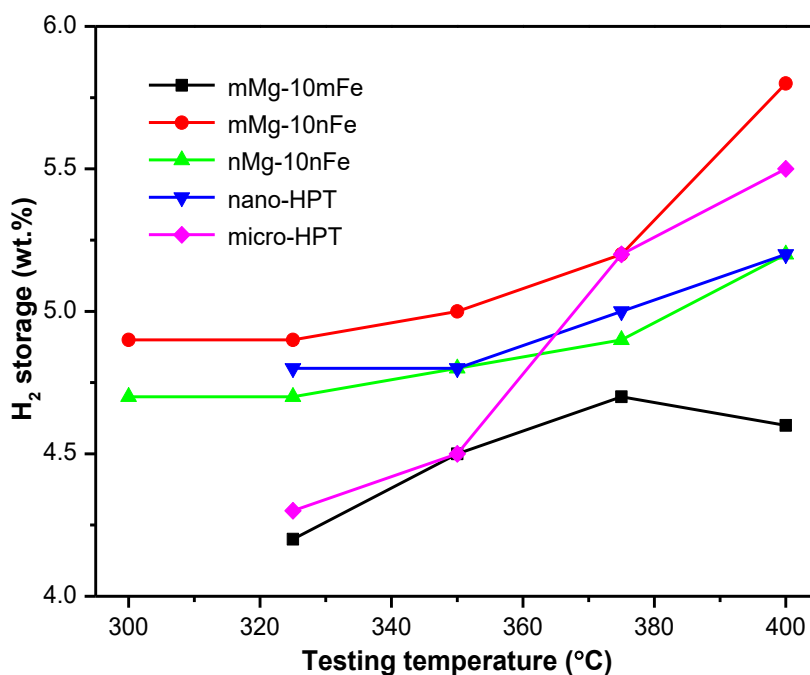


**Figure 5.7** – The variations in hydrogen storage capacity with respect to temperature for the different types of HPT-consolidated products.

Furthermore, the nFe based two composites can desorb hydrogen even at 300 °C and did not show any incubation stage in their desorption isotherms in comparison with the mMg-10mFe composite produced from the atomized powder precursors (Figure 5.6). It is also clear from Table

5.3 that desorption properties have been radically improved upon the addition of Fe phase irrespective of the Mg powder precursors. Finally, the phenomenon of hysteresis in the absorption/desorption cycles for these three composites significantly improves compared to the HPT-consolidated Mg products without Fe additives (see Table 5.3).

**Table 5.3** – The characteristics data of the PCT diagrams for the 9Mg-Fe composites in comparison with that of the HPT Mg products.

9Mg-Fe composites	Temperature (°C)	H <sub>abs</sub> content (wt%)	H retained (wt%)	H <sub>des</sub> content (wt%)	P <sub>abs</sub> (MPa)	P <sub>des</sub> (MPa)	Pressure hysteresis (MPa)
mMg-10mFe	400	4.55	0.09	4.46	1.504	1.417	0.087
	375	4.67	0.15	4.52	0.879	0.809	0.070
	350	4.53	0.15	4.38	0.508	0.409	0.099
	325	4.21	0.39	3.82	0.298	0.143	0.155
mMg-10nFe	400	5.81	0.16	5.65	1.495	1.443	0.052
	375	5.17	0.09	5.08	0.880	0.837	0.043
	350	5.06	0.15	4.91	0.509	0.464	0.045
	325	4.96	0.22	4.74	0.278	0.239	0.039
	300	4.85	0.25	4.60	0.153	0.111	0.042
nMg-10nFe	400	5.16	0.05	5.11	1.574	1.479	0.095
	375	4.92	0.07	4.85	0.915	0.869	0.046
	350	4.79	0.07	4.72	0.509	0.476	0.033
	325	4.72	0.13	4.59	0.276	0.247	0.029
	300	4.72	0.32	4.40	0.145	0.119	0.026
nano-HPT Mg	400	5.20	0.10	5.10	1.440	1.371	0.069
	375	4.99	0.14	4.85	0.855	0.799	0.056
	350	4.84	0.20	4.64	0.483	0.434	0.049
	325	4.78	4.67	0.11	0.266	-	-
micro-HPT Mg	400	5.50	0.44	5.06	1.247	1.154	0.093
	375	5.21	0.19	5.02	0.928	0.826	0.102
	350	4.47	0.15	4.32	0.915	0.795	0.120
	325	4.26	4.20	0.06	0.287	-	-

The PCT isotherms for the 2Mg-Fe composites are shown in Figure 5.8, and their thermodynamics properties subtracted from these PCT diagrams are given in Table 5.4. The two kinds of 2Mg-Fe composites present significant differences in their thermodynamics measurements. Interestingly, the atomized powder based composite exhibits higher storage capacity than the nMg-33nFe composite obtained from condensed powder precursors (Table 5.4). At above 350 °C, there are two plateaus in the desorption isotherms for both the composites (Figure 5.8). The appearance of two plateaus could be associated with the formation of ternary complex hydrides (as detected by the XRD analyses, Figure 5.4(b)), which has different equilibrium pressure than that of MgH<sub>2</sub> during the release of hydrogen. It is also important to point out here that one plateau is only observed for absorption processes because the equilibrium pressures of MgH<sub>2</sub> and Mg<sub>2</sub>FeH<sub>6</sub> are similar [5.2]. Since the experimental conditions at the lower temperatures are not favorable to form these complex hydrides [5.15], which might have led to the absence of more than one plateau and also reduced the hydrogen storage capacities at the lower operating temperatures. Moreover, it is interesting to note that due to the uniform dispersions of nFe particles in the nanometric Mg matrix (Figures 5.2(c-d)), the nMg-33nFe composite demonstrates much lower desorption temperature than that of its micro-counterpart (i.e. 250 vs. 325 °C). In terms of pressure hysteresis between the absorption/desorption cycles, the nMg-33nFe composite shows significant improvement even at lower temperatures than that of the mMg-33mFe composite obtained from atomized powder precursors.

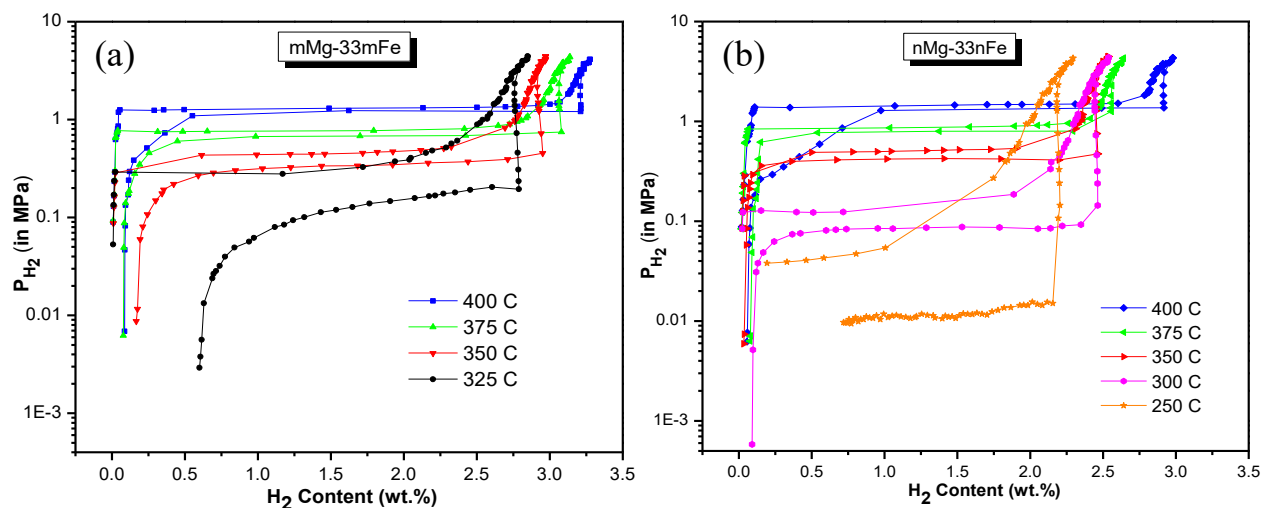


**Figure 5.8** – Pressure-composition-temperature (PCT) isotherms measured at different temperatures from the activated samples: (a) mMg-33mMg and (b) nMg-33nFe composites in the 2Mg-Fe stoichiometry.

**Table 5.4** – The characteristics data of the PCT isotherms for the 2Mg-Fe composites.

2Mg-Fe composites	Temperature (°C)	H <sub>abs</sub> content (wt%)	H retained (wt%)	H <sub>des</sub> content (wt%)	P <sub>abs</sub> (MPa)	P <sub>des</sub> (MPa)	Pressure hysteresis (MPa)
mMg-33mFe	400	3.28	0.08	3.20	1.305	1.237	0.068
	375	3.14	0.07	3.07	0.766	0.678	0.088
	350	2.97	0.16	2.81	0.446	0.339	0.107
	325	2.85	0.60	2.25	0.278	0.157	0.121
nMg-33nFe	400	2.98	0.06	2.92	1.444	1.324	0.120
	375	2.64	0.07	2.57	0.871	0.796	0.075
	350	2.54	0.03	2.51	0.505	0.422	0.083
	300	2.54	0.09	2.45	0.155	0.086	0.069
	250	2.29	0.72	1.57	0.036	0.012	0.024

In order to interpret the effects of SPD processing as well as the addition of Fe on the improvements in thermodynamic properties, the enthalpies of absorption/desorption were determined from the van't Hoff plots ( $\ln P$  vs.  $1000/T$ , not shown here) from the PCT isotherms. The values of enthalpy for all the assessed composites are listed in Table 5.5. It is readily apparent that the absolute values of the absorption enthalpy for the 2Mg-Fe composites are fairly lower ( $\Delta H_{abs} = -69$  and  $-71$  kJ/mol) than that of the 9Mg-Fe composites, while they show opposite trends in the desorption enthalpies (see Table 5.5). This phenomenon clearly implies that the 9Mg-Fe composites have improved pressure hysteresis than the 2Mg-Fe composites (see Tables 5.3 and 5.4). However, the current enthalpy values are substantially lower than the results reported in the literature for similar compositions ( $-77.4$  [5.1],  $-98$  [5.2] and  $-86$  kJ/mol [5.16]), and the current results show good agreement with the literature findings reported for the duplex-hydrides systems,  $MgH_2$ - $Mg_2FeH_6$  ( $-66$  [5.17] and  $-65$  to  $-68$  kJ/mol [5.18]). Thus, while the catalytic effects of Fe nanoparticles could be appreciated for the modest improvements in the enthalpy values, the SPD processing alone has negligible influence on the altering of thermodynamic properties of metal hydrides.

**Table 5.5** – The enthalpy of absorption/desorption, and the absorption properties of all the studied composites for both stoichiometric ratios (9Mg-Fe and 2Mg-Fe).

HPT composites	$\Delta H_{\text{abs}}$ (kJ/mol)	$\Delta H_{\text{des}}$ (kJ/mol)	Absorption rate (wt%/min) at 300 °C	H uptake (wt%) at 400 °C	Activation energy, $E_a$ (kJ/mol)
mMg-10mFe	$-72.3 \pm 1.2$	$86.5 \pm 1.9$	0.28	4.8	$49.0 \pm 5.0$
9Mg-Fe	mMg-10nFe	$-73.2 \pm 0.9$	0.31	5.6	$34.9 \pm 0.7$
	nMg-10nFe	$-76.5 \pm 0.7$	0.77	5.1	$34.0 \pm 2.0$
2Mg-Fe	mMg-33mFe	$-69.0 \pm 2.0$	0.22	3.4	$50.0 \pm 6.0$
	nMg-33nFe	$-71.5 \pm 0.8$	0.46	3.2	$56.5 \pm 0.9$

### 5.4.33 Kinetics of hydrogen absorption

The recycled samples after the PCT measurements were subsequently employed for the dynamic hydrogen absorption at 250 °C and 300 °C under a hydrogen pressure of 3.5 MPa, and the corresponding absorption profiles are displayed in Figure 5.9. The rate of absorption (wt% H/min) at 300 °C for 5 min hydrogen exposure was determined for all the composites and the results are given in Table 5.5. In addition, the steady-state hydrogen storage capacities of the all hydrided composites recorded at 400 °C are also listed in Table 5.5.

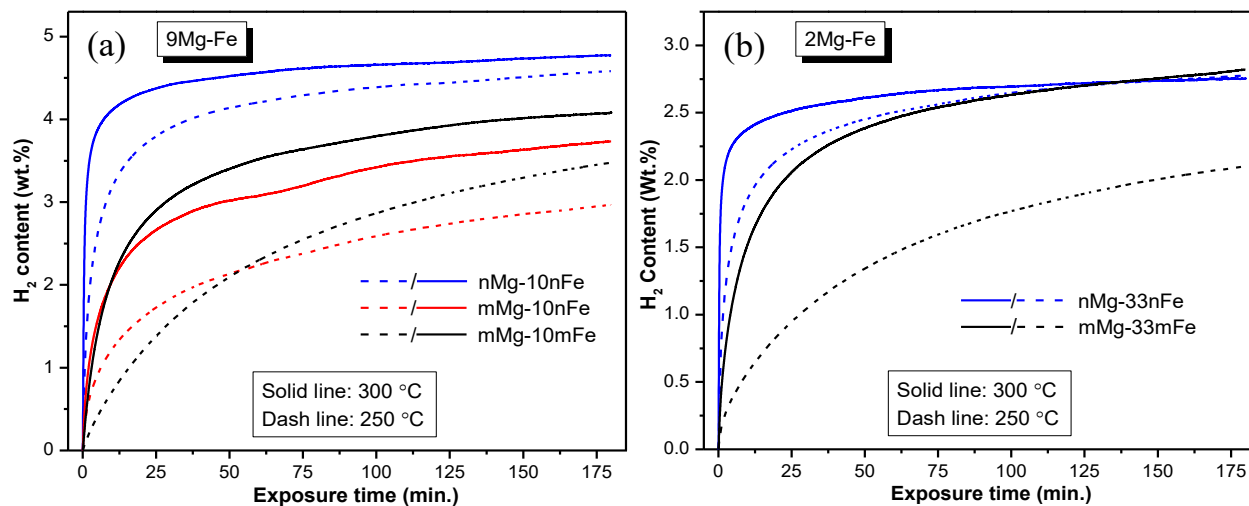


**Figure 5.9** – Hydrogen absorption kinetics recorded at 250 °C and 300 °C under a hydrogen pressure of 3.5 MPa on the same samples used for thermodynamic measurements in case of the (a) 9Mg-Fe and (b) 2Mg-Fe stoichiometry.

As can be noticed from Figure 5.9(a) for the 9Mg-Fe grade, the nMg-10nFe composite demonstrates much faster absorption kinetics, and higher hydrogen uptake quantities at both testing temperatures. At 300 °C, it can absorb 3.9 wt% H within 5 min at an absorption rate of ~ 0.77 wt% H/min, and reaches to 4.7 wt% after 2 h, while the other two composites exhibit relatively slower absorption rates at the identical experimental conditions (Table 5.5). Moreover, at 250 °C the nMg-10nFe composite can absorb more than 4 wt% within 35 min, while the other two composites can absorb less than 3.5 wt% even after 3 h of M-H interactions. It is also interesting to note that among the mMg-containing composites, the mMg-10mFe composite shows higher hydrogen uptake quantities than the mMg-10nFe composite at both testing temperatures.

The nMg-33nFe composite in the 2M-Fe stoichiometry reveals faster absorption kinetics than that of its micro-counterpart at both operating temperatures (Figure 5.9(b)). At 300 °C, the nMg-33nFe composite can absorb 2.3 wt% H within 5 min at the rate of 0.46 wt% H/min, and the mMg-33mFe composite can absorb only 1.1 wt% H at the same conditions, while both composites can absorb about 2.8 wt% H after 3 h (see Table 5.5). It is also apparent from Figure 5.9(b) that the absorption kinetics of the nMg-33nFe composite at 250 °C is still faster than that of the mMg-33mFe composite obtained at 300 °C.

The initial part of the kinetic curves was fitted by Johnson–Mehl–Avrami–Kolmogorov (JMAK) model [4.6], and Arrhenius equation was employed to determine the apparent activation energies for absorption. The activation energies for all studied composites are given in Table 5.5. The faster absorption kinetics of the nMg-10nFe and mMg-10nFe composites immediately corresponds to their much lower activation energies (see Table 5.5). Similarly, although the nMg-33nFe composite in the 2Mg-Fe grade demonstrates much faster absorption kinetics, the mMg-33mFe composite also shows fairly lower activation energy. The lowering in activation energies for the Mg-Fe based composites clearly indicates the catalytic effects of elemental Fe in comparison with the bare Mg materials (see Table 4.3 in **Chapter 4**).

#### **5.4.34 Hydrogen desorption by thermal decomposition**

A simultaneous DSC-TG technique was employed to characterize the desorption properties of all the hydrided composites as prepared by a final hydrogenation of the recycled samples at 400 °C for 6 h under a hydrogen pressure of 3.5 MPa. The DSC and TG curves obtained at a heating rate of 10 °C /min for the two stoichiometric ratios are shown in Figure 5.10. The onset of desorption, the peak maxima, and the amounts of desorbed hydrogen can be subtracted from these thermal curves, and they are given in Table 5.6.

The DSC curves for the 9Mg-Fe composites are compared in Figure 5.10(a). A non-symmetrical DSC curve comprised of double-shoulder peak is appeared for the mMg-10nFe composite, which may be a consequence of the presence of two metal hydrides (i.e. MgH<sub>2</sub> and Mg<sub>2</sub>FeH<sub>6</sub>). The low temperature shoulder generally refers to the Mg<sub>2</sub>FeH<sub>6</sub> decomposition while MgH<sub>2</sub> decomposes relatively at higher temperature [5.18,5.19]. Although the XRD pattern of the nMg-10nFe composite has confirmed the coexistence of duplex-hydrides (see Figure 5.4), its decomposition is associated with a fairly symmetrical DSC curve suggesting a possible overlapping of the two endothermic reaction peaks. On the contrary, a smooth and symmetrical DSC curve is observed for the mMg-10mFe composite, which is apparently associated with the decomposition of MgH<sub>2</sub> phase only.

Among the composites in the 9Mg-Fe stoichiometry (Figure 5.10(a)), the mMg-10nFe composite demonstrates much lower desorption temperatures. It starts to decompose at around 280 °C and passes through two peak maxima comparatively at the lower temperature ranges (Mg<sub>2</sub>FeH<sub>6</sub>: 328.0 °C and MgH<sub>2</sub>: 356.9 °C) than the nMg-10nFe one. In contrast, the mMg-10mFe composite decomposes at relatively higher temperature (413.7 °C), and exhibits a sharp

endothermic peak indicating a faster desorption kinetics. Nevertheless, the present 9Mg-Fe based composites demonstrate much lower desorption temperatures than that obtained for the HPT-consolidated Mg products without Fe additives (micro-HPT Mg: 403 °C and 421 °C and nano-HPT Mg: 380.7 °C and 417 °C, see Table 4.5, **Chapter 4**), suggesting a catalytic effect of Fe phases on the decomposition behavior of metal hydrides.

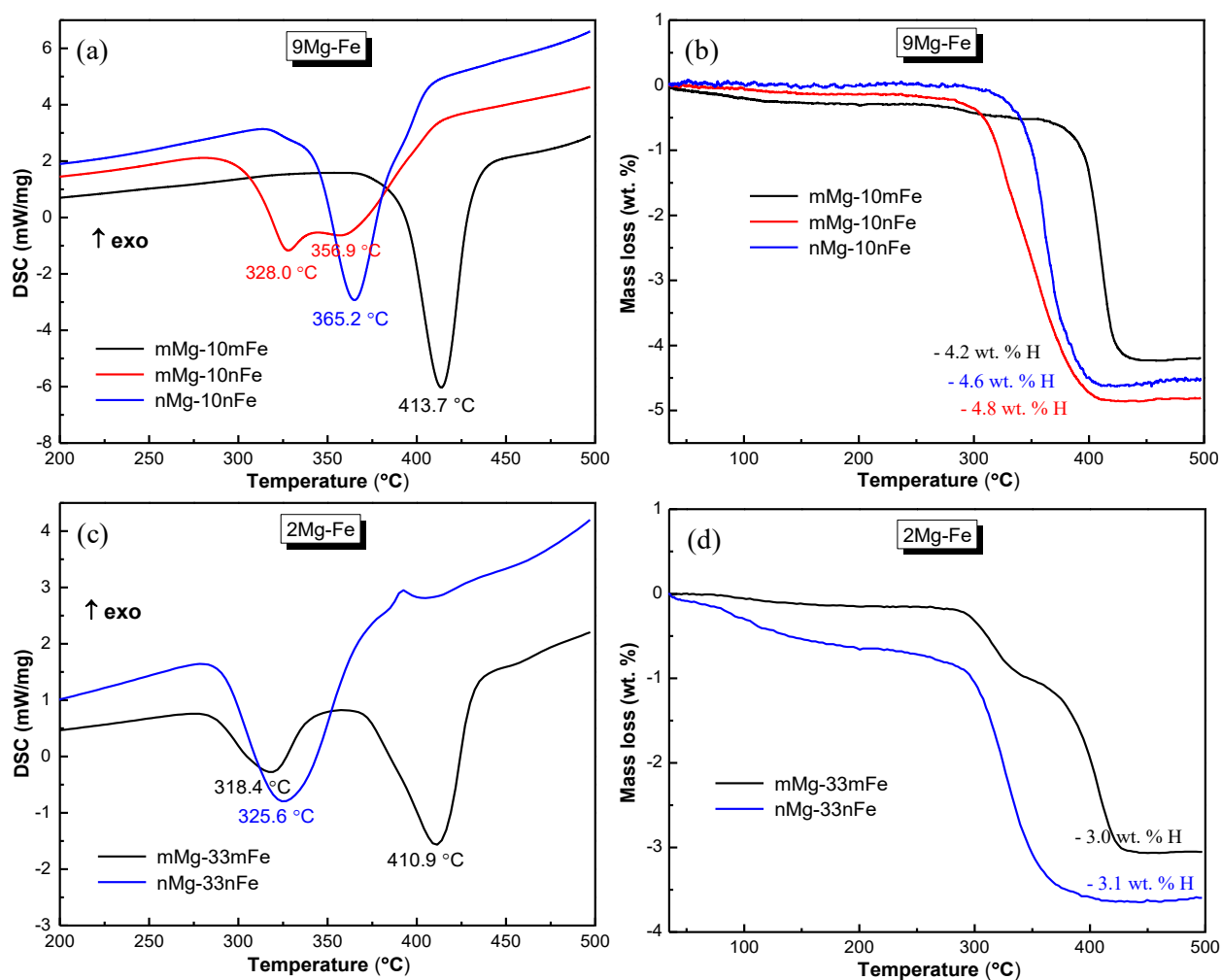


**Figure 5.10** – (a, c) DSC and (b, d) TG curves obtained at a heating rate of 10 °C/min from the hydrided composites for the (a, b) 9Mg-Fe and (c, d) 2Mg-Fe stoichiometric ratios.

**Table 5.6** – Desorption properties obtained from the DSC-TG analyses of the hydrided composites for both stoichiometric compositions (9Mg-Fe and 2Mg-Fe).

HPT composites	Onset of desorption (°C)	Peak maximum (°C)	H recovered (wt%)	Rate of desorption (wt%/min)	App. activation energy, $E_a$ (kJ/mol)	
					MgH <sub>2</sub>	Mg <sub>2</sub> FeH <sub>6</sub>
mMg-10mFe	364.7	413.7	4.2	1.20	142.0 ± 7.0	-
mMg-10nFe	280.5	328.0 356.9	4.8	0.57	108.0 ± 3.0	102.0 ± 4.0
nMg-10nFe	313.9	365.2	4.6	0.96	120.0 ± 7.0	-
mMg-33mFe	280.6	318.4 410.9	3.0	0.43	150.0 ± 8.0	144.0 ± 5.0
nMg-33nFe	280.7	325.6	3.1	0.46	153.0 ± 6.0	-

From the DSC curves of the 2Mg-Fe composites (Figure 5.10(c)), it is obvious that while the mMg-33mFe composite exhibits two distinguishable endothermic peaks due to the decomposition of two kinds of hydrides, the nMg-33nFe composite records a single-peak DSC curve which is also appeared to be little broadened. This broadening may be associated with the overlapping between two simultaneous endothermic reactions of duplex-hydrides. Although both the composites start to desorb hydrogen at the same temperature ranges (~ 280 °C, see Table 5.6), they end up with different peak maxima. Interestingly, the peak maximum of the nMg-33nFe composite is just appeared to be in between the two peak maxima for the mMg-33mFe composite. However, the current results demonstrated a substantial reduction in the peak maxima

of  $\text{Mg}_2\text{FeH}_6$  and/or  $\text{MgH}_2$  hydride in comparison with the values reported in the literature (345-430 °C [5.10-5.12] and  $\sim 435$  °C [5.20]) when processing through a similar kind of severe plastic deformation techniques.

The quantities of hydrogen released and the corresponding desorption kinetics were determined from the TG curves as shown in Figures 5.10(b, d), and they are given in Table 5.6. The mMg-10mFe composite releases 4.2 wt% H at relatively higher temperature, and a sharp change in the TG curve at its peak maximum suggests relatively faster desorption kinetics (i.e. 1.2 wt% H/min). The mMg-10nFe composite discharges 4.8 wt% H with a reasonably slower desorption rate (0.57 wt% H/min), while the nMg-10nFe composite releases 4.6% H following a moderate hydrogen desorption kinetics (0.96 wt% H/min).

Comparatively, the TG curves for the 2Mg-Fe stoichiometry mainly differ for two reasons. Firstly, an earlier desorption started at a lower temperature range for the nMg-33nFe composite could be associated with the decomposition of  $\text{Mg}(\text{OH})_2$  phase which might have formed during handling of the hydrided samples for the DSC-TG measurements. Secondly, the mMg-33mFe composite displays two distinct slopes indicating a two-step desorption for the duplex metal hydrides. A single-step desorption consistent with the single-peak DSC curve for the nMg-33nFe composite suggests an identical rate of dehydrogenation for the two types of metal hydrides. For the 2Mg-Fe composites, the rate of desorption is comparatively slower than that observed for the 9Mg-Fe composites, this may be ascribed to the slower desorption rate of the  $\text{Mg}_2\text{FeH}_6$  phase which is the main phase component in the 2Mg-Fe composites (see Figure 5.4(b)). However, the quantities of hydrogen recovered are little lower than the values recorded

after final hydrogenation as given in Table 5.5. This subtle difference in the hydrogen content could be attributed to the residual hcp-Mg,  $\alpha$ -Fe, and MgO phases as detected by the XRD analysis of the hydrided products (see Figure 5.4).

The apparent activation energy of desorption for all the assessed composites was estimated following the Kissinger method [2.15], and the results are summarized in Table 5.6. For the 9Mg-Fe stoichiometry, the calculated activation energies were mainly associated with the decomposition of  $\beta$ -MgH<sub>2</sub> phase except for the mMg-10nFe composite whose activation energy was calculated based on the two metal hydrides. As noted from the Table, the mMg-10nFe composite shows comparatively lower activation energy for the MgH<sub>2</sub> phase than the nMg-10nFe one. For the 2Mg-Fe composites, separate activation energies were obtained for the mMg-33mFe composite while it was a single value for the nMg-33nFe composite. Interestingly, they possessed almost similar values. However, these values are significantly lower than that of the HPT-consolidated Mg products (micro-HPT Mg:  $170.0 \pm 5.0$  kJ/mol H<sub>2</sub> and nano-HPT Mg:  $209.0 \pm 6.0$  kJ/mol H<sub>2</sub>, see Table 4.5, **Chapter 4**), which suggests that the presence of elemental Fe significantly reduces the energetic barrier for decomposition of metal hydrides. Furthermore, the activation energies for the current composites are substantially lower than the values reported in the literature (330-350 kJ/mol H<sub>2</sub> [5.10,5.11]) for a similar kind of SPD processing routes.

## **5.4 Discussion**

The hydrogen sorption characteristics of the Mg-Fe based composites demonstrated fairly diversified results that can be primarily attributed to the variations in the stoichiometric ratios as well as the distinct nature of the starting powder precursors. The severe plastic deformation through HPT has imposed significant impacts or even opposite trends on the improvements in hydrogen storage properties of the Mg-Fe composites. The principal results obtained in the present study can be elucidated on the lights of the following important issues: (i) effects of severe plastic deformation on the developments of peculiar microstructures and its consequences on hydrogen storage performances, (ii) influences of nature of the initial powder precursors on the microstructural inhomogeneities as well as the hydrogen absorption/desorption activities, and finally (iii) synergistic catalytic effects of the Fe additives and the inevitably formed MgO oxides on hydrogen sorption kinetics.

### **5.4.1 Effects of the processing route**

It was revealed that the HPT consolidation of different Mg-Fe powder combinations has led to the developments of significantly distinct microstructures between the assessed composites. It has induced substantial grain-size refinement in the Mg matrix and sometimes in the Fe phase up to a nanometric scale, and also fragmented the surface-oxide layers of the condensed and passivated ultrafine Mg powder into nano-sized MgO particles. In addition, it was also observed that there have been numerous microcracks in all the studied composites except mMg-10mFe composite, while the generation of these microcracks is mainly attributed to the intense shear straining by the HPT treatments and the presence of hard nano-sized Fe and MgO particles. Grosdidier et al. [1.44] have pointed out that the condensed ultrafine Fe particles added in Mg did not sustain any

kind of strain under such HPT deformation. They acted primarily as hard interfaces within the relatively soft Mg matrix. Consistently, with increasing the amount of the condensed Fe particles, as in the present study, they might have imposed severe resisting forces against the shear stresses, and thereby, led to the generation of fairly large fraction of microcracks. And also, due to this higher density of crack generations during massive shear straining, the flat consolidated sample for the nMg-33nFe composite could not hold as a single part after the HPT treatments.

Although the SPD processing has negligible effects on the altering of thermodynamic properties of the M-H systems [5.21], a little improvement on the absorption enthalpies for the 2Mg-Fe composites, and the desorption enthalpies for the 9Mg-Fe composites should be considerable in the present works (see Table 5.5). Moreover, the enhancement of the absorption kinetics particularly for the nMg-containing composites in both stoichiometric ratios could be attributed to two important factors: (i) the nanostructuring of the Mg matrix accelerating the hydrogenation kinetics, and (ii) the numerous microcracks may act as hydrogen diffusion pathways. Furthermore, the lowering of desorption temperatures especially for the nMg-containing composites could be explained based on the fact that the nano-structured Mg domains along with uniformly dispersed catalytic interphases (Fe and/or MgO) might have played a significant role to accelerate an earlier decomposition of metal hydrides.

The major drawback of the HPT processing is the reduction in hydrogen storage capacities of the Mg-Fe based composites, which was also noticed for the HPT-consolidated Mg products (referred to **Chapter 4**). It was found that the overall hydrogen uptake quantities of the Mg-Fe composites are substantially lower than their theoretical values (i.e. 6.8 wt% for 9Mg-Fe,

and 5.4 wt% for 2Mg-Fe, see Table 5.5). This observation is most likely to be due to the evolutions of microstructural heterogeneities in the Mg-Fe composites. Since the SPD processing through HPT is inherently a heterogeneous deformation, and develops inhomogeneities in the strain and microstructures within the sample volume for relatively thick-samples [3.5,3.20]; thus, it could be expected that the grain structure of the Mg-Fe composites rather heterogeneously developed across the sample volume, and thereby, could play an important role for an incomplete hydrogenation of the Mg-Fe sintered products. Therefore, a significant amount of un-reacted Mg and Fe phases was identified in the XRD patterns of the final hydrided products (see Figure 5.4).

#### **5.4.2 Nature of the initial powder precursors**

It has been shown that the differences in the physicochemical properties of the initial powder precursors had significant effects on the hydrogen sorption properties of the HPT-consolidated Mg products (referred to **Chapter 4**). Consistently, the present study also demonstrated significant variations in the hydrogen storage properties of the Mg-Fe composites depending on the nature of the initial powder types in both Mg and Fe phases. Firstly, due to the distinct origin of the powder particles - the less contaminated atomized Mg powder and the condensed and passivated Mg powder - there have been substantial microstructural differences between the processed composites for both the stoichiometries. The composites obtained from the atomized micro-sized powder precursor did not show homogeneous intermixing between the ingredient materials, while it was mostly achieved for the condensed ultrafine powder. In addition, due to the presence of nano-sized Fe particles while acting as hard interfaces towards the shear deformation of the soft Mg matrix, there have been significant amounts of microcracks particularly for the nanometric composites. Furthermore, it was revealed that a strong basal

texture for  $\alpha$ -Mg was developed for the mMg based composites obtained from the atomized powder precursor in comparison with the nMg containing counterparts. This is consistent with the results reported by Antiqueira et al. [5.20]. In the preparation of Mg-8 mol% Fe based alloys through extensive cold rolling (ECR) and/or accumulative roll bonding (ARB), they found a strong orientation of  $(0002)_{\text{Mg}}$  plane in the XRD analysis of the SPD processed alloys.

In the 9Mg-Fe stoichiometry, the differences in hydrogen uptake quantities for the mMg-10nFe and nMg-10nFe composites are partly due to the differences in the MgO oxide contents and also in the variations of  $\text{Mg}_2\text{FeH}_6$  phase formation. In contrast, the lower hydrogen storage capacity of the mMg-10mFe sample is most likely due to the incomplete hydrogenation that might be correlated with the improper intermixing between the ingredient phases, and also due to the coarser grain-structures of this composite (see Figures 5.1(a, b)). However, the mMg-33mFe composite in the 2Mg-Fe stoichiometry showed comparatively higher hydrogen storage capability than that of its nano-counterpart, which can be explained based on the fact the nMg-33nFe composite consisted of more oxides and also due to the variations in the  $\text{Mg}_2\text{FeH}_6$  phase formation (see Figure 5.4(b)). Nevertheless, for both types of stoichiometric ratios, at the given experimental conditions the nMg containing composites demonstrated much faster absorption kinetics in comparison with the mMg based composites. This is not only attributed to the nanostructuring features of the Mg matrix but also due to some catalytic effects of the uniformly dispersed Fe and MgO nanoparticles.

The desorption properties of the assessed composites were primarily associated with the decomposition behaviors of  $\text{MgH}_2$  and/or  $\text{Mg}_2\text{FeH}_6$  hydrides obtained in varying proportions for

the respective composites, while this variation is obviously accounted for the differences in the original powder precursors and the consequent completion of Mg-Fe-H reactions. Among the 9Mg-Fe composites, the mMg-10nFe composite exhibited the lower desorption temperatures as compared to the other two composites (see Table 5.6). Due to the fewer MgO oxide contents in the mMg-10nFe composite, it has less hydrogen trapping sites than the nMg-10nFe composite, and in a consequence that can basically prolong the decomposition reactions for the later composite. Although the desorption activation energy had an opposite trend to their dehydrogenation kinetics (see Table 5.6), the lowering in desorption activation energies particularly for the nFe containing composites could be related to the  $Mg_2FeH_6$  phase that may basically act as a trigger for the  $MgH_2$  dehydriding [5.3], while the significant amounts of microcracks, and the large fraction of grain boundaries providing as additional channels for hydrogen transport from the interior of the bulk matrix to their surfaces. Thus, it can be safely anticipated that the desorption properties of the studied composites are not only dependent on the varying proportions of  $MgH_2$ - $Mg_2FeH_6$  mixtures, but also the microstructural heterogeneities which is solely associated with the nature of the initial powder precursors.

### **5.4.3 Catalytic effects**

Although the sole purpose of the addition of Fe was to form the stoichiometric compounds, the un-reacted Fe particles as detected by the XRD analyses of all the hydrided samples may provide some catalytic activities. It is most likely to be believed that the dissociation of hydrogen molecules, and the recombination of atomic hydrogen into molecular form mainly take place in the association with catalytic Fe element due to its lower dissociation energy barrier compared to that of pure magnesium, even in the presence of small % of Fe [1.39,1.44,5.18]. A significant

improvement in the incubation stages of first hydrogenation (see Figures 4.1 and 5.5) as well as the pressure hysteresis (see Tables 4.1 and 5.3) for the present composites in comparison with the HPT-consolidated Mg products (referred to **Chapter 4**), could be an immediate consequence of the catalytic effects of the metallic Fe phase, and also due to the microstructural heterogeneities on the absorption/desorption cycles.

According to Zaluska et al. [5.22], the decomposition properties of the as-milled  $\text{Mg}_2\text{NiH}_4\text{-MgH}_2$  mixtures significantly enhanced due to the synergistic effect of coexisted metal hydrides. This fact was attributed to the interaction between  $\text{Mg}_2\text{NiH}_4$  and  $\text{MgH}_2$  through contraction-strain mechanisms upon dehydrogenation. Similarly, the current results also demonstrated that  $\text{Mg}_2\text{FeH}_6$  phase coexisted with  $\text{MgH}_2$  can reduce the structural stability of  $\text{MgH}_2$  and further improves its dehydrogenation properties [5.3], and thereby, the former  $\text{Mg}_2\text{FeH}_6$  dehydrogenation can activate the latter  $\text{MgH}_2$  decomposition lowering its peak maxima, and further acting as a destabilizing agent. Hence, the presence of ternary metal hydrides even in small amounts plays a significant role on the improvements of desorption properties in the Mg-Fe-H systems in comparison with that of the consolidated Mg products (Table 4.5, **Chapter 4**).

Moreover, it was also observed that the MgO nanoparticles dispersed in the Mg matrix can act as an efficient catalyst for hydrogenation/dehydrogenation processes [1.43,1.44,1.54-1.56], and thus, a synergistic catalytic effect of the metallic Fe and non-metallic MgO particles could be a possible reason for the significant improvements in hydrogen sorption kinetics of the present composites. That is this nanometric Fe and MgO particles essentially accelerate the breaking up of hydrogen molecules into its atomic state, and also promote the diffusion of atomic

hydrogen into the interior of the compacted composite materials. From the works of Oriani [5.23], it is well known that the hydrogen atoms show a strong tendency to diffuse and accumulate at the cracks and grain boundaries in Fe-rich materials, and this is one of the main reasons for hydrogen embrittlement in steels. Therefore, although a large fraction of grain boundaries and microcracks can act as trapping sites for hydrogen and may lead to reduce the hydrogen absorption/desorption kinetics, the uniformly dispersed nano-sized Fe and MgO oxide particles may provide the connecting tunnels to accelerate the hydrogen diffusion from the surface to the interior of the Mg matrix or in the reverse process during the decomposition of metal hydrides.

## **Chapter's conclusions**

In the present research, the severe plastic deformation through HPT consolidation of powder mixtures was employed to produce Mg-Fe based composites in the two stoichiometric ratios: 9Mg-Fe and 2Mg-Fe. The structural evolutions of these composites were characterized by XRD and SEM studies. They were mainly assessed for investigating the improvements in hydrogen sorption properties upon extreme plastic deformation of both the Mg and Fe matrixes. The effects of nature of the initial powder precursors on the hydrogen storage properties were also tested by employing two distinct powder precursors in both the phases: atomized micro-sized powder, and condensed ultrafine powder. The principal results obtained from the present study can be summarized as follows.

- 1) For the 9Mg-Fe stoichiometry, the HPT consolidation of the condensed powder precursors led to uniform dispersion of the Fe and MgO nanoparticles in the elongated Mg domains, while the mMg-10nFe composite consisted of recrystallized Mg domains with uniformly distributed Fe nanoparticles. In contrast, a heterogeneous microstructure was developed for the mMg-10mFe composite obtained from the micro-sized powder precursors. A significant amount of microcracks were generated particularly for the nFe containing composites.
- 2) For the 2Mg-Fe composition, the generation of microcracks has been further enhanced with the increasing amounts of nFe particles, and hence, the density of microcracks was such that the flat consolidated sample could not hold as a single part for the nMg-33nFe composite obtained from the condensed powder precursors.
- 3) The improvements in the hydrogen absorption/desorption thermodynamics were primarily due to the uniform dispersion of, particularly the nFe particles, within the Mg matrix and

their catalytic effects, and also due to the higher density of the microcracks especially for the nanometric composites generated through the massive shear straining by HPT.

- 4) In the 9Mg-Fe composition, the nMg containing composites revealed much faster absorption kinetics accompanied with lower activation energies, and also demonstrated the lower desorption temperatures; comparatively, the mMg-10mFe composite exhibited relatively faster desorption kinetics probably due to its higher peak maximum as well as the less trapping sites for hydrogen due to the negligible amount of Mg/MgO interfaces.
- 5) In the 2Mg-Fe stoichiometry, the nMg-33nFe composite showed faster absorption kinetics compared to the mMg-33mFe composite, while they demonstrated a similar kind of desorption properties plausibly due to the microstructural similarities achieved through the repetitive hydriding/dehydriding cycles.
- 6) The enhanced absorption kinetics accompanied with the lowering in activation energy for the nanometric composites in both the stoichiometries could be attributed to the peculiar microstructural developments characterized by the nanostructuring of the Mg matrix, the generation of microcracks, and the synergistic catalytic effects of the metallic Fe and non-metallic MgO nanoparticles.
- 7) Except for the mMg-10mFe composite, all the hydrided composites consisted of duplex-hydrides ( $\text{MgH}_2$ - $\text{Mg}_2\text{FeH}_6$ ) in varying proportions possibly due to the differences in the nature of the initial powder precursors as well as the microstructural heterogeneities between the composites. However, the presence of this ternary metal hydride indeed plays a significant role on the improvements in desorption properties of the Mg-Fe-H systems.

## References

- [5.1] Bogdanovic B, Reiser A, Schlichte K, Spliethoff B, Tesche B. "Thermodynamics and dynamics of the Mg-Fe-H system and its potential for thermochemical thermal energy storage." *J. Alloys Compd.* 345 (2002) 77-89.
- [5.2] Didisheim JJ, Zolliker P, Yvon K, Fischer P, Schefer J, Gubelmann M, Williams AF. "Dimagnesium iron (II) hydride, Mg<sub>2</sub>FeH<sub>6</sub> containing octahedral FeH<sub>6</sub><sup>4-</sup> anions." *Inorg. Chem.* 23 (1984) 1953-57.
- [5.3] Zhou DW, Li SL, Varin RA, Peng P, Liu JS, Yang F. "Mechanical alloying and electronic simulations of 2Mg-Fe mixture powders for hydrogen storage." *Mater. Sci. Engg. A* 427 (2006) 306-15.
- [5.4] Moffatt WG. "Handbook of Binary Phase Diagrams." New York: Genium Publishing; 1984.
- [5.5] Asselli AAC, Leiva DR, Jorge AM, Ishikawa TT, Botta WJ. "Synthesis and hydrogen sorption properties of Mg<sub>2</sub>FeH<sub>6</sub>-MgH<sub>2</sub> nanocomposite prepared by reactive milling." *J. Alloys Compd.* 536 (2012) S250-54.
- [5.6] Asselli AAC, Botta WJ, Hout J. "Formation Reaction of Mg<sub>2</sub>FeH<sub>6</sub>: Effect of Hydrogen Absorption/desorption Kinetics." *Mater. Res.* 16 (2013) 1373-8.
- [5.7] Hongo T, Edalati K, Arita M, Matsuda J, Akiba E, Horita Z. "Significance of grain boundaries and stacking faults on hydrogen storage properties of Mg<sub>2</sub>Ni intermetallics processed by high-pressure torsion." *Acta Mater.* 92 (2015) 46-54.
- [5.8] Leiva DR, Huot J, Ishikawa TT, Bolfarini C, Kiminami CS, Jorge AM, Botta Filho WJ. "Hydrogen activation behavior of commercial magnesium processed by different severe plastic deformation routes." *Mater. Sci. Forum* 667 (2011) 1047-1051.
- [5.9] Edalati K, Matsuda J, Iwaoka H, Toh S, Akiba E, Horita Z. "High-pressure torsion of TiFe intermetallics for activation of hydrogen storage at room temperature with heterogeneous nanostructure." *Int. J. Hydrogen Energy* 38 (2013) 4622-7.
- [5.10] Lima GF, Jorge AM, Leiva DR, Kiminami CS, Bolfarini C, Botta WJ. "Severe plastic deformation of Mg-Fe powders to produce bulk hydrides." *IOP Conf. Ser.: J. Phys.* 144 (2009) p. 012015.
- [5.11] Lima GF, Peres MM, Garroni S, Baro MD, Surinyach S, Kiminami CS et al. "Microstructural characterization and hydrogenation study of extruded MgFe alloy." *J. Alloys Compd.* 504 (2010) S299-01.
- [5.12] Cerutti R, Lima GF, Kiminami CS, Botta WJ, Jorge AM. "2Mg-Fe and 2Mg-Fe + 5%C mixtures processed by hot extrusion: Influence of carbon on hydrogen sorption properties." *J. Alloys Compd.* 509 (2011) S464-7.
- [5.13] Kai M, Horita Z, Langdon TG. "Developing grain refinement and superplasticity in a magnesium alloy processed by high-pressure torsion." *Mater. Sci. Eng. A* 488 (2008) 117-24.

- [5.14] Kubota K, Mabuchi M, Higashi K. "Review Processing and mechanical properties of fine-grained magnesium alloys." *J. Mater. Sci.* 34 (1999) 2255-62.
- [5.15] Puzkiel PA, Gennari FC, Larochette PA, Karimi K, Pistidda C et al. "Sorption behavior of the  $\text{MgH}_2\text{-Mg}_2\text{FeH}_6$  hydride storage system synthesized by mechanical milling followed by sintering." *Int. J. Hydrogen Energy* 38 (2013) 14618-30.
- [5.16] Konstanchuk IG, Ivanov EY, Pezat M, Darriet B, Boldyrev VV. "The hydriding properties of a mechanical alloy with composition Mg-25% Fe." *J. Less-common Met.* 131 (1987) 181-9.
- [5.17] Puzkiel JA, Larochette PA, Gennari FC. "Thermodynamic and kinetic studies of Mg-Fe-H after mechanical milling followed by sintering." *J. Alloys Compd.* 463 (2008) 134-42.
- [5.18] Puzkiel JA, Larochette PA, Gennari FC. "Hydrogen storage properties of  $\text{Mg}_x\text{Fe}$  (x: 2, 3 and 15) compounds produced by reactive ball milling." *J. Power Sources* 186 (2009) 185-93.
- [5.19] Castro FJ, Gennari FC. "Effect of the nature of the starting materials on the formation of  $\text{Mg}_2\text{FeH}_6$ ." *J. Alloys Compd.* 375 (2004) 292-6.
- [5.20] Antigueira FJ, Leiva DR, Ishikawa TT, Junior J, Moreira A, Botta WJ. "Severe Plastic Deformation and Additive Distribution in Mg-Fe to Improve Hydrogen Storage Properties." *Mat. Res.* 20 (2017) 61-70.
- [5.21] Panda S, Fundenberger JJ, Zhao Y, Zou JX, Toth LS, Grosdidier T. "Effect of initial powder type on the hydrogen storage properties of high-pressure torsion consolidated Mg." *Int. J. Hydrogen Energy* 42 (2017) 22438-48.
- [5.22] Zaluska A, Zaluski L, Strom-Olsen JO. "Synergy of hydrogen sorption in ball-milled hydrides of Mg and  $\text{Mg}_2\text{Ni}$ ." *J. Alloys Compd.* 289 (1999) 197-06.
- [5.23] Oriani RA. "The diffusion and trapping of hydrogen in steel." *Acta Mater.* 18 (1970) 147-57.



## **CHAPTER 6: HYDROGEN STORAGE PROPERTIES OF AS-SYNTHESIZED AND HIGH-PRESSURE TORSION (HPT) CONSOLIDATED MAGNESIUM-GRAPHENE BASED COMPOSITES**

---

Introduction .....	188
6.1 Structural characterizations .....	192
6.1.1 Morphology and microstructure .....	192
6.1.2 X-ray diffraction (XRD) analyses .....	195
6.1.3 Raman spectroscopic analysis .....	197
6.2 First hydrogenation characteristics .....	199
6.3 Hydrogen sorption properties .....	202
6.3.1 Thermodynamics of absorption/desorption .....	202
6.3.2 Kinetics of hydrogen absorption .....	205
6.3.3 Hydrogen desorption behaviors .....	207
6.4 Discussion .....	210
6.4.1 Peculiarity in powder formation and its consequences .....	210
6.4.2 Effects of severe plastic deformation through HPT .....	214
Chapter's conclusions .....	217
References .....	219

## **Introduction**

While magnesium and its alloys offer high gravimetric and volumetric storage capacity at relatively low cost, their main drawbacks include sluggish hydriding/dehydriding kinetics partly due to the formation of an impermeable native oxide layer as well as very high desorption temperatures due to the thermodynamics stability of  $\text{MgH}_2$  [6.1]. In recent years, the catalytic effects of carbon materials are increasingly investigated to modify the thermodynamics and kinetics of hydrogen sorption especially for the Mg-based materials [1.57-1.63,6.2-6.4]. Among the carbon allotropes, the nanostructured carbon materials such as graphene,  $\text{C}_{60}$ , carbon nanotubes (CNTs) and carbon nanofibers (CNFs) generally show a prominent catalytic effect possibly due to their unique electronic configuration (i.e. delocalized  $\pi$  electrons) and intriguing interaction between carbon and hydrogen.

The catalytic effects of graphitic carbon (G) on the hydriding/dehydriding properties of Mg was first investigated by Imamura et al. [1.57]. They found that the mechanical milling of Mg/G composites mainly generates cleavage cracking along the graphitic layers which provides an active site for the catalytic activation of hydrogen molecules and enhances the hydrogen sorption kinetics. Shang and Guo [1.59] examined the catalytic effect of crystalline graphite on hydrogen storage properties of the ( $\text{MgH}_2 + 10\text{G}$ ) mixture after milling for 8 h. They reported that the presence of graphitic carbon improves a rapid hydrogen uptake in the rehydrogenated sample but brings little effect on desorption kinetics and temperatures. In a recent study by Wu et al. [6.2], it was observed that among the carbon/noncarbon addition, single-walled carbon nanotubes (SWNTs) possess the most prominent catalytic activation to improve the hydrogen storage

properties of Mg, primarily due to its unique tubular structure built from a rolled-up of graphene sheets.

The most frequently used method to prepare the carbon-based nanocomposites is high energy ball-milling (HEBM) [1.57-1.63,6.2-6.4]. However, ball-milling can be detrimental to certain carbon allotropes due to the complete destruction of their peculiar microstructures, particularly for the graphene or graphene like structures [6.3,6.4]. Moreover, it is also difficult to avoid impurities coming from the milling tools and gas adsorption, which can significantly affect the hydrogen sorption properties of Mg [I.14]. In an effort to produce “clean” ultrafine precursors with controlled chemistry, an active plasma method has been developed for producing nanometric/ultrafine powder particles by vaporization/condensation of metals, alloys or ceramics in N<sub>2</sub>, H<sub>2</sub> and/or Ar atmosphere using a DC arc-plasma [6.5]. A wide variety of Mg-based ultrafine powder composites synthesized by this method have shown excellent hydrogen storage properties [2.2,2.3]. This improvement was mainly attributed to the fine scale of Mg particles and to a special type of “core-shell” morphology containing a Mg or Mg(RE) core (RE = rare earth metals) embedded by an oxide shell of MgO or RE<sub>2</sub>O<sub>3</sub> obtained by the passivation of condensed powder particles [6.6-6.8].

On the other hand, a fundamental problem of metal hydride powder particles lies with a low thermal conductivity while fabricating an effective hydrogen storage tank [6.9]. Hence, there have been significant researches pioneered on how to accelerate heat as well as mass transfer phenomena for the metal hydride powder beds. The compaction of metal hydride powder, sometimes admixing with carbonaceous materials, under moderate pressures is found to be an effective technique to improve the heat conduction properties of metal hydride beds [4.6,5.9,6.10-6.15]. In particular, Chaise et al [6.11] reported that the compression of ball-milled MgH<sub>2</sub> powder

blended with expanded natural graphite (ENG) markedly improves the radial thermal conductivity and doubles the volumetric hydrogen storage capacity. However, there has been limited exploitation of severe plastic deformation (SPD) techniques to manufacture bulk magnesium/carbon (Mg/C) based composites for modifying the hydrogen storage properties [5.12,6.16], at the same time those can be employed for the potential improvements in thermal conductivity due to the full consolidation as well as reduced porosity in the bulk SPD composites.

In the present study, graphene monolayer (GM) was employed to investigate its catalytic activity on hydriding/dehydriding properties of Mg in the as-synthesized as well as the severely deformed states. The Mg-3GM (i.e. 3 wt% GM) based composite powder was produced by the DC arc-plasma processing technique as described in **Chapter 2**. The identical processing parameters as the one described in **Chapter 2** were applied for the synthesis of the Mg-3GM composite powder. Before opening the collecting room, the powder particles were slowly passivated with a mixture of argon and normal air to prevent the nanoparticles from burning at the direct contact of Mg with the atmosphere. Finally, the as-synthesized powder was consolidated into compacted bulk products by the two-step HPT consolidation process following the one described in the section 2.2.3, **Chapter 2**. In the subsequent text, these consolidated bulk products will be denoted as HPT Mg-3GM.

Hydrogen sorption performance of the powder as well as the bulk HPT composites was investigated by using the conventional Sievert type pressure-composition-temperature (PCT) volumetric apparatus. Prior to hydrogen storage measurements, the bulk HPT composites were broken to micrometer range powder particles (using a ceramic mortar) to fit into the testing

vessel. Both the powder and ground samples were first activated by dynamic hydrogen absorption at 400 °C for 8 h under a hydrogen pressure of 3.5 MPa followed by hydrogen desorption at the same temperature under vacuum. Since the HPT-consolidated products were not completely activated at the first hydrogenation (as can be seen in Figure 6.5), this step was repeated for a second time under the identical conditions but only for 3 h. These two-cycled samples will be referred to as activated products in the subsequent text. The subsequent thermodynamic and kinetic measurements were performed following the identical procedure as the one described in **Chapter 4**. Finally, these cycled samples were fully hydrided through dynamic hydrogen absorption at 400 °C for 6 h under a hydrogen pressure of 3.5 MPa. Desorption properties of the fully hydrided samples were investigated by simultaneous differential scanning calorimetry-thermogravimetry (DSC-TG) analyses at a heating rate of 3, 5 and 10 °C/min in the temperature range of 25 to 500 °C.

The structural compositions of the as-synthesized powder and its HPT composite before and after hydrogenation were characterized by X-ray diffraction (XRD) analysis. The morphology and microstructure of the samples were inspected by high resolution scanning electron microscopy (SEM) and transmission electron microscopy (TEM). Raman spectroscopy was employed to interpret the modifications of graphene molecular structure before and after the HPT treatments.

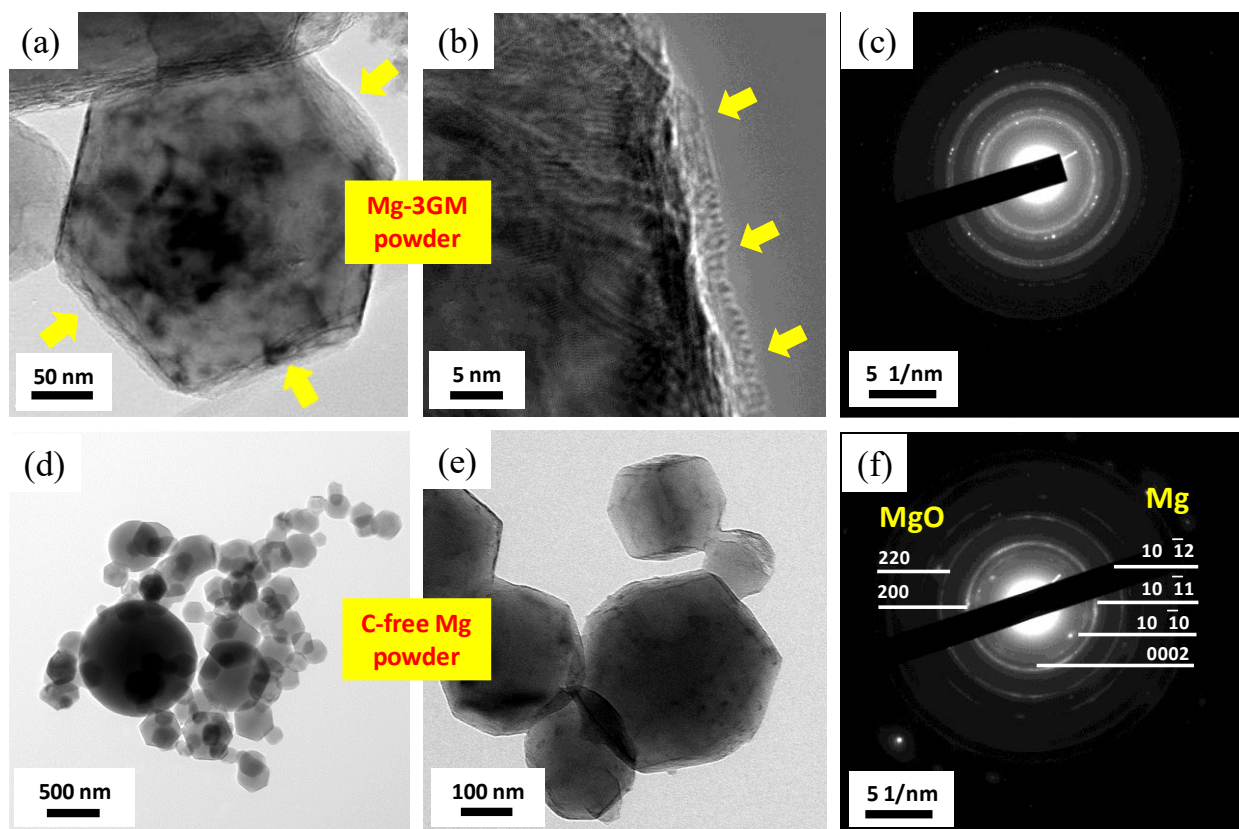
## **6.1 Structural characterizations**

### **6.1.1 Morphology and microstructure**

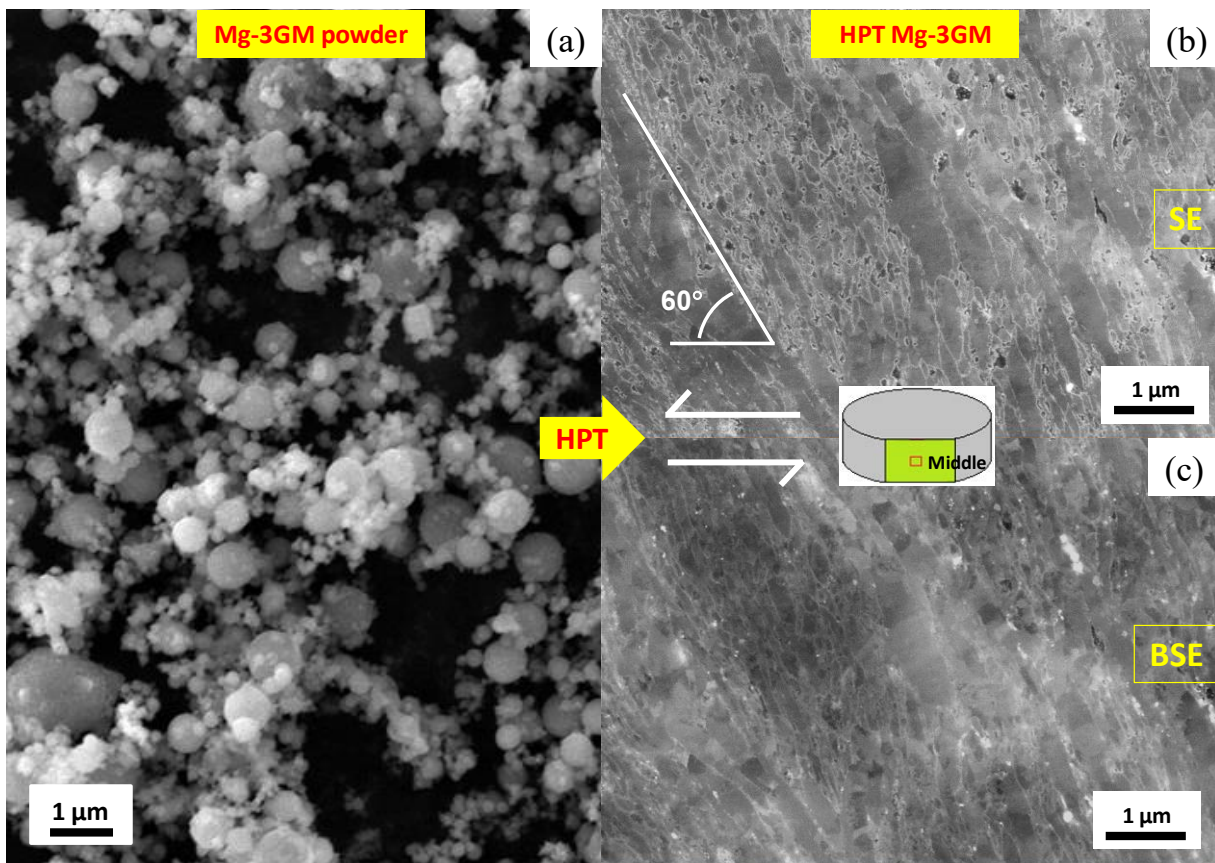
Figure 6.1 presents TEM images and the corresponding selected area electron diffraction (SAED) patterns for the condensed and passivated powder particles obtained from the Mg/graphene (Figures 6.1(a-c)) and the pure Mg precursors (Figures 6.1(d-f)). While the surface of the powder particles obtained from the pure Mg precursor is rather clean (Figures 6.1(d-e)), an additional - rather continuous - layer of carbonaceous material is present at the surface of Mg-3GM powder particles (yellow arrows in Figures 6.1(a-b)). The rather continuous covering of the surfaces is illustrated from the TEM image given in Figure 6.1(a), while Figure 6.1(b) shows that this layer has a thickness of about 2-3 nm. The SAED patterns clearly reveal the presence of the polycrystalline Mg and MgO diffraction rings. The absence of diffraction spots corresponding to C-containing phases suggests that the crystallinity of graphitic structure was either perturbed in the very thin layer of the Mg-3GM powder or that carbon was retained under an amorphous state.

Figure 6.2 gives SEM micrographs of the Mg-3GM powder particles and its HPT-deformed composite. It is clear that the morphology of the Mg particles, as seen from Figure 6.2(a), is mostly spherical or hexagonal in shapes accompanied with some finer satellites. It was estimated from several SEM and TEM images that the Mg-3GM powder particles had a wide range of particle size distribution starting from 50 nm to 800 nm, which is similar like a C-free Mg powder. Thus, the addition of carbonaceous materials did not affect the final size of the powder particles. Comparatively, in the preparation of Mg nanoparticles by acetylene plasma metal reaction, Zhang et al. [6.17] reported that the particle size of the obtained Mg is reduced

with increasing concentration of acetylene in the plasma, which was attributed to the carbon confinement restricting the growth of Mg nanoparticles.



**Figure 6.1** – TEM images and the corresponding SAED patterns of the Mg-3GM powder (a-c) in comparison with the C-free Mg powder (d-f), synthesized by the arc-plasma method.



**Figure 6.2** – SEM micrographs illustrating the morphology of the Mg-3GM powder (a) and the microstructure of its HPT consolidated composite (b, c).

Secondary electron (SE) and its backscattered electron (BSE) micrographs of the HPT consolidated composite obtained at the periphery and in the mid-thickness of the HPT-disk shown by a schematic are displayed in Figure 6.2(b) and 6.2(c), respectively. The applied shear direction is also given by arrows. It is readily apparent from the HPT micrographs that the initial ultrafine powder particles were severely deformed and fully consolidated after the 2 turns HPT treatments. The given microstructure mainly consists of elongated grain-structures with nanometric Mg domains essentially inclined at  $60^\circ$  from the shear plane (Figure 6.2(b)).

However, it is interesting to note that the present HPT Mg-3GM composite is likely to be more refined in comparison with the nano-HPT product obtained from the C-free Mg powder precursor (see Figure 3.9 in **Chapter 3**). Also, the grain inclination angle is substantially increased in the present study from  $45^\circ$  as observed for the nano-HPT composites. Furthermore, a thin layer of MgO oxides usually formed on the surface of Mg particles during the passivation treatments has been fragmented into fine particles by the intense shear straining through HPT, and appear as brightest spots in the BSE micrograph (see Figure 6.2(c)). Also, the nano-sized MgO oxide particles are very often aligned with grain boundaries restricting the evolutions of grain-structures within the nanometric range due to the effects of Zener pinning. While some part of the microstructures has been significantly refined, there are some coarser grain-structures probably originated from the initial larger powder particles.

### **6.1.2 X-ray diffraction (XRD) analyses**

Figure 6.3 presents XRD patterns of the as-synthesized powder and its HPT composite as well as their hydrided counterparts. The hydrided products were obtained by dynamic hydrogenation of the cycled samples at  $400^\circ\text{C}$  for 6 h under a hydrogen pressure of 3.5 MPa. From the XRD results of non-hydrided samples (Figures 6.3(a, b)), it is readily apparent that magnesium is the main contributor for the powder as well as its HPT composites. Surprisingly, it should be noted that no trace of graphitic peaks is detected by the XRD analysis of the Mg-3GM powder, while its characteristic peak at  $2\theta = 26.7^\circ$  is detected after the HPT treatments (shown by arrow in Figure 6.3(b)). The exact nature of graphitic phase for the bulk HPT composite was investigated by Raman spectroscopy in the next subsection. As expected from the SEM and TEM inspections,

the (200) MgO oxide peaks accompanying the Mg peaks are detected for both the samples. The presence of a tiny (101) peak belonging to Mg(OH)<sub>2</sub> is also revealed. The formation of the later phase was due to the passivation process that was carried out in pure air containing some moisture.

It can be readily assumed from the XRD results of hydrided samples (Figures 6.3(c, d)) that most of the Mg crystals have been transformed into the hydride phase (i.e.  $\beta$ -MgH<sub>2</sub>) followed by the repetitive hydriding/dehydriding cycles. However, it should be noted that this transformation was almost completed for the powder composite with a trace amount of unreacted Mg when compared to its hydrided HPT counterpart. While a trace of graphitic peaks is still detected in the XRD pattern of the hydrided HPT composite (shown by arrow in Figure 6.3 (d)), consistently there was no trace of graphitic peaks for the hydrided Mg-3GM powder (Figure 6.3(c)). Furthermore, if we compare the peak intensity of MgO oxide before and after the hydrogenation, it reveals that the oxide contents have been substantially increased in both the hydrided products. These additional oxides could be originated from the decomposition of Mg(OH)<sub>2</sub> at high temperature ( $\sim 330$  °C [6.18]) into MgO during the hydrogen sorption treatments.

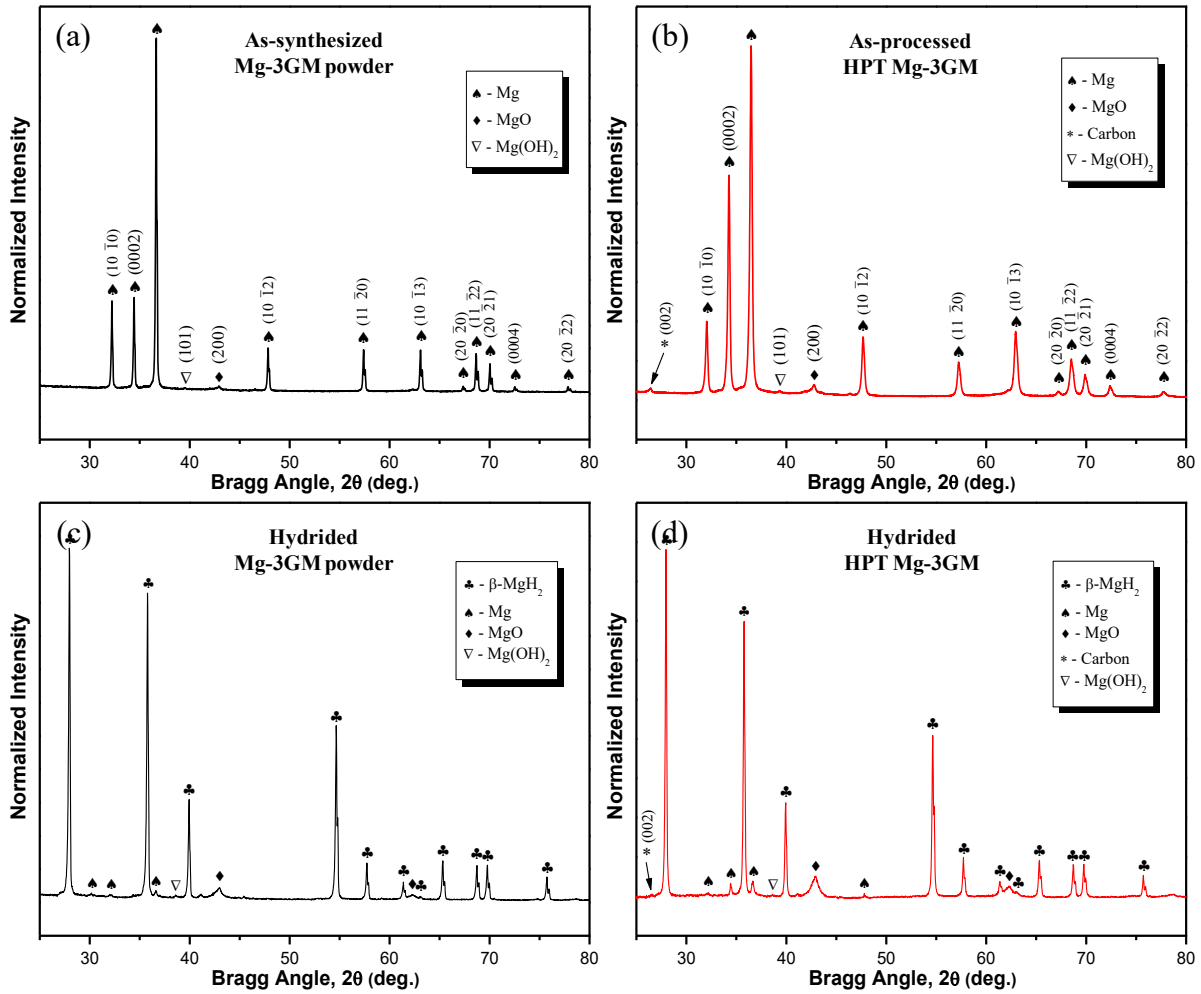


**Figure 6.3** – X-ray diffraction (XRD) patterns of (a) the as-synthesized Mg-3GM powder and (c) its hydrided products, and (b) the HPT composite and (d) its hydrided products.

### 6.1.3 Raman spectroscopic analysis

Since Raman spectroscopy can give rise to the “fingerprinting” of carbonaceous species, it has been employed to characterize the microstructural modifications occurred to the graphene additives after the arc-plasma synthesis as well as the HPT processing. The corresponding Raman

spectra for both the samples are given in Figure 6.4. Consistent with the XRD results, the as-synthesized composite powder did not reveal any Raman features relating to the graphitic carbon structures suggesting a non-crystallinity state of carbon phase. Under given experimental conditions for the arc-plasma processing, it is possible that the initial graphene powder precursor can be deposited as amorphous carbon films on the surface of condensed Mg crystal powders [6.17].

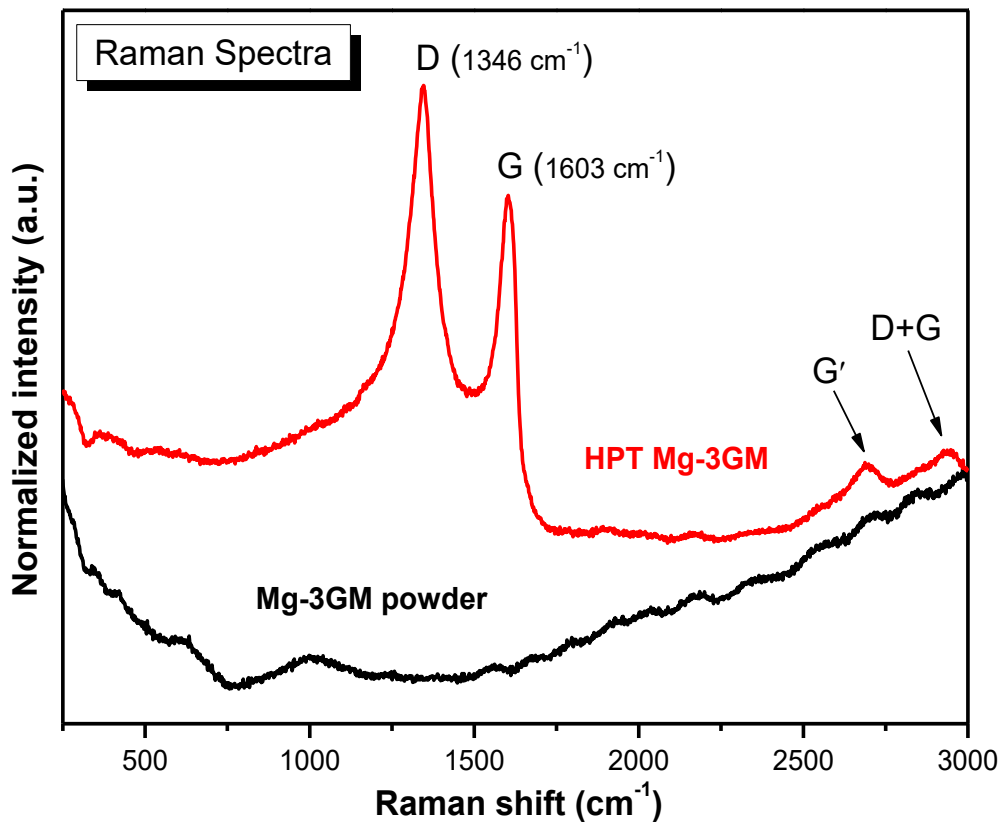


**Figure 6.4** – Raman spectra of the as-synthesized Mg-3GM powder and its HPT consolidated composites, indicating a strong microstructural modification after the HPT treatments.

In contrast to the powder composite, the Raman spectrum of the HPT Mg-3GM composite consists of two important characteristic bands - G band ( $1603\text{ cm}^{-1}$ ) and G' band ( $2687\text{ cm}^{-1}$ ) - belonging to the graphene or graphene-like structures [6.19]. This is also associated with a strong D band ( $1346\text{ cm}^{-1}$ ), which is usually originated from a hybridized vibrational mode associated with graphene edges and indicates the presence of some disorder in the graphene structure. The relative intensity of D to G band (i.e.  $I_D/I_G$ ) is often used as a measure of the quality of graphene structure. In this case, it was found to be close to 1.08 indicating a multilayer stack of graphene sheets. Therefore, it could be reasonable to anticipate that the severe plastic deformation through HPT under moderately high pressures and at the room temperature might have led to the graphitization of the amorphous carbon prevailed in the arc-plasma condensed powder precursor. However, it should be noted that the graphitization of amorphous carbon usually takes place under high-temperature-pressure conditions [6.20,6.21].

## **6.2 First hydrogenation characteristics**

The as-synthesized Mg-3GM powder and its HPT composite were activated at  $400\text{ }^\circ\text{C}$  by flushing with hydrogen under a pressure of  $3.5\text{ MPa}$  for two times ( $1^{\text{st}}$  activation for  $8\text{ h}$  and  $2^{\text{nd}}$  activation for  $3\text{ h}$ ), and the resultant activation curves are presented in Figure 6.5. In each cycle, the hydrided samples were desorbed at  $400\text{ }^\circ\text{C}$  under vacuum until complete dehydrogenation. These activation profiles present interesting behaviors on the first and second hydrogen exposure of the samples. The first transformation kinetics is remarkably faster for the powder sample than that of its HPT nanocomposite. Also, they possess significant differences in the steady-state hydrogen uptake quantities. The Mg-3GM powder exhibits significantly higher storage of  $8.1$

wt% H after 8 h of hydrogen exposure, which is even higher than the theoretical value for pure Mg (i.e. 7.6 wt%). This anomalous hydrogenation behavior of the powder composite, which is quite surprising, could be potentially associated with the presence of carbonaceous materials, on which some extra hydrogen could be adsorbed [6.22]. This observation was confirmed by repeating the experiments more than three times. Interestingly, however, under the identical experimental conditions, the HPT nanocomposite was able to store only 4.7 wt% H, which indicates that there must be incomplete hydrogenation for the HPT counterpart.

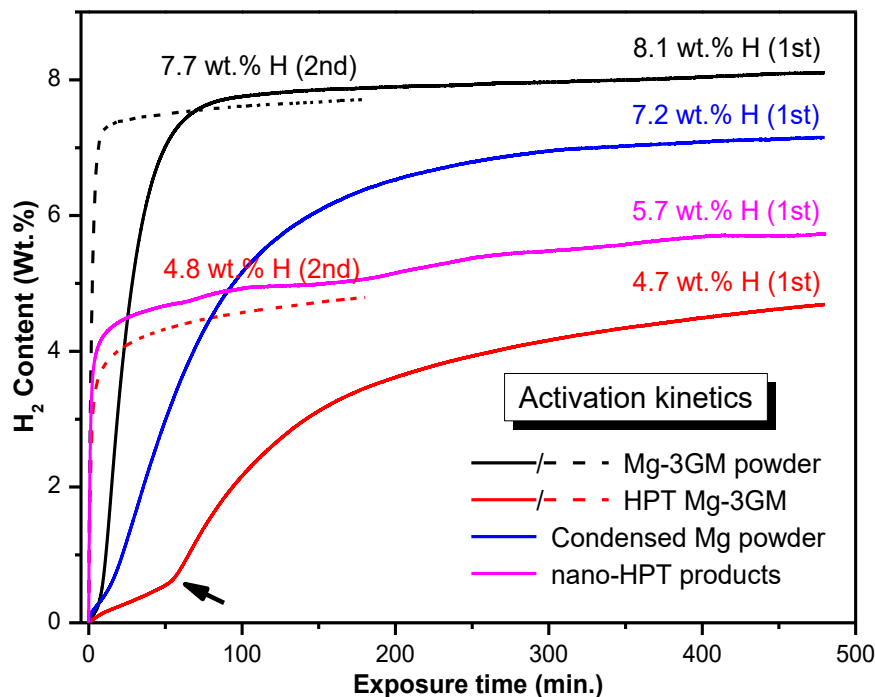


**Figure 6.5** – First and second hydrogenation kinetics obtained at 400 °C under a hydrogen pressure of 3.5 MPa for the as-synthesized Mg-3GM powder and its HPT composite. For comparison, the activation curves for the C-free Mg and its HPT product are also included.

For comparison, the first hydrogenation behavior of the condensed Mg powder and its nano-HPT product analyzed in **Chapter 4** is also given in Figure 6.5. It can be seen that the C-doped powder exhibits excellent hydrogenation kinetics as well as storage capacity than the C-free powder, which may be due to the catalytic effects of graphene additives in the former one. After the HPT treatments of these powder precursors, the results present a reverse trend where the C-doped HPT sample (i.e. HPT Mg-3GM) exhibits poor performance at the first hydrogenation compared to the nano-HPT product obtained from the C-free condensed powder. This is quite surprising while it has been considered that the SPD processing can significantly improve the activation characteristics of Mg [5.8,5.9,5.21,6.23].

Furthermore, it should be noted that the hydrogenation kinetics for both the C-doped samples has been significantly accelerated during the second activation, while it was more pronounced for the HPT composite. The inflexion observed at the beginning of the first hydrogenation of the C-doped HPT sample (shown by arrow), which is characteristic of the incubation stage, have completely disappeared at the second activation. The improvements in absorption kinetics, particularly for the HPT composite, could be explained based on the fact that due to the 30% volume expansions during the first hydrogenation either it can create numerous microcracks within the sintered products or it may even disintegrate the bulk materials into very fine powder particles. These structural modifications could significantly improve the hydride nucleation rate and also results in speeding up of the hydrogen storage kinetics. Nevertheless, while the powder composite maintains a relatively higher hydrogen storage capacity (~ 7.7 wt%) within 3 h of hydrogen exposure at the second activation, in spite of its faster absorption kinetics the HPT composite did not show much improvements in the storage capacity (~ 4.8 wt%). A

small reduction in the hydrogen storage capacity of the powder composite could be attributed to the fact that some of the chemically bonded hydrogen to the amorphous carbon could not release at 400 °C applied for the first dehydrogenation (chemisorbed hydrogen usually decomposing at above 600 °C [6.24,6.25]), and thus, may block these chemically active sites in the subsequent hydrogenation cycles.

## **6.3 Hydrogen sorption properties**

### **6.3.1 Thermodynamics of absorption/desorption**

The activated samples were employed to measure the pressure-composition-temperature (PCT) diagrams at different temperatures to investigate if any modifications in the thermodynamics properties of Mg due the carbon additives as well as the severe plastic deformation by HPT. Figure 6.6 presents the PCT isotherms for both the samples and the corresponding van't Hoff plots, and the thermodynamics properties subtracted from these tests are summarized in Table 6.1. The changes in enthalpy of formation for hydrogen uptake/release were estimated by using the van't Hoff equation following the procedure as the one described in Ref. [5.21].

**Table 6.1** – Thermodynamics properties of hydrogen absorption/desorption obtained from the PCT measurements of the powder and its HPT composite.

Samples	Temperature (°C)	H content (wt%)	P <sub>abs</sub> (MPa)	P <sub>des</sub> (MPa)	Pressure hysteresis (MPa)	$\Delta H_{abs}$ (kJ/mol)	$\Delta H_{des}$ (kJ/mol)
Mg-3GM powder	400	7.37	1.885	1.347	0.538	$-84.1 \pm 1.1$	$78.3 \pm 0.3$
	375	7.13	0.984	0.786	0.198		
	350	7.19	0.544	0.438	0.106		
	325	7.07	0.282	-	-		
HPT Mg-3GM	400	6.18	1.603	1.529	0.074	$-80.2 \pm 1.5$	$83.2 \pm 0.5$
	375	6.17	0.855	0.809	0.046		
	350	5.97	0.479	0.447	0.032		
	325	5.85	0.262	0.235	0.027		

As can be noticed from these PCT diagrams and the associated data, there are some interesting characteristic differences between the powder and its HPT composite. Firstly, the HPT composite possesses lower absorption and higher desorption equilibrium pressures compared to its initial powder precursor (Table 6.1). Consistently with the results in **Chapters 4** and **5**, it is also clear that the hydriding/dehydriding pressure hysteresis has been significantly improved upon HPT processing of powder precursor. Secondly, it can be readily apparent from Table 6.1 that under thermodynamic equilibrium conditions the hydrogen storage capacity of the HPT composite substantially increases from its initial value of 4.7 wt% H after the first activation process. Thirdly, it is interesting to note that while the HPT specimen can completely desorb at 325 °C, the initial condensed powder does not. Finally, it can be noticed from the enthalpy values given in Table 6.1 that while the HPT processing of powder sample has slightly improved its absorption enthalpy, there has been opposite trend for the desorption enthalpy which is higher for

the HPT-product. This is well consistent with the results obtained for the condensed Mg powder and its nano-HPT product; however, it was reverse for the atomized powder and its micro-HPT product (see Table 4.1, Chapter 4). It is also clear from this study that the addition of carbonaceous materials in the pure Mg precursor does not bring much improvement in the thermodynamic properties of magnesium hydride.

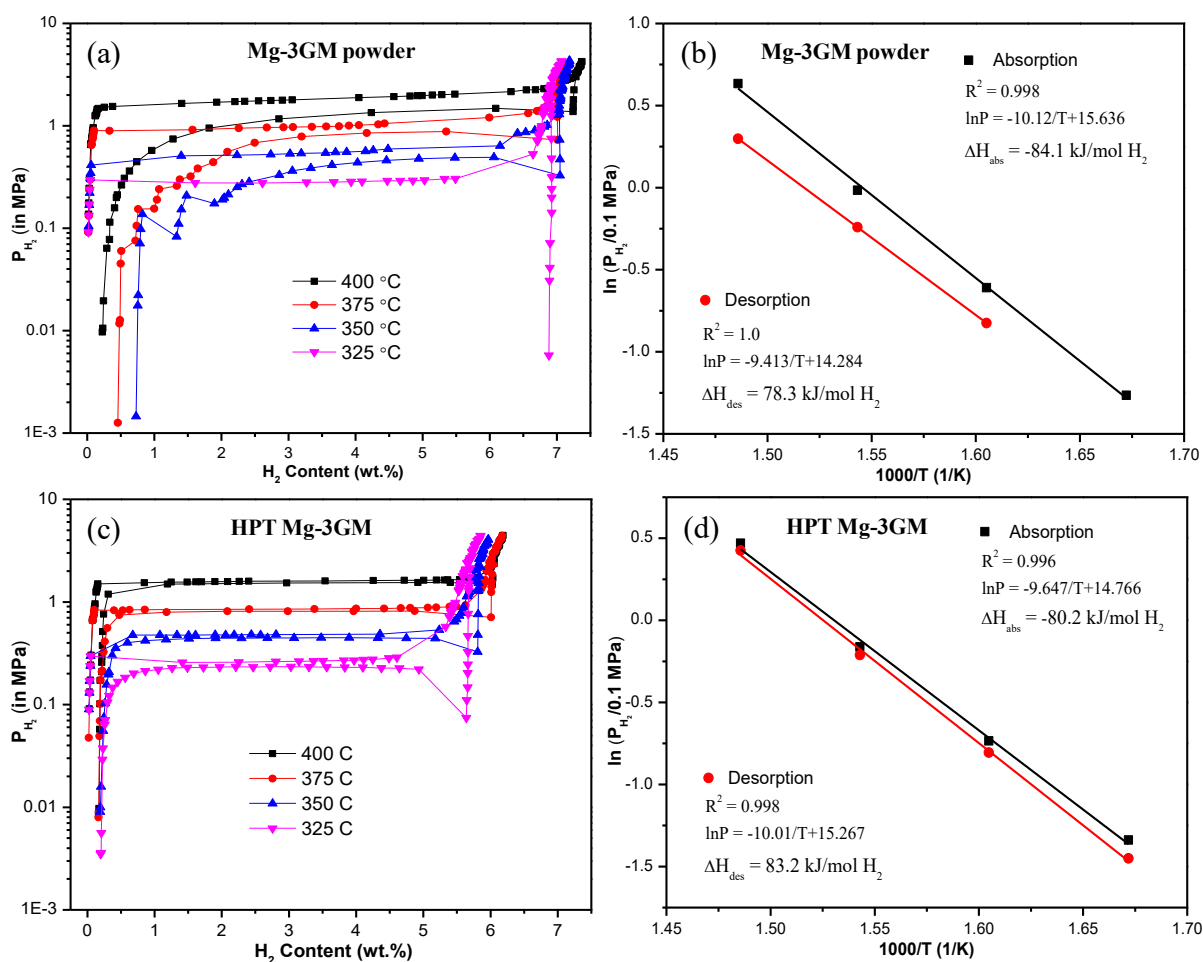


**Figure 6.6** – Pressure-composition-temperature (PCT) isotherms (a, c) recorded at different temperatures and (b, d) the corresponding van't Hoff plots for the Mg-3GM powder (a) and its HPT consolidated composite (b).

### **6.3.2 Kinetics of hydrogen absorption**

Both samples were tested for dynamic hydrogenation at 200, 250, 300 and 400 °C followed by the PCT measurements, and the resultant kinetic curves are given in Figure 6.7. For comparison, the second activation kinetics curves obtained at 400 °C are also included (dashed lines). If we compare the present kinetics behaviors recorded at 400 °C with that of the second hydrogenation kinetics (see Figure 6.5), it is obvious that both the transformation kinetics as well as the hydrogen storage capacity have been modified after the hydriding/dehydriding cycles.

While the absorption/desorption cycling applied on the powder sample have slightly diminished the storage capacity (Figure 6.7(a)), its effect was opposite for the HPT composite for which both the absorption kinetics as well as its hydrogen storage capacity were improved (Figure 6.7(b)). For example, at 400 °C the HPT product can absorb 3.5 wt% H within 2 min in comparison with the one (~ 2.8 wt%) recorded for the second activation process, and its hydrogen storage quantity after 2 h of hydrogen exposure increases from 4.8 wt% to 6.1 wt% due to the cycling operations. In a similar kind of study, Skripnyuk et al. [6.16] have reported that the equal channel angular pressing (ECAP) of the as-synthesized Mg-2 mass% multiwall CNTs composite resulted in slowing down of the absorption/desorption kinetics at the initial stages, and their acceleration in the later stages of processes. They claimed that this phenomenon was associated with the competitive factors of a decrease in hydrogen diffusion through the disordered CNTs and an increase in hydrogen diffusion kinetics in the ECAP Mg matrix.

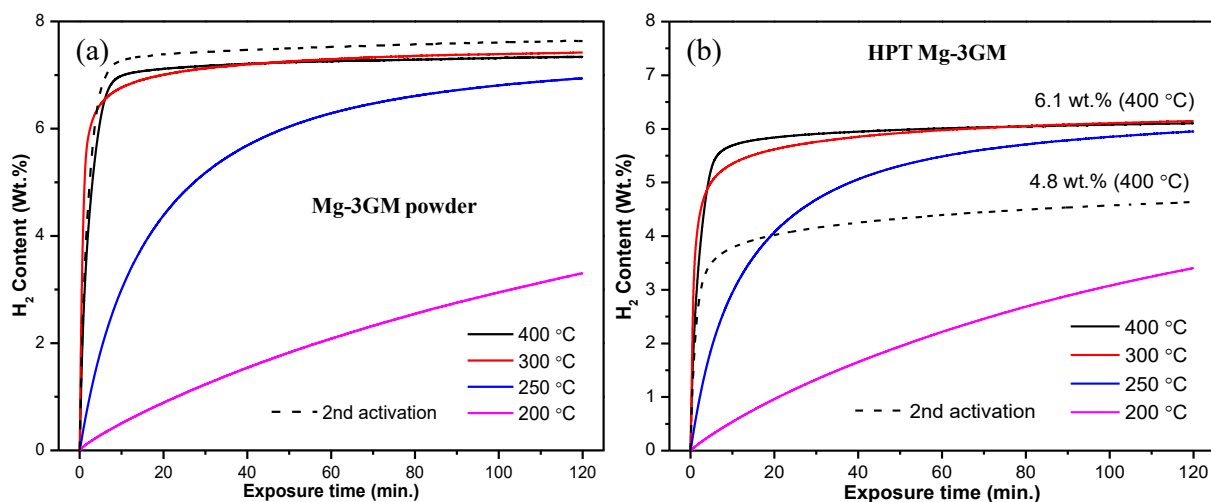


**Figure 6.7** – Dynamic hydrogen absorption kinetics recorded at different operating temperatures for (a) the powder precursor and (b) its HPT nanocomposite.

The Johnson–Mehl–Avrami–Kolmogorov (JMAK) model [4.6] was utilized to estimate the apparent activation energy for hydrogenation following the same procedure as the one described in Ref. [5.21]. Based on the Arrhenius equation, the average activation energy was reported to be  $50.0 \pm 5.0$  kJ/mol H<sub>2</sub> for the HPT product which is comparatively lower than the value ( $E_a = 64.0 \pm 8.0$  kJ/mol H<sub>2</sub>) obtained for the powder sample. However, these values are significantly lower than the one reported for the C-free Mg powder ( $E_a = 87.0 \pm 6.0$  kJ/mol H<sub>2</sub> [5.21]), and even further lower than those reported in the literature for other kinds of Mg powders ( $E_a = 90 \pm 10.0$  kJ/mol H<sub>2</sub> [6.26]). The improvements in absorption activation energy for the current samples could be ascribed to the excellent catalytic effects of the graphene additives.

### **6.3.3 Hydrogen desorption behaviors**

The dehydrogenation properties of the final hydrided samples, whose XRD patterns were given in Figure 6.3(b), were investigated by the DSC-TG measurements following the experimental conditions as mentioned previously. Figure 6.8 compares the resultant DSC and TG curves obtained at a heating rate of 10 °C/min for both the samples. For comparison, the DSC and TG curves for the first activated powder sample is also given in Figure 6.8. The most salient desorption properties subtracted from the DSC-TG curves are summarized in Table 6.2.

The DSC profiles presented in Figure 6.8(a) show a rather symmetrical endothermic peak for the powder precursor while a non-symmetrical peak for the HPT composite. The non-symmetry could be associated with the wide range of particle size distributions achieved through the repetitive hydriding/dehydriding cycles for the HPT product. It is readily apparent from Figure 6.8(a) and Table 6.2 that the desorption temperatures of the powder composite have been substantially modified through the hydriding/dehydriding cycles, and are slightly higher ranges than the activated powder and further higher than the HPT-product. However, the desorption kinetics of the powder composite, determined from the TG curves as a function of time (see Table 6.2), is relatively faster than that of its HPT counterpart.

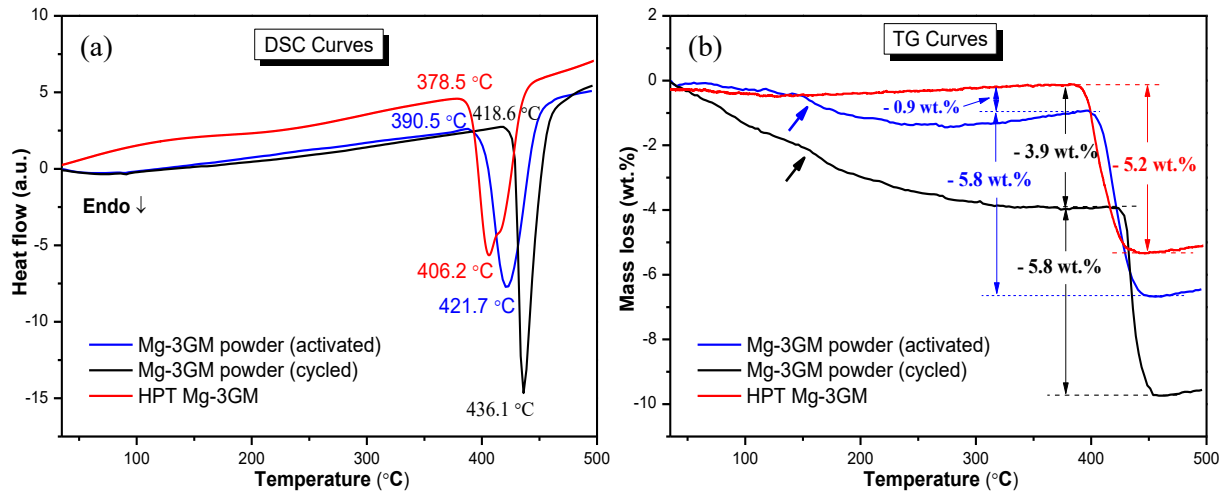


**Figure 6.8** – (a) DSC and (b) TG curves obtained at a heating rate of 10 °C/min from the final hydrided products for the powder and the HPT composites.

**Table 6.2** - Characteristic properties of hydrogen desorption subtracted from the DSC-TG analyses for both the samples.

Samples	Onset of desorption (°C)	Peak maxima (°C)	Desorption rate (wt%/min)	H uptake (wt%)	H release (wt%)	
					1 <sup>st</sup> step	2 <sup>nd</sup> step
Mg-3GM powder (cycled)	418.6	436.1	2.9	7.5	3.9	5.8
Mg-3GM powder (activated)	390.5	421.7	1.8	8.1	0.9	5.8
HPT Mg-3GM	378.5	406.2	1.6	6.4	-	5.2

The TG curves presented in Figure 6.8(b) clearly reveal that for the activated powder the mass loss starts at around 150 °C while it was even at around room temperature for the cycled powder composite. However, for both types of powders, there is a sudden drop in mass loss at around 150 °C (as shown by arrows). This interesting observation does not seem to be associated to any heat-flow in the DSC traces (see Figure 6.8(a)). This suggests that the hydrogen release recorded in the TG traces at the early stage of heating did not result from a phase transformation. Thus, it could be possible that the nature of carbon phase prevailed in the powder sample allows some hydrogen storage by adsorption. Thereby, the two powder samples exhibit two-step desorption processes while it was at the peak temperature where the hydrided HPT-product completely desorbs in one-step. Although the powder samples show significant differences in the mass loss during the early stages of desorption, they recover the same amount of hydrogen (~ 5.8 wt%) at their peak maxima due to the decomposition of MgH<sub>2</sub>. Moreover, while a small amount of mass loss (~ 0.9 wt%) for the activated powder could be reasonable to explain based on the potential adsorption of the carbon species, it is quite surprising for the cycled powder composite presenting a higher % of mass loss (~ 3.9 wt%) at the early stages of heating.

The Kissinger method [2.15] was applied to determine the apparent activation energy for desorption for both samples. It was estimated to be around  $170.0 \pm 5.0$  kJ/mol H<sub>2</sub> for both, which means that the HPT processing did not bring any changes in the activation energy of the Mg-3GM powder composite. However, this value is significantly lower than that obtained for the nano-HPT product ( $E_d = 209.0 \pm 6.0$  kJ/mol H<sub>2</sub>) obtained from C-free Mg powder precursor (see Table 4.5, **Chapter 4**). The lowering in activation energy for the C-doped HPT product could be associated with the catalytic effects of graphene additive.

## **6.4 Discussion**

It was uncovered from the present study that the introduction of graphene additives into the Mg matrix by an arc-plasma evaporation/condensation method demonstrated superior hydrogen storage properties in comparison with the C-free Mg powder (referred to **Chapter 4**). However, the severe plastic deformation through HPT of this as-synthesized powder precursor has imposed significant differences, and even opposite trends, in the hydrogen sorption characteristics. The fundamental differences in the hydrogen storage properties between the powder and its HPT-deformed composites have been emphasized, and most of these differences should be understood at the light of the powder morphology, the structural modifications upon HPT and the catalytic effects of graphene additives. Hence, in the following subsection the above mentioned factors are thoroughly discussed.

### **6.4.1 Peculiarity in powder formation and its consequences**

As confirmed by the TEM analysis (Figures 6.1(a-b)) and seen by the SEM image (Figure 6.2(a)), the size or shape of the Mg powder particles formed during the arc-plasma processing was not affected by the presence of the carbonaceous precursor. The XRD analysis did not reveal any shift of the Mg peaks that would witness incorporation of some amount of carbon in Mg matrix. Also, the SAED (Figure 6.1(c, f)), XRD (Figure 6.3(a)) and Raman (Figure 6.4) analyses did not confirm any contribution of specific crystalline carbon phase in the Mg-3GM composite powder. This suggests that (i) there was no chemical interaction between Mg and C that could yield to the presence of magnesium carbide and (ii) the crystalline carbon phases present in the starting precursor were modified by the arc-plasma evaporation/condensation process. These two

observations are rather common in the case of Mg/C based systems after high energy ball-milling for which crystalline graphite-like phases can hardly be detected [1.57-1.63,6.2-6.4].

In addition, the TEM inspection of the arc-plasma condensed composite powder revealed that a 2-3 nm thin layer of carbon species has accumulated on the overall surface of the Mg particles so that, the powder particles are surrounded by a continuous “protective” layer (see Figure 6.1(b)). This observations share some similarities with the findings by other group of researchers, where carbon components can either be inserted into the subsurface of Mg [6.22,6.27] or accumulated as a layer [6.28-6.30] on the surface of Mg domains/particles during high energy ball-milling. At this stage, it could be reasonable to anticipate from the present study that due to the very high arc-plasma reaction temperature reached up to around 15000 °C, the starting graphene powder precursor might have been evaporated and subsequently condensed onto the surface of Mg powder particles that were already condensed. A significant difference in the heat of vaporization between Mg (128 kJ/mol) and carbon (715 kJ/mol) could itself explain the above speculation. It could also be possible that the graphene structure has been completely destroyed and/or uncrystallized during the arc-plasma process forming an amorphous/glassy state of carbon in the obtained powder particles.

The superior hydrogen sorption properties exhibited by the as-synthesized powder particles are merely attributed to their unique morphological features. The excellent first hydrogenation kinetics clearly reveals the positive catalytic effects of graphene additives. The catalytic activation of Mg/C based systems processed by ball-milling in the presence of graphitic carbon was also reported by many researchers [1.58,6.31,6.32]. In particular, Bouaricha et al. [6.31] have reported that the Mg<sub>nano</sub>/graphite composite prepared by 40 h of high energy ball-

milling absorbed 3.5 wt% H after 30 min of first hydrogen exposure. If we recall the first activation kinetics (see Figure 6.5), the Mg-3GM powder could store 5.3 wt% H at the same time. However, these values are significantly higher than that recorded for the C-free Mg powder (~1.6 wt%) compared in Figure 6.5. While the presence of carbon species along with the MgO phase in the present composite powder could play an important role for accelerating the nucleation of MgH<sub>2</sub>, the formation of an impervious MgO oxide layer alone on the Mg particles might have retarded such kind of nucleation process in the case of C-free Mg powder, which in turn, prolongs the activation process through an incubation stage at the beginning of M-H interactions. However, the present results clearly demonstrated a radical improvement in the activation characteristics of Mg powders in the presence of graphene additives, consistently with the existing literature on other powder preparation processes [1.58,6.28,6.31,6.32].

According to the hydrogen spill-over mechanism [6.33,6.34], it could be possible that the dissociation of hydrogen molecules could take place on the surface of MgO substrates, and thus activated monatomic hydrogen could be transported by the carbonaceous species. Furthermore, a density functional theory (DFT) calculation on a Mg(0001) surface suggests that subsurface carbon atoms which might have incorporated into the metal phase during ball milling only slightly affects the hydrogen dissociation but mainly facilitates the diffusion of atomic hydrogen by lowering the transport activation barriers at the interfaces [6.35]. Hence, due to the peculiar surface morphology of the present composite powder it could be possible that the presence of carbon species may accelerate the nucleation of MgH<sub>2</sub> by promoting the catalytic activation of hydrogen molecules following the mechanism proposed in Ref. [6.35].

Furthermore, it was evidenced that the Mg-3GM powder composite demonstrated an anomalous hydrogen uptake capacity of 8.1 wt% at the first hydrogenation (Figure 6.5), while it has been reduced to 7.5 wt% in the subsequent hydrogenation (Table 6.2) which is almost 99% of the theoretical capacity of pure Mg. However, there has been a partial recovery of hydrogen (~ 6.7 wt% (0.9 + 5.8)) upon thermal decomposition of the first hydrided powder. This lower recovery of hydrogen could be explained based on the fact that the chemically bonded hydrogen did not release during the thermal decomposition up to 500 °C (chemisorbed hydrogen usually decomposing at above 600 °C [6.24,6.25]). It should be noted that the nature of carbon materials and their physicochemical interactions with the host metals are the most important aspects to achieve drastic improvements in the hydrogen sorption properties, particularly for the novel structure of graphene based allotropes such as CNTs, CNFs [1.62,1.63]. Thereby, while a strong interaction between Mg and graphene has led to the formation of a thin carbon layer in the arc-plasma condensed Mg-3GM powder, the hydrogen chemisorption by the distorted graphene structures could take place during the first hydrogenation conducted at relatively high temperature and high hydrogen pressure. In addition, the intercalation of hydrogen molecules within the distorted graphene sheets cannot be completely discarded in some cases [6.23,6.27,6.31,6.36], while the introduction of additional interfaces between the Mg and carbon species could provide some other kinds of potential sites for hydrogen trapping. Therefore, the formation of hydrocarbons with the dangling bonds and/or the intercalation/hydrogen trapping could be the possible reasons for overcharging of the composite powder at the first hydrogenation, while the synergistic catalytic effects of the MgO oxide particles and the graphene additive could allow them for superior reversible storage capacity.

#### **7.4.2 Effects of severe plastic deformation through HPT**

Severe plastic deformation through HPT is not only known for introducing a huge amounts of shear strains under very high hydrostatic pressures but also generating significant structural defects such as dislocations, large fraction of grain boundaries, vacancies, and sometimes numerous microcracks in the matrix phase. Due to these structural heterogeneities in the final HPT product, they have been widely investigated for modifying the hydrogen storage properties of Mg-based materials [4.4,4.10-4.12]. The HPT consolidation of the as-synthesized Mg-3GM powder has led to the significant structural modifications in the resultant bulk composite, and also to the characteristic differences in the hydrogen sorption properties. It was noticed that the consolidated C-doped microstructure (grain width < 200 nm) has been significantly refined in comparison with the C-free nano-HPT product (200 - 300 nm, see 3.9, **Chapter 3**). This could be associated with the Zener pinning effects of both the MgO oxide particles and the carbonaceous additives often confined to the grain boundaries (see Figures 6.2(b-c)). Moreover, although the presence of graphitic carbon was not detected for the composite powder, its evolution after the HPT processing was confirmed by the XRD and Raman analyses. The Raman spectrum suggests that the nature of the graphitic phase consists of the multiple stacks of graphene layer with significant disordered microstructures. The extreme shear deformation mode imposed by HPT at room temperature might have caused a partial graphitization of the initial amorphous/glassy state of carbon in the Mg-3GM powder precursor.

It was revealed that the consolidation of powder particles into bulk composite presents mixed-type of responses on the improvements in hydrogen sorption properties of Mg. At the first hydrogenation, the powder particles showed faster absorption kinetics than that of its HPT-

product and even further improved this kinetics during the second activation process (Figure 6.5). Consistently with the previous results presented in **Chapters 4 and 5**, the HPT processing has significantly improved the hydriding/dehydriding pressure hysteresis in comparison with the composite powder.

The main disadvantage of the HPT processing was that it has severely impaired the hydrogen storage capacity of the C-doped powder. The reduction in storage capacity for the HPT-product was a consequence of the absence of surface catalytic effect of the carbonaceous phase that was compressed inside the consolidated product. This has led to an incomplete hydrogenation which was confirmed by the XRD analysis of the final hydrided products revealing higher traces of un-reacted Mg crystals in the hydrided HPT products (see Figure 6.3(b)). The incomplete hydrogenation of the HPT-product is plausibly due to the combination of restricted hydrogen diffusion to the interior of bulk Mg matrix and some crystallographic perturbations generated by the HPT deformation that may alter the amounts of hydrogen that can be stored in the Mg lattice.

Increasing the number of hydriding/dehydriding cycles has generated significant differences in the hydrogen sorption properties of the powder composite and its HPT-product. While the absorption kinetics and the hydrogen storage capacity were slightly diminished for the powder sample, it was the HPT-product whose hydrogenation kinetics (from 1.4 to 1.75 wt%/min) and storage capability (from 4.8 to 6.4 wt% H) have been significantly improved upon the cycling operations. This is likely due to the opening of new pathways by formation of additional cracks upon cycling that brings additional fresh nanometric Mg domains decorated

with catalytic MgO oxide particles along with disordered graphene layers that restricted the grain growth upon the thermal treatments. Conversely, the loose powder particles could be sintered into larger particles due to the significant surface materials flow at the relatively higher operating temperatures (similar to the C-free Mg powder particles sustained several hydriding/dehydriding cycles, see Figure 4.7, **Chapter 4**). The enhancement in kinetics behaviors of the HPT composite was also associated with the lower activation energy for absorption compared to the powder composite.

Finally, although the HPT processing has substantially decreased the hydrogen desorption temperatures of the initial powder precursor, it has limited the kinetics of hydrogen desorption as well as its recovery when the hydrided products were characterized by the DSC-TG measurements. These results are consistent with the previously investigated HPT products with different chemistry (see **Chapters 4 and 5**). Although the reasons for this characteristic desorption behaviors of the HPT composites are less clearly understood, it could be possible that while the increased amounts of structural defects and grain boundaries in the HPT-deformed materials can provide the hydrogen diffusion pathways, the large fraction of grain boundaries and/or interfaces (Mg/MgO or Mg/C) acting as trapping sites for hydrogen are less effective in this type of consolidated products.

## **Chapter's conclusions**

The potential improvements in the hydrogen storage properties of Mg were investigated for the as-synthesized powder and its severely deformed composite in the presence of carbon additives. The novel form of carbon, graphene monolayer, was used together with Mg for preparing C-doped nanometric condensed powder by arc-plasma evaporation/condensation process. The effect of HPT processing was tested on the improvement in hydrogen sorption properties of the as-synthesized composite powder. The structure and morphology of the powder and its HPT-consolidated products were characterized by using a number of complementary techniques including XRD, Raman spectroscopy, high resolution SEM and TEM. The hydrogen sorption performances were examined by Sievert-type apparatus and DSC-TG analysis. The salient results obtained from the present study can be summarized as follows.

- 1) The peculiarity in the powder particle formation during the arc-plasma processing of Mg + graphene precursors has led to the formation of a “core-shell” type of powder morphology, in which the core of Mg powder particles was surrounded by a protective thin layer of amorphous carbon. Finally, the controlled passivation of the condensed powder particles has basically generated an Mg/C/MgO based composite.
- 2) The HPT consolidation of the as-synthesized powder has resulted in the development of severely elongated nanostructured Mg domains inclined by  $60^\circ$  from the shear plane. While the amorphous carbon layer has been partially graphitized under the extreme shear straining by HPT, the protective shell of oxides has been fragmented into the nanometric MgO particles often located along the grain boundaries.

- 3) At the first hydrogenation, the C-doped powder particles demonstrated faster storage kinetics than the C-free Mg nanopowder. The storage capacity of the powder sample was little diminished upon the repetitive hydriding/dehydriding cycles.
- 4) A significant effect of HPT processing was to reduce the pressure hysteresis between absorption/desorption processes and the hydrogenation enthalpy. Interestingly, the equilibrium plateau pressures are always lower for the HPT-processed samples than their initial powder precursors.
- 5) The main disadvantage of the HPT processing was to reduce the hydrogen storage capacity in comparison to the powder particles. While the Mg/C/MgO composite powder exhibited an excellent hydrogen storage capability of 8.1 wt% at the first hydrogenation and of 7.5 wt% at the subsequent hydriding/dehydriding cycles, the HPT-consolidated products did only reach to a maximum storage capacity of 6.4 wt% H.
- 6) The thermal decomposition results clearly revealed that although the HPT processing has led to the reduction in the desorption temperatures with respect to the powder sample, the hydrided HPT-product evidenced slower desorption kinetics and lower hydrogen recovery capacity as compared to its powder counterpart.

## References

- [6.1] Züttel A, Borgschulte A, Schlapbach L. eds. "Hydrogen as a future energy carrier." Wiley VCH Press, Germany, 2011.
- [6.2] Wu CZ, Wang P, Yao X, Liu C, Chen DM, Lu GQ, Cheng HM. "Effect of carbon/noncarbon addition on hydrogen storage behaviors of magnesium hydride." *J. Alloys Compd.* 414 (2006) 259-64.
- [6.3] Chen D, Chen L, Liu S, Ma CX, Chen DM, Wang LB. "Microstructure and hydrogen storage property of Mg/MWNTs composites." *J. Alloys Compd.* 372 (2004) 231-7.
- [6.4] Pierard N, Fonseca A, Colomer JF, Bossuot C, Benoit JM, Van Tendeloo G, Pirard JP, Nagy JB. "Ball milling effect on the structure of single-wall carbon nanotubes." *Carbon* 42 (2004) 1691-7.
- [6.5] Ohno S. "Generation rate of ultrafine metal particles in hydrogen plasma-metal reaction." *J. Japan Inst. Metals.* 48 (1984) 640-6.
- [6.6] Stephane P, Zou JX, Zeng XQ, Sun HQ, Ding WJ. "Preparation and hydrogen storage properties of ultrafine pure Mg and Mg-Ti particles." *Trans. Nonferrous Met. Soc. China* 22 (2012) 1849-54.
- [6.7] Zou JX, Zeng XQ, Ying Y, Chen X, Guo H, Zhou S, Ding WJ. "Study on the hydrogen storage properties of core-shell structured Mg-RE (RE = Nd, Gd, Er) nano-composites synthesized through arc plasma method." *Int. J. Hydrogen Energy* 38 (2013) 2337-46.
- [6.8] Zou JX, Long S, Chen X, Zeng XQ, Ding WJ. "Preparation and hydrogen sorption properties of a Ni decorated Mg based Mg@ Ni nano-composite." *Int. J. Hydrogen Energy* 40 (2015) 1820-8.
- [6.9] Hahne E, Kallweit J. "Thermal conductivity of metal hydride materials for storage of hydrogen: experimental investigation." *Int. J. Hydrogen Energy* 23 (1998) 107-14.
- [6.10] Kim KJ, Montoya B, Razani A, Lee KH. "Metal hydride compacts of improved thermal conductivity." *Int. J. Hydrogen Energy* 26 (2001) 609-13.
- [6.11] Chaise A, De Rango P, Marty P, Fruchart D, Miraglia S, Olives R, Garrier S. "Enhancement of hydrogen sorption in magnesium hydride using expanded natural graphite." *Int. J. Hydrogen Energy* 34 (2009) 8589-96.
- [6.12] Khandelwal A, Agresti F, Capurso G, Russo SL, Maddalena A, Gialanella S, Principi G. "Pellets of MgH<sub>2</sub>-based composites as practical material for solid state hydrogen storage." *Int. J. Hydrogen Energy* 35 (2010) 3565-71.
- [6.13] Pohlmann C, Röntzsch L, Kalinichenka S, Hutsch T, Kieback B. "Magnesium alloy-graphite composites with tailored heat conduction properties for hydrogen storage applications." *Int. J. Hydrogen Energy* 35 (2010) 12829-36.
- [6.14] Popilevsky L, Skripnyuk VM, Beregovsky M, Sezen M, Amouyal Y, Rabkin E. "Hydrogen storage and thermal transport properties of pelletized porous Mg-2 wt.%

- multiwall carbon nanotubes and Mg-2 wt.% graphite composites.” *Int. J. Hydrogen Energy* 41 (2016) 14461-74.
- [6.15] Popilevsky L, Skripnyuk VM, Amouyal Y, Rabkin E. “Tuning the thermal conductivity of hydrogenated porous magnesium hydride composites with the aid of carbonaceous additives.” *Int. J. Hydrogen Energy* 42 (2017) 22395-405.
- [6.16] Skripnyuk VM, Rabkin E, Bendersky LA, Magrez A, Carreño-Morelli E, Estrin Y. “Hydrogen storage properties of as-synthesized and severely deformed magnesium–multiwall carbon nanotubes composite.” *Int. J. Hydrogen Energy* 35 (2010) 5471-8.
- [6.17] Zhang X, Yang R, Yang J, Zhao W, Zheng J, Tian W, Li X. “Synthesis of magnesium nanoparticles with superior hydrogen storage properties by acetylene plasma metal reaction.” *Int. J. Hydrogen Energy* 36 (2011) 4967-75.
- [6.18] Burke PJ, Bayindir Z, Kipouros GJ. “X-ray photoelectron spectroscopy (XPS) investigation of the surface film on magnesium powders.” *Appl. Spectrosc.* 66 (2012) 510-8.
- [6.19] Ferrari AC, Meyer JC, Scardaci V, Casiraghi C, Lazzeri M, et al. “Raman spectrum of graphene and graphene layers.” *Phys. Rev. Lett.* 97 (2006) 187401.
- [6.20] Onodera A, Higashi K, Irie Y. “Crystallization of amorphous carbon at high static pressure and high temperature.” *J. Mater. Sci.* 23 (1988) 422-8.
- [6.21] Loh GC, Baillargeat D. Graphitization of amorphous carbon and its transformation pathways. *Journal of Applied Physics.* 2013 Jul 21;114(3):033534.
- [6.22] Lototsky M, Sibanyoni JM, Denys RV, Williams M, Pollet BG, Yartys VA. “Magnesium–carbon hydrogen storage hybrid materials produced by reactive ball milling in hydrogen.” *Carbon* 57 (2013) 146-60.
- [6.23] Floriano R, Leiva DR, Carvalho JA, Ishikawa TT, Botta WJ. “Cold rolling under inert atmosphere: A powerful tool for Mg activation.” *Int. J. Hydrogen Energy* 39 (2014) 4959-65.
- [6.24] Kapitonov IN, Konkov OI, Terukov EI, Trapeznikova IN. “Amorphous carbon: how much of free hydrogen?.” *Diam. Relat. Mater.* 9 (2000) 707-10.
- [6.25] Miyaoka H, Ichikawa T, Fujii T, Ishida W, Isobe S, Fuji H, Kojima Y. “Anomalous hydrogen absorption on non-stoichiometric iron-carbon compound.” *J. Alloys Compd.* 507 (2010) 547-50.
- [6.26] Fernandez JF, Sanchez CR. “Rate determining step in the absorption and desorption of hydrogen by magnesium.” *J. Alloys Compd.* 340 (2002) 189-98.
- [6.27] Amirkhiz BS, Danaie M, Barnes M, Simard B, Mitlin D. “Hydrogen sorption cycling kinetic stability and microstructure of single-walled carbon nanotube (SWCNT) magnesium hydride (MgH<sub>2</sub>) nanocomposites.” *J. Phys. Chem. C* 114 (2010) 3265-75.
- [6.28] Spassov T, Zlatanova Z, Spassova M, Todorova S. “Hydrogen sorption properties of ball-milled Mg–C nanocomposites.” *Int. J. Hydrogen Energy* 35 (2010) 10396-403.

- [6.29] Rud AD, Lakhnik AM, Mikhailova SS, Karban OV, Surnin DV, Gilmutdinov FZ. "Structure of Mg-C nanocomposites produced by mechano-chemical synthesis." *J. Alloys Compd.* 509 (2011) S592-4.
- [6.30] Rud AD, Lakhnik AM. "Effect of carbon allotropes on the structure and hydrogen sorption during reactive ball-milling of Mg-C powder mixtures." *Int. J. Hydrogen Energy* 37 (2012) 4179-87.
- [6.31] Bouaricha S, Dodelet JP, Guay D, Huot J, Schulz R. "Study of the activation process of Mg-based hydrogen storage materials modified by graphite and other carbonaceous compounds." *J. Mater. Res.* 16 (2001) 2893-905.
- [6.32] Huot J, Tremblay ML, Schulz R. "Synthesis of nanocrystalline hydrogen storage materials." *J. Alloys Compd.* 356 (2003) 603-7.
- [6.33] Lueking AD, Yang RT. "Hydrogen spillover to enhance hydrogen storage—study of the effect of carbon physicochemical properties." *Appl. Catal. A* 265 (2004) 259-68.
- [6.34] Du AJ, Smith SC, Yao XD Lu GQ. "Hydrogen spillover mechanism on a Pd-doped Mg surface as revealed by ab initio density functional calculation." *J. Am. Chem. Soc.* 129 (2007) 10201-4.
- [6.35] Du AJ, Smith SC, Yao XD Lu GQ. "Catalytic effects of subsurface carbon in the chemisorption of hydrogen on a Mg (0001) surface: an ab-initio study." *J. Phys. Chem. B* 110 (2006) 1814-9.
- [6.36] Orimo S, Majer G, Fukunaga T, Züttel A, Schlapbach L, Fujii H. "Hydrogen in the mechanically prepared nanostructured graphite." *Appl. Phys. Lett.* 75 (1999) 3093-5.



## CONCLUSIONS AND PERSPECTIVES

---

### Summary and conclusions

In the study of impacts of severe plastic deformation (SPD) processes on the improvements in hydrogen storage properties of lightweight metal hydrides, a new powder metallurgy route has been adopted to produce a wide variety of magnesium based materials for hydrogen storage applications. This novel processing route mainly consists of: (i) synthesis of a rather “clean” Mg based powder particles and (ii) structural modifications by high-pressure torsion (HPT) deformation of the as-synthesized powder precursors.

In **Chapter 3**, the quasi-constrained HPT processing was first implemented for the bulk samples to understand the deformation characteristics for relatively thick-HPT samples (~ 3 mm). Two lightweight bulk materials (i.e. aluminum and magnesium) with different crystallographic structures were investigated to analyze the development of structural heterogeneities in terms of strains and microstructures. The optimum experimental conditions obtained from the processing of bulk materials were applied on powder consolidation in the second part of this chapter. Two distinct Mg powders - atomized micro-sized Mg powder produced by the gas-atomization process and condensed Mg nanopowder synthesized by the arc-plasma method - were separately consolidated by the two-step HPT procedure, and the effect of the nature of powder types on the powder consolidation behavior was investigated.

In **Chapter 4**, the two types of consolidated Mg products – whose microstructural evolutions were characterized in **Chapter 3** – were tested for the improvements in hydrogen storage performances in comparison with their initial powder precursors. They were mainly

investigated for the hydrogen activation characteristics, the thermodynamics and kinetics of hydriding/dehydriding processes, and also for the dehydrogenation properties.

In **Chapter 5**, a wide varieties of Mg-Fe based composites in the 9Mg-Fe and 2Mg-Fe stoichiometry was produced by the two-step HPT consolidation of the prior powder compositions. Two distinct powder precursors - atomized micro-sized powder and condensed ultrafine powder - in both Mg and Fe phases were employed to study the effects of nature of the initial powder precursors on the evolutions of microstructures, and the associated improvements in the hydrogen sorption properties of these HPT-consolidated products.

In **Chapter 6**, the synergistic effects of carbonaceous additions and microstructural modifications upon severe plastic deformation were studied for the improvements in hydrogen sorption properties of Mg. The Mg/graphene based composite powder was synthesized by the arc-plasma evaporation/condensation method, and they were subsequently consolidated into bulk nanocomposite by the two-step HPT consolidation process. The nature of carbon species in the powder as well as its HPT product was featured by the Raman spectroscopic analysis.

The main conclusions drawn from **Chapter 3 to 6** can be summarized as follows.

1. Severe plastic deformation through HPT of relatively thick-sample led to significant structural heterogeneities within the sample volume that were primarily dependent on the nature of crystal structures as well as the starting powder types in the case of powder consolidation. The HPT processing of bulk Mg and atomized Mg powder precursor demonstrated identical responses in the evolution of the microstructure, texture and

microhardness while comparing with that for the arc-plasma condensed and passivated Mg powder precursor.

2. A significant effect of HPT processing was to break the impervious MgO oxide layers - usually considered to be obstacles for the efficient hydrogen diffusion - into the nanometric particles to obtain uniform dispersion of them along with other catalytic additives (in this case Fe, C etc.) within the Mg domains and often located along the grain boundaries.
3. The substantial grain size refinement for the HPT-consolidated Mg products (with or without catalytic additions) in comparison with the bulk HPT Mg was mainly associated with the presence of uniformly dispersed nanometric MgO oxide particles (and/or catalytic additives) imposed significant Zener pinning to the migrating grain boundaries and restricted the grain size evolution within the fine elongated domains for the condensed powder precursors.
4. The HPT consolidation of powder precursors has provided substantial differences, and even opposite trends, in the hydrogen sorption characteristics of Mg. Through the introduction of structural defects and microstructural refinement, the HPT processing has allowed significant improvements in the first hydrogenation kinetics for the consolidated Mg products compared to their starting powder precursors while it was reverse for the C-doped HPT product.
5. Another significant impact of the HPT processing was to improve the thermodynamics properties of metal hydrides. It was revealed that the equilibrium pressures are always lower for the HPT-processed products than their initial powder precursors. Although the HPT processing has significantly improved the pressure hysteresis between absorption and desorption processes as well as the hydrogenation enthalpy, the HPT products were characterized with the higher dehydrogenation enthalpy than the powder precursors.

6. The major drawback of the HPT processing was to impair the maximum hydrogen storage capacity of the initial powder precursors irrespective of the nature of materials chemistry. For example, while the initial C-free and C-doped Mg nanopowder respectively exhibited an excellent storage capacity of 7.0 wt% and 7.5 wt% H, it was only about 5.5 wt% and 6.4 wt% H for their respective HPT-consolidated products. Conversely, a significant storage capacity of 6.6 wt% H was achieved for the micro-HPT product compared to its starting atomized powder precursor (6.2 wt% H).
7. The types of grain boundaries in the HPT-consolidated products play an important role on the desorption properties of metal hydrides. Although the HPT processing has drastically reduced the hydrogen desorption temperatures for all the powder combinations inspected here, the rate of dehydrogenation and the percentage of hydrogen recovery has slightly diminished for these consolidated products. This could be attributed to the large fraction of HAGBs and Mg/MgO or Mg/Fe or Mg/C interfaces, particularly in the case of consolidated products obtained from the condensed and passivated powder precursors, acting as potential trapping sites for hydrogen, and thereby, can hinder or prolong the dehydrogenation reaction.

## **Perspectives**

The present dissertation work has revealed some important aspects of research directions, which can lead to significant outcome in their own fields. They are discussed as follows.

Firstly, the new powder metallurgy route proposed in the present study can offer a versatile processing route for fabricating a wide variety of metal matrix composites while incorporating a small fraction of secondary phase to improve the mechanical and/or functional properties. For example, it was demonstrated that HPT consolidation of various powder precursors led to the developments of three different types of metal matrix composites, namely Mg/MgO, Mg/MgO/Fe and Mg/C/MgO based composites. A significant microhardness improvement for these composites suggests that more studies should be carried out for potential improvements in mechanical properties of these kinds of metal matrix composites. Furthermore, it was noticed that the evolution of texture in the HPT-consolidated Mg/MgO based composite obtained from the condensed and passivated nanopowder precursor was crucial and deviated from the ideal shear texture. The exact nature of deformation behavior of these nanopowder particles can be experimentally validated and modeled by detailed texture analysis using synchrotron X-ray diffraction technique or any other suitable techniques.

Secondly, it was revealed that the HPT processing of the atomized Mg powder precursor demonstrated some interesting hydrogen sorption properties (i.e. thermodynamics, desorption properties and storage capacity) in comparison with that of the consolidated condensed Mg nanopowder. Thus, severe plastic deformation (SPD) processing of atomized powder particles

containing negligible MgO oxides may lead to potential improvements in the hydrogen storage properties of Mg.

Finally, a fundamental problem of metal hydride powder particles lies with a low thermal conductivity of loose powder materials while designing an effective hydrogen storage tank. Accordingly, there have been significant researches pioneered on how to improve heat as well as mass transfer phenomena for the metal hydride powder beds. The SPD techniques have recently been attracted much attention for the fabrication of bulk hydride composites for potential improvements in thermal conductivity due to their full consolidation as well as reduced porosity. Furthermore, presence of carbonaceous species is an added advantage to accelerate the thermal conductivity of the metal hydride beds. Hence, our HPT-consolidated Mg based products are promising energy storage materials to improve the heat management in the fuel cell applications.

## APPENDIX

---

### Calculation of hydrogen contents

The amount of hydrogen absorbed during the dynamic hydrogen absorption at specific temperature and pressure can be estimated from the following equation:

$$wt(H)\% = \left( \frac{\Delta PMV}{mRT + \Delta PMV} \right) * 100$$

m: the mass of sample

M: the molar mass of hydrogen, 2.0159 g/mol.

R: the ideal gas constant, 8.314 J/mol. K

T: the absolute temperature of manifold chamber, K (see Figure 2.9, **Chapter 2**)

P: the pressure of hydrogen (MPa).

V: the total volume of reaction chamber (ml).

## Lists of figures

<b>Figure 1.1</b> - (a) One-dimensional potential energy curve for the reaction of hydrogen gas with a metal, and (b) pressure-composition isotherms for hydrogen absorption in a typical metal system, after Ref. [1.7] .....	17
<b>Figure 1.2</b> - Hydrogen storage capacity (per mass and volume) of metal hydrides, carbon nanotubes, petrol and other hydrocarbons, after Ref. [1.7] .....	18
<b>Figure 1.3</b> - Schematic illustration of an equal channel angular pressing (ECAP) technique, after Ref. [1.25] .....	27
<b>Figure 1.4</b> - Pressure-composition-temperature (PCT) isotherms of the ZK60 system. Black lines and points determined on ECAP and/or HEBM processed ZK60 represent the findings of Skripnyuk et al. [1.24]. Colored data for ZK60-4x measured at 200 – 260 °C, after Ref. [1.27]. Open and filled symbols indicate hydrogen absorption and desorption, respectively .....	28
<b>Figure 1.5</b> - Activation curves of cold rolled Mg–Pd 2.5 at%, ball milled Mg–Pd 2.5 at%, and cold rolled pure magnesium. Activation temperature 350 °C, hydrogen pressure 1.3 MPa. CR = cold rolled, BM = ball-milled, after Ref. [1.31] .....	31
<b>Figure 1.6</b> - Schematic illustrations of a quasi-constraint HPT facility, after Ref. [1.38] .....	33
<b>Figure 1.7</b> - (a) DSC curves of the starting material (MgH <sub>2</sub> as-received) and milled with or without MgO for 100 h, and (b) evolution of MgH <sub>2</sub> decomposition temperature measured by DSC with the milling time, after Ref. [1.54] .....	37
<b>Figure 2.1</b> - Morphological aspects of the Mg powder precursors for (a) the atomized micro-sized powder and (b) the condensed ultrafine powder particles .....	47
<b>Figure 2.2</b> - Morphological aspects of the Fe powder precursors in the case of (a) atomized micro-sized powder and (b) condensed ultrafine-grained powder particles .....	48
<b>Figure 2.3</b> - (a) SEM and (b) TEM images illustrating the morphological features of the Mg-graphene based composite powder obtained by the DC arc-plasma method .....	49
<b>Figure 2.4</b> - Schematic illustrations of a DC arc-plasma processing route applied in the present study for producing different nature of ultrafine powder particles, after Ref. [2.4] .....	50
<b>Figure 2.5</b> - High-pressure torsion (HPT) facility and its associated experimental setup employed for the present dissertation work. This facility is available at the laboratory LEM3, Metz, France .....	52

**Figure 2.6** - (a) Uniaxial compression of the initial powders into an intermediate disk, and (b) HPT processing of the precompacted green body into consolidated bulk products ..... 53

**Figure 2.7** - Reconstructed 3D images of the HPT deformed disks for (a) Al alloy and (b) pure Mg, obtained from the XRT data using the Avizo<sup>®</sup> 3D software ..... 54

**Figure 2.8** - A cross-sectional plane of one-half of an HPT-disk showing the positions selected for the Vickers microhardness measurements ..... 56

**Figure 2.9** - A schematic diagram of the working principle for a Sievert-type volumetric apparatus [2.14] employed in the present research ..... 59

**Figure 3.1** - A schematic diagram of the working principle for a Sievert-type volumetric apparatus [2.14] employed in the present research ..... 70

**Figure 3.2** - The distribution of strains across the through-thickness in (a) Al alloy and (b) Mg for 180° and 270° rotations. The distribution of the radial strains is also provided in the insets of (a) and (b), respectively. Figure 3.2(c) delineates a schematic diagram of a processed HPT-disk for the calculation of shear strain localization ..... 72

**Figure 3.3** - EBSD orientation maps and the corresponding (111) pole figures for the (a) initial specimen and (b) after simple uniaxial compression by 3.3% in the Al alloy ..... 74

**Figure 3.4** - EBSD orientation maps of HPT-processed (270°) Al alloy and the corresponding (111) pole figures obtained (a) at the centre of the disk on its middle plane, and at the edge of the disk on its (d) top, (e) middle and (f) bottom sections. The location of the C (red circles) and B (red triangles) ideal orientations of fcc simple shear textures are also shown. Note the differences in scale bars ..... 76

**Figure 3.5** - EBSD orientation images and the corresponding (0002) pole figures for the (a) initial specimen and (b) after simple uniaxial compression by 5.3% in the commercial purity Mg ..... 78

**Figure 3.6** - EBSD orientation maps of the HPT-processed (270°) commercial purity Mg and the corresponding (0002) pole figures obtained (a) at the centre of the disk on its middle plane, and at the edge of the disk on its (b) top, (c) middle, and (d) bottom sections. Note the differences in scale bars ..... 80

**Figure 3.7** - Distributions of Vickers microhardness in the radial direction (a, c) on the top, middle and bottom planes; and in the axial direction (b, d) across the disk-thickness in Al alloy (a-b) and Mg (c-d) ..... 82

**Figure 3.8** - Normalized X-ray diffraction (XRD) patterns recorded on the initial powder precursors and their HPT-products: (a) atomized Mg powder and its micro-HPT product, and (b) condensed Mg powder and its nano-HPT product ..... 88

**Figure 3.9** - SEM backscattered electron micrographs acquired at the outer-edge and across the through-thickness of the HPT-disks for (a-c) micro-HPT product and (d-f) nano-HPT product ..... 92

**Figure 3.10** - In-situ FIB micrograph of the nano-HPT product recorded during the foil preparation for TKD measurements. Arrows indicate the vacancies left after the 2 turns HPT consolidation ..... 94

**Figure 3.11** - EBSD orientation images accompanied with grain boundary misorientations and associated microtexture in (0002) pole figure for the 1/2 turn (a-c), 3/4 turn (d-f) and 2 turns (g-i) micro-HPT product, acquired at the outer edge and middle-section of the HPT-disks (see the inset of Figure 3.11(b)). The Mackenzie distribution of misorientation angles (uncorrelated) is plotted by solid black line. Note the differences in scale bar ..... 96

**Figure 3.12** - TKD-based EBSD orientation maps accompanied with grain boundary misorientations and associated microtexture in (0002) pole figure for the 1/2 turn (a-c), 3/4 turn (d-f) and 2 turns (g-i) nano-HPT product, obtained at the outer edge and middle-section of the HPT-disks (see the inset of Figure 3.12(b)). Note the differences in scale bar ..... 100

**Figure 3.13** - Variations of Vickers microhardness (Hv) along the radial direction as well as across the disk-thickness for 2 turns (a) micro-HPT product and (b) nano-HPT product. The hardness values reported for bulk Mg [1.41,3.20,3.22] are also given in the same graph ..... 102

**Figure 4.1** - First hydrogenation (i.e. activation kinetics) recorded for all the studied samples at 400 °C under a hydrogen pressure of 3.5 MPa; maximum H-storage quantities under steady-state conditions are given in the parenthesis ..... 119

**Figure 4.2** - Pressure-composition-temperature (PCT) isotherms recorded on the one-cycled activated products at different temperatures for (a, b) the initial powder particles, and (c, d) their HPT-consolidated products ..... 122

**Figure 4.3** - The van't Hoff plots for (a) absorption and (b) desorption obtained from the PCT isotherms for determining the hydrogen absorption/desorption enthalpy and entropy ..... 125

**Figure 4.4** - Dynamic hydrogen absorption profiles recorded at 300 °C, 350 °C and 400 °C under a constant hydrogen pressure of 3.5 MPa for (a) the atomized powder and its micro-HPT products and (b) the condensed powder and its nano-HPT products. The inset of Figure 4.4(b) shows the absorption kinetics obtained for 1 min exposure ..... 126

**Figure 4.5** - X-ray diffraction (XRD) patterns recorded from the hydrided samples for (a) the atomized powder and its micro-HPT products and (b) the condensed powder and its nano-HPT products ..... 130

**Figure 4.6** - DSC and TG profiles obtained at a heating rate of 10 °C/min from the hydrided samples for (a) the atomized Mg powder and its micro-HPT product and (b) the condensed Mg powder and its nano-HPT product ..... 132

**Figure 4.7** - SEM micrographs illustrating the morphological modifications upon absorption/desorption cycling for (a) the atomized powder and (b) the condensed powder ..... 134

**Figure 4.8** - Representative backscattered electron (BSE) micrographs of the hydrided HPT-products showing the microstructural evolutions upon absorption/desorption cycling ..... 136

**Figure 5.1** - (a) SE and (b-d) BSE micrographs acquired on the middle-thickness of the HPT-disks for the (a, b) mMg-10mFe, (c) mMg-10nFe and (d) nMg-10nFe composites for the 9Mg-Fe stoichiometry ..... 151

**Figure 5.2** - SE (left) and BSE (right) micrographs obtained from the middle-thickness of the HPT-disks for the (a, b) mMg-33mMg and (c, d) nMg-33nFe composites in the 2Mg-Fe grade ..... 154

**Figure 5.3** - Normalized X-ray diffraction patterns obtained from the HPT-processed composites for the (a) 9Mg-Fe and (b) 2Mg-Fe stoichiometric ratios ..... 155

**Figure 5.4** - Normalized X-ray diffraction patterns recorded on the final hydrided composites for the (a) 9Mg-Fe and (b) 2Mg-Fe stoichiometries ..... 158

**Figure 5.5** - First hydrogenation kinetics curves obtained at 400 °C for 8 h under a hydrogen pressure of 3.5 MPa for the (a) 9Mg-Fe and (b) 2Mg-Fe composites ..... 159

**Figure 5.6** - Pressure-composition-temperature (PCT) isotherms obtained at different temperatures from the one-cycled activated composites: (a) mMg-10mFe, (b) mMg-10nFe and (c) nMg-10nFe for the 9Mg-Fe stoichiometry ..... 161

**Figure 5.7** - The variations in hydrogen storage capacity with respect to temperature for the different types of HPT-consolidated products ..... 162

**Figure 5.8** - Pressure-composition-temperature (PCT) isotherms measured at different temperatures from the activated samples: (a) mMg-33mMg and (b) nMg-33nFe composites in the 2Mg-Fe stoichiometry ..... 165

**Figure 5.9** - Hydrogen absorption kinetics recorded at 250 °C and 300 °C under a hydrogen pressure of 3.5 MPa on the same samples used for thermodynamic measurements in case of the (a) 9Mg-Fe and (b) 2Mg-Fe stoichiometry ..... 168

**Figure 5.10** - (a, c) DSC and (b, d) TG curves obtained at a heating rate of 10 °C/min from the hydrided composites for the (a, b) 9Mg-Fe and (c, d) 2Mg-Fe stoichiometric ratios ..... 171

**Figure 6.1** - TEM images and the corresponding SAED patterns of the Mg-3GM powder (a-c) in comparison with the C-free Mg powder (d-f), synthesized by the arc-plasma method ..... 193

**Figure 6.2** - SEM micrographs illustrating the morphology of the Mg-3GM powder (a) and the microstructure of its HPT consolidated composite (b, c) ..... 194

**Figure 6.3** - X-ray diffraction (XRD) patterns of (a) the as-synthesized Mg-3GM powder and (c) its hydrided products, and (b) the HPT composite and (d) its hydrided products ..... 197

**Figure 6.4** - Raman spectra of the as-synthesized Mg-3GM powder and its HPT consolidated composites, indicating a strong microstructural modification after the HPT treatments ..... 198

**Figure 6.5** - First and second hydrogenation kinetics obtained at 400 °C under a hydrogen pressure of 3.5 MPa for the as-synthesized Mg-3GM powder and its HPT composite. For comparison, the activation curves for the C-free Mg and its HPT products are also included ..... 200

**Figure 6.6** - Pressure-composition-temperature (PCT) isotherms (a, c) recorded at different temperatures and (b, d) the corresponding van't Hoff plots for the Mg-3GM powder (a) and its HPT consolidated composite (b) ..... 204

**Figure 6.7** - Dynamic hydrogen absorption kinetics recorded at different operating temperatures for (a) the powder precursor and (b) its HPT nanocomposite ..... 206

**Figure 6.8** - (a) DSC and (b) TG curves obtained at a heating rate of 10 °C/min from the final hydrided products for the powder and the HPT composites ..... 208

## Lists of tables

<b>Table 1.1</b> - Gravimetric and volumetric energy content of different kinds of fuels (container weight and volume are excluded), after Ref. [1.3] .....	14
<b>Table 3.1</b> - Phase compositions and crystallographic parameters for the two types of consolidated products determined from the XRD profile refinement .....	88
<b>Table 3.2</b> - Relative density of the HPT products consolidated from the atomized Mg and condensed Mg powder particles .....	105
<b>Table 4.1</b> - The characteristics data of the PCT diagrams for both initial powder precursors and their HPT products .....	124
<b>Table 4.2</b> - The thermodynamic properties obtained from the van't Hoff plots for both initial powders and their HPT products .....	124
<b>Table 4.3</b> - Details of absorption kinetics behaviors for all the studied samples subtracted from their absorption curves given in Figure 4.4 .....	127
<b>Table 4.4</b> – The steady-state hydrogen uptake capacity and phase composition of the hydrided samples .....	131
<b>Table 4.5</b> – The desorption properties of all the hydrided samples subtracted from the DSC-TG curves .....	133
<b>Table 5.1</b> - The compositional details of the HPT-consolidated composites, and their processing conditions applied in the present study .....	149
<b>Table 5.2</b> - The crystallographic data obtained by XRD profile fit analysis for the HPT-processed composites .....	156
<b>Table 5.3</b> - The characteristics data of the PCT diagrams for the 9Mg-Fe composites in comparison with that of the HPT Mg products .....	163
<b>Table 5.4</b> - The characteristics data of the PCT isotherms for the 2Mg-Fe composites .....	165
<b>Table 5.5</b> - The enthalpy of absorption/desorption, and the absorption properties of all the studied composites for both stoichiometric ratios (9Mg-Fe and 2Mg-Fe) .....	167
<b>Table 5.6</b> - Summary of the desorption properties obtained from the DSC-TG analyses of the hydrided composites for both stoichiometric compositions (9Mg-Fe and 2Mg-Fe) .....	172
<b>Table 6.1</b> - Thermodynamics properties of hydrogen absorption/desorption obtained from the PCT measurements of the powder and its HPT composite .....	203

**Table 6.2** - Characteristic properties of hydrogen desorption subtracted from the DSC-TG analyses for both the samples ..... 208

## **Acknowledgements**

To my forever interested, encouraging and always enthusiastic late grandmother Soudamini PANDA: she was always keen to know what I was doing in my study, although she could barely understand the subject. She always inspired me to become a medical doctor and serve the poor people; unfortunately, I couldn't qualify for the same. In the meantime I could able to confess my regrets to her, she left us forever. I always feel her blessings and miss her a lot.

My real so-called “scientific-life” was started from IISc, Bengaluru, which has been continued even at LEM3, Metz. Pursuing doctoral research at LEM3 has been inculcated into me the desire and ability to persevere and excel the excellent education and research. This dissertation work not only represents my work at the keyboard; it is a milestone in three years of work at LEM3 and almost one year of exchange work at NERC, Shanghai Jiao Tong University, China. I have encountered dozens of remarkable individuals whom I would wish to acknowledge.

First and foremost I would like to express my sincere gratitude to my advisor Prof. Thierry GROSDIDIER for his constant guidance and motivation during my doctoral work. Being a new subject it was really challenging for me to work on hydrogen storage in light metals/alloys; but his constant support and ideas made my work smoothly. I also would like to express my sincere gratitude to my co-advisor Prof. Laszlo TOTH whose generosity has no limits since his deliverance is unprejudiced. Prof. TOTH always inspired me for findings most out of my research and provided the moral supports during my stay in Metz. I also would like to extend my sincere gratitude to my co-researcher Prof. ZOU Jianxin for allowing me to work with his vibrant research group (NERC) and providing all facilities required to carry out some important studies. There is no doubt that without their constant guidance and boost ups, this work would not have been completed.

I also would like to thank all the faculty members at LEM3 for allowing me to use the laboratory facilities to carry out my experiments. I am also thankful to Labex DAMAS and LEM3 for funding me during my doctoral studies.

Similarly, I also would like to convey my immense gratitude to all my lab mates (Dr. Yajun, Dr. Cai, Dr. Youssef, Dr. Chunyang, Dr. Marc, Lu Chong, Xi Chen, Yang Bo and Mao) for their helps and encouragements towards my thesis work. Special thanks to Dr. Jean-Jacques for HPT processing, Dr. Julien for EBSD/TKD measurements, and Olivier for XRD/XRT measurements.

Personally, I would like to thank my close friends and junior researchers for being with me when I needed them the most. They helped me not only in my research work but also provided me moral supports and shared their ups and downs with me. They are Dr. Satyapriya, Dr. Satyaveer, Dr. Meriem, Dr. Ruma, Manoj, Sujayda, Monikadi, Nikesh, Harsh, Viet, Amal, Sabrine, Clement, Hua Ke, Yassine, Hana, Maria Rita, Dasha, Yan Ping and Minpeng.

Finally, I would like to mention my beloved parents who made many sacrifices and guided me to see this day. I owe everything to them and would like keep their esteem up for the rest of their lives. Also, I would like to thank Mr. Bikash PAHARI, brother-in-law for his significant contribution towards my educational journey. Though, nothing begins or ends without Him I would offer my humble gratitude to God for letting me be what I am.

## **Related papers published**

The experimental results, obtained from this doctoral program, together with detailed discussion were consequently published in the peer-reviewed international journals. A complete list of papers published or yet to be published are presented as follows.

1. Panda Subrata, Toth LS, Fundenberger JJ, Perroud O, Guyon J, Zou J and Grosdidier T. Analysis of heterogeneities in strain and microstructure in aluminum alloy and magnesium processed by high-pressure torsion. *Materials Characterization* 123 (2017) 159-65.
2. Panda Subrata, Fundenberger JJ, Zhao Y, Zou J, Toth LS and Grosdidier T. Effect of initial powder type on the hydrogen storage properties of high-pressure torsion consolidated Mg. *International Journal of Hydrogen Energy* 42 (2017) 22438-48.
3. Panda Subrata, Toth LS, Zou J and Grosdidier T. Effect of strain heterogeneities on the microstructure, texture, hardness and hydrogen storage activation of high-pressure torsion magnesium consolidated from atomized and condensed powders. Submitted to *Materials*.
4. Panda Subrata, Zou J, Toth LS and Grosdidier T. Effect of various carbonaceous materials on hydrogen sorption properties of Mg/MgO powders synthesized by arc-plasma condensation. Manuscript under preparation.
5. Panda Subrata, Zou J, Toth LS and Grosdidier T. Processing of 9Mg-Fe and 2Mg-Fe based composites using high-pressure torsion consolidation: Microstructures and hydrogen storage properties. Manuscript under preparation.
6. Panda Subrata, Zou J, Toth LS and Grosdidier T. Effects of graphene additive and high-pressure torsion (HPT) on hydrogen sorption properties of condensed Mg powder. Manuscript under preparation.

